

Study of Spectral Lags of Gamma-Ray Bursts Observed
by *HETE-2* and *Fermi*

Department of Physics, Graduate School of Science,
Tokyo Institute of Technology

Makoto Arimoto

February 20th 2009

Abstract

Gamma-Ray Bursts (GRBs) are the most energetic explosions in the universe. Past studies have found that GRBs consist of ultra-relativistic outflows with collimated jets at cosmological distances. It is also known that GRBs are very high-energy gamma-ray ($> \text{GeV}$) emitters. However, it is not clear how the central engine forms and how the electrons or protons are accelerated in shocks and photons are radiated. In addition, GRBs are quite important as a possible distance-indicator. Owing to their very intense brightness, GRBs have become a powerful tool to measure distances in the early universe.

The spectral lag is the time delay in the arrival of lower-energy emission relative to higher-energy emission. The spectral lag of GRBs may be not only a powerful tool to study the radiation mechanism, but also a distance indicator. It has been known that there exists an anti-correlation between the spectral lag and the luminosity from the study of BATSE GRBs above 50 keV energies. Since we can obtain the intrinsic luminosity of GRBs from the lag-luminosity relation, the distance of the GRBs can be derived from the observed flux.

We present the analysis of the spectral lags using 8 GRBs with known redshifts detected by the *HETE-2* satellite (GRB 010921, GRB 020124, GRB 020127, GRB 021211, GRB 030528, GRB 040924, GRB 041006, GRB 050408). Using the WXM and FREGATE instruments aboard *HETE-2*, we investigate the spectral lags between the traditional gamma-ray band (50–400 keV) and the X-ray band (6–25 keV) and derive relations between the spectral lag τ_{lag} and the luminosity L , and between the spectral lag and the duration w for the individual GRB pulses ($L \propto \tau_{\text{lag}}^{-1.2}$, $w \propto \tau_{\text{lag}}^{1.2}$) using a pulse-fit method. The obtained results are consistent with those of BATSE and we verify that the BATSE correlations are still valid at lower energies (6–25 keV). Here, we calculate the lag for the individual pulse, which means that the lag properties are characterized by the *pulse* rather than the whole burst. In addition, we derive a new lag– E_{peak} relation ($E_{\text{peak}} \propto \tau_{\text{lag}}^{-0.3}$) where E_{peak} is the characteristic synchrotron energy, and demonstrate that these relations are well explained by the off-axis model. If we assume that the Yonetoku relation ($L \propto E_{\text{peak}}^{1.8}$) is valid, we find that the lag– E_{peak} relation is inconsistent with the lag-luminosity relation and we can overcome this inconsistency by introducing a systematic uncertainty ($\sigma_{\text{sys}} \sim 0.05 \text{ s}$) or a redshift-dependent lag-luminosity relation (Tsutsui relation). However, only our results cannot determine if the redshift-dependent lag-luminosity (e.g., luminosity evolution) is required or not. Furthermore we investigate the temporal lag and pulse duration evolution as a function of energy. We find that for 60% of the examined pulses the geometrical curvature effect reproduces this evolution, while the evolution for the rest of the pulses cannot be explained only by the curvature

effect, which indicates that the hydrodynamical effect is important and must be taken into account.

We also perform the spectral lag analysis and time-resolved spectral analysis for GRB 080916C which displays GeV emission observed by the LAT and GBM instruments aboard *Fermi*. From the analysis, we find that the GeV emission is delayed from the first X-ray pulse and coincides with the subsequent pulse, suggesting that the origin of this emission is different from that of the X-ray emission. Furthermore we have discovered evidence for an extra high-energy component and its origin could be either (1) anomalous synchrotron emission for which not all the electrons are accelerated, or (2) a relativistic external forward shock.

Contents

1	Gamma-Ray Bursts	11
1.1	What are Gamma-Ray Bursts ?	11
1.1.1	Discovery	11
1.1.2	Compactness Problem and Relativistic Motion	12
1.2	Prompt emission	14
1.2.1	Temporal properties	14
1.2.2	Spectral properties	14
1.2.3	$E_{peak}^{src} - E_{iso}$ relation (Amati relation)	15
1.2.4	$E_{peak}^{src} - L_{iso}$ relation (Yonetoku relation)	16
1.3	Spectral lag	17
1.3.1	Lag - L_{iso} relation (Norris relation)	18
1.3.2	Redshift-dependent lag - L_{iso} relation (Tsutsui relation)	19
1.3.3	The Lag – Luminosity – Duration relation in GRB pulses	21
1.4	Line of Death	22
1.5	Extra High-Energy Component	23
1.6	High-Energy Delayed Emission	25
1.7	Afterglows	26
1.7.1	Evidence for a Relativistic Jet	28
1.7.2	Association with Supernovae	29
1.7.3	Long-lived central engine	30
2	The Fireball Model	32
2.1	Efficiency of Internal Shocks	33
2.2	Shock Conditions	34
2.3	Synchrotron Emission from Relativistic Shocks	37
2.4	Timescale	38
2.4.1	Synchrotron timescale	38
2.4.2	Curvature timescale	39

2.4.3	Hydrodynamical timescale	40
2.5	Integrated Synchrotron Spectrum	42
3	Instrumentation	45
3.1	The HETE-2 satellite	45
3.1.1	The FREGATE	46
3.1.2	The WXM	49
3.1.3	The SXC	54
3.2	<i>Fermi</i> Gamma-ray Space Telescope (GLAST)	57
3.2.1	<i>Fermi</i> Observatory	57
3.2.2	Large Area Telescope	57
3.2.3	Gamma-ray Burst Monitor	64
3.2.4	LAT Instrument Response Functions	67
4	<i>HETE</i> Observations & Analysis results	69
4.1	Motivation	69
4.2	Lag analysis	70
4.2.1	Sample and Selection	70
4.2.2	Method	71
4.2.3	Spectral Model Function	72
4.2.4	Energy Band	73
4.3	Spectral fitting	74
4.3.1	GRB010921	75
4.3.2	GRB020124	76
4.3.3	GRB020127	77
4.3.4	GRB021211	78
4.3.5	GRB030528	81
4.3.6	GRB030725	91
4.3.7	GRB040924	91
4.3.8	GRB041006	92
4.3.9	GRB050408	99
4.3.10	GRB060121	99
4.4	Correlation between spectral lag and other properties	104
4.4.1	Correlation between E_{peak} and L_{iso}	104
4.4.2	Correlation between spectral lag and duration	105
4.4.3	Correlation between spectral lag and L_{iso}	107
4.4.4	Correlation between spectral lag and E_{peak}	107

4.4.5	α index and spectral lag	109
4.5	Energy dependence of spectral lag and other properties	109
4.5.1	Definition and Fit	110
5	Discussion of <i>HETE</i> result	115
5.1	GRB with different viewing angles (off-axis model)	115
5.2	Consistency with the <i>Yonetoku</i> relation	118
5.2.1	Systematic Uncertainty	118
5.2.2	Luminosity evolution as a function of distance	120
5.3	Detailed Energy Dependence of Spectral lag and Other properties	127
5.3.1	Energy Dependence of Duration, Rise and Decay phase	128
5.3.2	Validity of the Curvature Effect on the Spectral Lag	130
5.4	Towards an Unified Theory	135
6	GRB 080916C detected by <i>Fermi</i>	139
6.1	Detection & Observation	139
6.2	Time resolved spectral analysis of the overall burst	140
6.2.1	EBL Effect	142
6.2.2	Amati and Yonetoku relations	143
6.3	Delayed Emission Analysis	143
6.4	Detailed Spectral Analysis for the first phase	147
6.4.1	Spectrum subtracted from the underlying emission	148
6.4.2	The spectrum superimposing the underlying emission	151
6.5	Origin of the extra high energy component	152
6.5.1	Inverse Compton emission (SSC model) ?	152
6.5.2	Synchrotron emission with very high E_{peak} ?	156
6.5.3	Proton induced emission ?	159
6.5.4	Summary of the origin	161
7	Conclusions & Future Prospects	163
7.1	Conclusions	163
7.2	Future Prospects	165
A	The Doppler effect	166
B	The pulse fitting function	168
C	Figure of various correlation-coefficient distributions	170

D	Theoretical model of the curvature effect	172
E	Other GRBs detected by the <i>Fermi</i> LAT	177
E.1	GRB 080825C	177
E.2	GRB 081024B	181
F	Works	184
F.1	Paper	184
F.2	International conference and symposium	188
F.3	National conference and symposium	189

List of Figures

1.1	All sky map by BATSE	12
1.2	T_{90} distribution of the BATSE GRBs	15
1.3	Example of a GRB spectrum (990123)	16
1.4	$E_{\text{iso}} - E_{\text{peak}}$ relation (Amati relation)	17
1.5	$L_{\text{iso}} - E_{\text{peak}}$ relation (Yonetoku relation)	18
1.6	Typical temporal profiles of GRBs at different energies	18
1.7	Lag – luminosity relation (Norris relation)	20
1.8	Redshift-dependent lag-luminosity relation (Tsutsui relation)	21
1.9	Correlation between lag, luminosity, and duration in GRB pulses	22
1.10	Line of death	24
1.11	Extra high-energy emission	25
1.12	High-energy and very long delayed emission of GRB 941017	27
1.13	Images of the fading X-ray afterglow associated with GRB970228	28
1.14	Jet break of GRB 990510	29
1.15	Evidence of the association between GRBs and supernovae	30
1.16	Early X-ray afterglow observed by <i>Swift</i>	31
2.1	Schematic view of <i>fireball model</i>	33
2.2	Schematic view of shocks	35
2.3	Geometrical sketch of the visible part of the fireball	40
2.4	Hydrodynamical evolution	42
2.5	Expected temporal profile and energy dependence of pulse width from the hydrodynamical model	42
2.6	Synchrotron cooling spectrum	44
3.1	Picture of <i>HETE</i> satellite	46
3.2	<i>HETE</i> satellite on the Pegasus rocket	46
3.3	Schematic figure of the <i>HETE</i> satellite	47
3.4	Picture of the FREGATE detector	48

3.5	Schematic drawing of one FREGATE detector	48
3.6	Effective area of FREGATE	49
3.7	Picture of WXM	51
3.8	Dimensions of the entire WXM system	51
3.9	Cross section of one PSPC of the WXM	52
3.10	Effective area of one PSPC at the boresight incidence.	52
3.11	SXC (Soft X-ray Camera)	56
3.12	View of <i>Fermi</i> conceptual design with the GLAST burst monitor (GBM) and the Large-Area Telescope (LAT).	58
3.13	<i>Fermi</i> launch on 11 June 2008	58
3.14	Cutaway view of the LAT detector	59
3.15	Measurement of a gamma-ray conversion in the Tracker	60
3.16	Silicon strip sensor of the LAT detector	61
3.17	Exploded view of a tray	62
3.18	Inverted view of one tracker tower module without a sidewall	63
3.19	The Calorimeter (CsI crystal)	63
3.20	The assembled ACD	64
3.21	Side and cross views of the NaI(Tl) scintillator coupled with a PMT.	65
3.22	Side view of the BGO detector	65
3.23	Effective areas of NaI(Tl) and BGO detectors	66
3.24	Energy resolution of the NaI(Tl) and BGO detectors	66
4.1	Pulse function of Norris et al., 2005	72
4.2	Adopted energy bands in the burst-rest frame	74
4.3	Pulse fit for GRB 010921 in the observer's frame	76
4.4	Pulse fit for GRB 010921 in the rest frame	77
4.5	Pulse fit for GRB 010921 in the multi-divided bands	83
4.6	Pulse fit for GRB 020124 in the observer frame	84
4.7	Pulse fit for GRB 020124 in the rest frame	84
4.8	Pulse fit for GRB 020127 in the observer's frame	85
4.9	Pulse fit for GRB 020127 in the rest frame	85
4.10	Pulse fit for GRB 020127 in the multi-divided bands	86
4.11	Pulse fit for GRB 021211 in the observer frame	87
4.12	Pulse fit for GRB 021211 in the rest frame	87
4.13	Pulse fit for GRB 021211 in the multi-divided bands	88
4.14	Pulse fit for GRB 030528 in the multi-divided bands	89
4.15	Pulse fit for GRB 030528 in the observer frame	90

4.16	Pulse fit for GRB 030528 in the rest frame	90
4.17	Pulse fit for GRB 030725 in the multi-divided bands	95
4.18	Pulse fit for GRB 040924 in the observer frame	96
4.19	Pulse fit for GRB 040924 in the rest frame	96
4.20	Pulse fit for GRB 040924 in the multi-divided bands	97
4.21	Pulse fit for GRB 041006 in the observer frame	98
4.22	Pulse fit for GRB 041006 in the rest frame	98
4.23	Pulse fit for GRB 050408 in the observer's frame	100
4.24	Pulse fit for GRB 050408 in the rest frame	101
4.25	Pulse fit for GRB 0050408 in the multi-divided bands	102
4.26	Pulse fit for GRB 060121 in the multi-divided bands	103
4.27	Scatter plot of E_{peak} vs. L_{iso}	105
4.28	Scatter plot between spectral lag and duration in the observer's frame . . .	106
4.29	Distribution of the correlation coefficient between spectral lag and duration in the observer's frame	106
4.30	Scatter plot of spectral lag vs. duration in the rest frame	107
4.31	Scatter plot of spectral lag vs. luminosity	108
4.32	Scatter plot of spectral lag vs. E_{peak}	108
4.33	Scatter plot of spectral lag vs. α	109
4.34	Energy vs. T_{peak} plots	111
4.35	Energy vs. Duration (FWHM) plots.	112
4.36	Energy vs. rise time plots.	113
4.37	Energy vs. decay time plots	114
5.1	Schematic view of off-axis model	116
5.2	Spectral shape with different smoothness	117
5.3	Analytical result of lag-luminosity or -duration relations	117
5.4	Observational results superimposing theoretical curves for lag-duration and - E_{peak} relation	119
5.5	Lag-luminosity and - E_{peak} plots including the systematic uncertainty . . .	120
5.6	Redshift-dependent lag-luminosity relation	121
5.7	Redshift-dependent lag- E_{peak} relation	122
5.8	Contour map over a range of α_z and $\alpha_{\tau_{\text{lag}}}$ for L_{iso}	123
5.9	Contour map over a range of α_z and $\beta_{\tau_{\text{lag}}}$ for E_{peak}	124
5.10	Selection effect in the derived Tsutsui relation	127
5.11	Scatter plots of α_{lag} and α_{FWHM} , α_{rise} , α_{dec} , α_{photon}	129
5.12	The scatter plots for indices of α_{FWHM} , α_{rise} and α_{dec}	131

5.13	Theoretical relationship between the lag and the energy	132
5.14	Schematic view of the spectral lag by curvature effect	135
5.15	Energy vs T_{peak} plots with the theoretical model, showing good agreement with the curvature case	137
5.16	Energy vs T_{peak} plots with the theoretical model, showing poor agreement with the curvature case	138
6.1	Light curve of 080916C observed by the GBM and LAT detectors, from lower to higher energies.	141
6.2	Plots of GRB080916C for the Amati and Yonetoku relation	143
6.3	Count spectra for corresponding time intervals of (a), (b), (c), (d) and (e).	144
6.4	Light curve of 080916C at $T_0 - 5$ s to $T_0 + 20$ s and pulse-fit result.	146
6.5	Energy vs. t_{peak} plots and energy vs. duration plots for GRB 080916C	147
6.6	Zoom on the light curve from -2 s to 12 s with fine time resolution	147
6.7	Detailed spectral analysis for the early phase of GRB 080916C	149
6.8	Average spectrum during $T_0 + 4$ s to 5 s and $T_0 + 7$ s to 8 s (underlying emission)	150
6.9	Underlying emission subtracted spectrum	150
6.10	Subtracted count spectrum around 0 counts/keV	151
6.11	Underlying emission superimposed on the extra spectrum	154
6.12	Theoretical proton-induced spectrum of GRB 080916C	160
6.13	Proton-induced spectrum of GRB 080916C superimposed on the observa- tional data	161
C.1	Distributions of the correlation coefficient	171
E.1	Light curve of 0800825C observed by the GBM and LAT detectors	178
E.2	Pulse-fit result for GRB 080825C	179
E.3	Spectral-fit result for GRB 080825C	180
E.4	Long sub-GeV emission	180
E.5	Light curves for GRB 081024B	182
E.6	Energy vs. t_{peak} plot for GRB081024B	182
E.7	Spectral lag of CCF for GRB 081024B	183

List of Tables

3.1	Specifications of the <i>HETE</i> satellite	46
3.2	Performance of FREGATE	48
3.3	FREGATE data types	49
3.4	Characteristics of the WXM	53
3.5	WXM data types	53
3.6	Performance of LAT	60
4.1	GRB samples	70
4.2	Lag properties of GRB 010921 in the observer frame	75
4.3	Lag properties of GRB010921 in the rest frame	75
4.4	Spectral properties of GRB 010921	76
4.5	Lag properties of GRB 020124 in the observer's frame	78
4.6	Lag properties of GRB020124 in the rest frame	78
4.7	Spectral properties of GRB 020124	79
4.8	Lag properties of GRB 020127 in the observer's frame	79
4.9	Lag properties of GRB020127 in the rest frame	79
4.10	Spectral properties of GRB 020127	80
4.11	Lag properties of GRB 021211 in the observer frame	80
4.12	Lag properties of GRB021211 in the rest frame	80
4.13	Spectral properties of GRB 021211	81
4.14	Lag properties of GRB 030528 in the observer's frame	81
4.15	Lag properties of GRB 030528 in the rest frame	82
4.16	Spectral properties of GRB 030528	82
4.17	Spectral properties of GRB 030725	91
4.18	Lag properties of GRB 040924 in the observer frame	92
4.19	Lag properties of GRB 040924 in the rest frame	92
4.20	Spectral properties of GRB 040924	92
4.21	Lag properties of GRB 041006 in the observer's frame	93
4.22	Lag properties of GRB 041006 in the rest frame	94

4.23	Spectral properties of GRB 041006	94
4.24	Lag properties of GRB 050408 in the observer's frame	99
4.25	Lag properties of GRB 050408 in the rest frame	99
4.26	Spectral properties of GRB 050408	100
4.27	Spectral properties of GRB 060121	101
5.1	Summary of the temporal evolution of the duration and spectral lag as a function of energy	134
6.1	Fit parameters for the Band function for GRB 080916C	140
6.2	Lag at different energies for GRB 080916C	147
6.3	Fit parameters for the underlying emission	148
6.4	Fit parameters for the underlying emission subtracted spectrum	151
6.5	Spectral-fit results of underlying emission and extra components	153
E.1	Spectral properties for GRB 081024B	183

Chapter 1

Gamma-Ray Bursts

In this chapter, we introduce the observed properties, historical background, emission features including the spectral lags and high energy gamma-rays and discuss some possible origins of gamma-ray bursts.

1.1 What are Gamma-Ray Bursts ?

1.1.1 Discovery

Gamma-ray bursts (GRBs) are the brightest explosions in the entire sky. The first GRB was discovered accidentally by the Vela military satellites (Klebesadel et al. 1973) in the late 1960's.

GRBs have the following properties; (1) their durations are $10 \text{ ms} \sim 1000 \text{ s}$, (2) typical photon energies ranges from a few keV to a few MeV, (3) their spectra are well fitted by two powerlaw functions connected smoothly, called the Band function (Band et al. 1993), implying that GRB emission is non-thermal. (4) after the main emission, called *prompt emission*, GRBs emit a faint fading emission over a wide range from radio to X-ray, called the *afterglow*. However note that not all the GRBs display an afterglow.

The BATSE detector on the Compton Gamma-Ray Observatory (CGRO: Preece et al. 2000) gave us invaluable information about GRB spectra and their angular distribution. In particular BATSE showed that the angular distribution of GRBs is isotropic as shown in Fig. 1.1 and that the GRBs are likely to come not from galactic sources, but extragalactic ones, that is, the GRBs occur at *cosmological* distances. (Meegan et al. 1992). The critical discovery was the afterglow of GRB 970508 (Metzger et al. 1997). GRB 970508 was detected by instruments aboard the Italian-Dutch satellite BeppoSAX (Boella et al. 1997) and the X-ray telescope succeeded in localizing the GRB position with a $3'$ error

radius at the 99-percent confidence level (Heise et al. 1997). Then optical telescopes on the ground performed spectroscopic observations pointing at the reported field after receiving the position information. As a result of the observation, a few prominent absorption lines, which were reddened by cosmological expansion, were found and the presence of an absorption system along the line of sight at $z = 0.835$ was discovered. This result showed that the GRBs are definitely at cosmological distances.

2704 BATSE Gamma-Ray Bursts

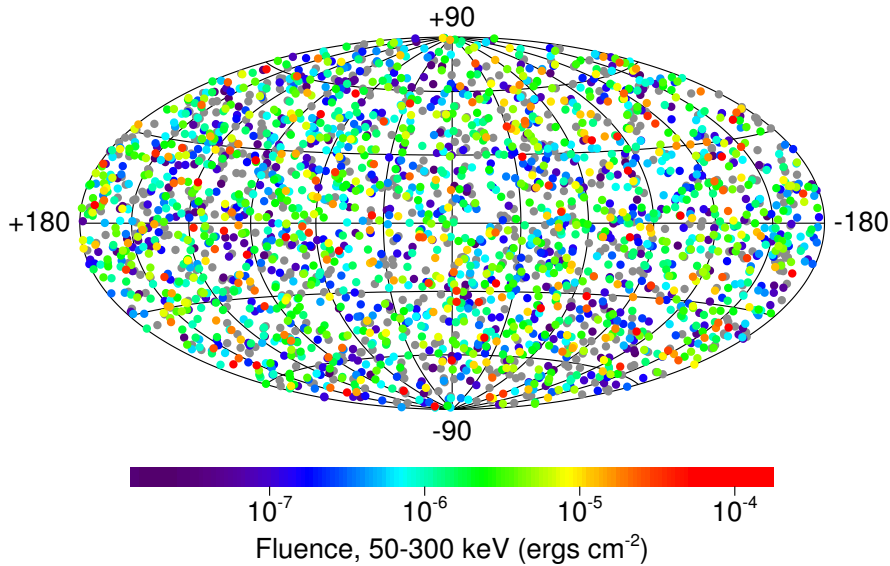


Figure 1.1: All sky map of 2704 BATSE GRBs during the nine year mission. Not clustering along the Galactic plane but isotropic distribution was found. The corresponding colors represent the intensity of GRBs (<http://www.batse.msfc.nasa.gov/batse/grb/skymap/>).

1.1.2 Compactness Problem and Relativistic Motion

Now, we understand that GRBs are cosmological and assuming a typical distance $d \sim 3000 \text{ Mpc} \sim 10^{28} \text{ cm}$ and a typical observed flux $f \sim 10^{-6} \text{ erg cm}^{-2} \text{ s}^{-1}$, the isotropic luminosity L_γ is $4\pi d^2 f \sim 10^{51} \text{ erg s}^{-1}$. Considering that an ordinary galaxy has $L_g \sim 10^{43} \text{ erg s}^{-1}$, $L_\gamma \sim 10^8 L_g \sim$ the total luminosity of all the galaxies, suggesting that the GRBs are the most intense explosions in the universe. But this brightness causes a serious problem. The rapid temporal variability on a time scale $\Delta t \sim 10 \text{ ms}$ implies that the sources are compact with a size $R < c\delta t \sim 3000 \text{ km}$. During such a timescale, an energy $L_\gamma \Delta t \sim 10^{49} \text{ erg}$ is released. The observed non-thermal spectrum contains a large

fraction of high energy γ -ray photons. These photons (with energy E_1) could interact with lower energy photons (with E_2) and produce electron-positron pairs via $\gamma + \gamma \rightarrow e^+ + e^-$ if $\sqrt{E_1 E_2} > m_e c^2$. Denote by f_p the fraction of photon pairs that satisfy this condition. The cross section where one electron-positron pairs can be created is approximately equal to the Thomson cross section σ_T , so the total pair-creation cross section is $\sigma_T f_p L_\gamma \Delta t / m_e c^2$. The optical depth is given by the ratio of the total pair-creation cross section to the region size

$$\tau_{\gamma\gamma} \sim \frac{f_p \sigma_T L_\gamma \Delta t}{R^2 m_e c^2} \sim 10^{14} f_p \left(\frac{L_\gamma}{10^{51} \text{ erg}} \right) \left(\frac{\Delta t}{10 \text{ ms}} \right)^{-1} \quad (1.1)$$

This optical depth is very large, which means that the photon cannot escape from inside since the created photons induce pair creations. However, the observed non-thermal spectrum indicates with certainty that the sources must be optically thin.

Relativistic motion enables us to overcome this problem. Consider a source of radiation that is moving towards an observer at rest with a relativistic velocity characterized by a Lorentz factor, $\Gamma = 1/\sqrt{1 - v^2/c^2} \gg 1$. Photons with an observed energy $h\nu_{\text{obs}}$ have been blue shifted and their energy at the source frame was $\sim h\nu_{\text{obs}}/\Gamma$, e.g., the hard X-ray photons ~ 100 keV in the observer frame has a few keV energy (soft X-ray) in the source frame assuming $\Gamma \sim 100$. Since the energy in the source frame is lower fewer photons have sufficient energy to produce pairs. Now the observed fraction f_p of photons that could produce pairs is not equal to the fraction of photons that could produce pairs at the source frame. Here the count spectrum of the observed spectrum is $N(E)dE \propto E^{\beta_B} dE$, where β_B is the high-energy photon index (typically -2) and the pair creation condition is $E'_1 E'_2 > (m_e c^2)^2$ in the source frame. Then in the observer frame, as $E_1 > \Gamma^2 (m_e c^2)^2 / E_2 \propto \Gamma^2$, the fraction $f_p \propto \int_{E_1} N(E) dE \propto E_1^{\beta_B+1} \propto \Gamma^{2(\beta_B+1)}$. This is smaller by a factor $\Gamma^{2(\beta_B+1)}$ than the observed fraction. At the same time, relativistic effects allow the radius from which the radiation is emitted, $R_e < \Gamma^2 c \Delta t$ to be larger than the original estimate, $R_e < c \Delta t$, by a factor of Γ^2 . We have

$$\tau_{\gamma\gamma} \sim \frac{10^{14}}{\Gamma^{4-2(\beta_B+1)}} f_p \left(\frac{L_\gamma}{10^{51} \text{ erg}} \right) \left(\frac{\Delta t}{10 \text{ ms}} \right)^{-1} \quad (1.2)$$

The compactness problem can be resolved if the source is moving relativistically towards us with a Lorentz factor $\Gamma > 10^{14/(4-2(\beta_B+1))} \sim 100$, which satisfies $\tau_{\gamma\gamma} < 1$. Thus, we have found that GRBs are ultra-relativistic explosions.

1.2 Prompt emission

1.2.1 Temporal properties

GRBs have a variety of temporal pulse profiles (Fishman & Meegan 1995, Fishman et al. 1994). Some GRBs have a single pulse or spike, or distinct well-separated pulses, while other GRBs are very chaotic, spiky and show overlapping bursts. A particular subclass of these GRBs are the so-called FREDs (Fast Rise, Exponential Decay), in which the rise time is very much shorter than the fall time. The decaying portion is not strictly an exponential function but has a continually decreasing slope. As for the durations, interestingly a bimodal distribution was found as shown in Fig. 1.2. Approximately, GRBs may be divided into two types; short GRBs which have $T_{90} < 2$ s and long GRBs which have $T_{90} > 2$ s, where T_{90} is the observed duration including 90 % of the total observed counts from GRBs. Furthermore the bimodal distribution indicates that the two different kinds of GRBs have different origins. Actually, only very recently have a few of the short bursts been well localized, and initial studies of their apparent hosts indicate that these bursts may be formed by the merger of neutron-star or black-hole binaries (Gehrels et al. 2005). In contrast, the afterglows of over 80 long GRBs have been detected in the optical and/or radio parts of the spectrum. As a result of these detections, it has become clear that long GRBs, like core-collapse supernovae, are related to the deaths of young, massive stars (e.g. GRB 030329; Hjorth et al. 2003).

1.2.2 Spectral properties

The GRB non-thermal spectrum is well represented by the Band function (Band et al. 1993) empirically. The Band function consists of 2 power-laws connected smoothly. The function is given by

$$N(E) = \begin{cases} A(E/K)^\alpha \exp\left(-\frac{E}{E_0}\right) & \text{for } E \leq (\alpha - \beta)E_0 \\ A(E/K)^\beta \exp(\beta - \alpha) \left(\frac{(\alpha - \beta)E_0}{K}\right)^{\alpha - \beta} & \text{for } E \geq (\alpha - \beta)E_0 \end{cases} \quad (1.3)$$

where $N(E)$ is the amplitude in units of photons $\text{s}^{-1} \text{cm}^{-2} \text{keV}^{-1}$, E_0 is the spectral break energy in the count flux space, α and β are the low- and high-energy spectral indices, and K is an arbitrary pivot energy (typical value 100 keV). In the case of $\beta < -2$ and $\alpha > -2$, the maximum peak energy in νF_ν space is given by $E_{\text{peak}} \equiv (2 + \alpha) E_0$ (Here, the νF_ν space has a dimension of $E^2 N(E)$), because the peak of νF_ν is determined at the energy where the differential coefficient of $E^2 N(E)$ is equal to zero.

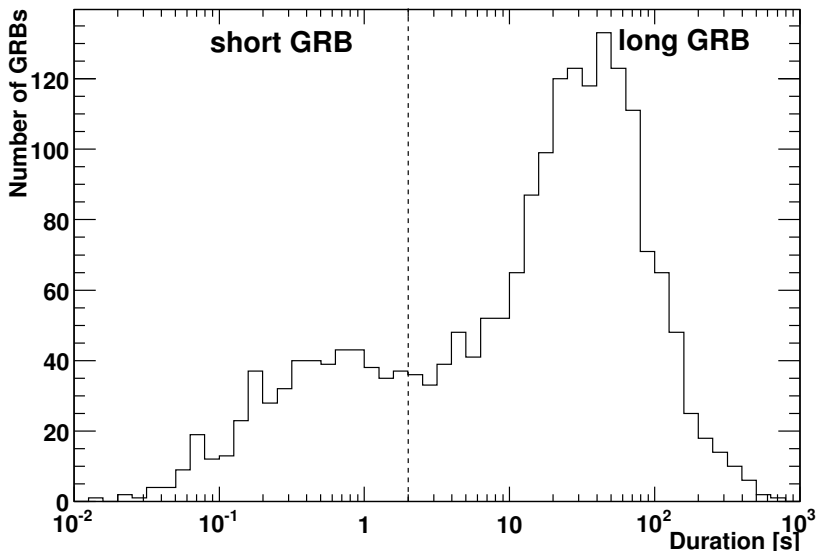


Figure 1.2: T_{90} distribution of the BATSE GRBs from the archive of the current catalog (<http://www.batse.msfc.nasa.gov/batse/grb/catalog/current/>). There exists roughly two populations; short GRBs ($T_{90} < 2$ s) and long GRBs ($T_{90} > 2$ s)

Using $E_{\text{peak}} = (2 + \alpha) E_0$, the above formula is transformed to the following.

$$N(E) = \begin{cases} A(E/K)^\alpha \exp\left(-\frac{E}{E_{\text{peak}}/(2+\alpha)}\right) & \text{for } E \leq (\alpha - \beta)E_{\text{peak}}/(2 + \alpha) \\ A(E/K)^\beta \exp(\beta - \alpha) \left(\frac{(\alpha - \beta)E_{\text{peak}}/(2 + \alpha)}{K}\right)^{\alpha - \beta} & \text{for } E \geq (\alpha - \beta)E_{\text{peak}}/(2 + \alpha) \end{cases} \quad (1.4)$$

This smooth-broken powerlaw shape represents the emission mechanism of GRBs which is synchrotron radiation via shock accelerated electrons. An example of a GRB spectrum and its superimposed Band function is given in Fig. 1.3 (Briggs et al. 1999).

1.2.3 $E_{\text{peak}}^{\text{src}} - E_{\text{iso}}$ relation (Amati relation)

Amati et al. 2002 investigated the spectral and energetic properties of 12 *BeppoSAX* GRBs with known redshifts. They calculated the spectral parameters of time-averaged spectra in the GRB rest frame, which means the redshift-corrected spectra, and the isotropic equivalent energies E_{iso} in the 1–10000 keV range. They then found a strong correlation between E_{iso} and $E_{\text{peak}}^{\text{src}}$, which corresponds to the synchrotron-emission peak energy for the lowest energy of electrons γ_m in the rest frame; $E_{\text{peak}}^{\text{src}} \propto E_{\text{iso}}^{0.5}$ (Fig. 1.4). They updated their own study (Amati 2006) using 41 long GRBs and furthermore Sakamoto et al. 2005 and Sakamoto et al. 2008 investigated a large number of *HETE* and *Swift* GRBs, and

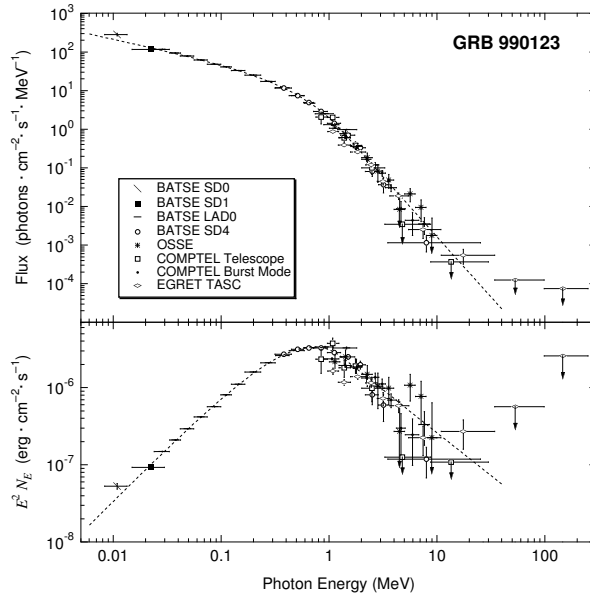


Figure 1.3: Example of a GRB spectrum (990123) observed by CGRO Briggs et al. 1999. The horizontal axis presents the energy at the GRB’s rest frame. The upper panel shows the count spectrum in units of photon $\text{cm}^{-2} \text{s}^{-1} \text{MeV}^{-1}$ and the lower one shows the νF_ν spectrum in units of $\text{erg cm}^{-2} \text{s}^{-1}$. The dashed line represents the best-fit Band function.

found that the correlation was strongly confirmed as shown in Fig. 1.4. Furthermore they determined new categories of GRBs such as X-ray Flashes (XRFs) and X-ray Rich GRBs (XRRs), distinguished from the classical GRB. As their distribution is continuous, we can consider that XRFs, XRRs and classical GRBs have the same origin.

An empirical relation which is a very powerful tool as a redshift indicator to estimate the distance to GRBs with unknown redshift determines the *pseudo* redshift. Pélangéon et al. 2008 presented a study of a sample containing all the GRBs detected by *HETE* and derived the GRB rate in the local universe.

1.2.4 $E_{peak}^{src} - L_{iso}$ relation (Yonetoku relation)

Yonetoku et al. 2004 investigated the time-resolved spectral characteristics detected by BeppoSax with firmly known redshift and BATSE, and found that the relation between the spectral peak energy E_{peak}^{src} in the GRB rest frame and peak luminosity L_{iso} (Fig. 1.5).

$$L_{52} = (2.34_{-1.76}^{+2.29}) \times 10^{-5} \left(\frac{E_{peak}^{obs}(1+z)}{1keV} \right)^{2.0 \pm 0.2}$$

where the quoted uncertainties have a 1σ uncertainty, L_{52} is the luminosity in units of 10^{52}

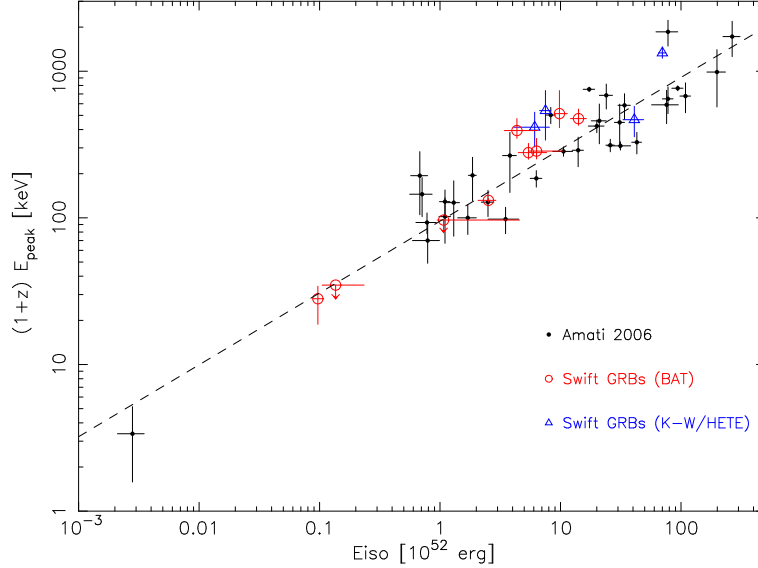


Figure 1.4: Isotropic equivalent energy, E_{iso} , vs. the peak energy in the GRB rest frame, $E_{\text{peak}}^{\text{src}} = E_{\text{peak}}(1+z)$. The known redshift BAT GRBs are presented by circles, BATSE, *BeppoSax* and *HETE*, *Konus-Wind* by dots, and the known redshift *Swift* GRBs observed by *Konus-Wind* or *HETE* by triangles. The dashed line is the best-fit correlation reported by Amati 2006.

ergs s^{-1} , $E_{\text{peak}}^{\text{obs}}$ is the E_{peak} in the observer frame, and z is the redshift. The correlation is very robust (correlation coefficient: $R = 0.958$). This relation is also a powerful tool as a redshift indicator like that described in Sec. 1.2.3.

They estimated the GRB formation rate using the relation with 689 unknown-redshift GRBs detected by BATSE. The result indicates that the GRB formation rate does not decrease toward higher z as shown in Fig. 1.5.

1.3 Spectral lag

One of the characteristics of GRB prompt emission is the spectral lag. It is the delay of the photons in the soft energy band with respect to the higher energy one in the GRB light curve. Fig. 1.6 demonstrates the observed and schematic spectral lags in GRB temporal profiles. From the theoretical point of view, the spectral lag is important because it could be an indicator of the jet opening angle and of the Lorentz factor suggested by Ioka & Nakamura 2001.

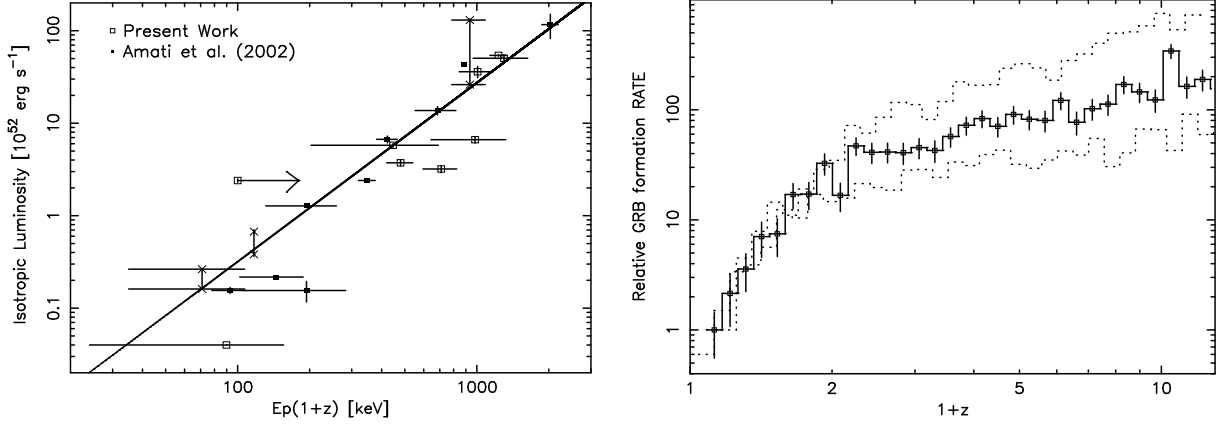


Figure 1.5: *left*: Isotropic peak luminosity, L_{iso} , vs. the peak energy in the GRB rest frame, $E_{\text{peak}}^{\text{src}} = E_{\text{peak}}(1+z)$. The BATSE GRBs with know redshift are presented by open circles, *BeppoSax* GRBs by filled squares (Amati et al. 2002). The solid line is the best-fit power-law model. *right*: GRB formation rate normalized at the first point. The solid line is the result based on the best fit of the $E_{\text{peak}}^{\text{src}} - L_{\text{iso}}$ relation. Two dotted lines indicate the upper and lower bounds caused by the uncertainty of the $E_{\text{peak}}^{\text{src}} - L_{\text{iso}}$ relation, and they are also normalized at the first point. (Yonetoku et al. 2004)

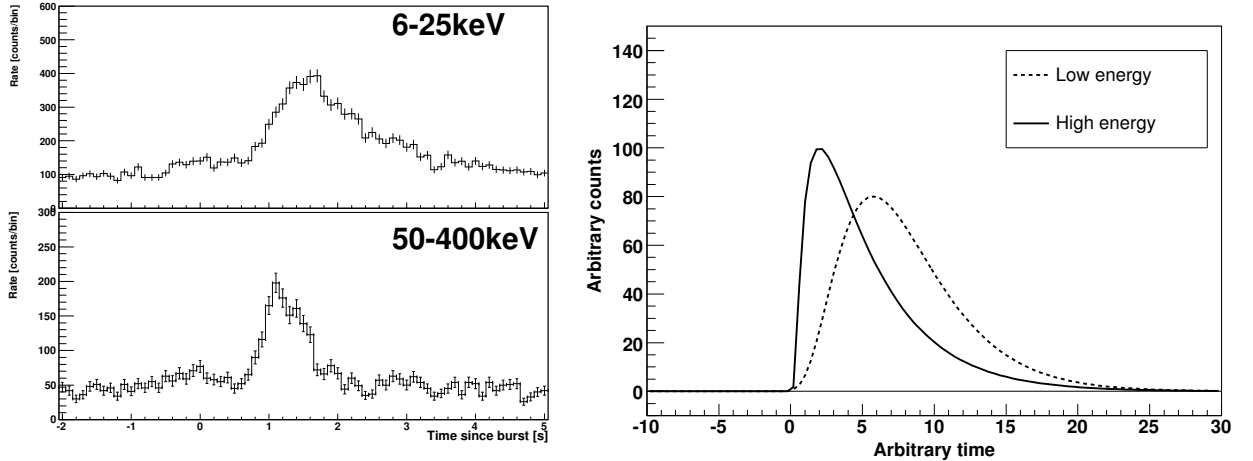


Figure 1.6: Typical temporal profiles of GRBs at different energies. *left*: light curves of GRB 040924 detected by *HETE-2* in the 6–25 keV and 50–400 keV ranges. Many GRBs display spectral lags (the delay of the photons in the soft energy band with respect to the higher energy band). *right*: a schematic view of the spectral lag in light curves of GRBs.

1.3.1 Lag - L_{iso} relation (Norris relation)

Norris et al. 2000 found a connection between the spectral lag and luminosity for their subset of six GRBs with known redshift. They calculated the lags of GRBs detected by

BATSE and *BeppoSAX* using the cross-correlation function (CCF) between 25 – 50 keV and 100 – 300 keV. The relationship they obtained is illustrated in Fig. 1.7 and is,

$$L_{53} \approx 1.3 \times (\tau/0.01s)^{-1.14}$$

where L_{53} is the luminosity in units of 10^{53} erg s^{-1} and τ is the CCF lag corrected for time dilation using $(1+z)$. An anti-correlation was obtained. The right panel of figure 1.7 shows the luminosity and lag ranges expanded to include GRB 980425, which has a single long pulse. The lag of the GRB was very long (~ 4.5 s) and its luminosity was extremely low; this signature falls below the fitted power-law function for the 6 bursts by a factor of $\sim 400 - 700$.

Ioka & Nakamura 2001 computed the kinematic dependence of the peak luminosity, the pulse duration, and the spectral lag of the peak luminosity on the viewing angle θ_v of a jet. By choosing appropriate model parameters, they obtained a peak luminosity – spectral lag relation which can account for the observed anti-correlation, including GRB 980425. The model says that a bright (dim) peak with short (long) spectral lag corresponds to a jet with small (large) viewing angle.

1.3.2 Redshift-dependent lag - L_{iso} relation (Tsutsui relation)

Tsutsui et al. 2008a investigated the CCF lag-luminosity relation to validate the Amati relation ($E_{\text{peak}} - E_{\text{iso}}$), the Yonetoku relation ($E_{\text{peak}} - L_{\text{iso}}$) and the Norris relation ($\tau_{\text{lag}} - L_{\text{iso}}$).

They compared redshifts z_Y estimated from the Yonetoku relation and z_{lag} from the Norris (lag-luminosity) relation using 565 GRBs detected by BATSE. Assuming that the luminosity and spectral lag τ_{lag} leads to z_Y and z_{lag} , respectively, they showed that z_Y is not compatible with z_{lag} (the left panel of Fig. 1.8) and that some modification is therefore needed. Next, they used z_Y and confirmed the validity of the Amati relation and the Yonetoku one; this implies that the Norris relation is responsible for the incompatibility. They then found that the existence of the redshift dependence effect should be taken into account and the empirical redshift-dependent relation was derived as

$$L_{52} = 0.0758 \times (1+z)^{2.53} (\tau_{\text{lag}})^{-0.282} \quad (1.5)$$

where L_{52} is the luminosity in units of 10^{52} erg s^{-1} . The plot in the right panel of Fig. 1.8 shows the new anti-correlation between the peak luminosity and redshift-dependent lag; its correlation coefficient is 0.77 with a chance probability of 7.9×10^{-75} . Furthermore, the relation is valid not only for the data set of their samples but also that of the same 6 GRBs used by Norris et al. 2000.

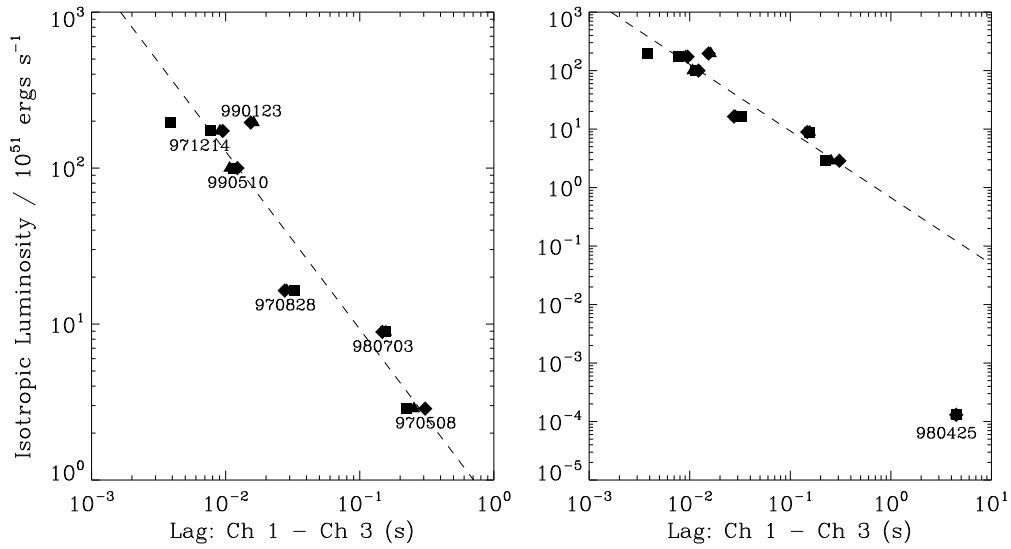


Figure 1.7: *left*: CCF lags between 25 – 50 keV and 100 – 300 keV vs. peak luminosity, for the subset of 6 bursts with known redshift. The dashed line is a fitted power-law to the lags for intervals including count rates greater than $0.1 \times$ peak intensity (*squares*), yielding $L_{53} \approx 1.3 \times (\tau/0.01s)^{-1.14}$. *right*: the luminosity range is expanded to include GRB 98045, which falls below the extrapolated power-law by a factor of $\sim 400 - 700$. (Norris et al. 2000)

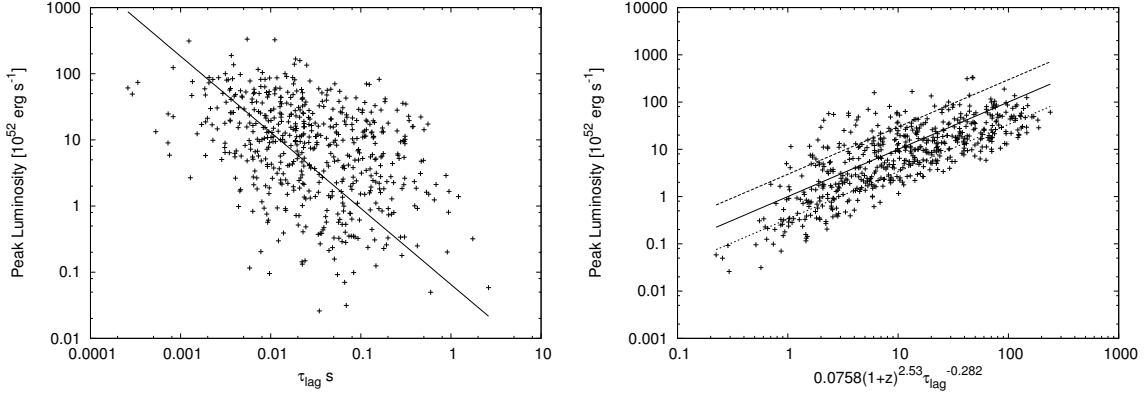


Figure 1.8: *left*: τ_{lag} vs. L_{52} using z_Y for 565 BATSE GRBs. The points are scattered and the correlation coefficient is low ($R = 0.38$). *right*: The redshift-dependent lag-luminosity relation (Tsutsui relation, $0.0758(1+z)^{2.53}\tau_{\text{lag}}^{-0.282}$ vs. L_{52}). The correlation coefficient is high ($R = 0.77$). The solid line is the best and the two dashed lines are 1σ confidence levels. (Tsutsui et al. 2008a)

1.3.3 The Lag – Luminosity – Duration relation in GRB pulses

Hakkila et al. 2008 derived a peak lag versus peak luminosity relation for GRB pulses. In past studies the spectral lag was calculated by the CCF method over the whole burst. In this manner, the calculated lag characterizes the delay of the entire burst, not each pulse, with regard to the high-energy emission. Hakkila et al. 2008 studied the spectral lag for “each pulse” using the pulse model of Norris et al., 2005. They defined *pulse peak lags* as the differences between the pulse peak times in different energy bands (especially 25 – 50 keV and 100 – 300 keV). The definition of pulse duration w was based on time intervals at the intensity level Ae^{-3} (where A is the pulse amplitude).

They found two important correlations in a sample of 12 pulses in 7 BATSE GRBs with known redshifts and 38 pulses from 22 BATSE GRBs without known redshift (assuming $z = 1$). The correlations are (1) the luminosity decreases with increasing lag and (2) pulse duration increases with increasing lag as illustrated in Fig. 1.9. The pulse peak lag, pulse duration, and pulse intensity are corrected to the GRB rest frame. The left panel of Fig. 1.9 demonstrates the pulse peak luminosity L_{51} (the isotropic pulse luminosity L in units of 10^{51} ergs s^{-1}) versus the rest-frame pulse peak lag l_0 (observer-frame lag divided by $1+z$); this is similar to the Norris relation (Norris et al. 2000), except that it has been applied to *pulses* rather than to the bursts themselves (The best fit functional form is $\log(L_{51}) = (0.54 \pm 0.05) - (0.62 \pm 0.04) \log(l_0)$ with $R = -0.72$). The power-law index is slightly different from that of the Norris relation (-1.14 ± 0.10). This is because the pulse peak lag versus pulse peak luminosity relation is a fundamental one while the CCF lag

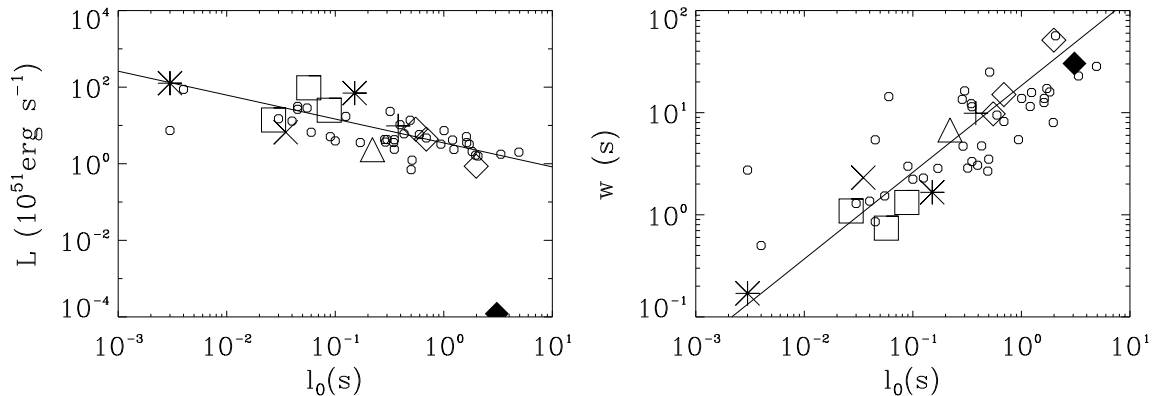


Figure 1.9: *left*: Pulse peak luminosity L vs. pulse peak lag l_0 for pulses of BATSE GRBs having known redshifts. The sample consists of pulses from GRB 971214 (*asterisks*), GRB 980703 (*open diamonds*), GRB 970508 (*triangles*), GRB 990510 (*squares*), GRB 991216 (*crosses*), and the under-luminous GRB 990123 (*filled diamonds*). Also plotted are 38 pulses in 22 BATSE GRBs without known redshifts (*small circles*) assuming $z = 1$. *right*: Pulse duration w_0 vs. pulse peak lag l_0 . (Hakkila et al. 2008)

versus peak luminosity relation is of secondary importance. The right panel of Fig. 1.9 demonstrates the the rest-frame pulse duration w_0 versus pulse lag l_0 ; its correlation is very robust over 4 orders of magnitude in both duration and lag (The best fit functional form is $\log(w_0) = (1.27 \pm 0.01) + (0.85 \pm 0.01) \log(l_0)$ with $R = 0.95$).

Furthermore, from the above two correlations, they found a strong correlation between *pulse width and pulse peak luminosity* (the best fit functional form is $\log(L_{51}) = (1.53 \pm 0.02) + (-0.85 \pm 0.02) \log(w_0)$ with $R = -0.88$). This result shows that the pulse lag, pulse luminosity, and pulse duration are strongly correlated, implying that most GRB pulses have similar physical mechanisms.

1.4 Line of Death

Preece et al. 1998 studied the distribution of the low-energy spectral index (α) of the BATSE GRBs and Sato et al. 2005 also investigated α for GRB 020813 detected by *HETE*.

The synchrotron shock model (SSM; see a review by Piran 1999 and Rybicki & Lightman 1986) predicts that the low energy power-law photon number spectral index α ($dN/dE \propto E^\alpha$) cannot exceed $-2/3$. But there are a large number of GRBs that violate the limit on the low-energy spectral behavior imposed by the basic synchrotron emission

mechanism acting in a relativistic shock. Fig. 1.10 shows the results from the time-resolved spectra of BATSE bright bursts and the $\alpha = -2/3$ (“death line”, represented by a dashed line) and the lower boundary of the cooling spectrum ($\alpha = -3/2$, represented by a dotted line) which corresponds to the characteristic cooling distribution of particles with a power-law index p of -2. (The electron power-law index p is translated into the photon power-law index of $-3/2$ using $\alpha = -(p - 1)/2$, Rybicki & Lightman 1986)

To explain the violation, several models are suggested: a Compton-upscattering model, a synchrotron self-absorption model, and a jitter radiation model.

In the first case, Compton upscattering of soft photons by an energetic distribution of particles can significantly change the basic synchrotron emission spectrum, with energetic particles upscattering their own synchrotron radiation into the observed X-ray or gamma-ray band (Liang et al. 1997). In this case we could observe bursts with the low-energy photon index $\alpha > -2/3$.

In the second case, synchrotron self-absorption (SSA) would tend to steepen the low-energy continuum. The maximum photon spectral index that could be obtained is $3/2$ (Rybicki & Lightman 1986). In the model, the photon opacity in the low-energy range must be close to 1 in SSM-violating GRBs to be self-absorbed. For SSA to work, the optical depth must be greater than one at energies below E_{peak} .

The third case is jitter radiation (Medvedev 2000). Jitter radiation is the radiation emitted by ultra-relativistic electrons in highly non-uniform, small-scale magnetic fields which is different from synchrotron radiation, if the electron’s transverse deflections in these fields are much smaller than the beaming angle. In this case, the low-energy photon index α becomes 1.

The origin of the low-energy depletion has not been definitively explained by any of these three models, however.

1.5 Extra High-Energy Component

González et al. 2003 found an extra high-energy component having a photon index of -1 up to ~ 200 MeV from analysis of GRB 941017 with the EGRET calorimeter TASC (Total Absorption Shower Counter). Since the flux of the extra component is larger than that of the lower-energy component (below ~ 1 MeV) by orders-of-magnitude and the evolution of the Compton fluxes did not trace the behavior of the synchrotron emission, the leptonic scenario would not explain the extra-component (Fig. 1.11).

Another possible explanation for the observations is that ultra-relativistic hadrons produce the multi-MeV gamma-rays by inducing electromagnetic cascades through pho-

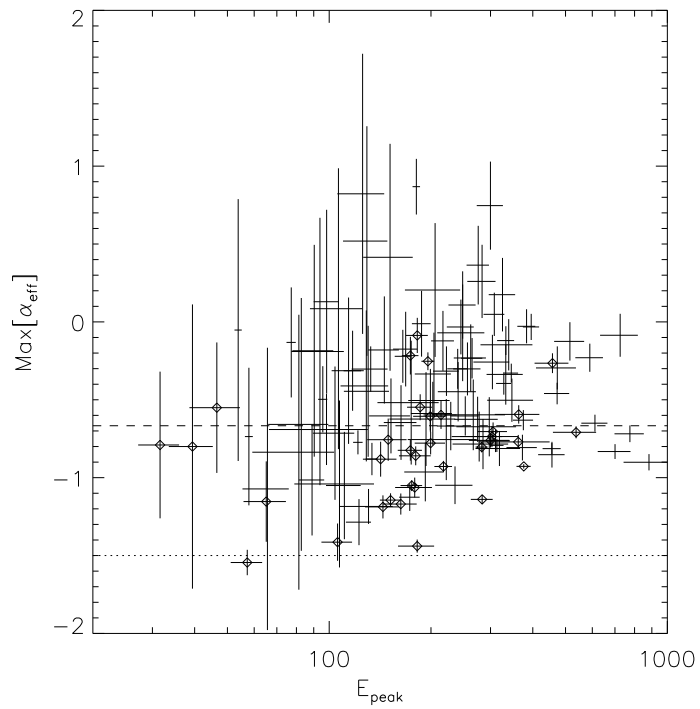


Figure 1.10: Plot of the low-energy powerlaw index α versus E_{peak} . The standard synchrotron-model line of death ($\alpha = -2/3$) is represented by a dashed line and the acceptable region in the synchrotron-cooling spectrum ($\alpha = -3/2$) is represented by a dotted line (Preece et al. 1998).

meson and photo-pair production. Unfortunately, this observation did not extend to high enough gamma-ray energies to know the total luminosity in the high-energy component or the gamma-ray energy at which the flux peaks. However, such a phenomenon could be clarified by a new observatory which has a good sensitivity above ~ 100 MeV (e.g., *Fermi* discussed later).

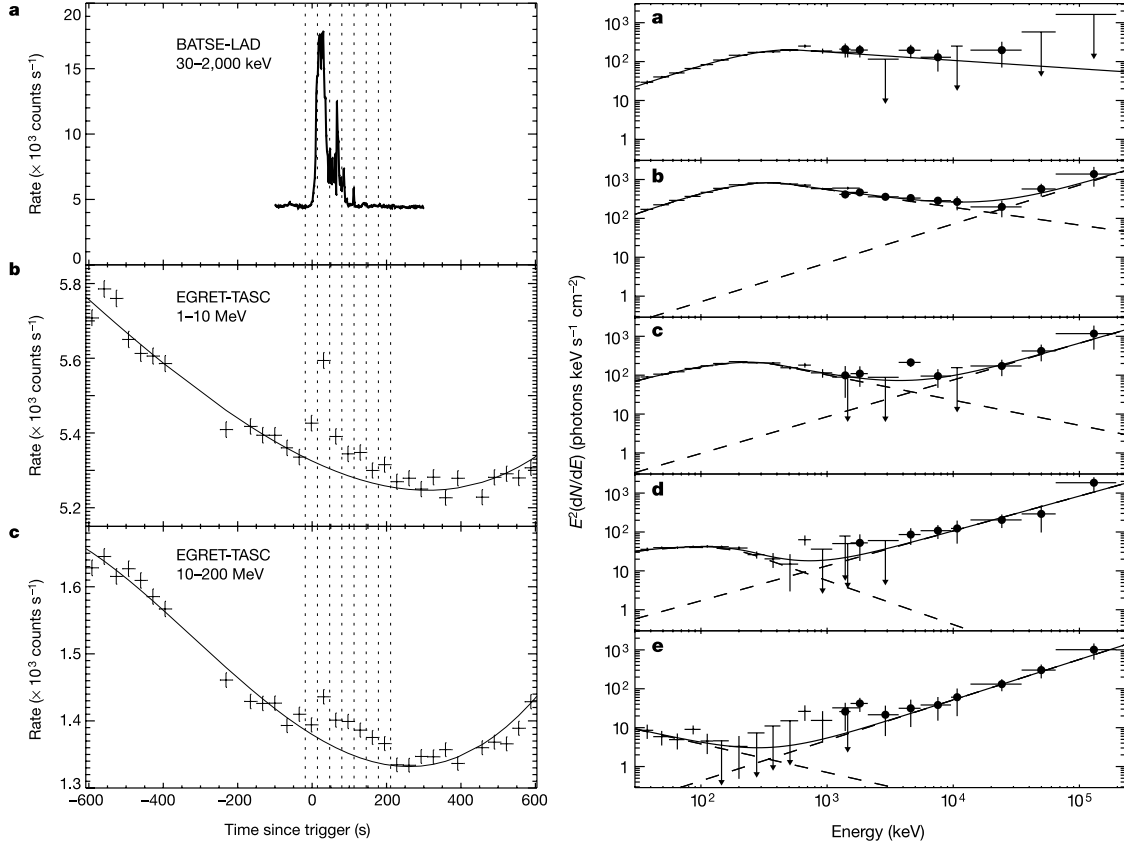


Figure 1.11: *left*: Light curves of GRB 941017, **a**: BATSE-LAD (30 keV – 2 MeV), **b**: EGRET-TASC (1 – 10 MeV), **c**: EGRET-TASC (10 – 200 MeV). The TASC background fit is shown as a line in **b** and **c**. *right*: Time evolution of the νF_ν spectrum with **a** and **e** being the earliest and latest time intervals, respectively. The two spectral components are most obvious at later times. (González et al. 2003)

1.6 High-Energy Delayed Emission

Hurley et al. 1994 reported the discovery of a GRB of very long duration and very high energy. GRB 940217 was detected by BATSE and EGRET on CGRO and the Interplanetary Network (Ulysses). The left panel of Fig. 1.12 shows the Ulysses 25–150

keV count rates with 1-s resolution. The burst is clearly visible as a 180-s event at the start of the plot. High-energy (MeV–GeV) photons were detected by EGRET and the EGRET spark-chamber counted 10 photons while the low-energy burst was in progress. Following this, an additional 18 photons were recorded for $\sim 5,400$ s, including an 18-GeV photon $\sim 4,500$ s after the low-energy emission had ended.

As indicated in the left panel of Fig. 1.12, the source position was Earth-occulted for $\sim 3,700$ s, however, as the EGRET count rates before and after occultation appear to be steady, it is possible that continuous emission was present for the entire 5,400-s (1.5-hour) period after the low-energy burst.

The right panel of Fig. 1.12 shows the background-subtracted energy spectrum for the first 180 s, and its inset shows the background-subtracted 30 MeV to 30 GeV EGRET spectrum for the 5,400-s time interval following the burst. The highest-energy point is based on the single 18-GeV photon and is consistent with the power-law fit at the 99% confidence level.

Meszaros & Rees 1994 and Katz 1994 suggested that this delayed high-energy emission may be the consequence of the collision between an expanding shell of debris, created by a binary neutron-star merger, and an external cloud of matter. Such a delay, however, is not necessarily a signature of cosmological origin.

The advent of the *Fermi* era will make it possible to find these events with better sensitivity, and further detailed analysis will be done.

1.7 Afterglows

The afterglows follow the prompt emission of GRBs and they are seen over a very wide range from radio to X-rays. The X-ray afterglows are observed in almost all GRBs ($\sim 90\%$) by the Swift satellite Gehrels et al, 2005 while the optical or radio counterparts are found only in a fraction of 50 % or less.

The first X-ray afterglow was discovered by the BeppoSAX satellite for GRB 970228 (Costa et al. 1997) as shown in Fig. 1.13. The prompt emission was detected with the Gamma-Ray Burst Monitor (GRBM) and Wide Field Camera (WFC) which have a wide field of view of $20^\circ \times 20^\circ$ and the capability to localize bursts with ~ 5 arc-min accuracy. In follow-up observations with the Narrow Field Instrument (NFI) ~ 8 hours after the trigger, an unidentified X-ray transient, which was not listed in any X-ray survey catalog, was discovered and its flux decayed to about 1/20 of its initial value at 3.5 days after the trigger.

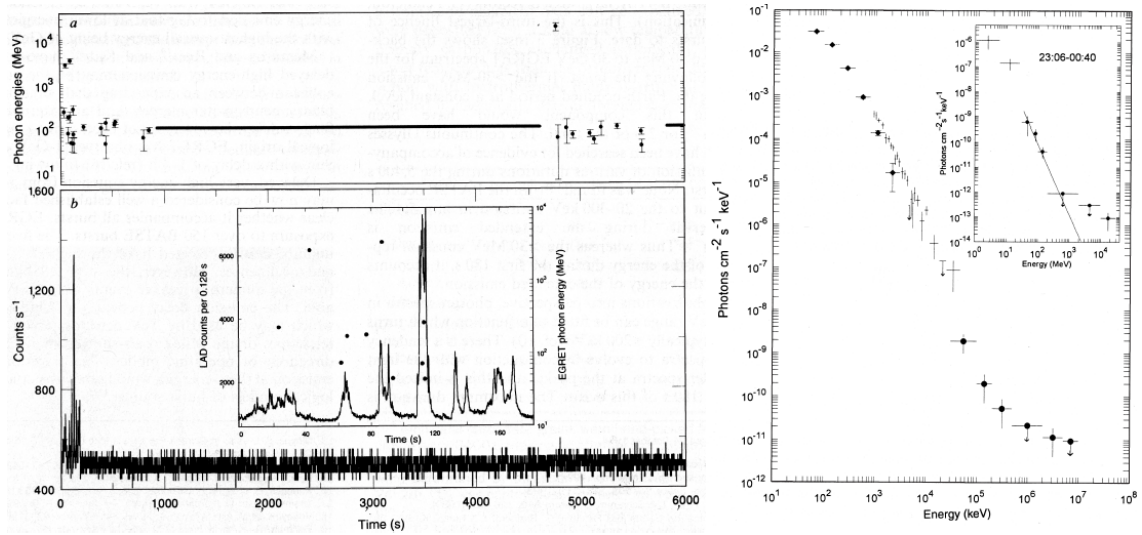


Figure 1.12: GRB 941017 *left*: (a) EGRET spark chamber energies (30 MeV – 30 GeV) as a function of time; horizontal lines indicate periods where no data is available. (b) The Ulysses 25-150 keV count rates as a function of time. The 180-s burst is evident at the start. Because the Ulysses detector (25-150 keV) operates in interplanetary space with >95% data recovery, it is not subject to interruptions such as Earth occultation. Inset, expanded plot of the first 200 s as observed by BATSE (30–1000 keV), showing the arrival times and energies of the EGRET photons. *right* : deconvolved BATSE (crosses with diamonds) and EGRET (plain crosses and crosses with circles) energy spectra of the first 180 s of the burst. Inset, deconvolved EGRET spectra of the delayed emission. The highest-energy point is based on the single 18-GeV photon and is consistent with the power-law fit at the 99% confidence level. (Hurley et al. 1994)

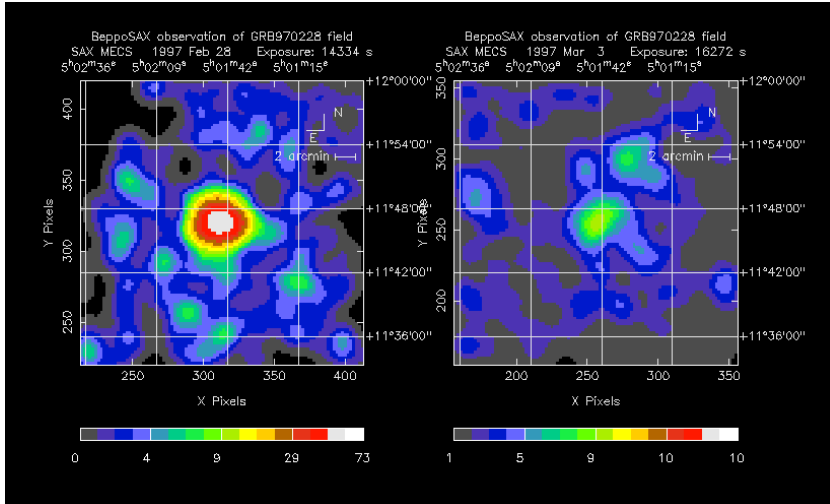


Figure 1.13: Images of the fading X-ray afterglow associated with GRB970228 detected by BeppoSAX (Costa et al. 1997). The left and right panel shows the X-ray afterglow \sim 8 hours and 3.5 days after the trigger, respectively.

1.7.1 Evidence for a Relativistic Jet

Due to the relativistic beaming effect, the emission with moving at a Lorentz factor γ is concentrated in the forward direction within $\theta \sim \gamma^{-1}$. Thus we see only the outflow from the GRB along the line of sight and we do not know how the GRB outflow forms, e.g. jet-like or spherical.

Here we assume that the GRB outflow forms a collimated jet-like shell and the shell expands to radius R in a time $\sim R/c$ with an initial angular jet size θ_j . Since the relativistic shock has a very large internal energy and its velocity is nearly the speed of light, the shell expands sideways in fact. As a result, the jet opening angle θ is not constant but time-dependent, and

$$\theta \sim \theta_j + \frac{1}{\gamma} \quad (1.6)$$

As long as $\gamma \ll 1/\theta_j$, the opening angle is almost constant, $\sim \theta_j$. Once the shell is decelerated to $\gamma \sim 1/\theta$, it begins to spread sideways prominently. The more material that is swept by the shell, the more the shell decelerates rapidly the shell. This transition can be observed as a steepening break in a light curve, called the “jet break”. Before the epoch of the jet break the light curve declines as t^{-1} while after the epoch of the jet break the light curve declines as t^{-p} , where p is the index of the electron distribution (typically $-2 \sim -2.5$). This model was verified by the afterglow observations of GRB 990510 (Stanek et al. 1999). They performed four-color observation of the optical counterpart. The temporal analysis of the data indicates a steepening decay independent of wavelength,

approaching asymptotically $t^{-0.76}$ at early times ($t \ll 1$ day) and $t^{-2.40}$ at late times, with the break time at $t_j = 1.57 \pm 0.03$ days as shown in Fig. 1.14. Since the jet break is due to the geometrical transition, the break should be wavelength-independent. Thus the observations support the idea that GRBs have a collimated jet-like outflow.

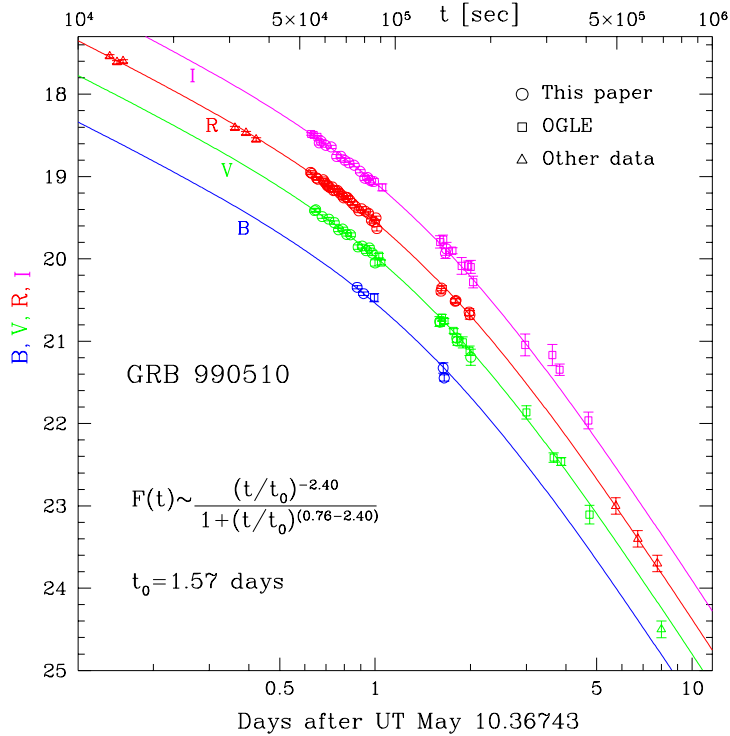


Figure 1.14: Four-color ($BVRI$) afterglow light curves of GRB 990510. The time-dependent jet-break feature was clearly observed. (Stanek et al. 1999)

1.7.2 Association with Supernovae

GRB 030329 played a large role in connecting GRBs and supernovae definitively. Thanks to the rapid notice from *HETE-2* (Vanderspek et al. 2004), the afterglow of GRB 030329 was continuously observed around the world (e.g., Sato et al. 2003, Matheson et al. 2003, Bloom et al. 2004, Urata et al. 2004, Kosugi et al. 2004). This GRB occurred at the redshift of $z = 0.168$ (Greiner et al. 2003), which is very close. 12 days after the GRB trigger, spectral evidence of a type Ic supernova emerged from the afterglow reported by Hjorth et al. 2003. This supernova is named SN2003dh. As seen in the left panel of Fig. 1.15 the spectrum of SN2003dh is very similar to the type Ic supernova SN1998bw (Galama et al. 1998) where SN1998bw/GRB 980425 was marginally suggestive of the relation between GRBs and supernovae. Here we find distinct evidence of the association

between GRB progenitors and massive stars.

In some afterglows, brightening components are detected, as for GRB980326 as shown in the right panel of Fig. 1.15. Comparing the light curve of the bump phase with that of SN1998bw, these structures are interpreted as supernova signatures (Bloom et al. 1999). Therefore these bumps are also direct evidence of the association between GRB progenitors and massive stars.

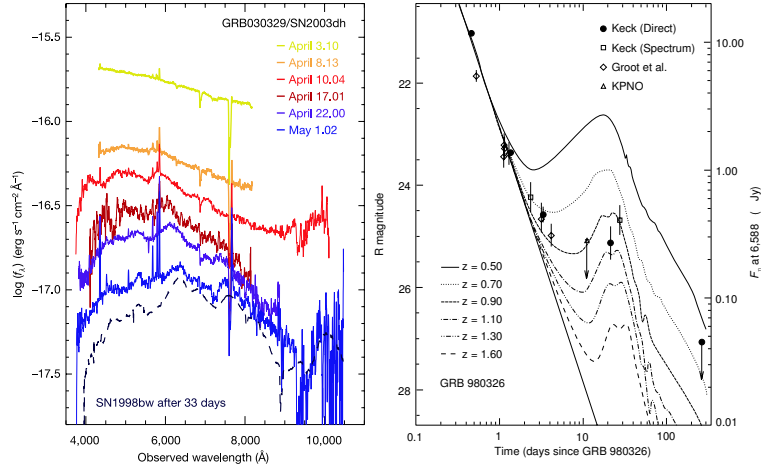


Figure 1.15: *left*: Spectral evolution of the optical flux density, f_λ , of the afterglow of GRB030329, the associated SN2003dh, and its host galaxy (Hjorth et al. 2003). The upper spectrum is rather well fitted by a powerlaw. At later times, the features (emission lines) characterizing the supernova components emerged. *right*: Light curve of the optical afterglow of GRB 980326. A supernova-like feature (i.e., a bump) appears 10 days after the trigger. The overlaid line is a power-law afterglow decline added to a bright supernova light curve at different redshifts.

1.7.3 Long-lived central engine

The X-Ray Telescope (XRT) of Swift allows prompt follow-up observation tens of seconds after the trigger by rapid slewing. Thanks to this promptness, the afterglow at early phases could be observed in detail. Nousek et al. 2006 showed the canonical afterglow and at early phases with a very complex behavior as shown in Fig. 1.16. The phases are divided into four parts as shown schematically in the right panel of Fig. 1.16; (1) steep decay phase with $3 \leq \alpha_1 \leq 5$ for $t < t_{\text{break},1}$, (2) shallow decay phase with $0.5 \leq \alpha_2 \leq 1$ for $t_{\text{break},1} < t < t_{\text{break},2}$, (3) ordinary decay phase $1 \leq \alpha_3 \leq 1.5$ for $t_{\text{break},2} < t$, where the ordinary phase is the well-known behavior before the Swift era, (4) X-ray flares (large flux variability) phase for $t < t_{\text{break},2}$ as shown in the left panel of Fig. 1.16.

The rapid decay in phase (1) is thought to be due to the observer receiving the progressively delayed emission from higher latitudes, the so-called curvature effect (Liang et al. 2006). The shallow decay in phase (2) is likely to be caused by continuous energy injection into the external shock. When this energy injection stops, the second break is then observed in the light curve. The X-ray flares at phase (4) are most likely caused by internal shocks due to a long-lived central engine. Furthermore, other models such as ambient density fluctuations of the X-ray afterglow, patchy shell, or refreshed shock models cannot explain such large flux variability (Ioka et al. 2005).

In addition, the same phenomenon as an X-ray flare was also detected by *HETE-2* (GRB 040916; (Arimoto et al. 2007)). Because the prompt emission was extremely soft ($E_{\text{peak}} < 10$ keV), the result showed that for the very soft GRBs (e.g., XRFs) which can not be detected by *Swift*, X-ray flares also occur.

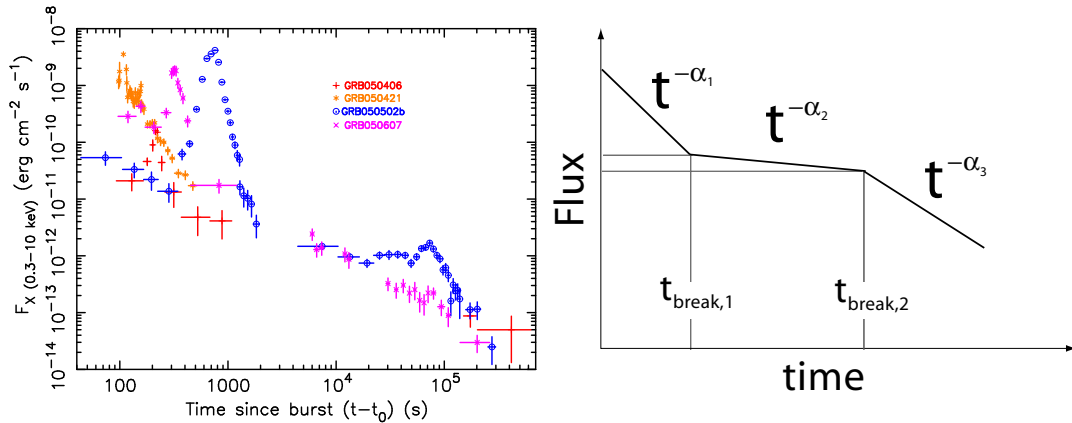


Figure 1.16: *left*: Early X-ray afterglow light curve observed by *Swift* XRT. *right*: Schematic diagram of the canonical behavior of the early X-ray light curve. It consists of three power-law segments; (1) a fast initial decay with $3 \leq \alpha_1 \leq 5$, (2) a very shallow decay with $0.5 \leq \alpha_2 \leq 1$ and (3) a somewhat steeper decay with $1 \leq \alpha_3 \leq 1.5$.

Chapter 2

The Fireball Model

As described in Chapter 1, GRBs are characterized by a relativistic outflow with a collimated jet ($\gamma \sim 100$). It is widely believed that the prompt emission and the subsequent afterglows are explained by internal-external shocks of the relativistic shells. The standard model is called *Fireball* model (see reviews by Piran 2005 and Meszaros 2006).

The basic idea of the fireball model is the following

1. An enormous energy ($\sim 10^{51}$ erg) is released in a small sphere with radius $R_0 \sim c\Delta t \sim 10^7$ cm, where Δt is the variability timescale < 10 ms.
2. The released energy is transferred to a small mass as kinetic energy. Then, the mass is accelerated to relativistic velocities with a Lorentz factor of ~ 100 . As a result, many relativistic shells are generated.
3. An outflow with large Lorentz factor catches up with a slower shell, and a collision occurs (called an internal shock). A lot of internal shocks, corresponding to the observed pulses, are generated. Then, in the internal shock, particle acceleration occurs and the accelerated electrons emit X-ray to γ -ray photons via synchrotron radiation, which corresponds to the prompt emission.
4. After the prompt emission, the shells which collided move forward into the interstellar medium (ISM). At this time, the collision between the relativistic shells and the ISM occurs, called an external shock, and the shells are decelerated while radiating photons in a range from radio to X-rays via synchrotron radiation. This is caused by the electrons accelerated in the external shock, and it is seen as an afterglow.

The schematic diagram is shown in Fig. 2.1.

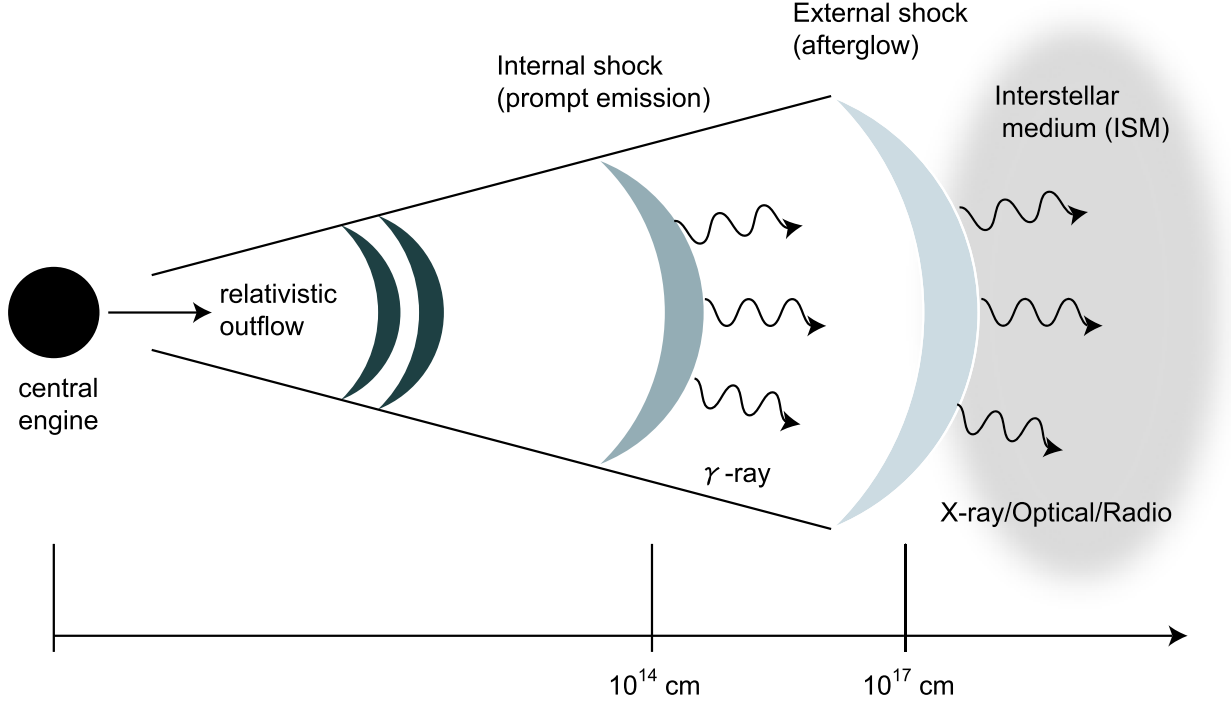


Figure 2.1: Schematic view of *fireball model*

2.1 Efficiency of Internal Shocks

The transferred kinetic energy itself cannot be observed as a GRB. Some mechanisms to change the kinetic energy into radiation are needed. Let us consider the collision between two shells with masses m_r and m_s that are moving at different relativistic velocities ($\gamma_r \geq \gamma_s \gg 1$) in the case of the internal shock. Note that the external shock can be described with the condition; $\gamma_s = 1$. The two shells collide and merge, with a merged mass m_m and a merged Lorentz factor γ_m . Energy and momentum conservation yield:

$$m_r \gamma_r + m_s \gamma_s = (m_r + m_s + E_m/c^2) \gamma_m, \quad (2.1)$$

$$m_r \sqrt{\gamma_r^2 - 1} + m_s \sqrt{\gamma_s^2 - 1} = (m_r + m_s + E_m/c^2) \sqrt{\gamma_m^2 - 1} \quad (2.2)$$

where E_m is the internal energy generated in the collision (in the rest frame of the merged mass). The resulting bulk Lorentz factor γ_m and internal energy E_m in an elastic collision are:

$$\gamma_m = \frac{m_r \gamma_r + m_s \gamma_s}{\sqrt{m_r^2 + m_s^2 + 2m_r m_s \gamma_{\text{rel}}}} \simeq \sqrt{\frac{m_r \gamma_r + m_s \gamma_s}{m_r/\gamma_r + m_s/\gamma_s}} \quad (2.3)$$

$$E_m/c^2 = \sqrt{m_r^2 + m_s^2 + 2m_r m_s \gamma_{\text{rel}}} - m_r - m_s \quad (2.4)$$

where γ_{rel} is the relative Lorentz factor of m_s in the m_r frame. The second term in Eq. 2.3 corresponds to $\gamma_r \geq \gamma_s \gg 1$ (the case of the internal shock). We have E_{int} , in the observer frame, of the merged shell: $E_{\text{int}} = \gamma_m E_m$, is the difference between the kinetic energies before and after the collision:

$$E_{\text{int}} = m_r c^2 (\gamma_r - \gamma_m) + m_s c^2 (\gamma_s - \gamma_m) \quad (2.5)$$

The conversion efficiency of kinetic energy into internal energy is

$$\epsilon = 1 - \frac{(m_r + m_s)\gamma_m}{(m_r\gamma_r + m_s\gamma_s)} \quad (2.6)$$

As can be expected a conversion of a significant fraction of the initial kinetic energy to internal energy requires that the difference in velocities between the shells are significant: $\gamma_r \gg \gamma_s$ and that the two masses are comparable, $m_r \simeq m_s$. If $m_r = m_s$, $\epsilon \sim 6\%$ and 43% for $\gamma_r = 2\gamma_s$ and $\gamma_r = 10\gamma_s$, respectively. Internal shocks take place when an inner shell overtakes a slower outer shell. Then the inner shell will overtake the outer one at:

$$R_i \sim \frac{c^2 \Delta t}{v_r - v_s} \sim \frac{2c\Delta t}{\gamma_s^{-2} - \gamma_r^{-2}} \sim 10^{13} \left(\frac{\delta t}{0.1 \text{ s}} \right) \left(\frac{\gamma_s}{100} \right)^2 \text{ cm} \quad (2.7)$$

If $\gamma_s = 1$ and $\gamma_r \gg 1$, this corresponds to the external shock, or a shock between relativistic ejecta and a non-relativistic material that was ejected from the source before it exploded. $m_s \sim m_r/\gamma_r$ requires $\gamma_m \sim \gamma_r/2$ and $E_m \sim m_r/2$. Thus, the external mass needed to convert half of the kinetic energy is smaller than the original mass by a factor of γ_r (Katz 1994). From this result, we can estimate a radius for the external shocks where the kinetic energy is released.

If the number density of the ISM is n , we can take $m_s \sim \frac{4\pi}{3} R^3 n m_p$ within a certain radius R , where m_p is the proton mass. As the total energy is written as $E = \gamma_r m_r c^2 \sim \gamma_r^2 m_s c^2 \sim \frac{4\pi}{3} R^3 n m_p c^2 \gamma_r^2$, the radius of the external shocks is

$$R_e \sim 10^{17} \left(\frac{E}{10^{53} \text{ erg}} \right)^{\frac{1}{3}} \left(\frac{n}{1 \text{ cm}^{-3}} \right)^{-\frac{1}{3}} \left(\frac{\gamma_r}{100} \right)^{-\frac{2}{3}} \text{ cm} \quad (2.8)$$

The time t when the emission from the external shock should be observed is $t \sim R_e/c\gamma_r^2 \sim 300 (E/10^{53} \text{ erg})^{1/3} (n/1 \text{ cm}^{-3})^{-1/3} (\gamma_r/100)^{-2/3} \text{ s}$ approximately.

2.2 Shock Conditions

The observed prompt emission must be generated by energetic particles that have been accelerated within the collisionless shocks because the probability of the occurrence of the Coulomb collision is extremely small due to the sparse density.

Here, let us consider a situation where a relativistic cold shell (whose internal energy is negligible compared to the rest mass) collides with another cold shell or moves into the cold ISM in Fig. 2.2 (Sari et al. 1996, Sari & Piran 1995). The conservation of mass, energy and momentum determine the Hugoniot shock jump conditions.

The quantities: n_i , p_i , and e_i (particle number density, pressure, and internal energy density) are measured in the rest frame of the shell. The ISM and the unshocked shell are cold the shocked shell is extremely hot:

$$e_1 = e_4 = p_1 = p_4 = 0, \quad p_2 = e_2, \quad p_3 = e_3 \quad (2.9)$$

For $\gamma = \gamma_4 \gg 1$ the equations governing the shocks are calculated by Blandford & McKee 1976

$$e_2/n_2 m_p c^2 = \gamma_{12} - 1, \quad n_2/n_1 = 4\gamma_{12} + 3 \simeq 4\gamma_{12} \quad (2.10)$$

$$e_3/n_3 m_p c^2 = \gamma_{24} - 1, \quad n_3/n_4 = 4\gamma_{24} + 3 \simeq 4\gamma_{24} \quad (2.11)$$

where γ_{ij} is the relative Lorentz factor between the shells in regions i and j . Equality of pressures and velocities along the contact discontinuity yields

$$e_2 = e_3, \quad \gamma_{24} = \gamma_{34} \simeq \frac{1}{2} \left(\frac{\gamma_2}{\gamma_4} + \frac{\gamma_4}{\gamma_2} \right) \quad (2.12)$$

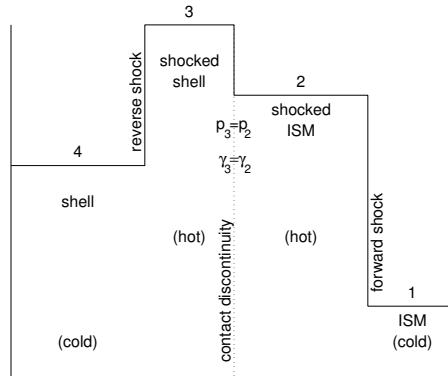


Figure 2.2: Schematic view of the four zones that are present when a relativistic fireball interacts with the ISM. The solid line indicates the density as a function of radius. The unshocked ISM is zone 1 at large radius, and the unshocked inner shell is zone 4 at small radii. The shocked outer shell or ISM at zone 2 and the shocked inner shell at the zone 3, are the result of the forward and reverse shocks and are separated by a contact discontinuity.

Then the ratio f of n_4 to n_1 is written as an equation for γ_{12} ,

$$f = \frac{n_4}{n_1} = \frac{(4\gamma_{12} + 3)(\gamma_{12} - 1)}{(4\gamma_{24} + 3)(\gamma_{24} - 1)} \quad (2.13)$$

Since the relative Lorentz factor $\gamma_{14} = \gamma_{12}\gamma_{24} - (\gamma_{12}^2 - 1)^{1/2}(\gamma_{24}^2 - 1)^{1/2}$, the quantity γ_{12} depends only on γ_{14} and f . Once γ_{12} is given in terms of γ_{14} and f , the energy, pressure, and density depends linearly on the third parameter n_1 from Eq. 2.10 and 2.11

Let us consider three main cases:

1. Ultra-relativistic shock ($\gamma_4 \gg 1$, $\gamma_1 = 1$) with $f > \gamma_{14}^2$. This happens during the early phase of an external shock or during the very late external shock evolution when there is only a single shock ($\gamma_1 = 1$ and then $\gamma_{14} = \gamma_4$, $\gamma_{12} = \gamma_{13} = \gamma_3 = \gamma_2 \gg 1$; Newtonian external reverse shock case). We call this configuration ‘‘Newtonian’’ because the reverse shock is non-relativistic ($\gamma_{24} - 1 \ll 1$). The particle and energy densities in the shocked regions satisfy

$$n_2 \simeq 4\gamma_{12}n_1, \quad n_3 = 7n_4 = 7fn_1, \quad e_2 = 4\gamma_{12}^2n_1m_p c^2 \quad (2.14)$$

2. Later as the shell propagates the density ratio decreases and $f < \gamma_{14}^2$ and $\gamma_1 = 1$ ($\gamma_1 = 1$ and then $\gamma_{14} = \gamma_4$, $\gamma_{12} = \gamma_{13} = \gamma_3 = \gamma_2 \gg 1$; ultra-relativistic external reverse shock case). Both the forward and the reverse shocks are relativistic ($\gamma_{24} \gg 1$). The shock equations between region 1 and 2 yield

$$n_2 \simeq 4\gamma_{12}n_1, \quad n_3 = 4\gamma_{24}n_4 = 4\gamma_{24}fn_1, \quad (2.15)$$

$$e_2 = e_3 = 4\gamma_{12}^2n_1m_p c^2, \quad (2.16)$$

$$\gamma_{12} = \gamma_{14}^{1/2}f^{1/4}/\sqrt{2}, \quad \gamma_{24} = \gamma_{14}^{1/2}f^{-1/4}/\sqrt{2} \quad (2.17)$$

Comparable amounts of energy are converted to thermal energy and both shocks are relativistic. But only a negligible amount energy is converted to thermal energy in the reverse shock if it is Newtonian.

3. Internal shocks are characterized by $\gamma_1 \gg 1$ and $f \simeq 1$. This corresponds to the internal shock $\gamma_4 \geq \gamma_1 \gg 1$, when both shells have similar densities and the relative Lorentz factor γ_{14} is an order of a few (~ 2 to 10). We have

$$n_2 = (4\gamma_{12} + 3)n_1 \sim 4\gamma_{12}n_1, \quad n_3 = 4\gamma_{24}n_4 = 4\gamma_{24}fn_1, \quad (2.18)$$

$$e_2 = e_3 = 4\gamma_{12}^2n_1m_p c^2, \quad (2.19)$$

$$\gamma_{12} \sim \gamma_{24} \sim \frac{\gamma_1}{\sqrt{2}} \sim \sqrt{(\gamma_{14} + 1)/2}, \quad \gamma_{24} = \gamma_{14}^{1/2}f^{-1/4}/\sqrt{2} \quad (2.20)$$

Both shocks are mildly relativistic and their strength depends on the relative Lorentz factors of the two shells.

2.3 Synchrotron Emission from Relativistic Shocks

From the observed non-thermal spectra, the most likely radiation process in GRBs is “synchrotron radiation”. The characteristic parameters that determine synchrotron emission are the magnetic field strength B , and the electrons’ energy distribution. The distribution is characterized by a minimum Lorentz factor $\gamma_{e,\min}$, and the index of the expected power-law electron energy distribution p . $\gamma_{e,\min}$ reflects the spectral break of the synchrotron emission which corresponds to a peak energy E_{peak} . These parameters should be determined from the microscopic physical processes that take place in the collisionless shocks. However, it is difficult to estimate the processes from first principles. Instead, we define two dimensionless parameters, ϵ_B and ϵ_e , that incorporate our ignorance and uncertainties.

The dimensionless parameter ϵ_B measures the ratio of the magnetic field energy density to the total thermal energy density $e \equiv e_2 = e_3$ in the shocked material

$$\epsilon_B = \frac{U_B}{e} = \frac{B^2}{8\pi e} \quad (2.21)$$

so that, after substituting the shock conditions derived in the previous section we have

$$B = (32\pi\epsilon_B\gamma_{\text{sh}}n_1m_p c^2)^{1/2} \quad (2.22)$$

where n_1 and γ_{sh} are the density of unshocked material and the relative Lorentz factor of the shock that is measured at the rest frame of the unshocked shell, respectively.

The second parameter, ϵ_e , measures the fraction of the total thermal energy $e \equiv e_2$ which goes into random motions of the electrons in the shocked material

$$\epsilon_e = \frac{U_e}{e} \quad (2.23)$$

In some case, we often have $\epsilon_e \sim 1/3$, $\epsilon_B \sim 1/3$

Let us consider a “typical” electron with ϵ_e . Assuming that the number densities of the proton and electron are same and a proton transfers its energy by a factor of ϵ_e to a electron,

$$\langle \gamma_e \rangle m_e c^2 = \epsilon_e \gamma_{\text{sh}} m_p c^2 \quad (2.24)$$

Then,

$$\langle \gamma_e \rangle = \epsilon_e \gamma_{\text{sh}} \frac{m_p}{m_e} \quad (2.25)$$

Since the electrons receive their random motions through shock-heating, we assume that they develop a power-law distribution of Lorentz factors

$$N(\gamma_e)d\gamma_e = A\gamma_e^{-p}d\gamma_e \text{ for } \gamma_e > \gamma_{e,\min} \quad (2.26)$$

where A is the normalization factor and γ_e is the electron's Lorentz factor measured in the rest frame of the shocked material. Using the number density of shocked material n_2 ,

$$n_2 = \int_{\gamma_{e,\min}} N(\gamma_e)d\gamma_e \quad (2.27)$$

$$U_e = \epsilon e_2 = m_e c^2 \int_{\gamma_{e,\min}} N(\gamma_e)\gamma_e d\gamma_e \quad (2.28)$$

From the above equations and total energy density $e_2 \sim \gamma_{\text{sh}} n_2 m_p c^2$, we get

$$\gamma_{e,\min} = \frac{m_p p - 2}{m_e p - 1} \epsilon_e \gamma_{\text{sh}} = \frac{p - 2}{p - 1} \langle \gamma_e \rangle \quad (2.29)$$

Here we assume $p > 2$.

The shock acceleration mechanisms cannot accelerate the electrons to arbitrary high energy. For the maximum electron's energy, with a corresponding $\gamma_{e,\max}$, the acceleration time equals the cooling time. The acceleration time t_{acc} is determined by the Larmor radius R_L and the Alfvén velocity v_A ,

$$t_{\text{acc}} = \frac{cR_L}{v_A^2} \quad (2.30)$$

This time should be compared with the synchrotron cooling time.

2.4 Timescale

The timescales of GRBs are thought to come from three effects: synchrotron cooling, curvature effect, and hydrodynamical effect.

2.4.1 Synchrotron timescale

The *synchrotron timescale* comes from the relativistic electron's cooling time. The dominant emission of GRBs is synchrotron radiation. The typical energy of synchrotron photons as well as the synchrotron cooling time depend on the Lorentz factor γ_e of the relativistic electron. The characteristic photon energy in the comoving frame of the relativistic shell is given by Rybicki & Lightman 1986 as

$$h\nu'_{\text{syn}} = \frac{\hbar q_e B}{m_e c} \gamma_e^2 \quad (2.31)$$

where B is the magnetic field strength, γ_e is the Lorentz factor of the relativistic electron, c is the velocity of light, m_e is the electron mass, q_e is the electron charge, \hbar is the Planck constant, the prime denotes the comoving frame of the relativistic shell and no prime denotes the observer frame. Since the emitting material moves with a Lorentz factor Γ (the so-called bulk Lorentz factor), the photons are blue-shifted by a factor of Γ . Then the characteristic photon energy in the observer frame is given by

$$h\nu_{\text{syn}} = \frac{\hbar q_e B}{m_e c} \gamma_e^2 \Gamma \quad (2.32)$$

The power emitted by a single electron due to synchrotron radiation in the comoving frame (Rybicki & Lightman 1986) is,

$$P'_{\text{syn}} = \frac{4}{3} \sigma_T c U_B \gamma_e^2 \quad (2.33)$$

where σ_T is the Thomson cross section and U_B is the magnetic energy density ($U_B = B^2/8\pi$). The cooling time of the electron in the comoving frame is thus $\gamma m_e c^2/P$. The observed cooling time τ_{syn} is shorter by a factor of Γ than that in the comoving frame, unlike the time dilation ($\Gamma \gamma m_e c^2/P$),

$$\tau_{\text{syn}} = \frac{\gamma m_e c^2}{P \Gamma} = \frac{3 m_e c}{4 \sigma_T U_B \gamma_e \Gamma} \quad (2.34)$$

Substituting the typical values into Eq. 2.34, we obtain the typical cooling time scale,

$$\tau_{\text{syn}} = 2 \times 10^{-6} \epsilon_B^{-3/4} \left(\frac{h\nu}{100 \text{keV}} \right)^{-1/2} \text{ [s]} \quad (2.35)$$

This time scale is far *shorter* than the decay timescale of the light curve or the spectral lag timescale.

2.4.2 Curvature timescale

The *curvature timescale* arises from the relativistic effects in a sphere expanding with a high bulk Lorentz factor Γ (~ 100). Because of the curvature of the shell, there will be a time delay between the photons emitted simultaneously in the comoving frame from different points on the surface. Fig. 2.3 shows the geometry of the situation (Ryde & Petrosian 2002). Because of the relativistic aberration of light, isotropically emitted radiation in the comoving frame will be beamed into a cone with opening angle $\theta \sim \Gamma^{-1}$ (Rybicki & Lightman 1986). Only photons emitted from the fireball surface within a narrow cone of opening angle $\sim \Gamma^{-1}$ around the line of sight (LOS) will be detected by the observer. The typical time decay τ_{ang} is thus

$$\tau_{\text{ang}} = R[1 - \cos(1/\Gamma)]/c \quad (2.36)$$

For large Γ , $(1 - \cos(1/\Gamma))$ is approximately $1/(2\Gamma^2)$. This gives a lower bound for the observed duration or spectral lag of a pulse,

$$\tau_{\text{ang}} = 1.7 \left(\frac{R}{10^{15} \text{cm}} \right) \left(\frac{\Gamma}{100} \right)^{-2} \text{ [s]} \quad (2.37)$$

This value is comparable to that of the observed duration or spectral lag. A quantitative estimate of the spectral lags has been done by Lu et al. 2006 based on Qin & Lu, 2005, and Qin 2002 (see appendix D).

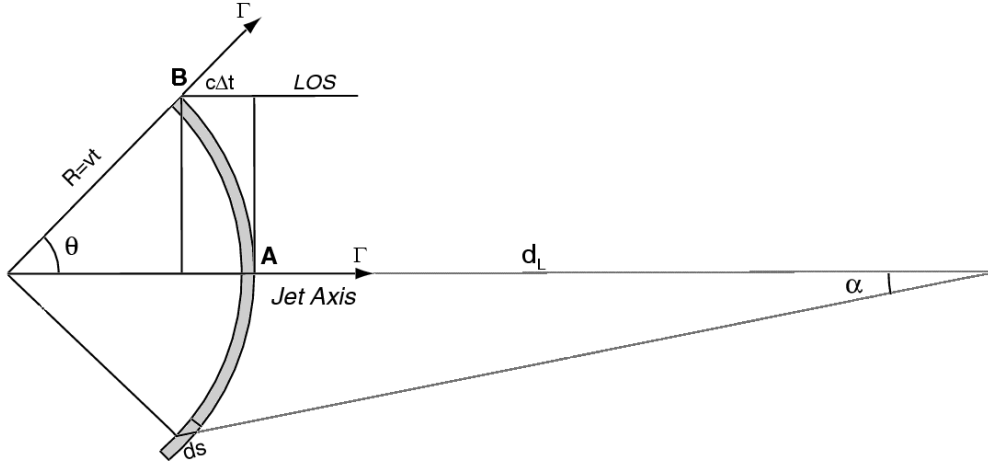


Figure 2.3: Geometrical sketch of the visible part of the fireball. Because of the relativistic aberration of light, the main part of the radiation comes out within a small cone with half opening angle $\theta \sim \Gamma^{-1}$. Note that the line of sight (LOS) does not need to be parallel to the jet axis. The photons from point A boosted by 2Γ lead those from point B boosted by the Doppler factor $\delta = [\Gamma(1 - \beta \cos \theta)]^{-1}$. The difference in the arrival times is $\Delta t = R/c(1 - \cos \theta)$.

2.4.3 Hydrodynamical timescale

The *hydrodynamical timescale* for a single pulse is the actual crossing (or merger) time of one shell with another. Often the shell collision is assumed to be an inelastic collision and the merged shells expand as a single shell. The shell crossing time τ'_{dyn} in the comoving frame is

$$\tau'_{\text{dyn}} = \frac{\Delta'}{v'_{\text{sh}}} \quad (2.38)$$

where v'_{sh} is the velocity of the shock in the comoving frame of the preshocked flow. The initial value, and the evolution with radius, of the shell width Δ' are not well understood

and depend, among other factors, on the structure and internal dynamics of the shell and on its interaction with the external medium. Some theoretical calculations of the hydrodynamical effect have been performed by Daigne & Mochkovitch 1998, Daigne & Mochkovitch 2003, Bosnjak et al. 2008 and others. But the true hydrodynamical problem is very hard to solve and first we consider the timescale of the hydrodynamical effect.

If there exists a differential flow with a faster leading and a slower trailing edge with velocities β_r and β_s and corresponding Lorentz factors Γ_r and Γ_s , respectively, then the generated shell width is

$$\Delta(R) = R(\beta_r - \beta_s) = \frac{R}{2\Gamma_s^2} \left[1 - \left(\frac{\Gamma_s}{\Gamma_r} \right) \right] \sim \frac{R}{2\Gamma_s^2} \quad (2.39)$$

where for the last relation we have assumed that $\Gamma_s \ll \Gamma_r$. In the comoving frame $\Delta'(R) = R/(2\Gamma_s)$. The shell crossing time is then $\tau'_{\text{dyn}} = \Delta'/v'_{\text{sh}} = R/(\Gamma_s v'_{\text{sh}})$. In the observer frame these times will be time dilated (Γ) and affected by the motion of the fireball toward the observer (Γ^{-2})

$$\tau_{\text{dyn}} = \frac{\tau'_{\text{dyn}}}{2\Gamma} = \frac{R}{4\Gamma_s \Gamma v'_{\text{sh}}} = 1 \beta_{\text{sh}}'^{-1} \left(\frac{R}{10^{15}} \right) \left(\frac{\Gamma}{100} \right)^{-2} \left(\frac{\Gamma}{\Gamma_s} \right) \text{ [s]} \quad (2.40)$$

The timescale is comparable to the curvature-effect timescale and we can regard the dominant timescale of temporal properties as either the hydrodynamical timescale or curvature timescale, or both timescales.

We introduce the simple hydrodynamical model by Daigne & Mochkovitch 1998. They assume the situation in the left panel of Fig. 2.4: the initial distribution of Γ consists of 5000 layers with $\Gamma(n) = 400$ for $n = 1$ to 4000 and $\Gamma(n) = 100$ for $n = 4001$ to 5000 ($n = 1$ for the last emitted layer). The total masses injected in the slow and rapid parts are equal. After the first fast layer collides the slow one, a reverse and a forward shocks are generated and propagate into the wind. Then the forward shock traverses the whole slow part, and subsequently the reverse shock reaches the end of the rapid part. From the study of the temporal properties of their burst models, the physical parameters as a function of arrival burst time t_a , fraction α_{syn} (the ratio of synchrotron emission to the total emission), Lorentz factor Γ_e of the relativistic electrons, equipartition magnetic field B_{eq} and synchrotron energy E_{syn} , are represented in the right panel of Fig. 2.4. The expected temporal profiles for a single pulse burst in the four BATSE energy bands (25–50 keV, 50–100 keV, 100–300 keV and 300 keV – 1 MeV) from their synthetic burst models are shown in the top panel of Fig. 2.5. The bottom panel shows that the pulse width (half-maximum) decreases at high energy as a power-law function ($\propto E^{-0.4}$)

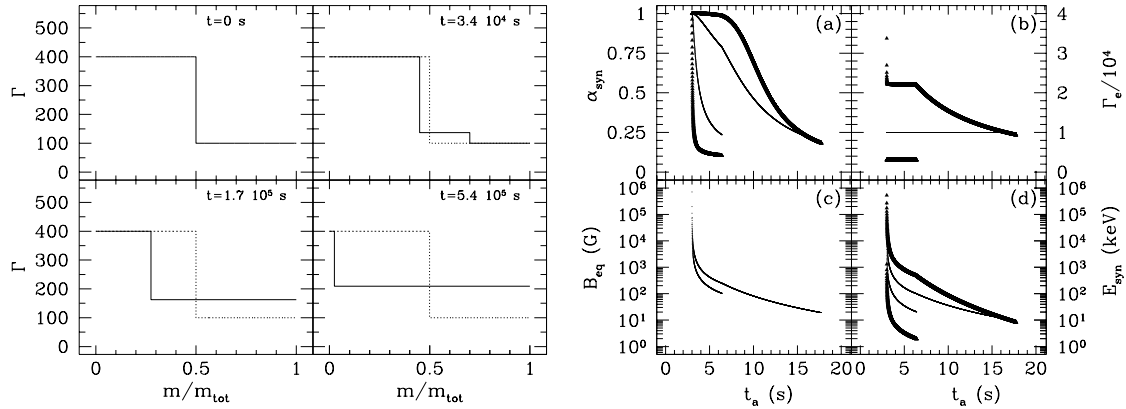


Figure 2.4: (*left*): Distribution of the Lorentz factor in the wind at different times vs. m/m_{tot} where m_{tot} is the total mass of the wind. After the collision, the forward shock transverses the whole slow part and then the reverse shock reaches the end of the rapid part. Note that the dashed line represents the initial distribution of the Lorentz factor. (*right*): Physical parameters as a function of arrival time. (a) fraction α_{syn} of the energy radiated by the synchrotron process; (b) Lorentz factor Γ_e of the relativistic electrons; (c) equipartition magnetic field B_{eq} ; (d) synchrotron energy E_{sync} . In (a), (b) and (d) the thick lines correspond to Γ_e including the effect of scattering of electrons by turbulent magnetic field fluctuations. and the thin lines to $\Gamma_e = 10^4$. The two branches corresponds to the forward and the reverse shocks. (Daigne & Mochkovitch 1998)

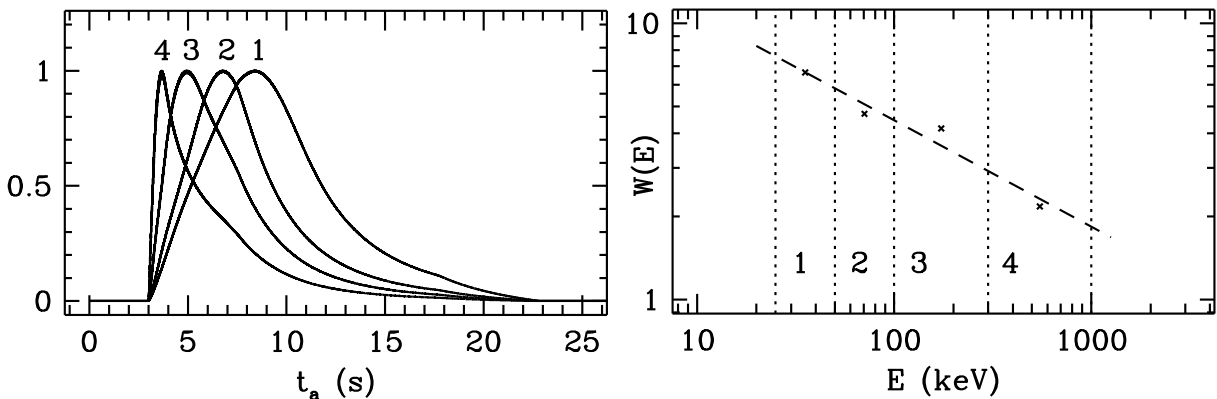


Figure 2.5: Expected temporal profile (left panel) and energy dependence of pulse width (right panel) from the hydrodynamical model of Daigne & Mochkovitch 1998, where corresponding energy bands (1), (2), (3) and (4) are 25–50 keV, 50–100 keV, 100–300 keV and 300 keV – 1 MeV, respectively. The fitted slope is $p = -0.4$.

2.5 Integrated Synchrotron Spectrum

The instantaneous synchrotron spectrum of a single electron with an initial energy $\gamma_e m_e c^2$ is a power law with $F_\nu \propto \nu^{1/3}$ up to $\nu_{\text{sync}}(\gamma_e)$ and an exponential decay above it (Rybicki

& Lightman 1986). If the electron is energetic it will cool rapidly until it reaches $\gamma_{e,c}$. This is the Lorentz factor of an electron that cools on a hydrodynamic time scale. For a rapidly cooling electron we have to consider the time integrated spectrum. The frequency of the synchrotron emission varies as $\nu \propto \gamma_e^2$, while the electron energy varies as γ_e . Thus $F_\nu \propto \nu^{-1/2}$ from $\nu_{\text{sync}}(\gamma_e, c) = \nu_c$ up to $\nu_{\text{sync}}(\gamma_e)$.

We consider a power-law electron distribution with a power-law index p and minimum Lorentz factor $\gamma_{e,\text{min}}$ (Eq. 2.26). Synchrotron self-absorption may be important in the late time afterglow and typically in radio emission, but it is irrelevant during the prompt GRB phase. To estimate the self-absorption frequency ν_a , we need the optical depth along the line of sight, approximated as $\sim \alpha'_{\nu'} \Delta / \gamma_E$, where Δ and α' are width of the emitting shell, moving at a Lorentz factor γ_E , measured in the observer frame and the absorption coefficient in the comoving frame given by

$$\alpha'_{\nu'} = \frac{p+2}{8\pi m_e \nu'^2} \int_{\gamma_{e,\text{min}} \text{ or } \gamma_{e,c}} d\gamma_e P'_{\nu'}(\gamma_e) \frac{N(\gamma_e)}{\gamma_e} \quad (2.41)$$

(Rybicki & Lightman 1986) where primes denote the comoving frame. The self absorption frequency ν_a satisfies $\alpha'_{\nu_a} \Delta / \gamma_E \sim 1$. At frequencies below ν_a , the system is optically thick to self-absorption and the observer sees the Rayleigh-Jeans form of the blackbody spectrum $P_\nu \propto \nu^2 \gamma_{\text{typ}}(\nu)$. If $\gamma_{\text{typ}}(\nu) = \gamma_{e,\text{min}}$ or $\gamma_{e,c}$, we have $P_\nu \propto \nu^2$.

Overall we expect a broken power-law spectrum with a break frequency around the synchrotron frequency of the lower energy electrons $\nu_{\text{sync}}(\gamma_{e,\text{min}}) = \nu_m$. The power-law indices depend on the cooling rate. The most energetic electrons will always be cooling rapidly (independently of the behavior of the ‘‘typical electron’’). From Eq. 2.26, we have $F_\nu = N(\gamma_e) \gamma_e m_e c^2 d\gamma_e / d\nu \propto \nu^{-p/2}$ at $\nu > \nu_m$ (electrons emit practically all their energy $\gamma_e m_e c^2$ at their synchrotron frequency; fast cooling). The low energy electrons will always be cooling slowly and thus the lower part of the spectrum will behave as $F_\nu \propto \nu^{1/3}$. The summarized observed spectrum at the fast cooling phase is described as

$$F_\nu = F_{\nu_{\text{max}}} \times \begin{cases} (\nu/\nu_c)^{1/3} (\nu/\nu_a)^2, & (\nu < \nu_a) \\ (\nu/\nu_c)^{1/3}, & (\nu_a < \nu < \nu_c) \\ (\nu/\nu_c)^{-1/2}, & (\nu_c < \nu < \nu_m) \\ (\nu_m/\nu_c)^{-1/2} (\nu/\nu_m)^{-p/2}, & (\nu_m < \nu) \end{cases} \quad (2.42)$$

where $F_{\nu_{\text{max}}}$ is the observed peak flux. This phase corresponds to internal shocks or early external shocks.

For the slow cooling ($\gamma_{e,\text{min}} < \gamma_{e,c}$), unlike the fast cooling, the electrons do not cool effectively and the spectrum at $\nu_m < \nu < \nu_c$ is $F_\nu = N(\gamma_e) P(\gamma_e) d\gamma_e / d\nu \propto \nu^{-(p-1)/2}$ using

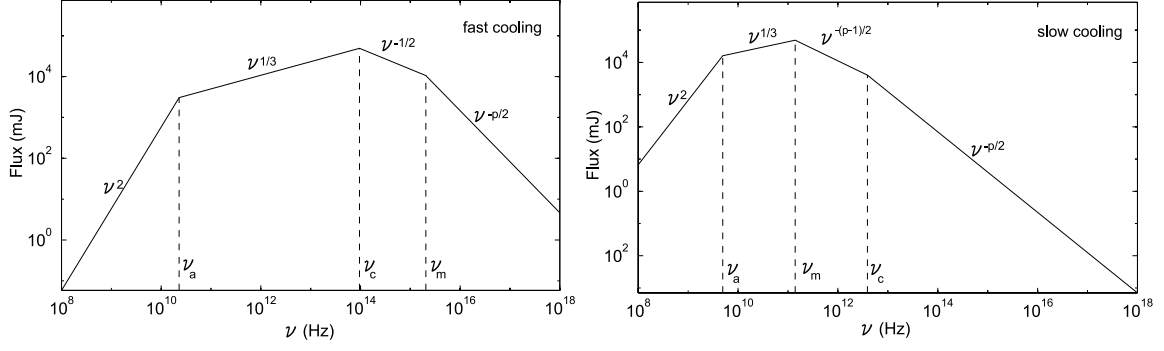


Figure 2.6: Synchrotron cooling spectrum. *left*: fast cooling phase. *right*: slow cooling phase. (Sari et al. 1998)

Eq. 2.26 and $\nu \propto \gamma_e^2$. The expected spectrum is summarized as

$$F_\nu = F_{\nu_{\max}} \times \begin{cases} (\nu_a/\nu_c)^{1/3}(\nu/\nu_a)^2, & (\nu < \nu_a) \\ (\nu/\nu_c)^{1/3}, & (\nu_a < \nu < \nu_m) \\ (\nu/\nu_c)^{-(p-1)/2}, & (\nu_m < \nu < \nu_c) \\ (\nu_m/\nu_c)^{-(p-1)/2}(\nu/\nu_m)^{-p/2}, & (\nu_c < \nu) \end{cases} \quad (2.43)$$

This phase corresponds to the late-time external shocks.

Chapter 3

Instrumentation

3.1 The HETE-2 satellite

The High Energy Transient Explorer 2 (*HETE-2*; Ricker et al. 2003) is the first astronomical satellite dedicated to the observation of GRBs. The *HETE-2* (hereafter *HETE*) satellite was successfully launched on October 9, 2000 on a Pegasus rocket (Fig. 3.1 and 3.2). There two unique features to *HETE*. First, *HETE* can provide the location of GRBs with localizations of a few tens of arc-minutes to a few tens of arc-seconds, with delay times of 10 s to a few hours, to ground observers. This capability gives us the opportunity to observe GRB afterglows in many wavelengths from a very early phase. Second, broadband spectroscopy (2–400 keV) of GRBs is possible with the combination of the X-ray and γ -ray instruments. This not only allows us to detect the various classes of GRBs, but also to determine the spectral parameters of the prompt emission. The information about the prompt emission is essential for the study of the central engine, since even excellent observations of the afterglows only provide limited information.

The three scientific instruments on-board *HETE* are: the FRENch GAMMA-ray TELEscope (FREGATE; Atteia et al. 2003), which gives the trigger for GRBs; the Wide-field X-ray Monitor (WXM; Kawai et al. 2003), which is the key instrument to localize GRB to $\sim 10'$ accuracy within a few tens of seconds; and the Soft X-ray Camera (SXC; Villasenor et al. 2003, Monnelly et al. 2003), which localizes GRB with a few arc-seconds accuracy. The details of each instrument are described in the next section. *HETE* characteristics are summarized in the table 3.1 and a schematic figure is shown in Fig. 3.3.

There are three Primary Ground Stations (PGS; Crew et al. 2003); these are located at Singapore, at the Kwajalein Atoll in the Republic of the Marshall Islands, and at Cayenne, French Guyana. The commanding and the data downloads are performed with these three PGSs. These stations operate at S-band frequencies (2.272 GHz), with data

rates of 31.25 kbps for uplink and 250 kbps for downlink.

The Burst Alert Network (BAN) consists of fourteen burst alert stations (Crew et al. 2003, Villasenor et al. 2003). Information about GRBs detected by *HETE* is transmitted to the BAN in real time at a frequency of 137.96 MHz with 300 bps, immediately relayed to the *HETE* Mission Control Center at MIT, and then sent to the GRB Coordinates Distribution Network (GCN). The GCN then sends the information in the various forms (E-mail, pager, and/or internet socket messages) to observers around the world.

Table 3.1: Specifications of the *HETE* satellite

Mass	124 kg
Dimension	89 cm × 66 cm
Orbit	625 km circular, 0-2 degree inclination
Mission Life	2000 ~ 2006
Attitude	Pointing in the anti-solar direction
Data Processing	4 T805 transputers, 8DSP56001
Downlink	S-band (2.272 GHz) via 250 kbps VHF (137.96 MHz) via 300 bps
Uplink	S-band (2.092 GHz) 31kbps



Figure 3.1: *HETE* satellite

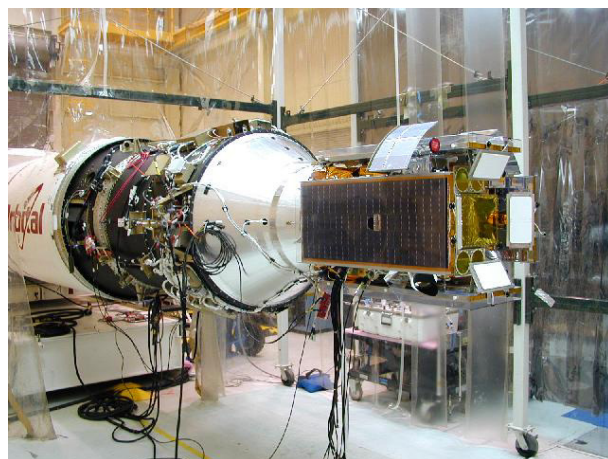


Figure 3.2: *HETE* satellite on the Pegasus rocket

3.1.1 The FREGATE

The FRENch GAMMA-ray TELESCOPE (FREGATE) plays a crucial role by initiating *HETE* activity for each GRB triggered events. Thanks to its wide energy coverage, FREGATE

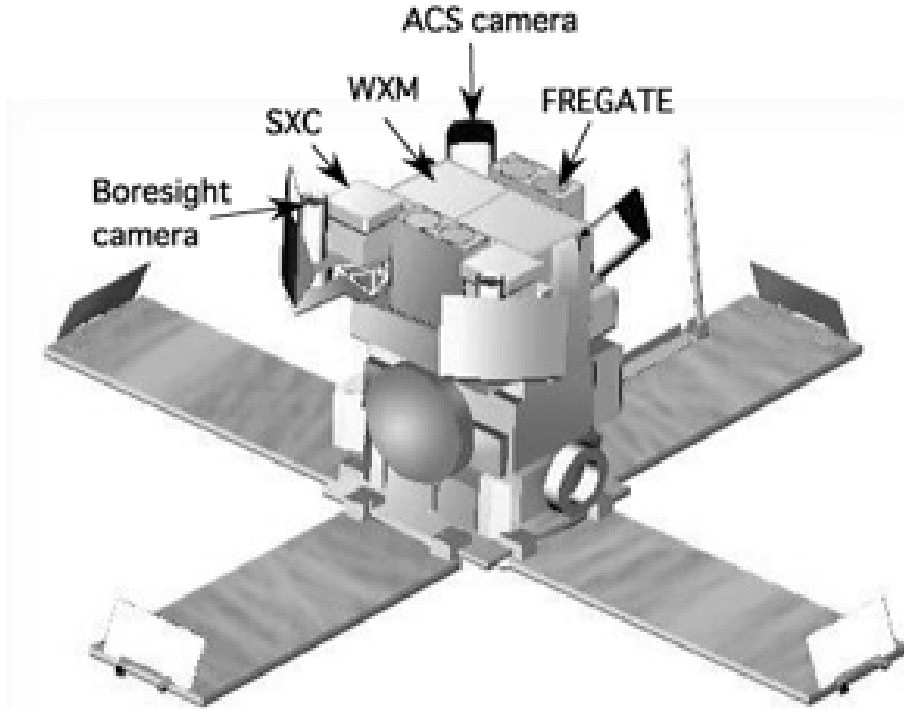


Figure 3.3: Schematic figure of the *HETE* satellite

is also a key instrument for the spectroscopic study of GRB prompt emission. Since the solid-angle coverage of FREGATE is larger than that of the WXM, bursts which occur outside the field of view of the WXM can be localized by the Inter planetary network (IPN) collaboration (Hurley et al. 2003).

The FREGATE detector (Fig. 3.4) consists of a cleaved NaI crystal (a cylinder 10 mm thick and 71 mm in diameter) with a beryllium read by a photomultiplier tube (Hamamatsu 1848, Fig. 3.5). The NaI crystals have no dead layer, and are used to extend the spectral coverage into the low energy band (~ 6 keV). The geometric area of the sum of the four detectors is ~ 160 cm². To monitor the gain of the detector, two radioactive sources (¹³³Ba) are located outside of the detector. The effective-area curve at several incident angles is shown in Fig. 3.6. The performance of FREGATE is summarized in Table 3.1.1.

The NaI crystals are shielded by a graded shield made of lead, tantalum, tin, copper and aluminum which block photons originating from the diffuse X-ray background and the atmosphere.

The data products of FREGATE are summarized in Table 3.1.1. The data are categorized into two types, similar to the WXM. One is survey data (TH and SP) which is always recorded while the detector is on. The other is burst photon data (PH) which is only produced when the burst is triggered.

The energy response matrix of FREGATE was calculated using the Geant4 Monte Carlo package (<http://geant4.web.cern.ch/geant4/>). More than 50 detector components are included in the Monte Carlo simulations. The result of the simulations were examined before launch with the ground calibrations using a large set of radioactive sources and various incident angles. The in-orbit calibration of the FREGATE response matrix is performed using data from Crab Nebula and its Earth-occultation. It successfully reproduces the Crab Nebula spectrum with a photon index of (2.16 ± 0.03) ($\chi^2_\nu = 1.19/84$ d.o.f.).

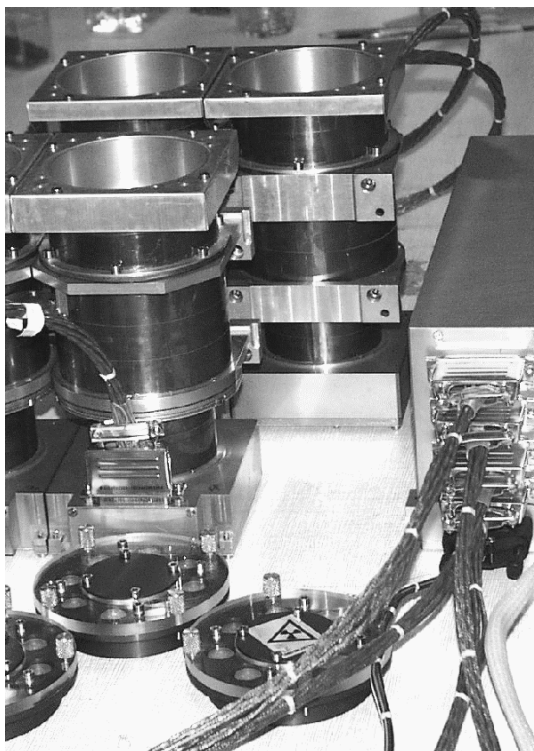


Figure 3.4: FREGATE in the laboratory before its integration on the spacecraft. The four detectors on the left are 20 cm high.

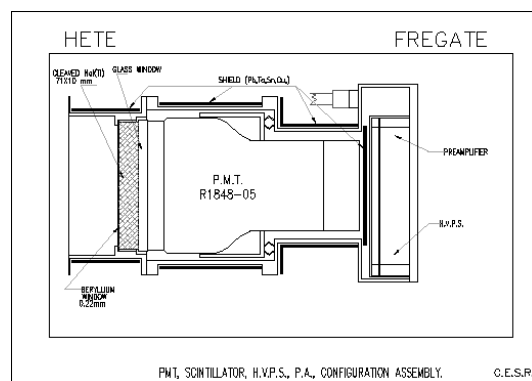


Figure 3.5: Schematic drawing of one FREGATE detector. The crystal has a diameter of 71mm and a thickness of 10mm. The length of the detector is 20cm.

Table 3.2: Performance of FREGATE

Energy range	6–400 keV
Effective area (4 elements on axis)	160 cm ²
Field of view (FWHM)	70°
Energy resolution	~ 12% @ 122 keV

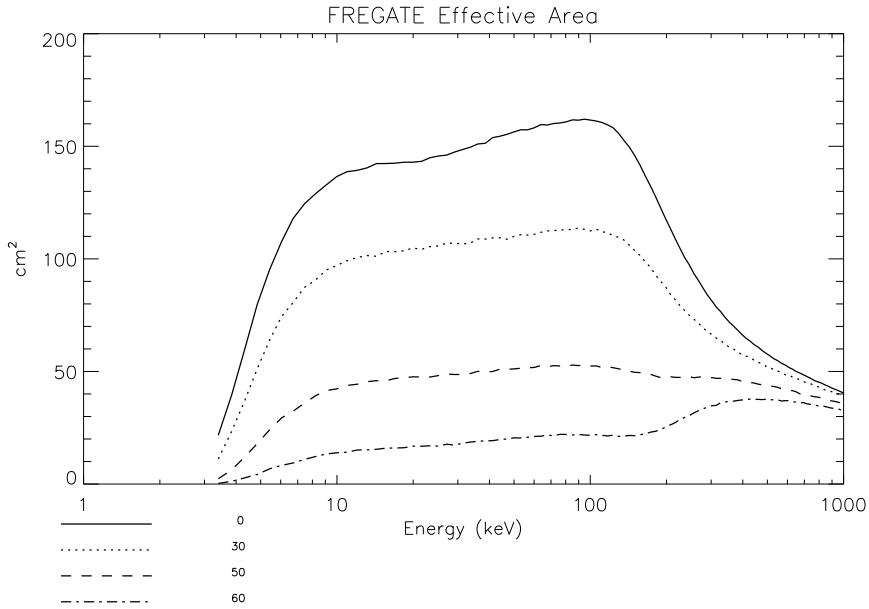


Figure 3.6: Effective area of FREGATE with some incident angles (0° , 30° , 50° and 60°)

Table 3.3: FREGATE data types

Data type	time resolution	description
HK	-	House keeping data (Available continuously)
TH	0.16s / 0.32 s	Time history data in 4 energy bands (6–40 keV, 6–80 keV, 32–400 keV and > 400 keV, approximately)
SP	5s / 10 s	128 channel-energy spectral data
PH	$6.4 \mu\text{s}$	Time tagged photon data available when a burst is triggered. (256 channels)

3.1.2 The WXM

The Wide-field X-ray Monitor (WXM: Shirasaki et al. 2003) is located at the center of the spacecraft and is the key instrument to localize GRB. The WXM consists of one-dimensional position sensitive proportional counters (PSPC) with coded mask apertures (Fig. 3.7). The one-dimensional coded mask is located 187 mm above the PSPCs (Fig. 3.8). The are two counters are called the X-camera and the Y-camera. Each camera has two PSPCs referred to as YA and YB. The orientation of the X-camera is perpendicular to the Y-camera, and the X and Y localizations of GRBs are determined separately.

The area of each coded mask is twice that of that of the total detector area to ensure

a wide field of view. The masks are supported by an aluminum support structure. The mask consists of a plate of aluminum (0.5 mm thickness) plated with gold (50.8 μm). The widths of the slits are randomly varying integer multiples of 2mm (Fig. 3.8). The open fraction of the mask is 0.33. A 7.6 μm thick aluminum-coated kapton foil is placed in front of the mask, as a thermal shield. The location of the GRB is calculated from the shift distances of the mask shadow on the X and Y cameras independently.

The cross-sectional view of the PSPC is shown in Fig. 3.9. The PSPC has three anode wires which are composed of carbon fibers 10 μm in diameter and 120 mm in length. The counter is divided into an upper layer with three anode cells and a lower veto layer. The veto layer is to distinguish the charged particles from the X-ray photons. The counters have windows of 100 μm thickness. The detector body is made of titanium. The geometrical area of the entrance window is 88 cm^2 . The effective-area curve of the WXM is shown in Fig. 3.10 as a function of energy for normal incidence. A radioisotope is contained in a slit case and both sides of each counter at 40 mm distance from the center of the counter are irradiated. The WXM performance is shown in Fig. 3.1.2.

One of the key features of the WXM is on-board triggering and localization of GRBs. There are 68 criteria with time scales from 80 ms to 27 s, and the threshold levels from 4.7 to 8.0 σ depending on the time scales. There are also “bracket-type” triggers which have two background regions taken before and after the foreground region. This trigger reduces the number of false triggers due to increases or fluctuations in the background. When a GRB triggers the WXM or FREGATE, the position histograms of the X and Y cameras for the optimized foreground and background regions are extracted from the memory data. The histogram is cross-correlated with the templates for all the incident angles. If each localization is completed successfully, the trigger process continues to search for better time intervals based on the signal-to-noise (S/N) ratio, and the localization is performed for each set of updated foreground and background regions. The cross-correlation scores between the position histogram data and the Monte Carlo simulated templates of various incident angles are compared to find the template which matches best with actual data. The GRB location in WXM detector coordinates is converted to celestial coordinates using the aspect information of the spacecraft (i.e., X-Y coordinates are converted to RA-Dec coordinates). A conservative error (90% confidence radius) is 30' in flight. More sophisticated ground analysis gives $\sim 10'$ accuracy.

The data products of the WXM are summarized in Table 3.1.2. The data used for scientific studies are TAG, POS, TH and PHA.

Unfortunately, the YB detector was lost to a micrometeorite impact in 2003 January. As a result, while the WXM could be used to determine the X position very precisely, the

Y position could only be crudely determined, based on the relative illumination of the six wires in the X detectors.

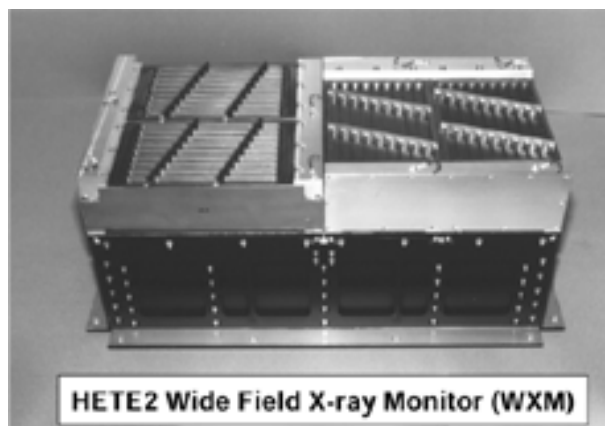


Figure 3.7: WXM detector: The left side is the X camera, while the right side is the Y camera.

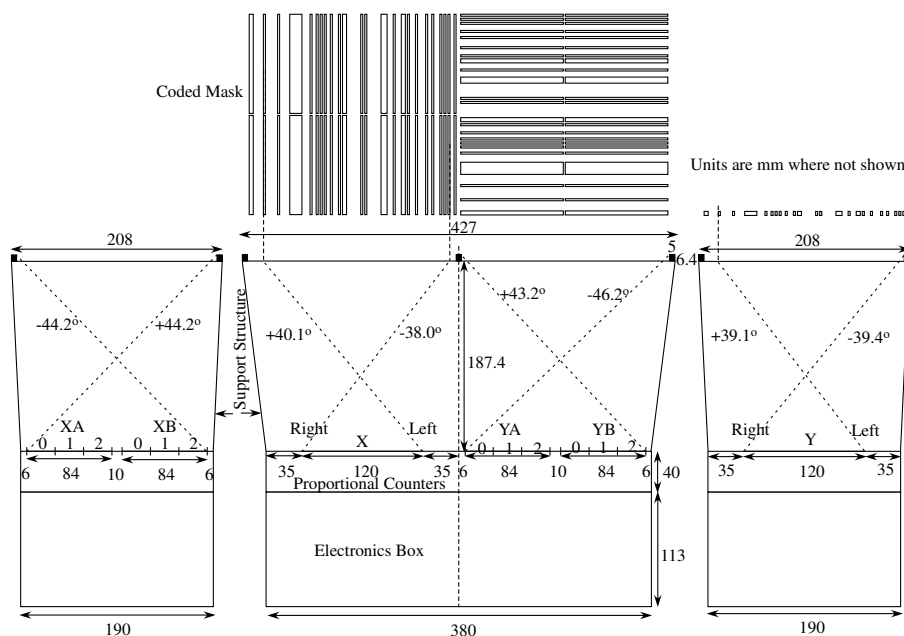


Figure 3.8: Dimensions of the entire WXM system (Units are mm where not shown) : A coded mask is placed at 187.37 mm above the proportional counters and supported by an aluminum structure. The upper panels represent the coded mask pattern. The field of view is restricted by the masks and fasteners, which fix the coded mask on the support structure.

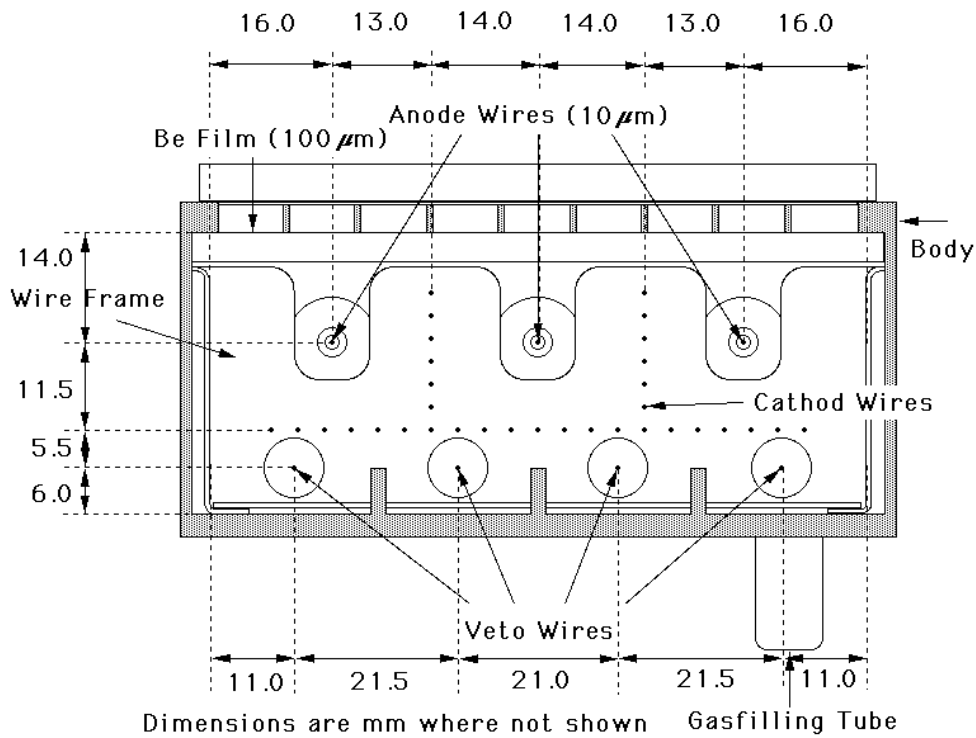


Figure 3.9: Cross section of one PSPC of WXM. The anode wires in the three upper cells are for X-ray detection and those in the lower cells are for rejection of charged particles events by the anti-coincidence method.

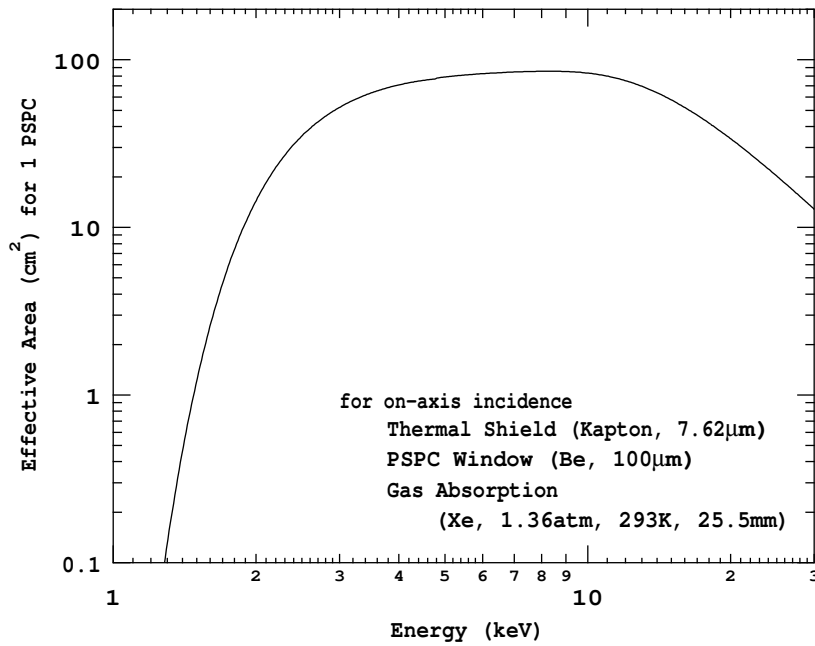


Figure 3.10: Effective area of one PSPC at the boresight incidence.

Table 3.4: Characteristics of the WXM

Energy range	2–25 keV
Effective area (1 PSPC, without coded mask on axis)	$\sim 80 \text{ cm}^2$
Position resolution	$\sim 1 \text{ mm @ } 8\text{keV}$
Energy resolution (FWHM)	$\sim 20 \% @ 8\text{keV}$
Angular resolution	$\sim 10'$

Table 3.5: WXM data types

Data type	Time resolution	Description
HK	4 s	House keeping data (Power status, HV setting temperatures of the electronics board and the wall of the support structure)
RAW	1 μs	Unprocessed photon data. This data is used as a WXM health check and the calibration of the energy response.
TH	1.2 s	Time history data in 4 energy bands (2–5 keV, 5–10 keV, 10–17 keV and 17–25 keV, approximately)
POS	6.6 s	Position histogram data in two energy bands (2–7 keV and 7–25 keV)
PHA	4.9 s	4.9s time-binned energy spectrum. Available for each anode wire. The position information is not available.
TAG	6.4 μs	This data generated when a trigger occurs. Time-tagged photon data with position, energy and wire ID.

Selected TAG data

The burst data includes time-tagged photon data, while the survey data produce time-integrated (4.92 s) data for each wire in the WXM proportional counters. In order to improve the signal to noise ratio, and consequently the spectral analysis, we apply a cut to the WXM photon time- and energy-tagged data (TAG data), using the photons from the pixels on the six wires of the X-detector and those of the Y-detector which are illuminated well by the GRB. Moreover, as the gain is not uniform at the end of the wires (Shirasaki et al. 2003), we use only the photon counts that registered in the center ± 50 mm region of the wires (the full wire range is ± 60 mm).

Otherwise, since the position information is not available in the spectral survey data

(PHA data), the photon selection cannot be applied to survey data, although the wire selection can be applied.

Procedure of selected TAG data

Because of the coded aperture, the signal to noise ratio (S/N) of the WXM data is usually low (the open fraction of the mask is $\sim 30\%$ at the boresight incident angle). However, it is possible to increase the S/N using its imaging capability. We apply the following steps to maximize the S/N:

1. Simulate positional distribution of the burst photons due to the mask shadows.
2. Sort the position bins according to the simulated counts in decreasing order.
3. Find the foreground/background time regions which maximize the S/N (They usually agree with the foreground/background time regions used in the localization of the burst).
4. Cumulate the foreground/background counts and compute the S/N for the position bins.
5. Choose N which shows the highest S/N.
6. Select the wire-position pairs from 1 to N.

The new data set created by this method is called “selected TAG data”. All the bursts for which the TAG data are available, create selected TAG data. The selected TAG data are used for both the temporal and spectral analysis. Note that since the selected TAG selects “artificially” the illuminated position bins from the GRB, we have to correct the effective area for the spectral analysis. We multiply the fraction in the response matrix of each wires defined as (simulated counts of selected bins)/(total simulated counts).

3.1.3 The SXC

The Soft X-ray Camera (SXC) is designed to provide a few arc-second location for GRBs. It consists of X-ray CCDs and a fine coded mask. The coded mask is located 95 mm above the CCD chips with a mask element size of $45 \mu\text{m}$. This corresponds to a characteristic angular resolution of $96''$.

The size of the SXC coded mask is $10 \text{ cm} \times 10 \text{ cm}$. The deviation of the slit edges of the mask is less than $5 \mu\text{m}$ rms and this gives ideal performance to achieve the SXC

angular resolution. The pattern consists of 2100 coded elements. The open fraction of the mask is ~ 0.2 .

The X-ray CCDs are front-side CCID-20 2048 \times 4096 arrays (15×15) μm pixels; 6.1 cm \times 3.1 cm size) fabricated at MIT Lincoln Labs. They operate in the role of a collection of 2048 long and narrow detectors. The integration time is 1.2 s. To minimize the power consumption, the CCDs are passively cooled to -50 $^{\circ}\text{C}$ in flight using a radiator plate attached to the base plate.

Two optical blocking filters (OBFs) were mounted on the SXC. OBFs are designed to prevent non-X-ray photons like moonlight from reaching the CCDs. The outer OBFs were made of a 0.05 μm aluminized polyimide film, covering the whole aperture. The inner OBF was made from a 25 μm ^4Be foil, covering one half of the CCD area. Unfortunately, because of the increase of the density of atomic oxygen from intense solar flares in the period of late 2000 to early 2001, the outer OBFs were lost. The polyimide was eroded because of this unexpected high flux of atomic oxygen. After that the SXC was not operated at the bright moon phases.

To monitor the gain variation in orbit, a ^{55}Fe radioisotope was attached to the mask frame.

The localization procedure of the SXC was restricted to the search region $\pm 1^{\circ}$ around the best WXM location to avoid false localizations. With this restriction, there is only a 1% chance probability that the resultant location is false. Empirical measurements show a $20''$ radius RMS localization accuracy in the X and Y directions. This corresponds to a 90% confidence, two-dimensional error circle of $43''$ radius.

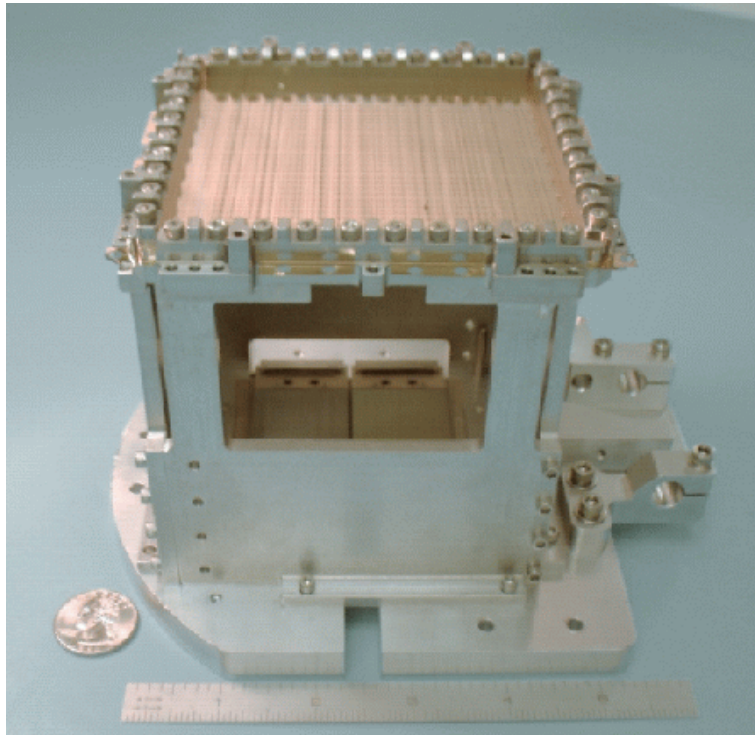


Figure 3.11: SXC (Soft X-ray Camera)

3.2 *Fermi* Gamma-ray Space Telescope (GLAST)

3.2.1 *Fermi* Observatory

The *Fermi* Gamma-ray Space Telescope (hereafter *Fermi*, formerly known as GLAST; Gamma-ray Large Area Space Telescope) (Fig. 3.12; Atwood et al. 2008) was successfully launched into a low earth orbit of 550 km altitude at a 28.5 degree inclination, on 11 June 2008 (Fig. 3.13). *Fermi* is an international space observatory to explore high-energy objects and space. The advantage of *Fermi* is the broadest energy range (8 keV– 200 GeV) among past astronomical observatories. In particular, the GeV region is one of the last poorly observed parts of the celestial electromagnetic spectrum. The ancestor of *Fermi* was the Energetic Gamma Ray Experiment Telescope (EGRET) detector (Nolan et al. 1992), which flew on-board the Compton Gamma Ray Observatory (CGRO). EGRET detected gamma rays with a spark chamber for direction measurements and a NaI(Tl) calorimeter, the Total Absorption Shower Counter (TASC), for energy measurements. EGRET completed the first survey of the whole sky in the 30 MeV – \sim GeV band and made detailed studies of high-energy gamma-ray emitting sources. CGRO was safely deorbited and re-entered the Earth’s atmosphere on June 4, 2000. But the all-sky survey above the GeV region still remained and a lot of faint gamma-ray emitting objects were not identified due to a large angular certainty. *Fermi* has been expected to unveil the EGRET unidentified sources and clarify the emission mechanisms of active galactic nuclei, pulsars, pulsar wind nebulae, GRBs and so on.

The main instrument on board the *Fermi* detector is the Large Area Telescope (LAT; Atwood et al. 2007) which is an electron-pair conversion telescope, to cover the 20 MeV – 200 GeV range. A secondary instrument is the GLAST Burst Monitor (GBM). This monitor plays a crucial role for one of the key scientific objectives of the mission. Especially for GRBs, its task is very important - it increases the detection rate of GRBs for the LAT and extends the energy range to lower energies (from 8 keV to \sim 30 MeV). Since the E_{peak} characteristic of synchrotron radiation is distributed between \sim 100 keV and \sim MeV, with only the LAT detector E_{peak} could not be determined. Furthermore, GBM provides real-time burst locations over a wide field of view with sufficient accuracy to allow re-pointing the *Fermi* spacecraft.

3.2.2 Large Area Telescope

Below the MeV region, photons are absorbed via the photoelectric effect or scattered via Compton scattering, leading to ejecting an electron. Above \sim 10 MeV, the main

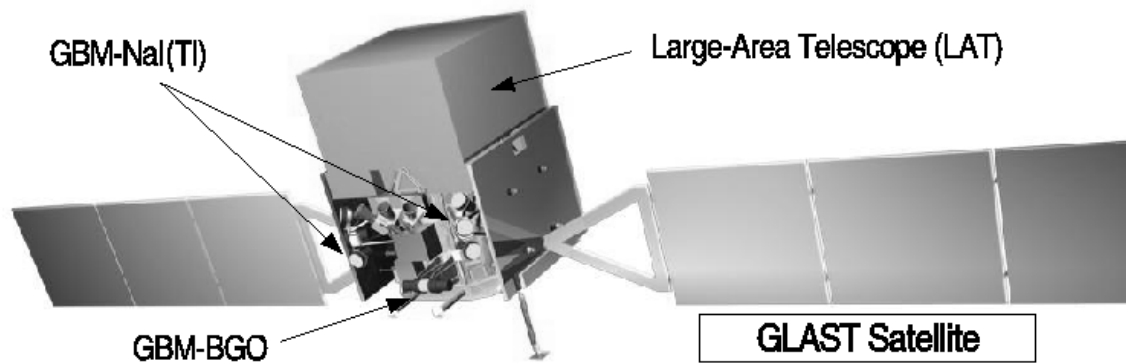


Figure 3.12: View of *Fermi* conceptual design with the GLAST burst monitor (GBM) and the Large-Area Telescope (LAT).



Figure 3.13: *Fermi* launch on 11 June 2008

interaction is the conversion of a photon into a e^+e^- pair. The cross section remains flat beyond the GeV region over the wide energy range. By using the pair-conversion characteristics, the LAT detector (Fig. 3.15) can determine the incident photon direction via the reconstruction of the trajectories of the resulting e^+e^- pairs. The incident photon first passes through an anti-coincidence shield, which is sensitive to high-energy charged particles, then through thin layers of a high-Z (tungsten) material called a *conversion foil* to cause increased pair-conversion.

High-energy (>20 MeV) gamma-rays convert into e^+e^- pairs in one of 16 layers of the tungsten foils. The e^+e^- pair then passes through up to 36 planes of position-sensitive detectors (silicon strips) interleaved with the tungsten foils in the Tracker, leaving behind tracks pointing back toward the origin of the gamma ray. This technique is demonstrated in Fig. 3.15. After passing through the last tracking layer they enter the Calorimeter, which consists of bars of cesium-iodide (CsI) crystals, read out by PIN diodes. The Calorimeter provides the energy measurement of the incident gamma ray. A third detector system, the anti-coincidence detector (ACD: Moiseev et al. 2007), encloses the top and sides of the tracker to reject charged cosmic-ray events such as electrons, protons or heavier nuclei. The performance of the LAT detector is summarized in table 3.2.2.

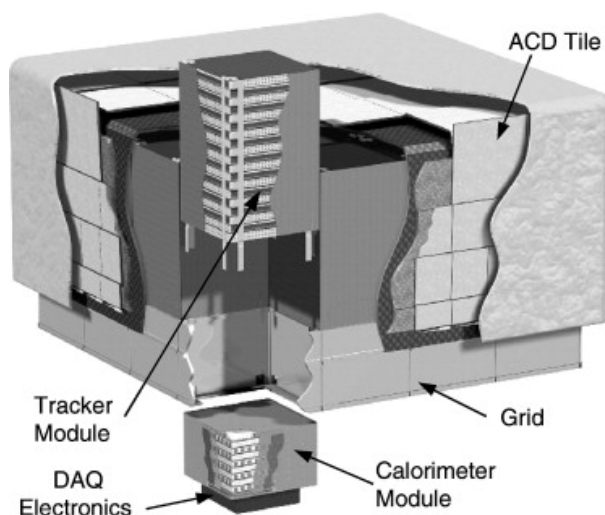


Figure 3.14: Cutaway view of the LAT detector. Each tower consists of a Tracker and a Calorimeter, and is in a 4×4 array.

Tracker

The tracker (Tajima 2006) has 4×4 towers; each tower consists of a stack of 19 tray structures, and each tray is composed of silicon sensors and the conversion foil. We explain

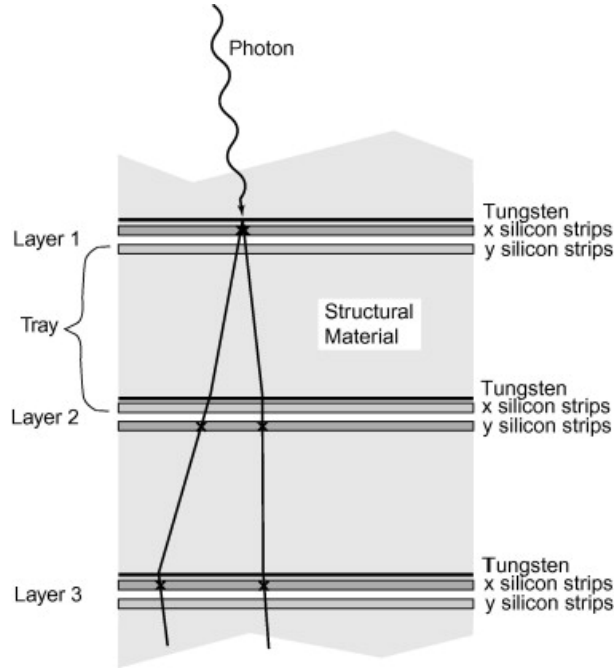


Figure 3.15: Schematic views of the measurement of a gamma-ray conversion in the Tracker.

Table 3.6: Performance of the LAT instrument

Dimension	1.8 m × 1.8 m × 0.72 cm
Power consumption	650 W
Mass	2,789 kg
Energy range	20 MeV– 200GeV
Effective area (at 10 GeV)	~ 10,000 cm ²
Energy resolution 100 MeV on-axis	9 %
Energy resolution 10 GeV on-axis	8 %
Energy resolution 10 – 300 GeV on-axis	< 15 %
Point Spread Function 68 % 100 MeV on-axis	4°
Point Spread Function 68 % 10 GeV on-axis	0.1°
Field of view	2.4 sr

theses elements in detail below.

The “Silicon Strip Detectors” (SSD) play a crucial role on localizing the positions of $e^- - e^+$ interactions. The detectors are obtained from high resistivity ($> 5 \text{ k}\Omega/\text{cm}$) wafers (Fig. 3.16); they are single sided, AD coupled and passivated with glass; 384 p^+ strips (56 μm wide) are implanted on a 400 μm thick n-type substrate and biased through poly-

silicon resistors, for a total active area of $87.5 \times 87.5 \text{ mm}^2$. For each strip there are two AC pads for wire bonding (on the Al decoupling electrode) and one DC pad (contacting the implant) for testing purposes.

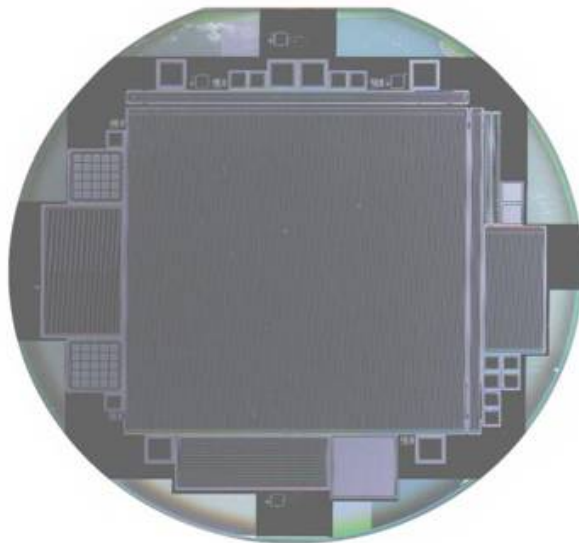


Figure 3.16: Silicon strip sensor of the LAT detector

The “Tray” is the mechanical module which supports the silicon sensors and the conversion foils, and builds a tower structure once stacked with other trays. The structure of the tray is complex and imposes tight requirements on the dimensions of each components for ensuring the perfect alignment of the tower. Each tray, as illustrated in Fig 3.17, is made up of a honeycomb structure, covered on each faces with carbon fiber sheets. Depending on the tray’s position in the stack, tungsten foils of different thicknesses are glued onto the bottom face of the tray. A kapton bias circuit is then glued onto the surface of the trays and finally, on both sides the silicon strip detectors are glued onto the kapton foil. The SSDs are bonded together in strip of 4 tiles, building a ladder. Thus, four ladders together build the silicon surface of the tray. The strips of the silicon detectors run parallel in both the surfaces of the tray.

Each of the 4×4 tracker “Tower” modules consists of a stack of 19 tray structures (Fig. 3.18). The first 12 trays (“medium trays”) has 0.025 radiation lengths of conversion material, while the following 4 trays (“heavy trays”) are equipped with 0.25 radiation lengths of tungsten, for maximizing the conversion efficiency. The last two trays then have no tungsten on them (“light trays”). Since the SSD wafers cover both sides of a tray with the strips on each side running in the same direction, when a tray is stacked into a tower it is rotated by 90° with respect to the adjacent trays. In this way each tungsten

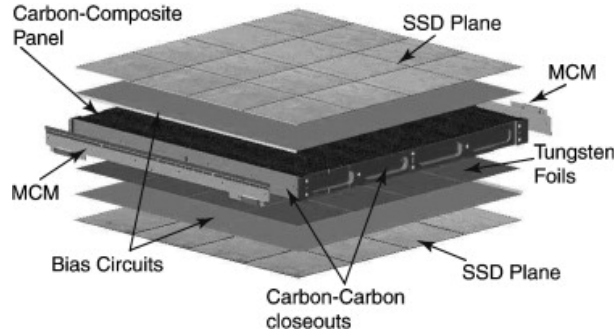


Figure 3.17: Exploded view of a tray. The internal structure of a tray is covered by a carbon fiber face sheet (carbon-composite panels). On the on the bottom face of the tray tungsten foils are glued. SSDs are glued, through the kapton bias circuit on the tray. MCM stands for read out electronics multi-chip module.

foil is followed immediately by an X, Y plane of detectors with a 2 mm gap between X and Y layers. The detectors are located close to the conversion foils to minimize multiple-scattering errors. The bottom tray is mounted on the support grid, and for this reason it has an extra flange which requires a slightly different production chain.

Calorimeter

The calorimeter (Fig. 3.19) is made up of 96 CsI crystals (thallium doped) per tower arranged into a hodoscopes imaging configuration and with PIN diode read-out on each end. The electronics chain for each PIN diode is composed of a preamplifier which feeds two shaping amplifiers. Discriminators divide the energy domain into four energy ranges, with two peak-detecting track and holds. A second faster shaping amplifier, peaking at $0.5 \mu\text{s}$ is used for fast trigger discrimination. The main features of the calorimeter detector are the large dynamic range (5×10^5), low nonlinearity (less than 2%), low power consumption, and minimal dead time (less than $20 \mu\text{s}$ per event).

Anti-coincidence Detector

The purpose of the Anti coincidence Detector (ACD: Moiseev et al. 2007, Fig. 3.20) is the detection of incident charged cosmic-ray particles; they outnumber cosmic gamma-rays by ~ 5 orders of magnitudes. The ACD has a segmented plastic scintillator in anti-coincidence with the incident charged particles, to enhance the background rejection. The estimated Monte Carlo efficiency of background rejection is greater 0.9997. Signals from the ACD can be used as a veto trigger or can be used later in the data analysis. One advantage of the LAT detector is the short dead time and the consequent high trigger



Figure 3.18: Inverted view of one tracker tower module without a sidewall

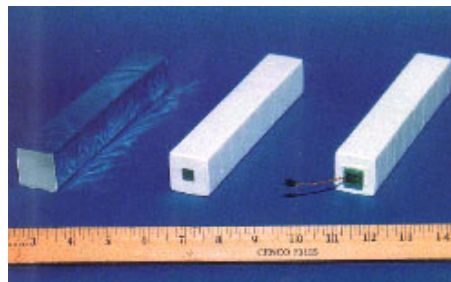


Figure 3.19: The Calorimeter (CsI crystal)

rate.

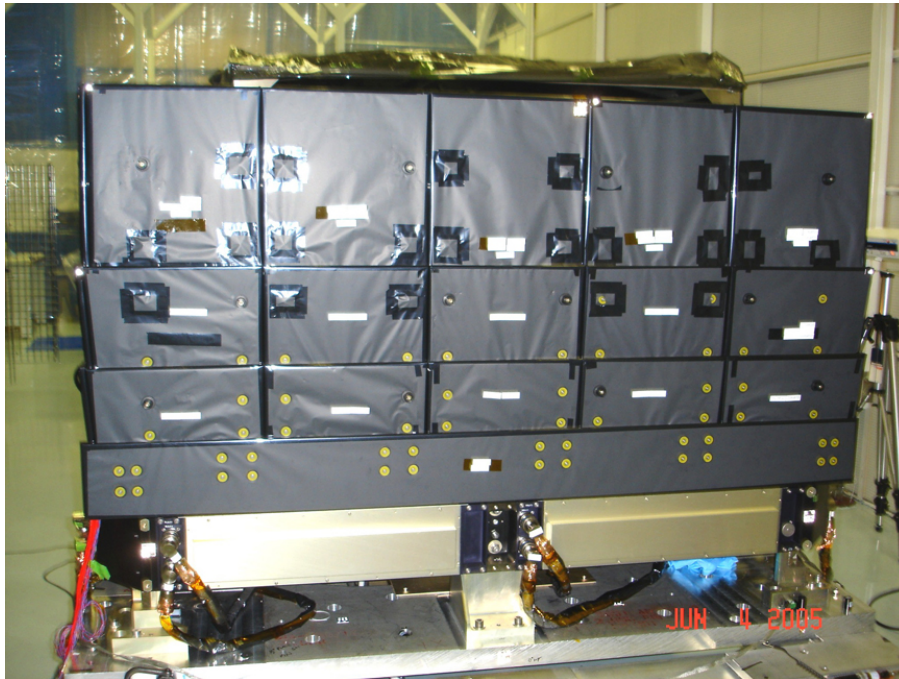


Figure 3.20: The assembled ACD

3.2.3 Gamma-ray Burst Monitor

Detector

The Gamma-ray Burst Monitor (GBM: Hoover et al. 2008, Meegan et al. 2008) instrument has been designed for helping the LAT detector in the discovery of GRBs. The GBM consists of 12 thin NaI(Tl)-plates, which cover the energy range between 8 keV and ~ 1 MeV, and two BGO detectors, which can cover the higher-energy range between ~ 200 keV and ~ 30 MeV, and are responsible for the overlap at the low energy end with the LAT detector.

The 12 NaI(Tl) and 2 BGO scintillators are mounted on the spacecraft as shown in Fig. 3.12. The pointing orientations of the 12 NaI(Tl) scintillators are aligned in the following manner: six crystals in the equatorial plane (hexagonal), four crystals at 45° (on a square) and two crystals at 20° (on opposite sides). This arrangement results in a large field of view for the GBM detector of > 8 sr and makes it possible to locate the origin of the burst by comparing the count rates of different NaI scintillators. The two BGO scintillators are mounted on opposite sides of the space craft, providing nearly a 4π sr field of view. Both the NaI(Tl) and BGO scintillators are read-out by photo-multiplier

tubes (PMTs).

The design of the NaI(Tl) detector is shown in Fig. 3.21. These detectors consist of circular crystal disks made from NaI(Tl) having a diameter of 127 mm and a thickness of 12.7 mm. To prevent light leakage and seal the crystals against atmospheric moisture due to its hygroscopic behavior, each crystal is packed tightly in a hermetically sealed Al-housing (except for the glass window to which the PMT is attached).

The two BGO scintillators are cylindrical, with a diameter of 127 mm and a length of 127 mm. The BGO cover shown in Fig. 3.22 is made of carbon fiber reinforced plastic with interface parts made of titanium. The performance of the NaI(Tl) and BGO detectors expressed in effective area and energy resolution is summarized in Fig. 3.23 and 3.24.

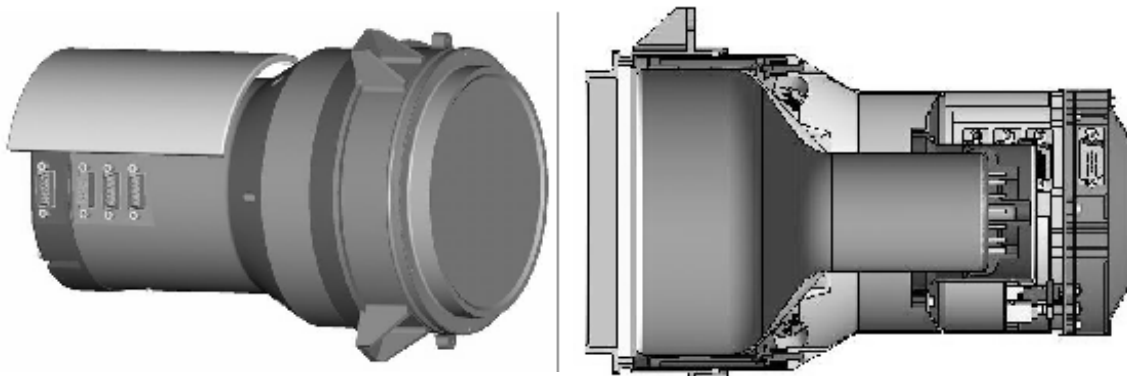


Figure 3.21: Side and cross views of the NaI(Tl) scintillator coupled with a PMT.

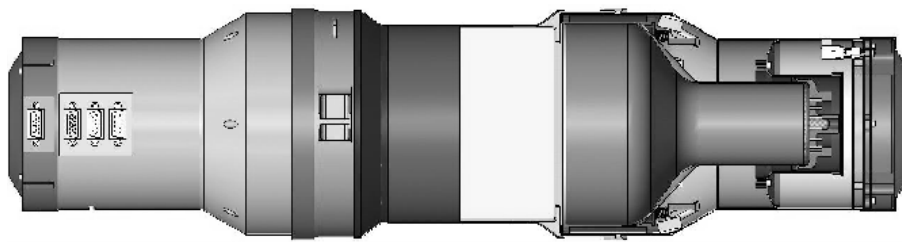


Figure 3.22: Side view of the BGO detector. Its shape is cylindrical with a diameter of 127 mm (5 inch) and a length of 127 mm. The BGO detector is read-out from both ends by a 5 inch PMT.

GBM burst localization

The GBM detector localizes GRBs by comparing count rates of NaI(Tl) detectors, which are facing the sky in different directions. It is planned to increase the localization accuracy in three stages: on board, automatic and manual on ground. The burst location will be

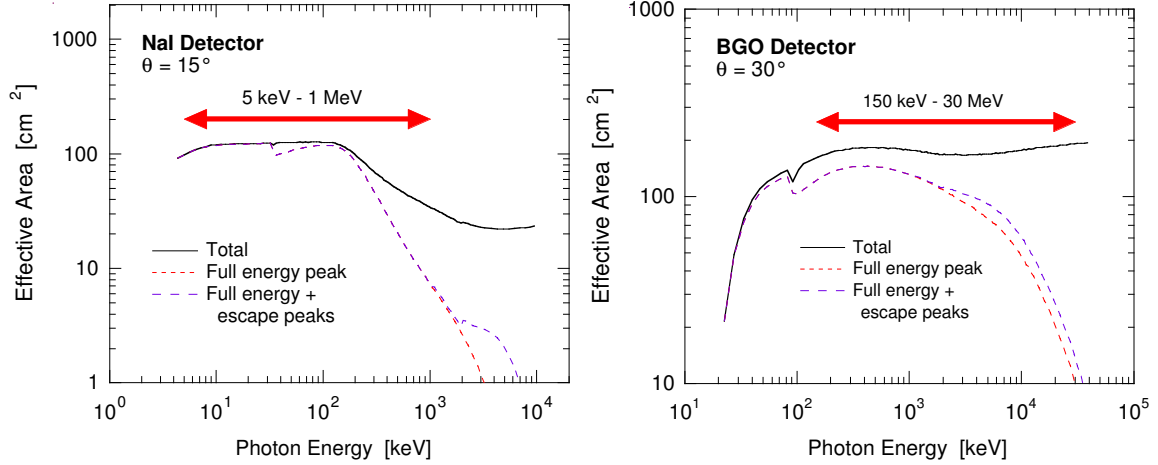


Figure 3.23: Effective areas of NaI(Tl) and BGO detector, with 15° and 30° as angle of incidence, respectively.

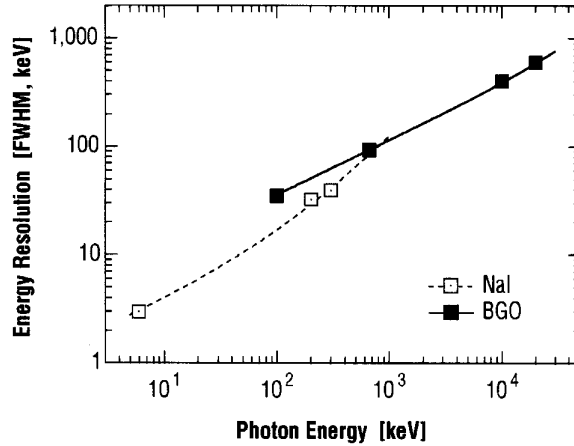


Figure 3.24: Energy resolution of the NaI(Tl) and BGO detectors

calculated on board in real time, yielding an accuracy of $< \sim 15^\circ$ (1σ confidence radius) within 1.8 s, which can be used as a LAT trigger. If the burst occurred in the LAT field of view, data-reduction modes (reducing the LAT background by isolating the area of the GBM burst direction) can be initiated in the LAT, leading to increasing the LAT sensitivity for some weak bursts. If the burst occurred outside the LAT field of view, a rough localization within $\sim 20^\circ$ is enough to cover the LAT field of view (~ 2 sr) after re-pointing (in a few minutes). In this way, the delayed high-energy emission from the GRB can be detected (e.g. in the case of GRB 940217, Hurley et al. 1994).

After the transmission of the detector count rates to ground, the burst location can be calculated with an improved accuracy of less than 5° within 5 s. This information can be used to search for afterglow emission at other wavelengths, as input for the GRB

Coordinate Network (GCN) and as input for the Interplanetary Network (IPN).

3.2.4 LAT Instrument Response Functions

As the LAT detector has a strong energy-dependence for the Point Spread Function (PSF), the intrinsic source spectrum is affected by the degree of source confusion. Furthermore, the LAT field of view is large and there is a strong variation of the response as a function of incident angle with respect to the instrument axes and scan mode. Since each event effectively has its own response function, the estimate of the LAT response at any time, any attitude is important and we introduce an instrument response function.

The instrument response functions (IRFs) describe the response of the instrument in terms of transformation probability from a *true* physical quantity (e.g. energy and direction of photons) to the corresponding measured quantity. Here, the IRFs depend on not only the instrument itself, but also the reconstruction algorithms, the background rejection algorithms, any possible selection of the events, and furthermore they are time variable. The observed count rate is basically the convolution between the real flux and the IRFs. Thus, in order to calibrate the instrument, the raw data has to be de-convolved with the IRFs.

Especially for gamma-ray astronomy, the number of observed gamma-ray photons is small and the statistics are poor compared with that of X-ray astronomy, so maximum likelihood analysis is needed, not a χ^2 test. The maximum likelihood analysis provides, in principle, the best possible estimate of source characteristics.

The likelihood is given as,

$$L = \prod_k \frac{\theta_k^{n_k} \exp(-\theta_k)}{n_k!} \quad (3.1)$$

where θ is the predicted counts and n_k is the measured count in map pixel k . If the size of the pixel becomes infinitesimal, n_k has a value of 1 or 0 (in this case, unbinned likelihood method). In order to reduce its burden to compute the likelihood, a certain number of pixels is binned (in this case, binned likelihood). The method is suitable for the LAT analysis described above.

The IRFs are matrices that describe the responses of the detector such as the detection efficiency (effective area A_{eff}), the angular resolution (PSF), and the energy reconstruction. We use a standard factoring of the total response R as

$$R(E', \Omega'; E, \Omega, t) = A(E, \Omega, \vec{L}(t)) D(E'; E, \Omega, \vec{L}(t)) P(\Omega'; E, \Omega, \vec{L}(t)) \quad (3.2)$$

where A is effective area, D is energy dispersion, P is PSF, E and Ω are the “true” photon energy and direction, E' and Ω' are “measured” photon energy and direction and

$\vec{L}(t)$ represents the time variation of the instrument orientation and internal degrees of freedom, respectively. R represents the probability that we measure a photon having E' and Ω' when a photon having E and Ω with a flux of 1 photon per unit of area per unit of time comes into the LAT detector. Thus, a source model S (photons per unit of momentum per unit of energy) in the case of only a point source (e.g., GRB) is,

$$S(E, \Omega, t) = s_1(E, t)\delta(\Omega - \Omega_1) \quad (3.3)$$

The region-of-interest (ROI) is the extraction region for the data in measured energy E' , direction Ω' , and t . Folding the source model through the instrument response yields the event distribution function, M (i.e., the expected counts given the model) in the space of measured quantities. M is written as

$$M(E', \Omega', t) = \int_{SR} dE d\Omega R(E', \Omega'; E, \Omega, t) S(E, \Omega, t) \quad (3.4)$$

where SR (source region) is the part of the sky defined to contain all sources that contribute significantly to the ROI. For standard analysis, we will treat “steady” sources, so that we regard $S(E, \Omega, t)$ as $S(E, \Omega)$. Furthermore the predicted counts from the observed events is the integral of M over the ROI. the predicted counts N_{pred} are defined as

$$N_{pred} = \int_{ROI} dE' d\Omega' dt M(E', \Omega', t) \quad (3.5)$$

Finally the likelihood function we would like to maximize is

$$\log L = \sum_j \log M(E'_j, \Omega'_j, t_j) - N_{pred} \quad (3.6)$$

The sum is taken over all events, indexed by j , lying within the ROI. In this way, we can derive a source flux and spectrum from observed photon having E' , Ω' at the time t .

For a faint object (e.g., supernova remnants, pulsar wind nebulae and so on), the likelihood including the background count (e.g. Galactic- or extragalactic diffuse emission) must be taken into account. But for GRBs, since their durations are quite short (~ 10 s) and during such an interval there are few events within its ROI, we can ignore the background counts.

Chapter 4

HETE Observations & Analysis results

4.1 Motivation

First, the spectral lag is expected to be a redshift indicator. In past studies, Type Ia supernovae are candidates for the distance indicator because they have a constant luminosity. Thanks to a sample of a large number of Type Ia supernovae, the cosmological parameter can be constrained (e.g., Riess et al. 2007 etc.). But for the range $z > 2$, supernovae are too dim to measure the luminosity and so GRBs are one of the other possible indicators of distance whose observed maximum redshifts are higher than those of Type Ia supernovae. Furthermore, GRBs are keys for not only constraining the cosmological parameter but also deriving the star formation rate in the early universe, because the origin of GRBs are likely to be associated with the collapse of massive stars (Hjorth et al. 2003). For the above reasons, the study of GRBs as distance indicators is important.

We focus on the spectral lag which is one of characteristics of the GRB prompt emission which can be a distance indicator. The past spectral analyses have been done using a sample of many BATSE GRBs. The spectral lags have been investigated between typical energy bands 25–50 keV and 100–300 keV, using both CCF and peak-to-peak difference. From the results of the latest study, it is clear that the spectral lag characterizes *pulses* rather than the bursts themselves (Hakkila et al. 2008). Furthermore the systematic analysis of lag and temporal evolution was done by Zhang et al. 2007, inferring that the energy-dependent pulse properties come from the joint contribution of both the hydrodynamic process of the outflows and the curvature effect.

However, it is not significant that the BATSE results hold for the lower energy band (< 25 keV), and a temporal and spectral analysis in the lower-energy band might lead to

the clarification of the origin of the lag and temporal evolution. For these reasons, we do the spectral lag, temporal and spectral analysis using a sample of *HETE* GRBs.

4.2 Lag analysis

4.2.1 Sample and Selection

We study a sample of 9 GRBs with known and possible redshifts (Table 4.1) and 2 GRBs without known redshifts, with the criterion that $T_{90} > 2$ s (T_{90} is the time interval which includes 90% of the burst photons) and that time-tagged data are available. For the latter, time-tagged data was lost for some bursts due to downlink problems or invalidation of the instruments (e.g., GRB 030329, GRB 030328 etc.). Even in such bursts, we can do the spectral analysis. However, since the available energy band is too coarse (6–40 keV, 40–80 keV and 32 – 400 keV), we cannot conduct a detailed study of time- and energy-dependence.

In addition, while we select sufficiently non-overlapped pulses especially for GRBs without known redshift, we also adopt overlapped pulses of GRBs because the number of GRBs with known redshifts is very small (~ 20).

We show the list of 11 GRBs which satisfy the above requirements in Table 4.1.

Table 4.1: GRB samples

GRB	redshift	Reference
010921	0.45	Djorgovski et al. 2001
020124	3.20	Hjorth et al. 2003
020127	1.9 ¹	Berger et al. 2007
021211	1.01	Vreeswijk et al. 2003
030528	0.78	Rau et al. 2005
030725	-	Pugliese et al. 2005
040924	0.86	Wiersema et al. 2004
041006	0.72	Stanek et al. 2005
050408	1.24	Berger et al. 2005
060121	-	de Ugarte Postigo et al. 2006

¹: this is a possible value estimated from the afterglow investigation and spectral energy distribution (SED).

4.2.2 Method

Each GRB pulse is fitted with a four-parameter pulse model (Norris et al., 2005)

$$I(t) = A\lambda \exp(-\tau_1/(t - t_{\text{start}}) - (t - t_{\text{start}})/\tau_2) \quad (4.1)$$

$$= A\lambda \exp(-\tau_1/(t + \tau_{\text{peak}} - t_{\text{peak}}) - (t + \tau_{\text{peak}} - t_{\text{peak}})/\tau_2) \quad t > t_{\text{start}} \quad (4.2)$$

with background, where t is the time after the trigger, τ_1 and τ_2 are the pulse rise and pulse decay constants, $\lambda = \exp(2(\tau_1/\tau_2)^{1/2})$, t_{peak} is the time of the pulse’s maximum intensity A , t_{start} is the start time, $\tau_{\text{peak}} = (\tau_1\tau_2)^{1/2}$ is the peak time from the start time t_{start} , so that t_{peak} is given by $t_{\text{peak}} = t_{\text{start}} + \tau_{\text{peak}}$ as shown in Fig. 4.1. In Eq. 4.2, t_{peak} is treated as a primary fitting parameter in order to estimate the uncertainty in t_{peak} directly in the fitting procedure.

t_{start} is the formal time of pulse onset and often occurs at an intensity several orders of magnitude below the peak intensity, in which case t_{start} is not indicative of the visually apparent onset time. Especially in the case of $\tau_1 \gg 1$, t_{start} is extremely far from the peak of the pulse. Here, as described in Norris et al., 2005, we introduce an effective onset time t_{eff} arbitrarily defined as the time when the pulse reaches 0.01 times the peak intensity. The onset time is relative or corresponds to burst trigger time determined by the instruments as illustrated in Fig. 4.1. Furthermore, the values of t_{eff} are different in different energy bands. For *HETE* GRBs, the statistics of GRBs are not as rich as those of BATSE GRBs because, e.g., the effective area of the FREGATE detector ($\sim 150 \text{ cm}^2$) is lower by a factor of ~ 10 than that of the BATSE detector ($\sim 2000 \text{ cm}^2$). This causes t_{eff} to be scattered in different energy bands due to poor determination of τ_1 and τ_2 . To avoid this, we adopt an onset time of the “bolometric” light-curve profile, t'_{eff} , derived by fitting the light curve in the 6 – 400 keV band, which corresponds to the entire FREGATE-energy band. Thus, we define $\tau'_{\text{peak}} = t_{\text{peak}} - t'_{\text{eff}}$ in this thesis. The corresponding uncertainties are calculated using the error propagation formula.

The physical concept of this function is that some (quasi)exponential process supplies energy (on timescale τ_1) and another such process reduces it, a necessary condition for the continuance of supply (on timescale τ_2). For instance, the former could be a cascading injection of radiating particles and the latter an explosive expansion of the source or cooling process. These combined exponential dependences in the model, while only phenomenological, turn out to afford good fits to the wide pulses in long-lag bursts.

Spectral peak lags are defined as the difference between the maximum-intensity times (t_{max}) in different energy bands. Other measurable pulse properties include the pulse duration $w = 3\tau_2(1 + 4\sqrt{\tau_1/\tau_2}/3)^{1/2}$ defined as the time intervals where intensities equal Ae^{-3} . Details of these pulse formulae are given in appendix B.

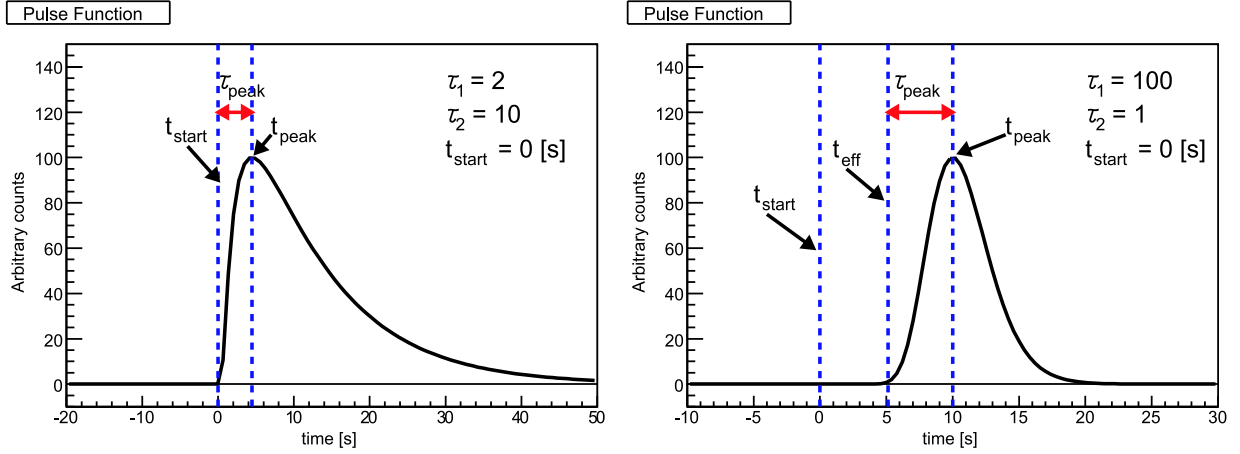


Figure 4.1: *left*: Pulse function of Norris et al., 2005 with $\tau_1 = 2$, $\tau_2 = 10$ and $t_{\text{start}} = 0$ s. In this case since $\tau_1 = 2$ and the rise time is relatively short, t_{eff} , defined as the time when the pulse reaches 0.01 times the peak intensity, is almost same as t_{start} . *right*: Pulse function with $\tau_1 = 100$, $\tau_2 = 1$ and $t_{\text{start}} = 0$ s. Since $\tau_1 = 100$ and the rise time is relatively large and the pulse shape is broad, t_{start} is different from the so-called observed trigger time. We thus regard t_{eff} as the effective pulse onset time (epoch of start).

Pulses and background are fitted simultaneously over the whole burst using the chi-square fitting routine ROOT (<http://root.cern.ch/>).

In case where the data include point coordinates, x_i and y_i with a function $f(x)$, the chi-square is defined as the following

$$\chi^2 = \sum_i \frac{[y_i - f(x_i)]^2}{\sigma_{y_i}^2 + \left[\frac{1}{2} (\sigma_{x_{\text{low},i}} + \sigma_{x_{\text{high},i}}) \frac{df(x_i)}{dx} \right]^2} \quad (4.3)$$

where the corresponding uncertainties are $\sigma_{x_{\text{low},i}}$ (or $\sigma_{x_{\text{high},i}}$) and σ_{y_i} . “low” (“high”) is the uncertainty below (above) the data point and in case the function lies below (above) the data point, σ_{y_i} is $\sigma_{y_{\text{low},i}}$ ($\sigma_{y_{\text{high},i}}$). If the uncertainty is symmetric, $\sigma_{x_{\text{low},i}} = \sigma_{x_{\text{high},i}}$ and $\sigma_{y_{\text{low},i}} = \sigma_{y_{\text{high},i}}$.

The χ^2 varies as the square of distance from a minimum, and an increase of 1 σ deviation in the parameter from the minimum increases χ^2 by 1. Thus the 1 σ uncertainty is calculated.

4.2.3 Spectral Model Function

We use the Band function (Eq. 1.3, 1.4) in the spectral analysis. Furthermore in some cases, since in the higher energy band the number of photons is smaller, we could not determine the high-energy photon index β well. We then introduce a cutoff power-law

function as shown in the following equation,

$$N(E) = A(E/K)^\alpha \exp\left(-\frac{E}{E_{\text{peak}}/(2+\alpha)}\right) \quad (4.4)$$

When we measure the observed energy flux f (ergs cm⁻² s⁻¹) during the observed foreground time Δt , the fluence F (ergs cm⁻²) is defined as $f\Delta t$, where we integrate the observed spectrum between 1 – 10000 keV in the observer frame (the same band as Amati et al. 2002) to cover the hard emission beyond the peak energy E_{peak} . Assuming the cosmological parameter set $(\Omega_m, \Omega_\Lambda, H_0) = (0.3, 0.7, 65)$, we can formulate a luminosity distance as

$$d_L(z) = (1+z) \frac{c}{H_0} \int_0^z \frac{dz'}{\sqrt{\Omega_\Lambda + (1+z')^3 \Omega_m}} \quad (4.5)$$

We can calculate the isotropic radiated energy E_{iso} (ergs) in the rest frame of GRBs with fluence F . The isotropic radiated energy is expressed as

$$E_{\text{iso}} = \frac{4\pi d_L(z)^2}{1+z} F \quad (4.6)$$

Here, the $(1+z)$ factor comes out from the fact that the luminosity distance is defined in a way to account for the cosmological time dilation and spectral redshift when converting the source flux to the observer's frame. Since the time $\Delta t'$ in the source frame is dilated from the time Δt in the observer frame by a factor of $(1+z)$, we can formulate the luminosity L_{iso} (ergs s⁻¹) as

$$\begin{aligned} L_{\text{iso}} &= \frac{4\pi d_L(z)^2}{1+z} F \times (1+z)/\Delta t \\ &= 4\pi d_L(z)^2 f \end{aligned} \quad (4.7)$$

4.2.4 Energy Band

In this thesis, we adopt two sets of energy bands in order to calculate the spectral lag in the two divided bands. The first one is 6–25 keV and 50–400 keV in the observer's frame. Although in the past study by BATSE, the energy bands between 25–50 keV and 100–300 keV had been adopted, we adopt the lower energy band (<25 keV) and test if the same relation (e.g., lag-luminosity relation) is established or not. Furthermore, for all the past studies of the spectral lag the energy bands refer to the *observer's* frame. However

if the spectral lag is a characteristic feature of GRBs, it is better to derive the spectral lags between the energy bands in the *burst-rest* frame. Thus we adopt energy bands 20–100 keV and 100–500 keV in the burst-rest frame to be covered by the FREGATE instrument, because the number of events detected by the WXM instrument is often small due to the low effective area and the fact that off-axis events are partially coded while the FREGATE instrument can detect more photons compared to those of the WXM due to its relatively large effective area ($\sim 150 \text{ cm}^2$). The adopted energy bands are shown in Fig. 4.2.

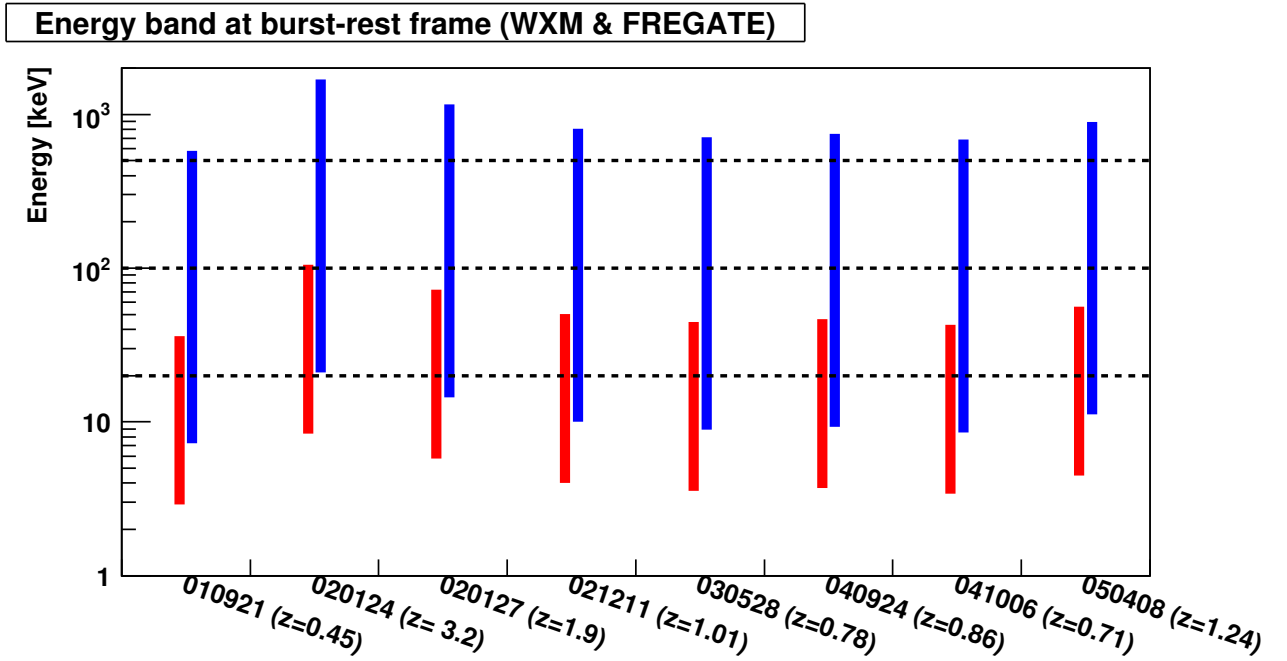


Figure 4.2: Adopted energy bands in the burst-rest frame. The red bars represent the WXM bands and the blue ones represent the FREGATE bands. The adopted energy ranges are the range between the dashed lines (20–100 keV and 100–500 keV).

4.3 Spectral fitting

We used the *XSPEC v.11.3.0* software package (Arnaud 1996) to perform the spectral analysis. We fitted the spectrum for time intervals of each peak in the GRBs using the WXM and FREGATE data. Here we adopt time intervals whose intensities are equal to half of the maximum intensity for each pulse, the full width at half maximum (FWHM).

4.3.1 GRB010921

GRB 010921 triggered FREGATE on 2001 September 21 and was promptly reported as a GCN notice at 05:16:08 UT, approximately 17 s after the burst (Ricker et al. 2001). Since the GRB had an extremely off-axis position in one of the WXM cameras, a significant localization was not performed, but a confirmation and definitive refinement of the WXM localization using IPN (*Ulysses*) data available 15.2 hr after the GRB, enabled ground based observers to successfully target GRB 010921 (Ricker et al. 2002). A redshift of 0.45 was determined by Djorgovski et al. 2001 and the burst is the first one whose redshift was identified (Price et al. 2002). The light curves show the GRB consists of a prominent single pulse and its duration is ~ 20 s almost independent of the energy in most energy bands. The durations of GRBs tend to be shorter at higher energies, which is a common feature observed in many GRBs (Fenimore et al. 1995). However this GRB does not show such a feature and seems to be anomalous. Its spectrum is fitted well by the Band function. The pulse-fit in the two-divided bands and multi-divided bands, and pulse-resolved spectral-fit results are shown in Fig. 4.3, Table 4.2, Fig. 4.4, Table 4.3, Fig. 4.5 and Table 4.4, respectively. $T_{\text{peak}}^{\text{low}}$ is the peak time in the lower energy band, $T_{\text{peak}}^{\text{high}}$ is the peak time in the higher energy band, l_{obs} is the lag which is the difference between $T_{\text{peak}}^{\text{low}}$ and $T_{\text{peak}}^{\text{high}}$, l_{rest} is the lag in the burst-rest frame ($l_{\text{rest}} = l_{\text{obs}}/(1+z)$), σ_l is the significance of the lag, $w_{\text{rest}}^{\text{low}}$ is the pulse duration in the lower energy band in the burst-rest frame and $w_{\text{rest}}^{\text{high}}$ is the pulse duration in the higher energy band in the burst-rest frame. We use the same notations hereafter.

Table 4.2: Lag properties of GRB010921 (6–25 keV and 50–400 keV in the observer frame)

	$T_{\text{peak}}^{\text{low}}$	$T_{\text{peak}}^{\text{high}}$	l_{obs}	l_{rest}	σ_l	$w_{\text{rest}}^{\text{low}}$	$w_{\text{rest}}^{\text{high}}$
	[s]	[s]	[s]	[s]		[s]	[s]
1	9.72 ± 0.18	8.32 ± 0.36	1.40 ± 0.40	0.96 ± 0.27	3.5	21.1 ± 4.1	20.7 ± 6.6

Table 4.3: Lag properties of GRB010921 (10–100 keV and 100–500 keV in the rest frame)

	$T_{\text{peak}}^{\text{low}}$	$T_{\text{peak}}^{\text{high}}$	l_{obs}	l_{rest}	σ_l	$w_{\text{rest}}^{\text{low}}$	$w_{\text{rest}}^{\text{high}}$
	[s]	[s]	[s]	[s]		[s]	[s]
1	8.97 ± 0.20	8.12 ± 0.48	0.85 ± 0.52	0.59 ± 0.36	1.6	20.9 ± 3.7	21.0 ± 9.4

Table 4.4: Spectral properties of GRB 010921

Model	$E_{\text{peak}}^{\text{src}}$ [keV]	α	β	L_{iso} 10^{52} [ergs/s]	χ^2_{ν} (d.o.f.)
1 Cutoff p.l.	$108.6^{+6.1}_{-9.9}$	$-1.41^{+0.07}_{-0.07}$	-	$8.9^{+0.5}_{-1.1} \times 10^{-2}$	0.88 (80)

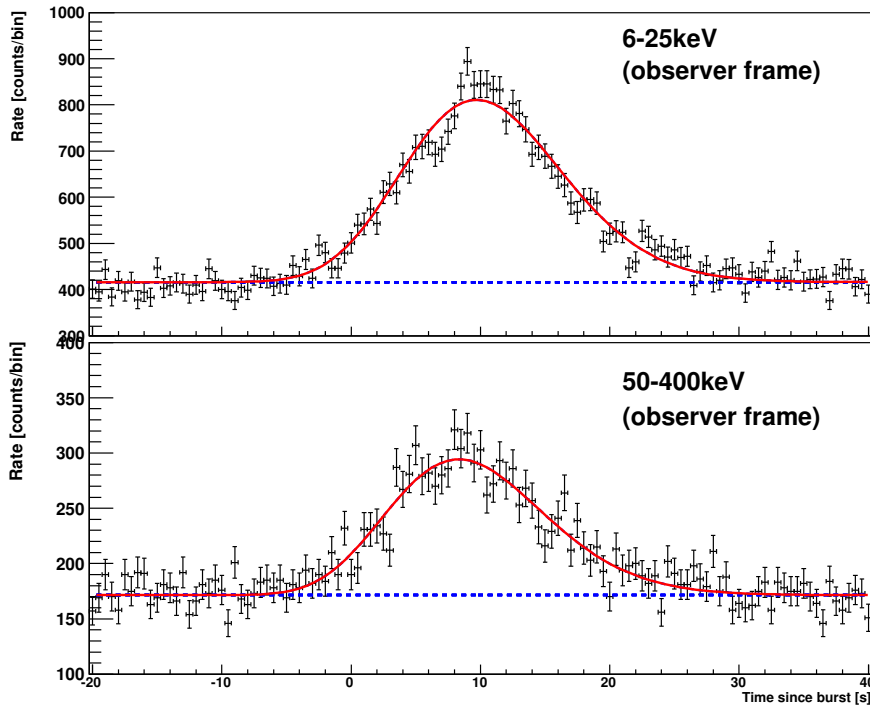


Figure 4.3: Pulse-fitting result: GRB 010921 at 6–25 keV (top panel) and 50–400 keV (bottom panel) in the observer’s frame.

4.3.2 GRB020124

At 10:41:15.15 UTC (38475.15 s UT) on 24 January, the FREGATE and WXM instruments detected and localized GRB 020124 (Ricker et al. 2002). Optical observations started 1.6 hours after the burst, as well as subsequently Very Large Array (VLA) and *Hubble Space Telescope* (*HST*) observations. A faint afterglow in the optical and radio was detected (Berger et al. 2002). Hjorth et al. 2003 also performed optical and near-infrared observations between 2 and 68 hr after the burst. Then they reported that the burst occurred in a very faint ($R > \sim 29.5$) damped Ly α absorber (DLA) at a redshift of 3.2.

The duration time of this burst is ~ 60 s and the burst consists of multiple pulses (~ 6). For the spectral evolution, it seems that there are soft-to-hard and then soft-to-hard

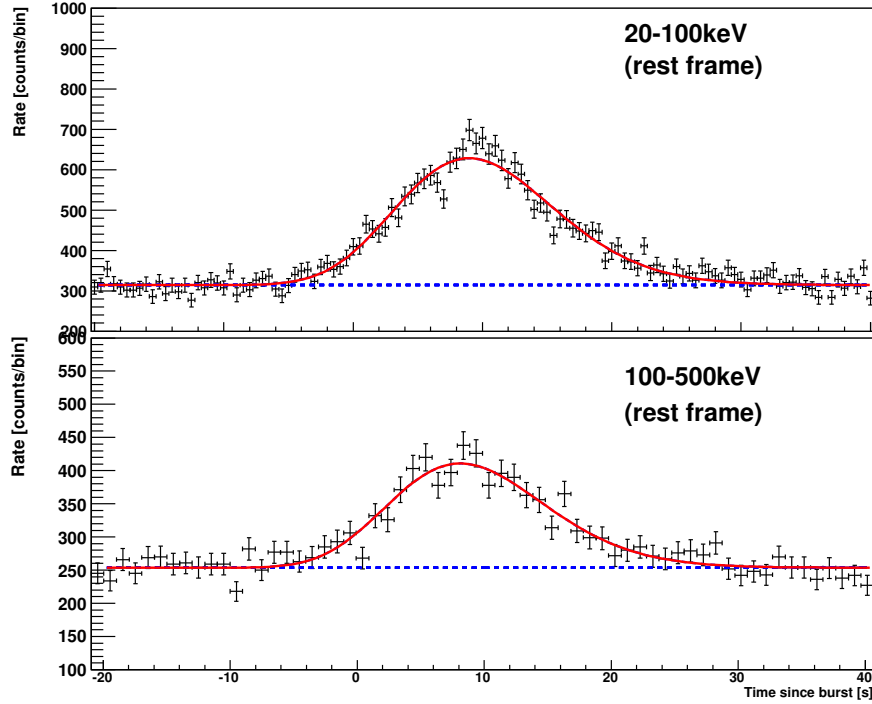


Figure 4.4: Pulse-fitting result: GRB 010921 at 20–100 keV (top panel) and 100–500 keV (bottom panel) in the rest frame.

features. Especially for the low-energy photon index α , at the early stage of the burst α exceeds the line of death and at the later stage α is below it. The same feature was also detected in GRB 020813 (Sato et al. 2005), which has a long duration (> 100 s), multiple pulses and the same α trend. This means that these long and multi-spike GRBs have deficiencies of low-energy photons at their early phases. The pulse-fit in the two-divided bands and pulse-resolved spectral-fit results are shown in Fig. 4.6, Table 4.5, Fig. 4.7, Table 4.6, Table 4.7, respectively.

4.3.3 GRB020127

GRB020127 triggered the FREGATE and WXM instruments at 20:57:24.73 UTC (75444.73 s UT) on 27 January, and was localized (Ricker et al. 2002). GRB020127 consists mainly of two peaks separated by ~ 5 s and ~ 1 -s long pulses. The optical counter-part was not detected (Lamb et al. 2002). Berger et al. 2007 performed optical and near-IR observations of the host galaxy of GRB 020127 determined by the X-ray afterglow, detected in two 10 ks observations of *Chandra* 4.14 and 14.64 days after the burst. From the spectral energy distribution (SED) using a dusty starburst galaxy, a most probable redshift of 1.9 was derived. The pulse-fit in the two-divided bands and multi-divided bands, and pulse-resolved spectral-fit results are shown in Fig. 4.8, Table 4.8, Fig. 4.9, Table 4.9,

Table 4.5: Lag properties of GRB020124 (6–25 keV and 50–400 keV in the observer’s frame)

	$T_{\text{peak}}^{\text{low}}$	$T_{\text{peak}}^{\text{high}}$	l_{obs}	l_{rest}	σ_l	$w_{\text{rest}}^{\text{low}}$	$w_{\text{rest}}^{\text{high}}$
	[s]	[s]	[s]	[s]		[s]	[s]
1	-1.13 ± 0.12	-0.96 ± 0.21	-0.16 ± 0.24	-0.04 ± 0.06	-0.68	1.53 ± 0.19	1.70 ± 0.87
2	5.15 ± 0.17	4.66 ± 0.16	0.49 ± 0.23	0.12 ± 0.06	2.1	1.81 ± 0.23	2.83 ± 0.08
3	11.31 ± 0.16	12.38 ± 0.08	-1.07 ± 0.18	-0.25 ± 0.04	-6.0	1.97 ± 0.21	0.57 ± 0.12
4	16.01 ± 0.12	15.09 ± 0.01	0.92 ± 0.12	0.22 ± 0.03	7.6	1.09 ± 0.13	0.89 ± 0.09
5	20.42 ± 0.28	20.94 ± 0.41	-0.53 ± 0.49	-0.13 ± 0.12	-1.07	2.57 ± 0.34	1.74 ± 1.03
6	26.79 ± 0.82	27.36 ± 0.62	-0.57 ± 1.03	-0.14 ± 0.25	-0.55	6.52 ± 2.26	1.85 ± 3.60
7	33.14 ± 0.28	31.81 ± 0.44	1.33 ± 0.53	0.32 ± 0.13	2.5	0.79 ± 0.31	2.14 ± 1.10
8	41.22 ± 5.81	41.21 ± 0.02	0.01 ± 5.81	0.00 ± 1.38	0.0	6.47 ± 7.97	4.68 ± 0.62

Table 4.6: Lag properties of GRB020124 (10–100 keV and 100–500 keV in the rest frame)

	$T_{\text{peak}}^{\text{low}}$	$T_{\text{peak}}^{\text{high}}$	l_{obs}	l_{rest}	σ_l	$w_{\text{rest}}^{\text{low}}$	$w_{\text{rest}}^{\text{high}}$
	[s]	[s]	[s]	[s]		[s]	[s]
1	-1.13 ± 0.12	-0.91 ± 0.17	-0.22 ± 0.21	-0.05 ± 0.05	-1.0	1.53 ± 0.19	2.17 ± 0.38
2	5.15 ± 0.17	4.80 ± 0.001	0.35 ± 0.17	0.08 ± 0.04	2.1	1.81 ± 0.23	1.46 ± 0.06
3	11.31 ± 0.16	12.00 ± 0.02	-0.69 ± 0.16	-0.16 ± 0.04	-4.3	1.97 ± 0.21	1.80 ± 0.18
4	16.01 ± 0.12	15.60 ± 0.11	0.41 ± 0.16	0.10 ± 0.04	2.5	1.09 ± 0.13	0.81 ± 0.25
5	20.42 ± 0.28	21.39 ± 0.31	-0.97 ± 0.41	-0.23 ± 0.10	-2.36	2.57 ± 0.34	1.67 ± 2.21
6	26.79 ± 0.82	28.32 ± 0.73	-1.53 ± 1.10	-0.36 ± 0.26	-1.4	6.52 ± 2.26	3.58 ± 0.80
7	33.14 ± 0.28	32.51 ± 0.13	0.64 ± 0.31	0.15 ± 0.07	2.0	0.80 ± 0.31	0.82 ± 0.36
8	41.22 ± 5.81	42.40 ± 0.19	-1.18 ± 5.81	-0.28 ± 1.38	-0.20	0.79 ± 0.31	2.87 ± 0.38

Fig. 4.10, and Table 4.10, respectively.

4.3.4 GRB021211

This bright GRB was detected by FREGATE and localized by the WXM and SXC instruments at 11:18:34.03 UT on 2002 December 11 and The localized position was sent to the GCN 22 s after the trigger (Crew et al. 2002 and Crew et al. 2003). The optical

Table 4.7: Spectral properties of GRB 020124

Model	$E_{\text{peak}}^{\text{src}}$ [keV]	α	β	L_{iso} 10^{52} [ergs/s]	χ^2_{ν} (d.o.f.)
2 Cutoff p.l.	$204.4^{+24.3}_{-20.4}$	$-0.32^{+0.40}_{-0.35}$	-	$2.20^{+0.22}_{-0.24}$	0.64 (47)
4 Cutoff p.l.	$391.0^{+258.5}_{-96.5}$	$-1.19^{+0.28}_{-0.26}$	-	$2.95^{+0.49}_{-0.89}$	1.23(19)
7 Cutoff p.l.	$479.7^{+209.6}_{-102.0}$	$-0.53^{+0.48}_{-0.39}$	-	$2.14^{+0.38}_{-0.57}$	0.78(19)

Table 4.8: Lag properties of GRB 020127 (6–25 keV and 50–400 keV in the observer’s frame)

	$T_{\text{peak}}^{\text{low}}$ [s]	$T_{\text{peak}}^{\text{high}}$ [s]	l_{obs} [s]	l_{rest} [s]	σ_l	$w_{\text{rest}}^{\text{low}}$ [s]	$w_{\text{rest}}^{\text{high}}$ [s]
1	-1.13 ± 0.02	-1.05 ± 0.24	-0.07 ± 0.24	-0.03 ± 0.08	-0.30	1.78 ± 0.72	1.73 ± 0.83
2	0.06 ± 0.07	0.03 ± 0.06	0.03 ± 0.09	0.01 ± 0.03	0.37	0.61 ± 0.16	0.40 ± 0.24
3	1.01 ± 0.002	1.39 ± 0.16	-0.38 ± 0.16	-0.13 ± 0.06	-2.34	0.56 ± 0.16	0.57 ± 0.36
4	5.36 ± 0.03	5.29 ± 0.02	0.07 ± 0.04	0.026 ± 0.017	1.6	1.07 ± 0.38	0.33 ± 0.10

transient was detected (e.g., Fox & Price 2002, Chornock et al. 2002). The host galaxy of the burst was identified in *Hubble Space Telescope (HST)* images taken on December 18 (Fruchter et al. 2002) and the redshift of the host galaxy was determined to be $z = 1.01$ by Vreeswijk et al. 2003.

The light curves above 40 keV display two pulses while below 40 keV a single pulse is

Table 4.9: Lag properties of GRB020127 (10–100 keV and 100–500 keV in the rest frame)

	$T_{\text{peak}}^{\text{low}}$ [s]	$T_{\text{peak}}^{\text{high}}$ [s]	l_{obs} [s]	l_{rest} [s]	σ_l	$w_{\text{rest}}^{\text{low}}$ [s]	$w_{\text{rest}}^{\text{high}}$ [s]
1	-1.13 ± 1.52	-1.10 ± 0.27	-0.03 ± 1.55	-0.01 ± 0.53	-0.02	2.64 ± 3.46	2.03 ± 0.65
2	0.04 ± 0.02	0.03 ± 0.07	0.01 ± 0.07	0.01 ± 0.02	0.12	0.56 ± 0.05	0.45 ± 0.23
3	1.01 ± 0.01	1.35 ± 0.11	-0.35 ± 0.11	-0.12 ± 0.04	-3.07	0.55 ± 0.01	0.41 ± 0.38
4	5.37 ± 0.03	5.28 ± 0.02	0.09 ± 0.045	0.03 ± 0.01	2.5	0.88 ± 0.05	0.36 ± 0.07

Table 4.10: Spectral properties of 020127

Model	$E_{\text{peak}}^{\text{src}}$ [keV]	α	β	L_{iso} 10^{52} [ergs/s]	χ^2_{ν} (d.o.f.)
1 powerlaw	-	-1.35 ± 0.15	-	$29.1^{+108.7}_{-29.1}$	0.94 (19)
2 Cutoff p.l.	$247.9^{+26.1}_{-20.9}$	$-0.35^{+0.22}_{-0.20}$	-	$1.53^{+0.13}_{-0.12}$	1.13 (34)
3 Cutoff p.l.	$144.4^{+52.1}_{-30.4}$	$-0.56^{+1.00}_{-0.65}$	-	$0.27^{+0.06}_{-0.08}$	1.23 (19)
4 Cutoff p.l.	$252.0^{+35.0}_{-29.2}$	$-0.62^{+0.12}_{-0.11}$	-	$2.27^{+0.15}_{-0.16}$	0.72(49)

seen. In both cases, we can see a FRED (Fast Rise Exponential Decay)-like pulse shape and the typical hard-to-soft feature (at the lower energy band, the duration is longer) as shown in Fenimore et al. 1995. For the spectral-lag analysis, since in the low-energy band there are not two components, we fit the pulse as a single one. The peak of the low-energy pulse corresponds to the second peak of the high-energy pulse, so we derive the lag only for the second peak. The pulse-fit in the two-divided bands and multi-divided bands, and pulse-resolved spectral-fit results are shown in Fig. 4.11, Table 4.11, Fig. 4.12, Table 4.12, Fig. 4.13, and Table 4.13, respectively.

Table 4.11: Lag properties of GRB021211 (6–25 keV and 50–400 keV in the observer frame)

	$T_{\text{peak}}^{\text{low}}$ [s]	$T_{\text{peak}}^{\text{high}}$ [s]	l_{obs} [s]	l_{rest} [s]	σ_l	$w_{\text{rest}}^{\text{low}}$ [s]	$w_{\text{rest}}^{\text{high}}$ [s]
2	1.23 ± 0.05	0.88 ± 0.04	0.36 ± 0.06	0.18 ± 0.03	5.8	3.10 ± 0.19	1.07 ± 0.13

Table 4.12: Lag properties of GRB 021211 (10–100 keV and 100–500 keV in the rest frame)

	$T_{\text{peak}}^{\text{low}}$ [s]	$T_{\text{peak}}^{\text{high}}$ [s]	l_{obs} [s]	l_{rest} [s]	σ_l	$w_{\text{rest}}^{\text{low}}$ [s]	$w_{\text{rest}}^{\text{high}}$ [s]
2	1.06 ± 0.03	0.85 ± 0.038	0.21 ± 0.05	0.10 ± 0.03	4.0	2.63 ± 0.13	1.08 ± 0.11

Table 4.13: Spectral properties of GRB 021211

Model	$E_{\text{peak}}^{\text{src}}$ [keV]	α	β	L_{iso} 10^{52} [ergs/s]	χ^2_{ν} (d.o.f.)
1 Band	$92.9^{+18.6}_{-13.8}$	$0.00^{+0.25}_{-0.23}$	$-1.89^{+0.09}_{-0.13}$	$1.80^{+0.34}_{-0.32}$	1.01 (78)
2 Cutoff p.l.	$130.3^{+6.2}_{-5.5}$	$-0.25^{+0.10}_{-0.10}$	-	$1.02^{+0.08}_{-0.10}$	0.63(82)

4.3.5 GRB030528

The trigger for this event came from the FREGATE instruments in the 32–400 keV band, on 28 May 2003 at 13:03:02.83 UT (Villasenor et al. 2003). The afterglow was detected in the X-ray and infrared, but not in the optical band (e.g., Greiner et al. 2003, Rau et al. 2004, Butler et al. 2004, Mirabal & Halpern 2003). A redshift of 0.78 was reported by Rau et al. 2005. As we can see in Fig. 4.14, the light curves show a prominent hard-to-soft evolution during the burst. The duration of the burst is ~ 60 s in the lower energy band and ~ 10 s in the high energy band. We see a two component pulse and the first peak is seen above 10 keV. For the second peak, we can see a prominent spectral lag.

Due to a problem with the primary ground station, several data types were not properly downlinked. For the WXM, we use TH and PHA data (no TAG is available). Since half of the PHA data was lost every 10 sec, the PHA could be used only in the first pulse while the TAG data of FREGATE could be used in both pulses. The pulse-fit in the two-divided bands and multi-divided bands, and pulse-resolved spectral-fit results are shown in Fig. 4.15, Table 4.14, Fig. 4.16, Table 4.15, Fig. 4.14, and Table 4.16, respectively.

Table 4.14: Lag properties of GRB 030528 (6–25 keV and 50–400 keV in the observer frame)

	$T_{\text{peak}}^{\text{low}}$ [s]	$T_{\text{peak}}^{\text{high}}$ [s]	l_{obs} [s]	l_{rest} [s]	σ_l	$w_{\text{rest}}^{\text{low}}$ [s]	$w_{\text{rest}}^{\text{high}}$ [s]
1	1.10 ± 5.57	1.29 ± 0.48	-0.19 ± 5.59	-0.11 ± 3.14	-0.03	16.99 ± 51.43	10.74 ± 3.94
2	22.32 ± 1.61	10.66 ± 0.52	11.66 ± 1.70	6.55 ± 0.95	6.87	53.4 ± 15.11	10.02 ± 2.78

Table 4.15: Lag properties of GRB 030528 (10–100 keV and 100–500 keV in the rest frame)

	$T_{\text{peak}}^{\text{low}}$ [s]	$T_{\text{peak}}^{\text{high}}$ [s]	l_{obs} [s]	l_{rest} [s]	σ_l	$w_{\text{rest}}^{\text{low}}$ [s]	$w_{\text{rest}}^{\text{high}}$ [s]
1	2.33 ± 1.36	1.12 ± 0.46	1.21 ± 1.44	0.68 ± 0.81	0.84	29.83 ± 17.23	10.54 ± 3.96
2	16.90 ± 0.77	10.73 ± 0.47	6.17 ± 0.90	3.46 ± 0.51	6.84	58.74 ± 5.05	8.65 ± 3.03

Table 4.16: Spectral properties of GRB 030528

	Model	$E_{\text{peak}}^{\text{src}}$ [keV]	α	β	L_{iso} 10^{52} [ergs/s]	χ_{ν}^2 (d.o.f.)
1	Band	$143.5^{+27.2}_{-25.1}$	$0.16^{+0.66}_{-0.43}$	$-2.32^{+0.24}_{-0.53}$	0.12 ± 0.03	0.58(57)
2	Cutoff p.l.	$56.4^{+3.9}_{-4.4}$	$-1.14^{+0.22}_{-0.22}$	-	$7.86^{+0.75}_{-0.97} \times 10^{-2}$	0.58(61)

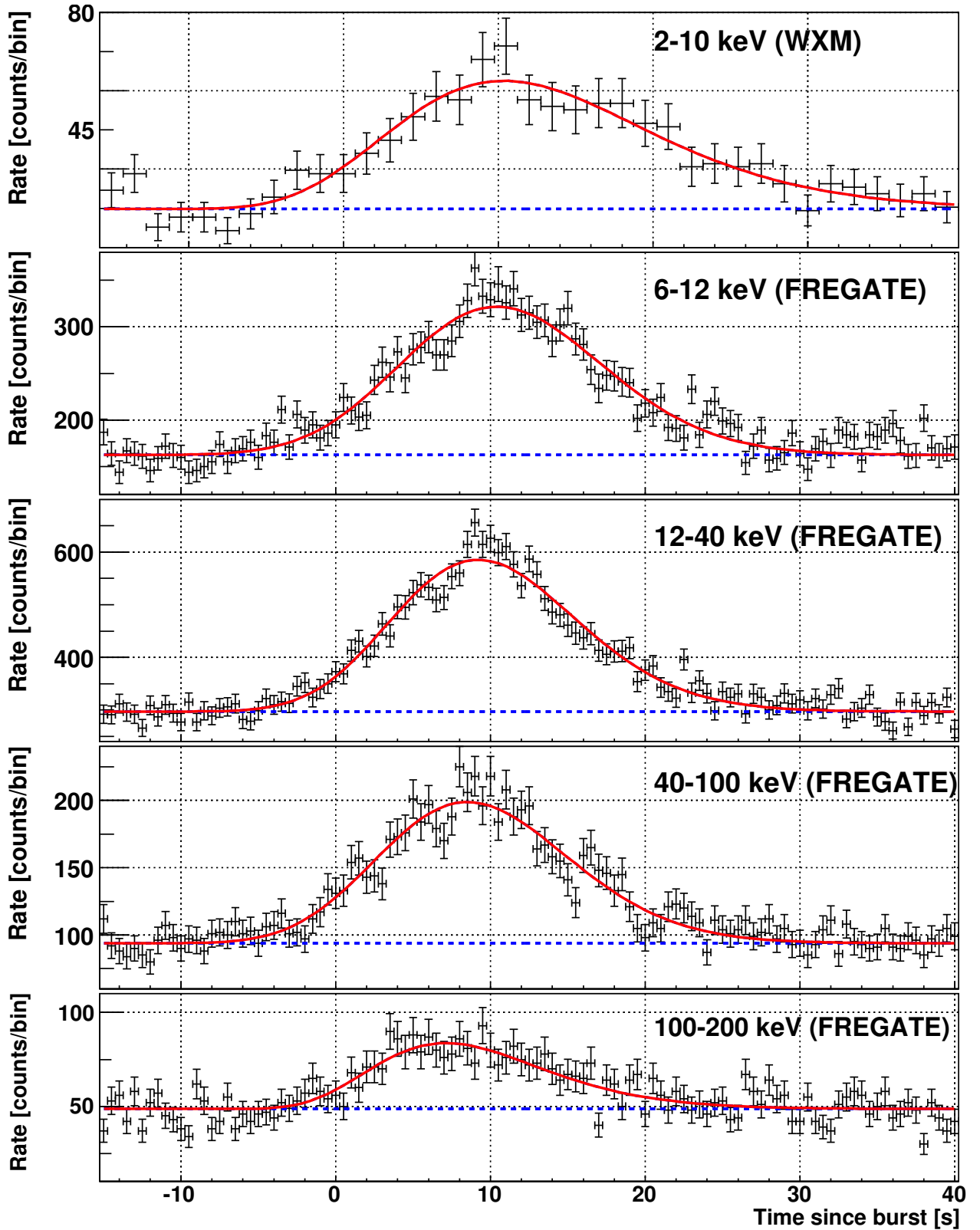


Figure 4.5: Pulse fit are GRB 010921 in the multi-divided bands. The energy bands from the top to the bottom are 2–10 keV (WXM), 6–12 keV (FREGATE), 12–40 keV (FREGATE), 40–100 keV (FREGATE), and 100–200 keV (FREGATE). Solid lines represents the best pulse-fitting function.

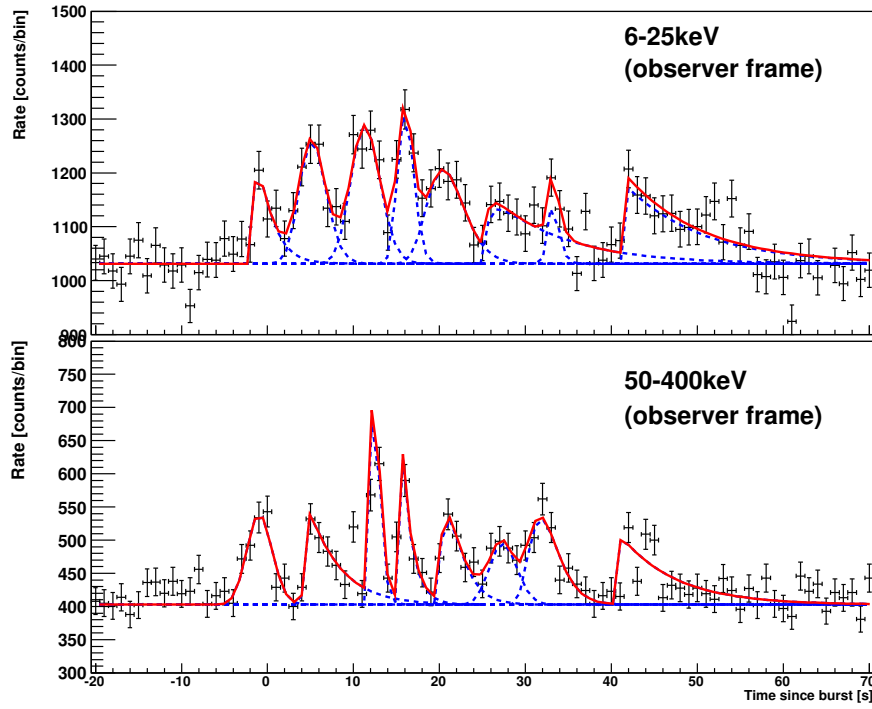


Figure 4.6: Pulse-fitting result: GRB 020124 at 6–25 keV (top panel) and 50–400 keV (bottom panel) in the observer’s frame.

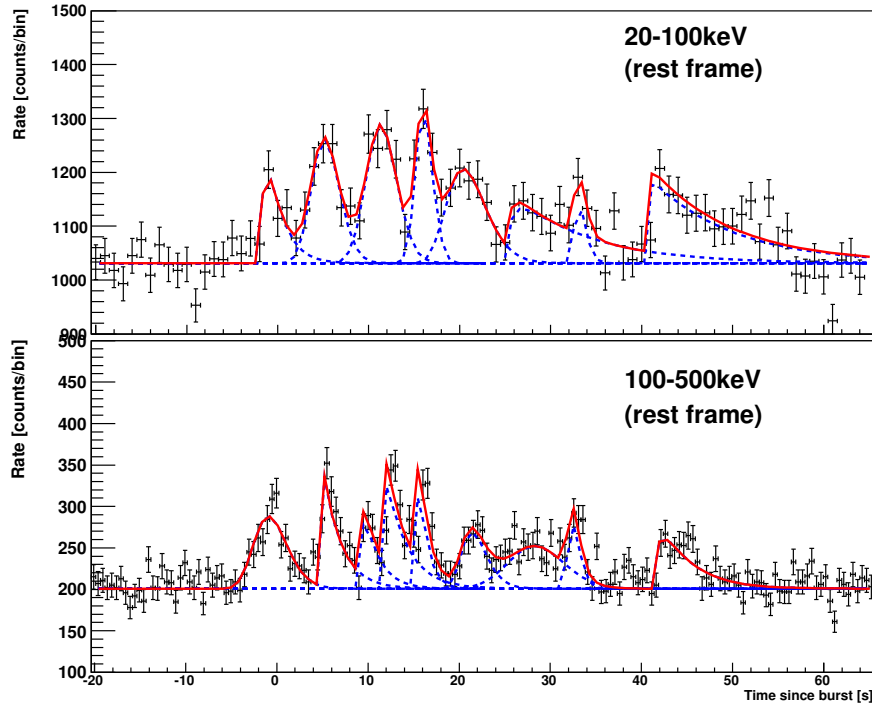


Figure 4.7: Pulse-fitting result: GRB 020124 at 20–100 keV (upper panel) and 100–500 keV (lower panel) in the rest frame.

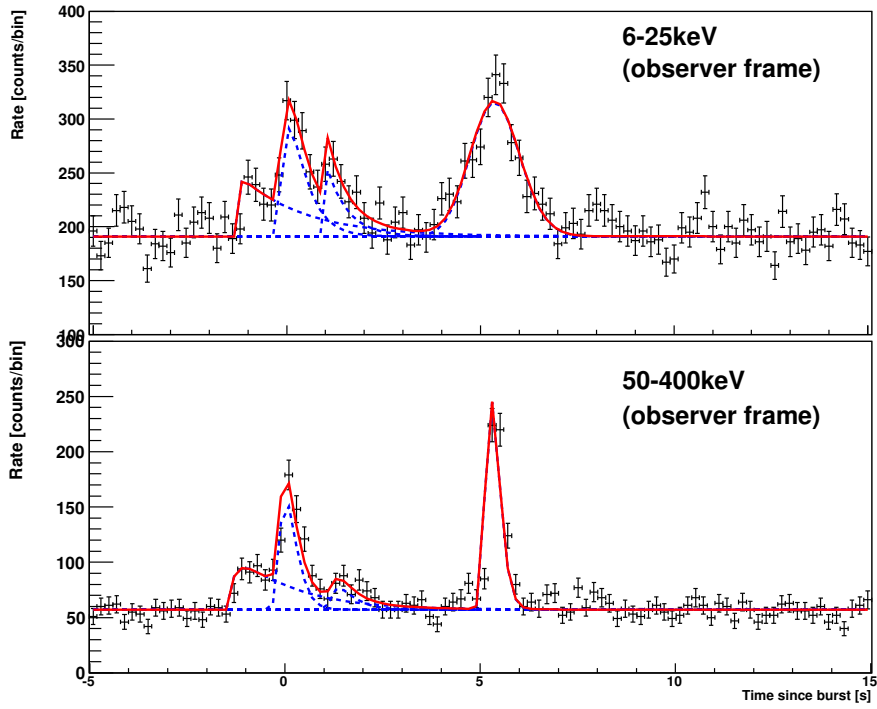


Figure 4.8: Pulse-fitting result: GRB 020127 at 6–25 keV (top panel) and 50–400 keV (bottom panel) in the observer’s frame.

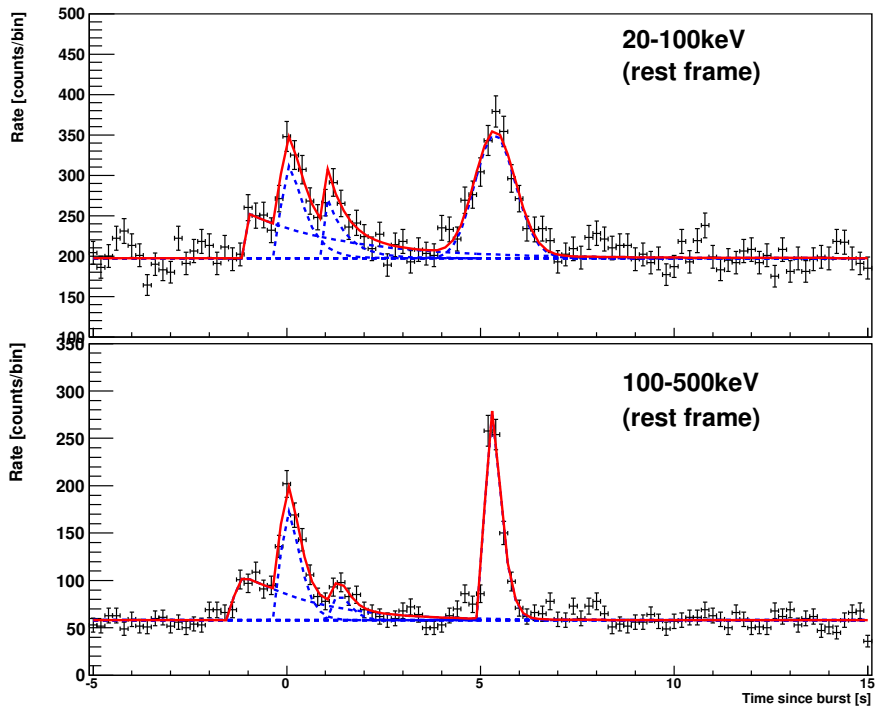


Figure 4.9: Pulse-fitting result: GRB 020127 at 20–100 keV (top panel) and 100–500 keV (bottom panel) in the rest frame.

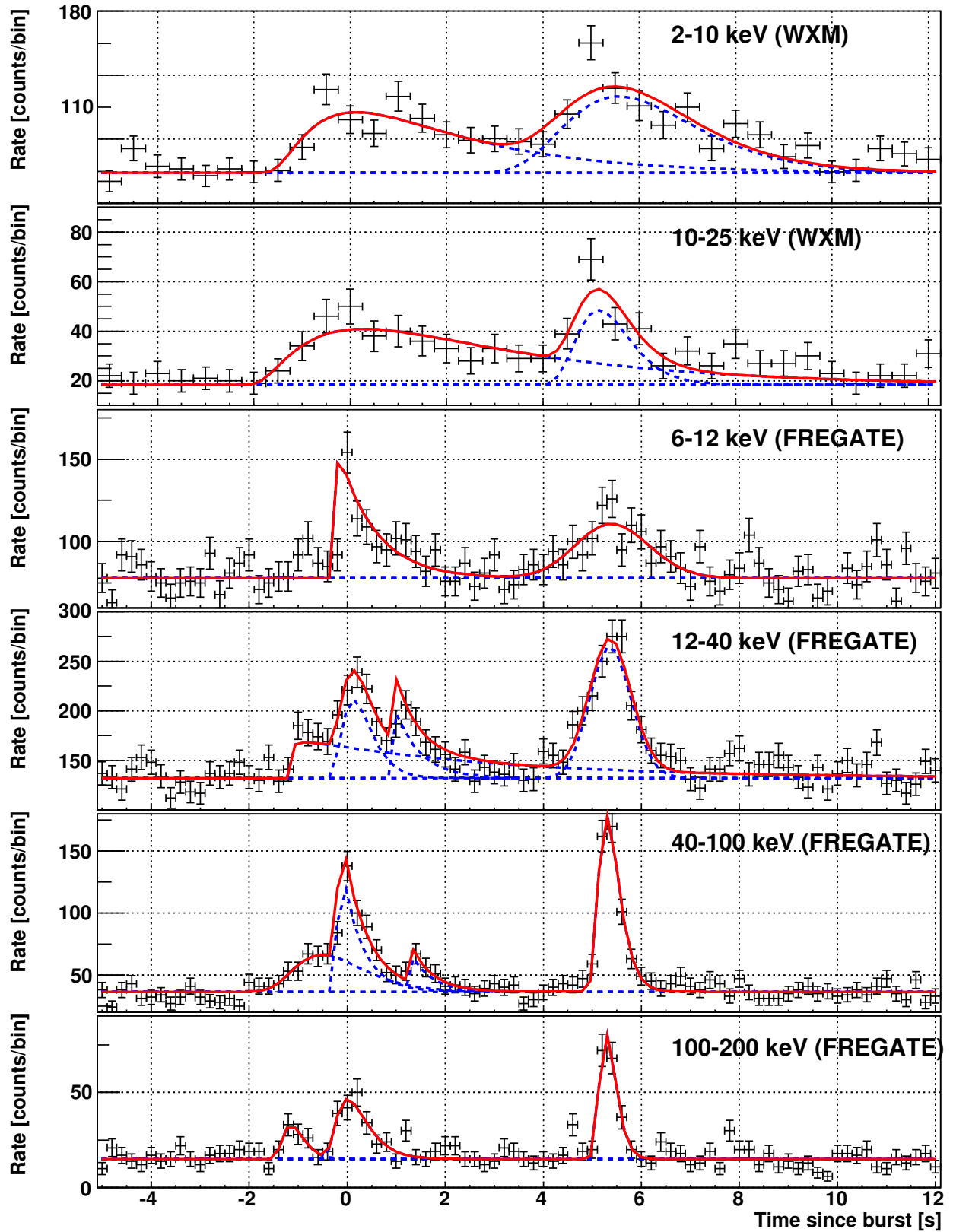


Figure 4.10: Pulse fit for GRB 020127 in the multi-divided bands. The energy bands from the top to the bottom are 2–10 keV (WXM), 10–25 keV (WXM), 6–12 keV (FREGATE), 12–40 keV (FREGATE), 40–100 keV (FREGATE), and 100–200 keV (FREGATE). Solid lines represents the best pulse-fitting function.

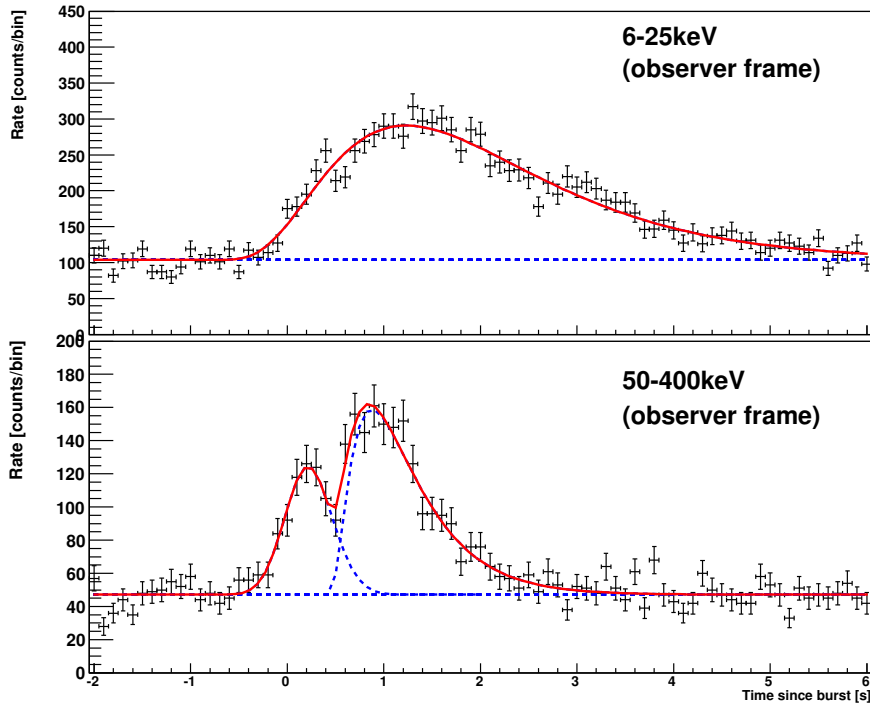


Figure 4.11: Pulse-fitting result: GRB 021211 at 6–25 keV (top panel) and 50–400 keV (bottom panel) in the observer’s frame.

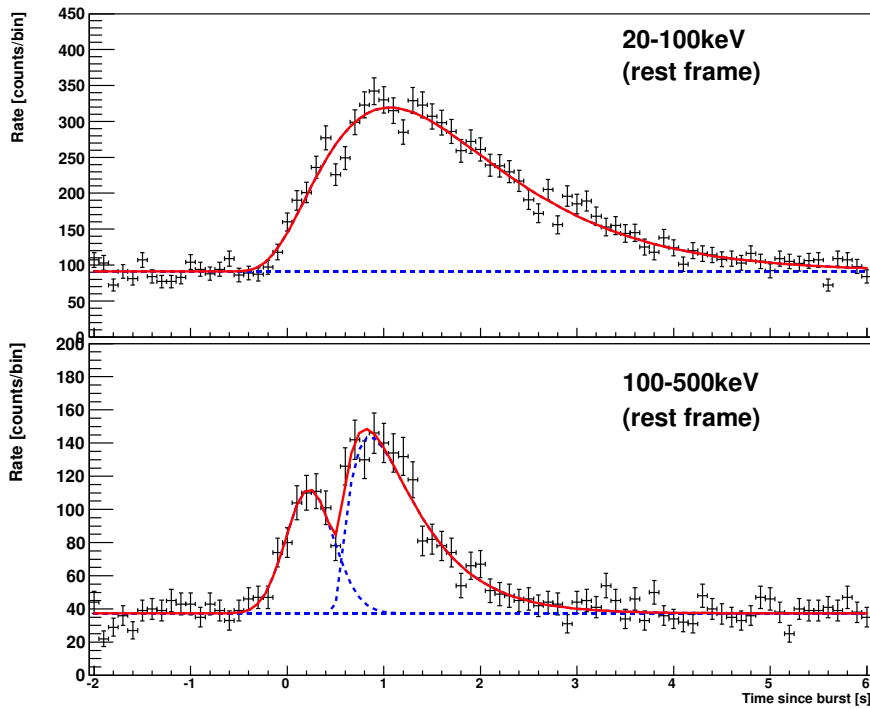


Figure 4.12: Pulse-fitting result: GRB 021211 at 20–100 keV (top panel) and 100–500 keV (bottom panel) in the rest frame.

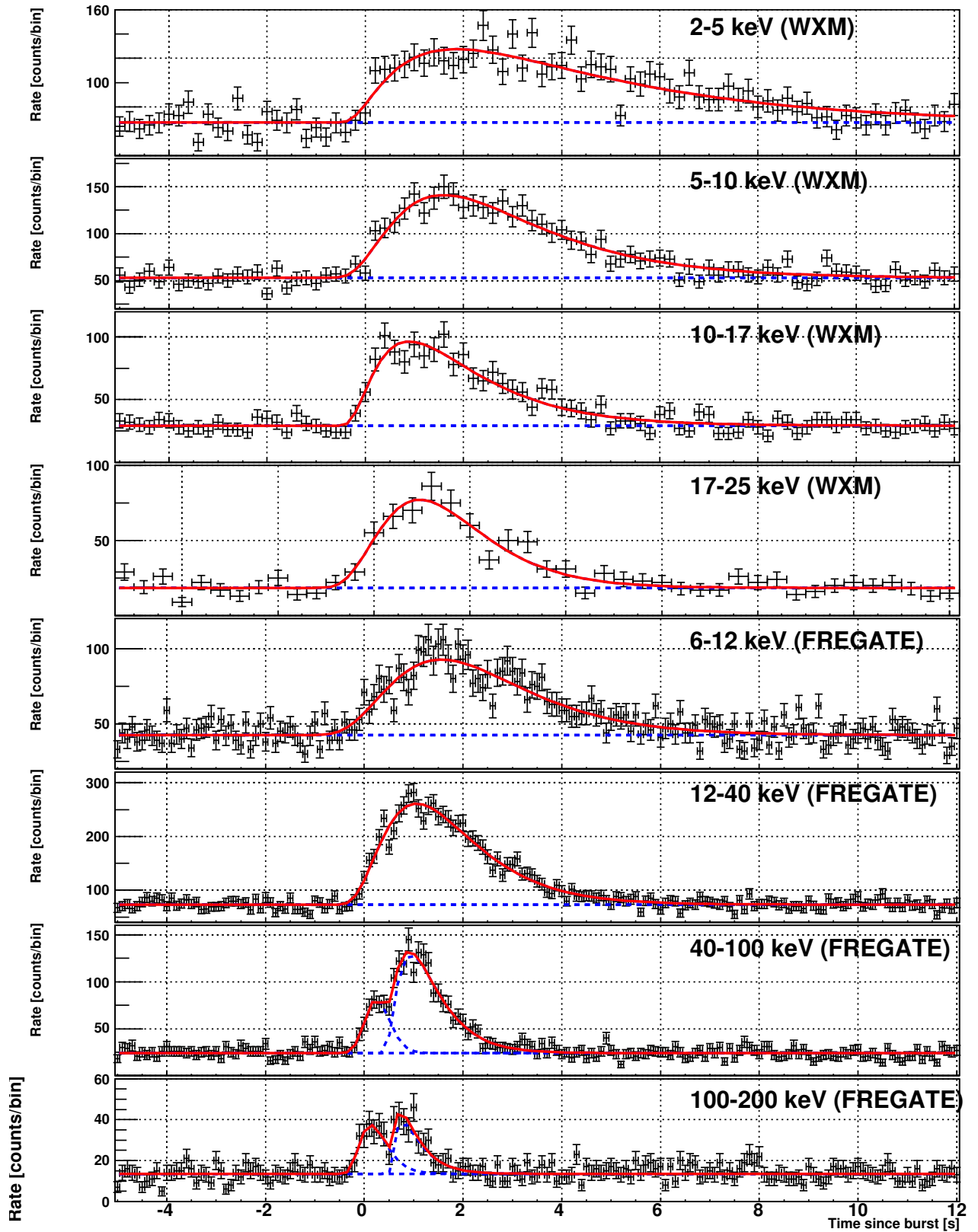


Figure 4.13: Pulse fit for GRB 021211 in the multi-divided bands. The energy bands from the top to the bottom are 2–5 keV (WXM), 5–10 keV (WXM), 10–17 keV (WXM), 17–25 keV (WXM), 6–12 keV (FREGATE), 12–40 keV (FREGATE), 40–100 keV (FREGATE), and 100–200 keV (FREGATE). Solid lines represents the best pulse-fitting function.

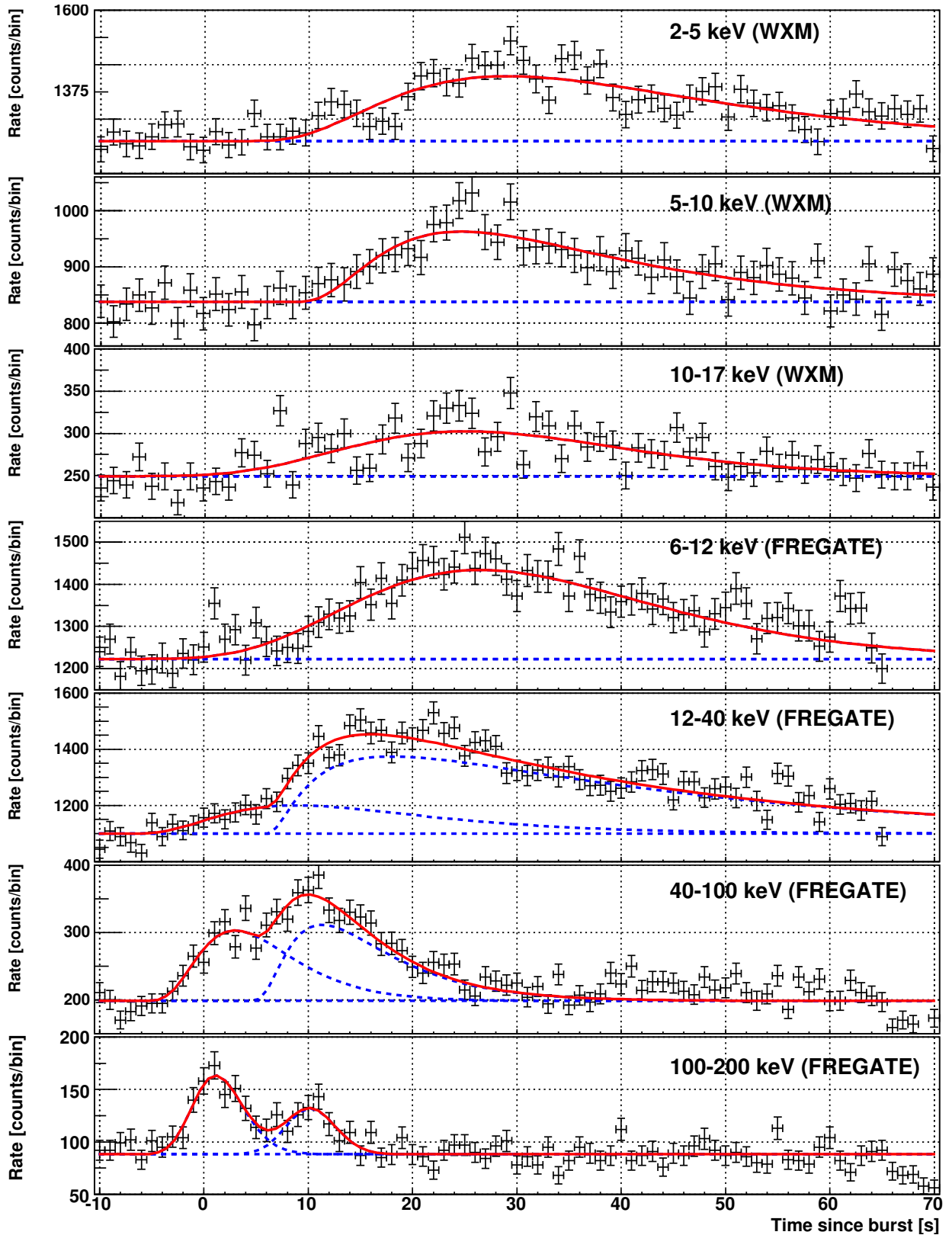


Figure 4.14: Pulse fit for GRB 030528 in the multi-divided bands. The energy bands from the top to the bottom are 2–5 keV (WXM), 5–10 keV (WXM), 10–17 keV (WXM), 6–12 keV (FREGATE), 12–40 keV (FREGATE), 40–100 keV (FREGATE), and 100–200 keV (FREGATE). Solid lines represents the best pulse-fitting function.

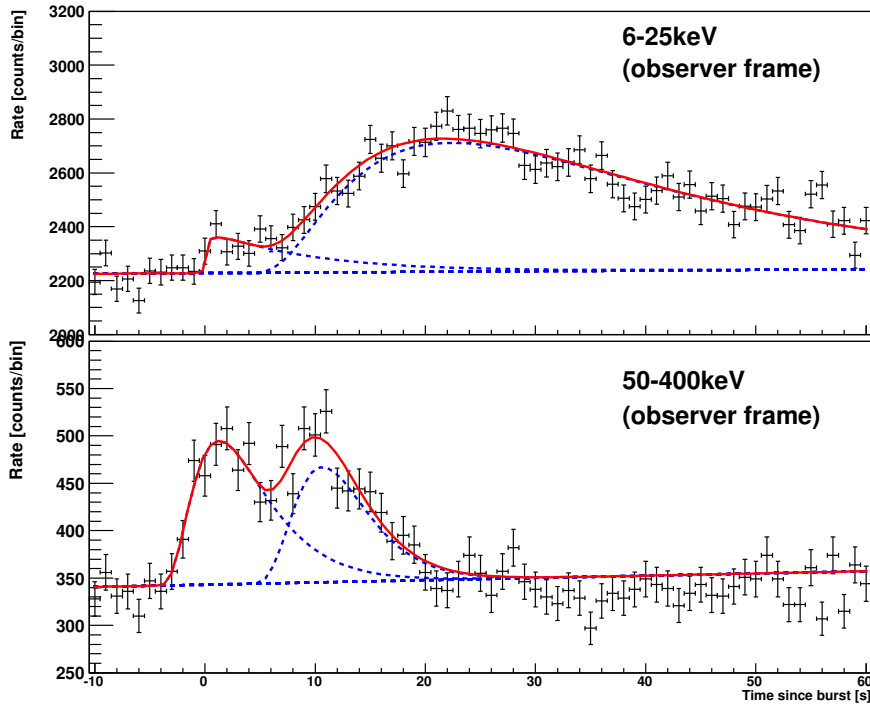


Figure 4.15: Pulse-fitting result: GRB 030528 at 6–25 keV (top panel) and 50–400 keV (bottom panel) in the observer’s frame.

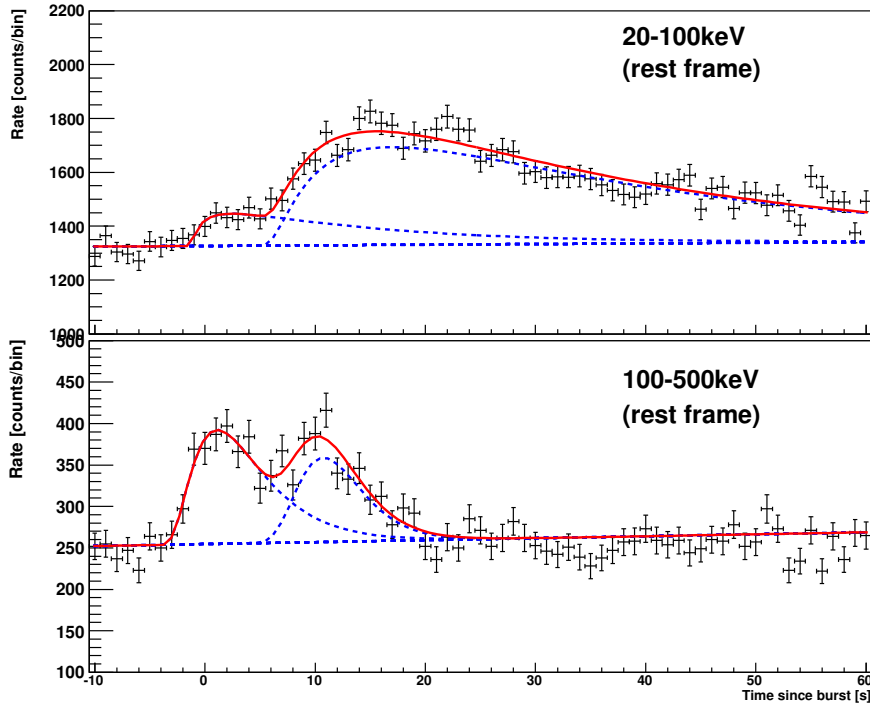


Figure 4.16: Pulse-fitting result: GRB 030528 at 20–100 keV (top panel) and 100–500 keV (bottom panel) in the rest frame.

4.3.6 GRB030725

GRB 030725 triggered the FREGATE instrument at 11:46:24.82 UTC (42384.82 s UT) on 25 July 2003 (Shirasaki et al. 2003) and is a bright long hard burst. No detection of an afterglow in the X-ray or radio bands has been reported although an optical afterglow was found (Pugliese et al. 2005). Pugliese et al. 2005 obtained not only the optical counter part but also the light curve with a break at ~ 1.3 days. This break seems to be a jet break but the lack of data during the first few days after the burst did not allow us to obtain a more accurate interpretation of the burst.

For the prompt emission, the single pulse has no complex structure and a typical FRED shape. The duration is around 10 to 30 s and its evolution (shorter duration at higher energy) is typical of previously observed GRBs. The pulse-fit in the multi-divided bands and pulse-resolved spectral-fit results are shown in Fig. 4.17, and Table 4.17, respectively.

Table 4.17: Spectral properties of GRB 030725

Model	$E_{\text{peak}}^{\text{obs}}$ [keV]	α	β	Normalization [†] [ph cm ⁻² s ⁻¹ keV ⁻¹]	χ^2_{ν} (d.o.f.)
1 Cutoff p.l.	$108.2^{+5.5}_{-3.6}$	$-1.32^{+0.04}_{-0.02}$	-	$4.33^{+0.05}_{-0.07} \times 10^{-1}$	1.27(133)

†: Normalization at 15 keV

4.3.7 GRB040924

The FREGATE instruments was triggered by GRB 040924 at 11:52:11 UT (42731 SOD) on 24 September 2004 and the WXM instrument localized the burst 14 s after the burst trigger (Fenimore et al. 2004). About 16 minutes after the burst, Fox & Moon 2004 detected the corresponding optical afterglow with an R -band magnitude of ~ 18 . From then on, the Russian-Turkish 1.5-m telescope (Khamitov et al. 2004) and other followup observations were done. A redshift of 0.86 was reported by Wiersema et al. 2004. In particular the Subaru Telescope (Terada et al. 2004) detected an extended source with magnitude $K' = 20.4 \pm 0.2$. It is probably the afterglow of GRB 040924 with a significant contribution from its host galaxy. Huang et al. 2005 obtained a light curve which can be described by two power-laws. The small difference in the spectral indices can probably be explained by the cooling break.

For the prompt emission observed by *HETE*, the burst has a short duration, although not particularly hard. The duration is ~ 1 to 3 s, which is slightly longer than a typical

short GRB (< 2 s). Furthermore, a significant spectral lag has been detected although typical short GRBs have no significant spectral lags from the observationally-based point of view. Taken together, this GRB probably belongs to the long GRB class. In addition, GRB 040924 also has a typical GRB (e.g., hard-to-soft evolution). The pulse-fit in the two-divided bands and multi-divided bands, and pulse-resolved spectral-fit results are shown in Fig. 4.18, Table 4.18, Fig. 4.19, Table 4.19, Fig. 4.20, and Table 4.20, respectively.

Table 4.18: Lag properties of GRB 040924(6–25 keV and 50–400 keV in the observer frame)

	$T_{\text{peak}}^{\text{low}}$	$T_{\text{peak}}^{\text{high}}$	l_{obs}	l_{rest}	σ_l	$w_{\text{rest}}^{\text{low}}$	$w_{\text{rest}}^{\text{high}}$
	[s]	[s]	[s]	[s]		[s]	[s]
1	0.10 ± 0.34	-0.11 ± 0.21	0.21 ± 0.40	0.11 ± 0.21	0.52	4.17 ± 3.39	0.94 ± 16.32
2	1.53 ± 0.03	1.17 ± 0.02	0.36 ± 0.03	0.19 ± 0.02	10.74	1.59 ± 0.02	0.80 ± 0.13

Table 4.19: Lag properties of GRB 040924 (10–100 keV and 100–500 keV in the rest frame)

	$T_{\text{peak}}^{\text{low}}$	$T_{\text{peak}}^{\text{high}}$	l_{obs}	l_{rest}	σ_l	$w_{\text{rest}}^{\text{low}}$	$w_{\text{rest}}^{\text{high}}$
	[s]	[s]	[s]	[s]		[s]	[s]
1	0.42 ± 0.06	-0.07 ± 0.07	0.49 ± 0.09	0.26 ± 0.05	5.4	3.34 ± 0.18	0.89 ± 0.744
2	1.43 ± 0.01	1.15 ± 0.02	0.28 ± 0.02	0.15 ± 0.01	12.0	1.29 ± 0.02	0.78 ± 0.16

Table 4.20: Spectral properties of GRB 040924

	Model	$E_{\text{peak}}^{\text{src}}$	α	β	L_{iso}	χ^2_{ν} (d.o.f.)
		[keV]			10^{52} [ergs/s]	
1	Cutoff p.l.	$112.4^{+37.5}_{-24.4}$	$-0.93^{+0.32}_{-0.25}$	-	$0.20^{+0.02}_{-0.03}$	1.06 (49)
2	Cutoff p.l.	$110.4^{+3.8}_{-3.6}$	$-0.26^{+0.15}_{-0.07}$	-	$1.14^{+0.04}_{-0.08}$	0.74 (59)

4.3.8 GRB041006

GRB 041006 was detected with the FREGATE instruments at 12:18:08 UT on 06 October 2004 (Galassi et al. 2004). The WXM flight software localized the burst in real time,

resulting in a GCN notice 42 sec after the burst trigger. 1.4 hours after the burst trigger the optical afterglow was found by da Costa et al. 2004 and a redshift of 0.72 was determined by Stanek et al. 2005. This GRB displays a soft X-ray emission, a precursor before the onset of the main event, and also a soft X-ray tail after the end of the main peak. At higher energy bands several peaks are seen in the light curve, while at lower energy bands broad bumps dominate. It is thought that these different features are the result of a mixture of several components suggested by Shirasaki et al. 2008.

In the pulse fit for the spectral analysis, to obtain a moderate reduced chi-square, we adopt 8 pulses for the fit model. For the 1st, 2nd and 7th pulses, since these are only seen in the low-energy band, we do not calculate spectral lags for the pulses. For the 9th pulse, since in the higher-energy band the pulse consists of a few spikes, we ignore it. The multi-divided analysis is not performed because the photon statistics are too poor to divide into several energy ranges.

The pulse-fit in the two-divided bands, and pulse-resolved spectral-fit results are shown in Fig. 4.21, Table 4.21, Fig. 4.22, Table 4.22, and Table 4.23, respectively.

Table 4.21: Lag properties of GRB 041006 (6–25 keV and 50–400 keV in the observer’s frame)

	$T_{\text{peak}}^{\text{low}}$	$T_{\text{peak}}^{\text{high}}$	l_{obs}	l_{rest}	σ_l	$w_{\text{rest}}^{\text{low}}$	$w_{\text{rest}}^{\text{high}}$
	[s]	[s]	[s]	[s]		[s]	[s]
3	9.95±0.11	9.27±0.22	0.68±0.24	0.40±0.14	2.8	4.24±1.14	3.28±1.37
4	12.73±0.21	12.54±0.23	0.19±0.31	0.11±0.18	0.61	2.89±1.18	2.49±3.36
5	15.02±0.12	14.00±0.18	1.02±0.22	0.60±0.13	4.7	2.70±0.98	2.11±0.87
6	16.95±0.21	15.74±0.334	1.21±0.40	0.71±0.23	3.0	4.52±1.02	5.14±1.66
8	24.38±0.11	23.85±0.05	0.54±0.12	0.31±0.07	4.38	4.83±1.23	2.63±0.32

Table 4.22: Lag properties of GRB 041006 (10–100 keV and 100–500 keV in the rest frame)

	$T_{\text{peak}}^{\text{low}}$	$T_{\text{peak}}^{\text{high}}$	l_{obs}	l_{rest}	σ_l	$w_{\text{rest}}^{\text{low}}$	$w_{\text{rest}}^{\text{high}}$
	[s]	[s]	[s]	[s]		[s]	[s]
3	9.86 ± 0.07	8.86 ± 0.48	0.99 ± 0.49	0.58 ± 0.29	2.0	3.71 ± 0.31	3.79 ± 1.97
4	12.44 ± 0.06	12.55 ± 0.12	-0.12 ± 0.14	-0.07 ± 0.08	-0.9	1.66 ± 0.28	0.89 ± 0.68
5	14.89 ± 0.07	13.90 ± 0.04	0.99 ± 0.08	0.580 ± 0.05	12.	3.20 ± 0.25	1.82 ± 0.39
6	16.85 ± 0.09	15.94 ± 0.33	0.92 ± 0.34	0.54 ± 0.20	2.7	3.68 ± 0.30	5.21 ± 1.58
8	24.26 ± 0.07	23.84 ± 0.05	0.42 ± 0.08	0.25 ± 0.05	5.2	4.12 ± 0.23	2.54 ± 1.09

Table 4.23: Spectral properties of GRB 041006

Model	$E_{\text{peak}}^{\text{src}}$	α	β	L_{iso}	χ_{ν}^2 (d.o.f.)
	[keV]			10^{52} [ergs/s]	
3 Band	$48.3_{-5.4}^{+5.3}$	$-0.97_{-0.08}^{+0.08}$	$-2.75_{-0.33}^{+0.21}$	$1.05_{-0.11}^{+0.09} \times 10^{-1}$	1.21 (65)
5 Cutoff p.l.	$74.4_{-5.6}^{+4.5}$	$-0.94_{-0.05}^{+0.04}$	-	$1.25_{-0.03}^{+0.06} \times 10^{-1}$	1.33 (74)
6 Cutoff p.l.	$61.7_{-4.7}^{+2.3}$	$-0.90_{-0.04}^{+0.04}$	-	$1.19_{-0.03}^{+0.06} \times 10^{-1}$	1.00 (60)
7 Cutoff p.l.	$32.5_{-4.7}^{+4.9}$	$-0.58_{-0.16}^{+0.20}$	-	$1.37_{-0.09}^{+0.08} \times 10^{-1}$	1.22(58)
8 Cutoff p.l.	$125.6_{-8.5}^{+7.7}$	$-1.04_{-0.04}^{+0.04}$	-	$1.73_{-0.06}^{+0.06} \times 10^{-1}$	0.87 (96)

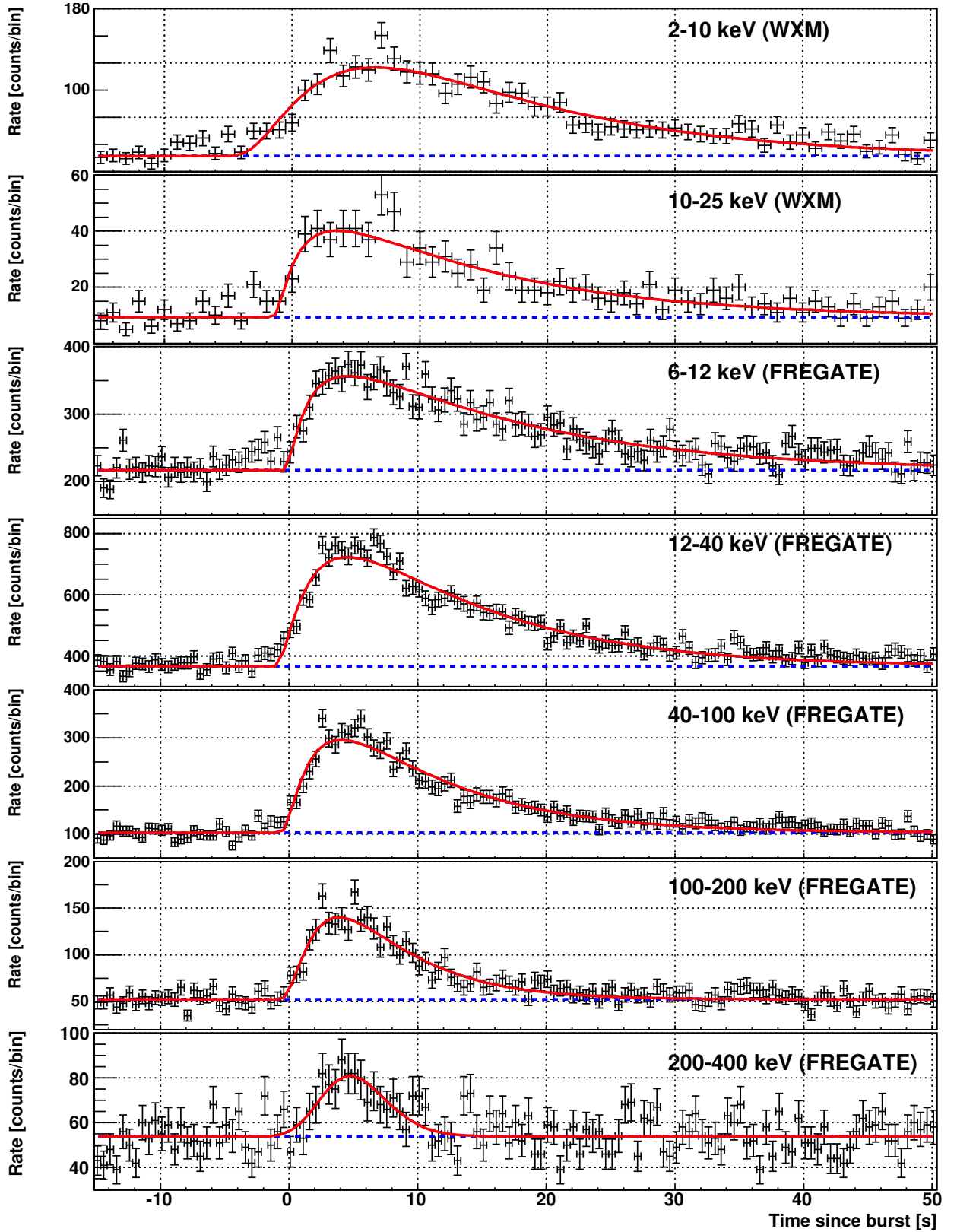


Figure 4.17: Pulse fit for GRB 030725 in the multi-divided bands. The energy bands from the top to the bottom are 2–10 keV (WXM), 10–25 keV (WXM), 6–12 keV (FREGATE), 12–40 keV (FREGATE), 40–100 keV (FREGATE), 100–200 keV (FREGATE), and 200–400 keV (FREGATE). Solid lines represents the best pulse-fitting function.

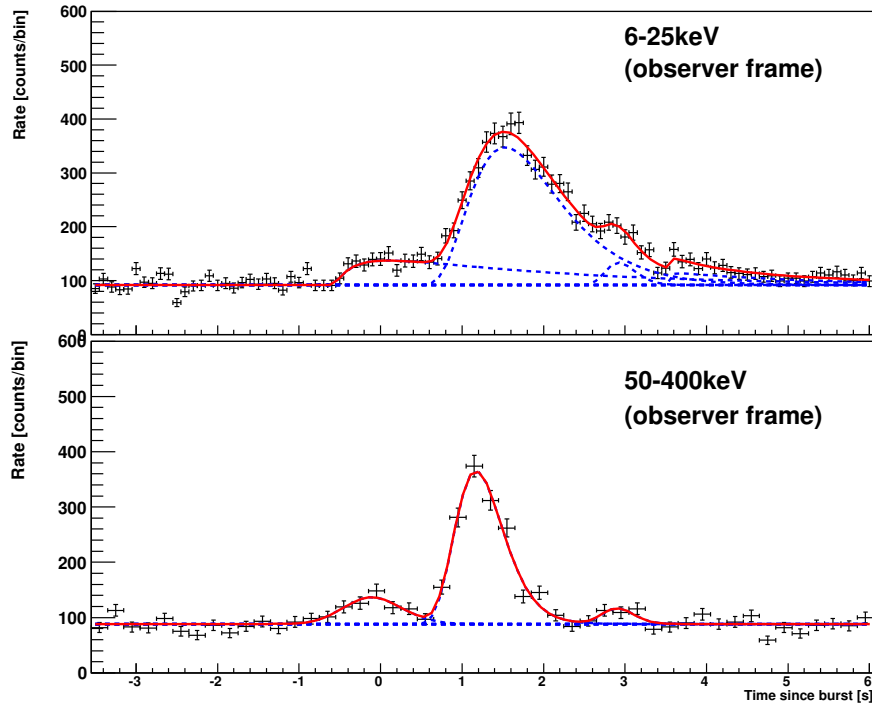


Figure 4.18: Pulse-fitting result: GRB 040924 at 6–25 keV (top panel) and 50–400 keV (bottom panel) in the observer’s frame.

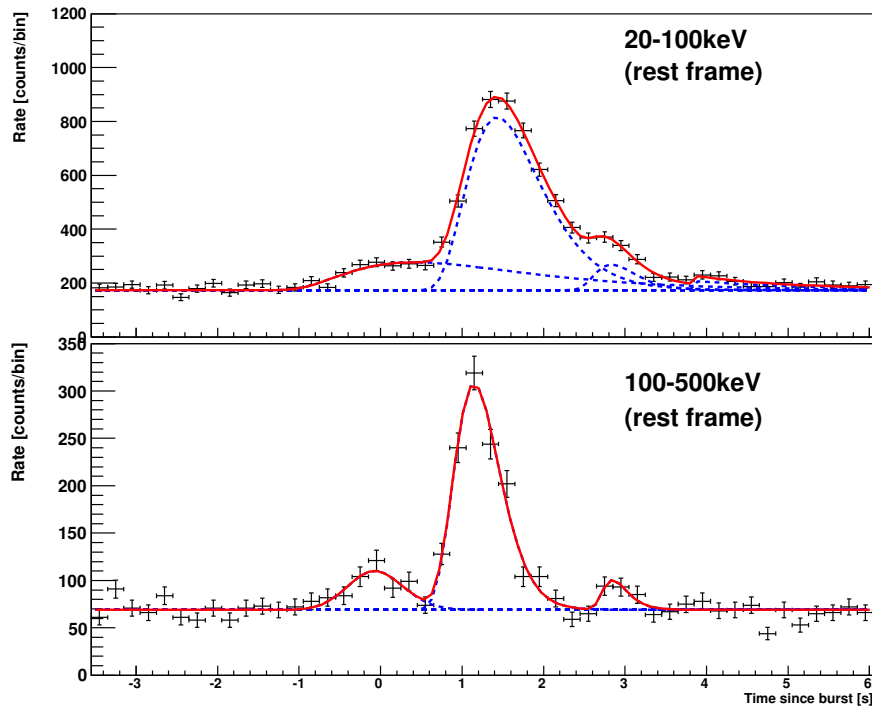


Figure 4.19: Pulse-fitting result: GRB 040924 at 20–100 keV (top panel) and 100–500 keV (bottom panel) in the rest frame.

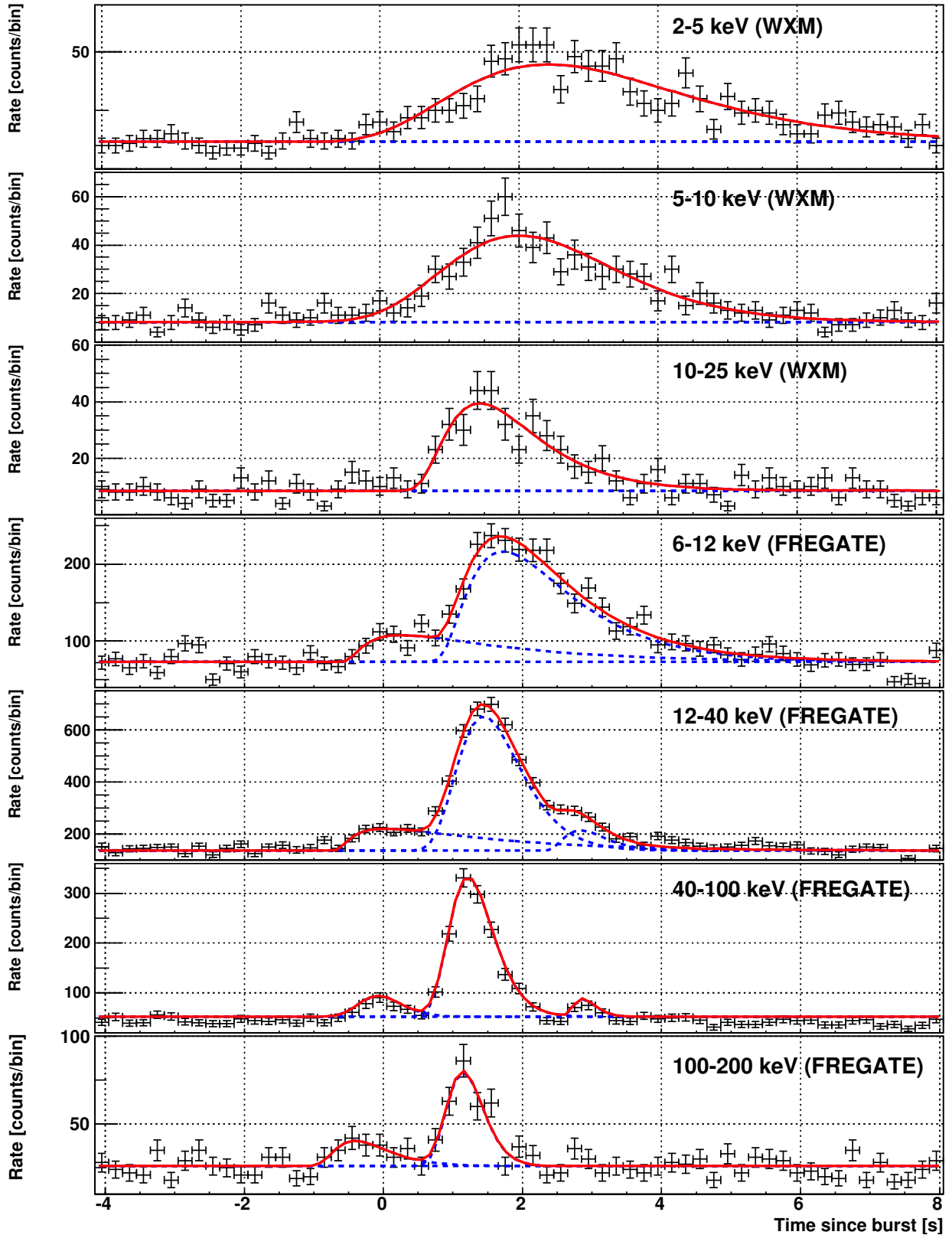


Figure 4.20: Pulse fit for GRB 040924 in the multi-divided bands. The energy bands from the top to the bottom are 2–5 keV (WXM), 5–10 keV (WXM), 10–25 keV (WXM), 6–12 keV (FREGATE), 12–40 keV (FREGATE), 40–100 keV (FREGATE), and 100–200 keV (FREGATE). Solid lines represents the best pulse-fitting function.

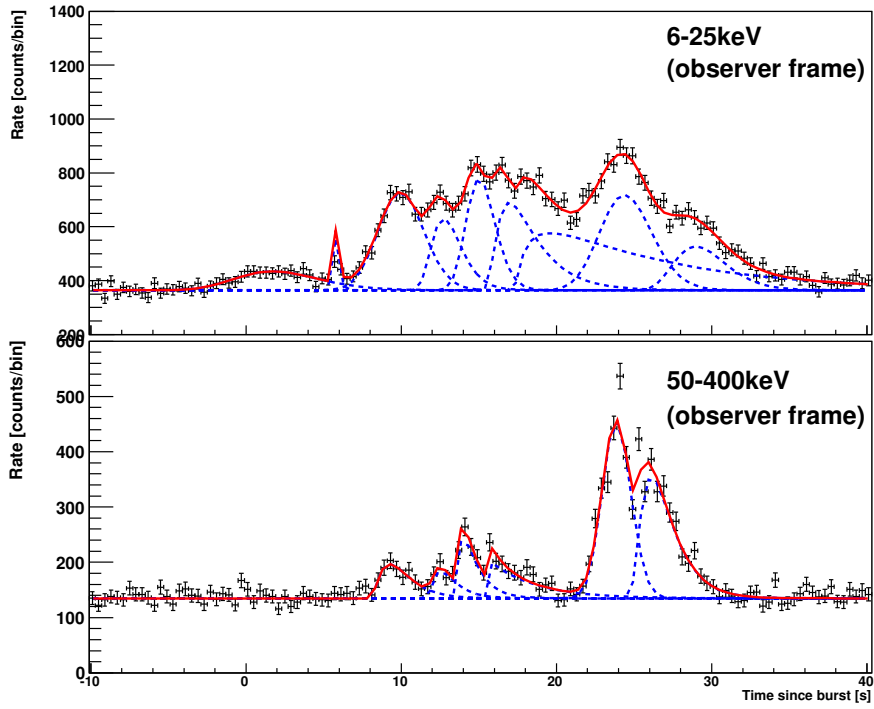


Figure 4.21: Pulse-fitting result: GRB 041006 at 6–25 keV (top panel) and 50–400 keV (bottom panel) in the observer’s frame.

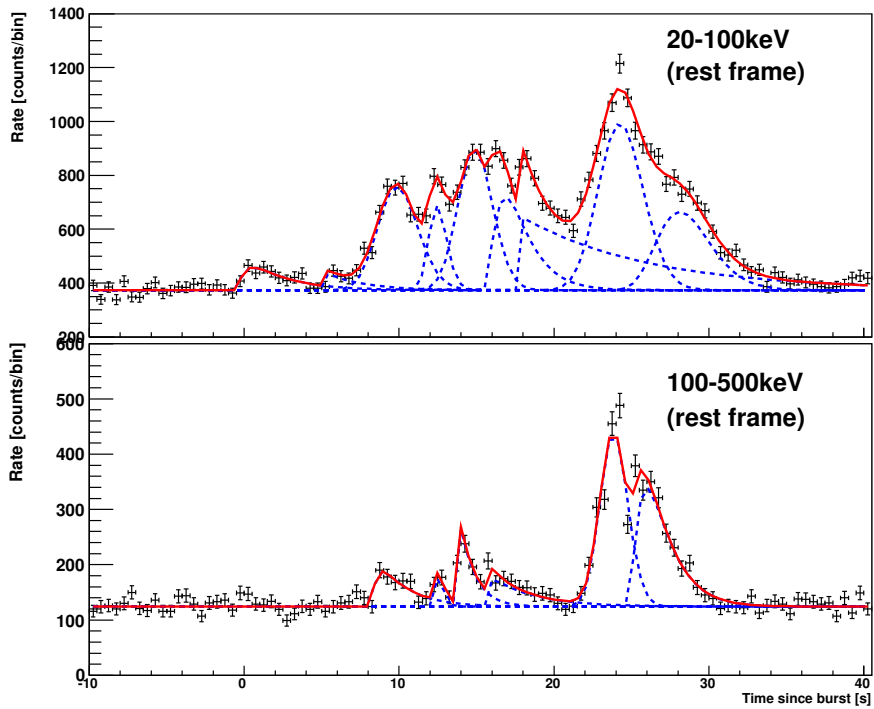


Figure 4.22: Pulse-fitting result: GRB 041006 at 20–100 keV (top panel) and 100–500 keV (bottom panel) in the rest frame.

4.3.9 GRB050408

GRB 050408 triggered the FREGATE, WXM, and SXC instruments at 16:22:50.93 UT on 8 April 2005. WXM and SXC flight localizations were reported in a GCN Notice issued at 16:23:02, which corresponded to 11 sec after the burst trigger and while the burst was still in progress (Sakamoto et al. 2005). After the burst, 60 photometric measurements in U, B, V, R_c and I_c bands from 12 telescopes and X-ray afterglow observations by *Swift* were done (compilation by de Ugarte Postigo et al. 2007).

The prompt emission consist of three pulses. The third one is not seen at higher-energies. This burst shows the typical hard-to-soft evolution. The pulse-fit in the two-divided bands and multi-divided bands, and pulse-resolved spectral-fit results are shown in Fig. 4.23, Table 4.24, Fig. 4.24, Table 4.25, Fig. 4.25, and Table 4.26, respectively.

Table 4.24: Lag properties of GRB 050408 (6–25 keV and 50–400 keV in the observer’s frame)

	$T_{\text{peak}}^{\text{low}}$ [s]	$T_{\text{peak}}^{\text{high}}$ [s]	l_{obs} [s]	l_{rest} [s]	σ_l	$w_{\text{rest}}^{\text{low}}$ [s]	$w_{\text{rest}}^{\text{high}}$ [s]
1	0.67 ± 0.08	0.13 ± 0.14	0.54 ± 0.16	0.24 ± 0.07	3.3	3.24 ± 0.62	1.86 ± 0.54
2	2.99 ± 0.09	2.68 ± 0.16	0.31 ± 0.18	0.14 ± 0.08	1.7	2.71 ± 0.62	1.60 ± 0.38

Table 4.25: Lag properties of GRB 050408(10–100 keV and 100–500 keV in the rest frame)

	$T_{\text{peak}}^{\text{low}}$ [s]	$T_{\text{peak}}^{\text{high}}$ [s]	l_{obs} [s]	l_{rest} [s]	σ_l	$w_{\text{rest}}^{\text{low}}$ [s]	$w_{\text{rest}}^{\text{high}}$ [s]
1	0.55 ± 0.07	0.26 ± 0.11	0.29 ± 0.13	0.13 ± 0.06	2.3	3.34 ± 0.6185	1.73 ± 0.40
2	3.05 ± 0.10	2.83 ± 0.11	0.23 ± 0.15	0.10 ± 0.07	1.5	2.19 ± 0.53	1.88 ± 0.31

4.3.10 GRB060121

On January 21 2006 at 22:24:54.5 UTC, GRB 060121 triggered the FREGATE instruments. GRB 060121 was localized correctly in flight by the WXM instruments and the position was relayed to the GCN network within 13 seconds after the burst trigger (Arimoto et al. 2006).

Table 4.26: Spectral properties of GRB 050408

Model	$E_{\text{peak}}^{\text{src}}$ [keV]	α	β	L_{iso} 10^{52} [ergs/s]	χ_{ν}^2 (d.o.f.)
1 Cutoff p.l.	$142.1^{+11.8}_{-13.9}$	$-0.68^{+0.09}_{-0.10}$	-	$0.54^{+0.02}_{-0.02}$	0.72 (63)
2 Cutoff p.l.	$116.6^{+10.5}_{-12.3}$	$-0.92^{+0.08}_{-0.08}$	-	$0.58^{+0.02}_{-0.02}$	0.91 (65)

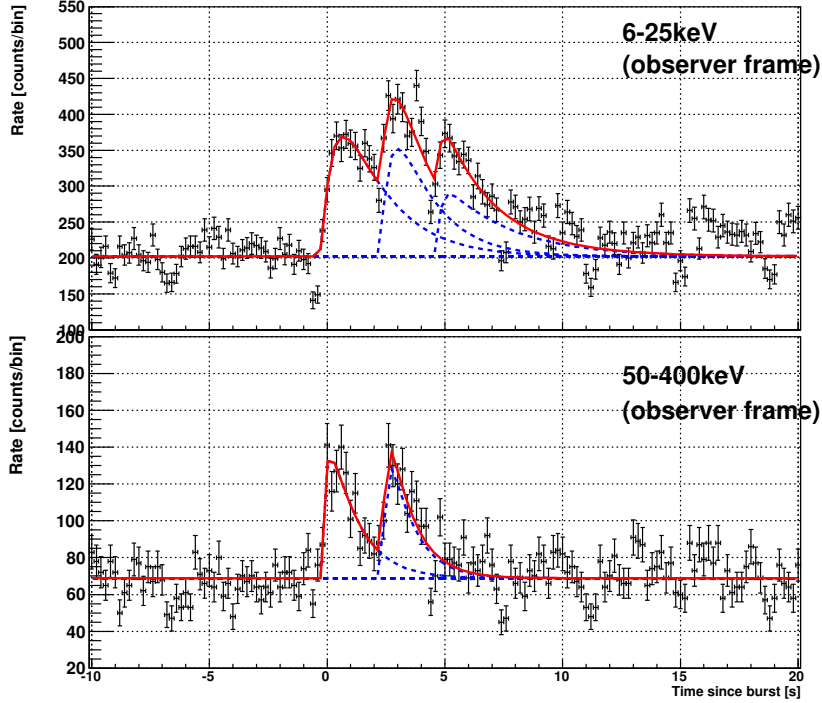


Figure 4.23: Pulse-fitting result: GRB 050408 at 6–25 keV (top panel) and 50–400 keV (bottom panel) in the observer’s frame.

From the observations after the burst occurrence, X-ray (Mangano et al. 2006), optical (Malesani et al. 2006) and near infrared counter parts (Hearty et al. 2006) were identified and its extended host galaxy was also found (Levan et al. 2006).

In the lowest energy band of the WXM (2–10 keV), the pulse is relatively broad and the duration is ~ 6 s. At higher energies, the duration decreases, which is typical for GRBs (Fenimore et al. 1995). In the low-energy band (< 40 keV) the burst consists of single pulse while the burst might consist of two pulses in the high-energy band (> 40 keV). However, the pulses in the high-energy band overlap and it is hard to perform a pulse fit. Thus we fit the burst as single pulse. The pulse-fit in the multi-divided bands and pulse-resolved spectral-fit results are shown in Fig. 4.26 and Table 4.27, respectively.

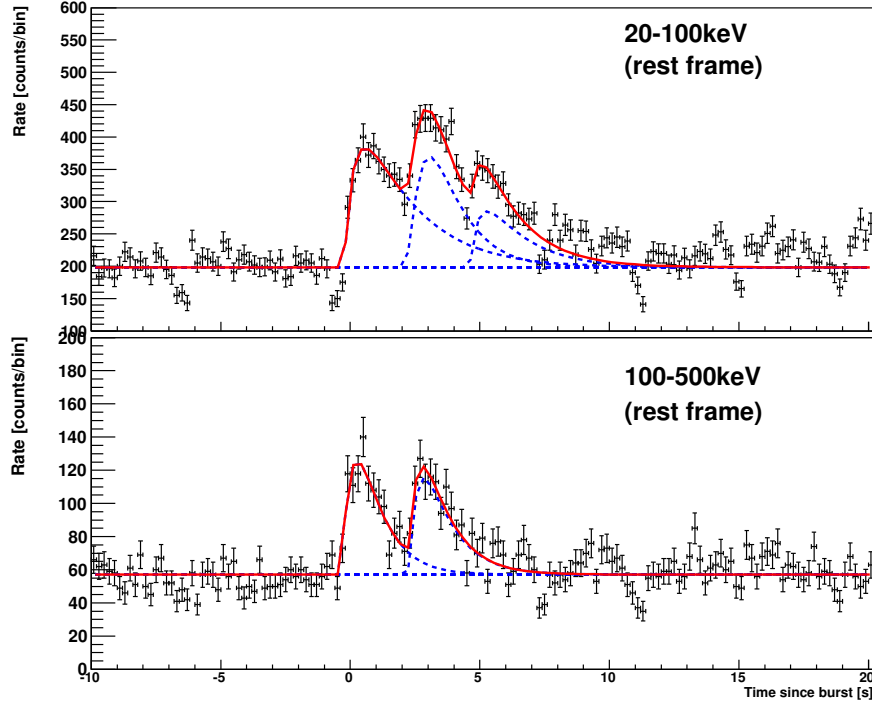


Figure 4.24: Pulse-fitting result: GRB 050408 at 20–100 keV (top panel) and 100–500 keV (bottom panel) in the rest frame.

Table 4.27: Spectral properties of GRB 060121

Model	$E_{\text{peak}}^{\text{obs}}$ [keV]	α	β	Normalization [†] [ph cm ⁻² s ⁻¹ keV ⁻¹]	χ^2_{ν} (d.o.f.)
1 Band	$108.2^{+5.5}_{-3.6}$	$-0.36^{+0.10}_{-0.10}$	$-2.55^{+0.20}_{-0.36}$	$5.18^{+0.25}_{-0.25} \times 10^{-1}$	0.74(69)

[†]: Normalization at 15 keV

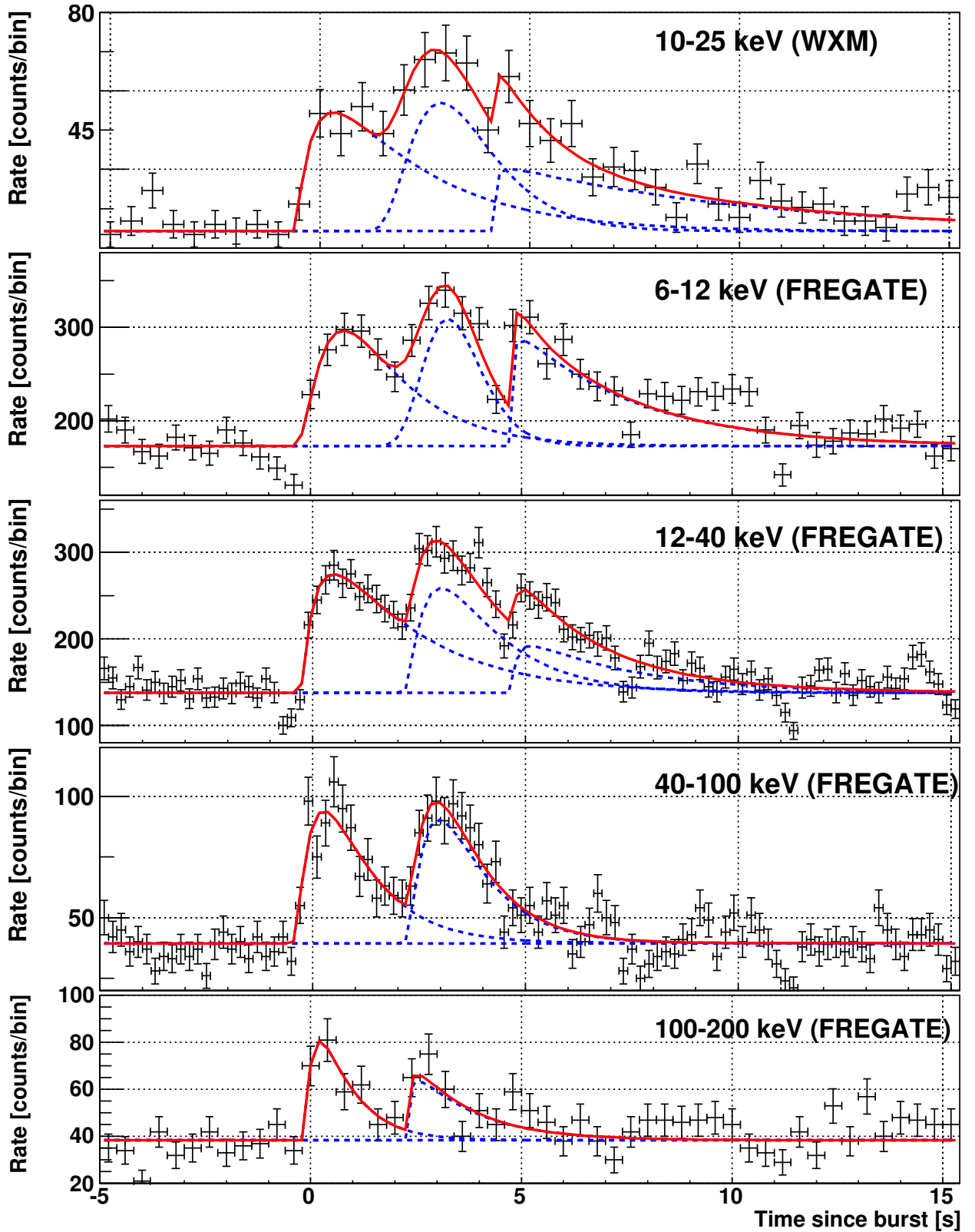


Figure 4.25: Pulse fit for GRB 050408 in the multi-divided bands. The energy bands from the top to the bottom are 10–25 keV (WXM), 6–12 keV (FREGATE), 12–40 keV (FREGATE), 40–100 keV (FREGATE), and 100–200 keV (FREGATE). Solid lines represents the best pulse-fitting function.

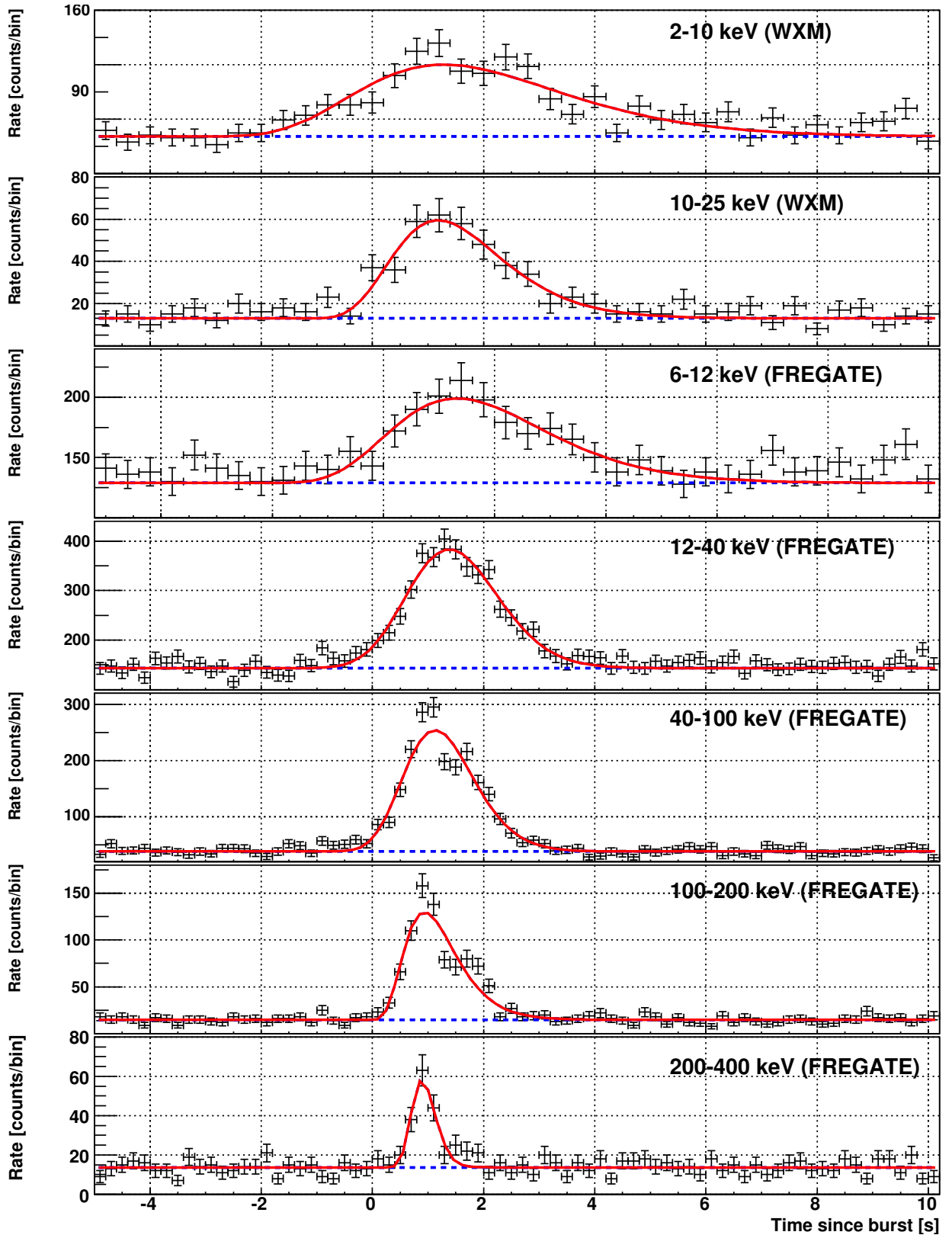


Figure 4.26: Pulse fit for GRB 060121 in the multi-divided bands. The energy bands from the top to the bottom are 2–10 keV (WXM), 10–25 keV (WXM), 6–12 keV (FREGATE), 12–40 keV (FREGATE), 40–100 keV (FREGATE), 100–200 keV (FREGATE), and 200–400 keV (FREGATE). Solid lines represents the best pulse-fitting function.

4.4 Correlation between spectral lag and other properties

We investigate the spectral lag, temporal evolution and spectral characteristics of the *HETE* GRB sample. To test if there are any correlations between the spectral lag and other parameters, we use pulses which satisfy the following requirement: the significance of the spectral lag $\sigma_{\text{lag}} > 1.5$ and positive lag $\tau_{\text{lag}} > 0$. In the analysis, we adopt 2 sets of energy bands: 6–25 keV and 50–400 keV for the “observer” frame, and 20–100 keV and 100–500 keV for the “burst-rest” frame.

Monte Carlo simulation

To estimate the correlation coefficient on the basis of the spectral lag’s confidence level, we perform a Monte Carlo simulation. First, we define l and σ_l as the value and confidence level (1σ) of the spectral lag. Since we have already obtained l and σ_l , we can generate a *pseudo* plot based on the specific probability distributions, that is, make a plot similar to Fig. 4.28 with random number seeds. Then we can calculate the value of the correlation coefficient R for the generated *pseudo* plot using the *Spearman rank-order* correlation test. Finally we repeat the same procedure 10000 times with different random number seeds. Hereafter, we adopt this method in the following analysis.

4.4.1 Correlation between E_{peak} and L_{iso}

Before we test the correlation between the spectral lag and other properties, we examine the correlation between E_{peak} and L_{iso} . There is a widely known Yonetoku relation between E_{peak} and L_{iso} ($L_{\text{iso}} \propto E_{\text{peak}}^{1.8}$) (Yonetoku et al. 2004; Tsutsui et al. 2008b). The plot with the *HETE* sample is shown in Fig. 4.27. Note that Fig. 4.27 includes 2 plots; one is a plot with the data for 6–25 keV and 50–400 keV (the “observer” frame), and the other plot for 20–100 keV and 100–500 keV (the “burst-rest” frame). Here the corresponding pulses which satisfy our criterion are slightly different between the observer and the burst-rest frame. The dashed line in Fig. 4.27 is the best-fit function whose index is fixed at 1.8. The reason why we fix the index at 1.8 is that the number of plots is small (~ 15) and the value of 1.8 is securely established from the past study. In our *HETE* sample, although there are systematic scatters around the best-fit line with reduced chi-square $\chi^2_{\nu} = 381.8/13$ and $384.2/14$, there is a strong correlation with the correlation coefficient $R = 0.88^{+0.02}_{-0.05}$ and $0.86^{+0.03}_{-0.05}$ (the corresponding chance probabilities are 3.3×10^{-5} and 3.9×10^{-5}). Thus we can say that our sample is consistent with the Yonetoku relation of

past studies. Here, when we calculate the correlation coefficient, we adopt the *Spearman rank-order* correlation test. The *Spearman rank-order* correlation test is a non-parametric measure of correlation, that is, it assesses how well an arbitrary monotonic function could describe the relationship between two variables, without making any assumptions.

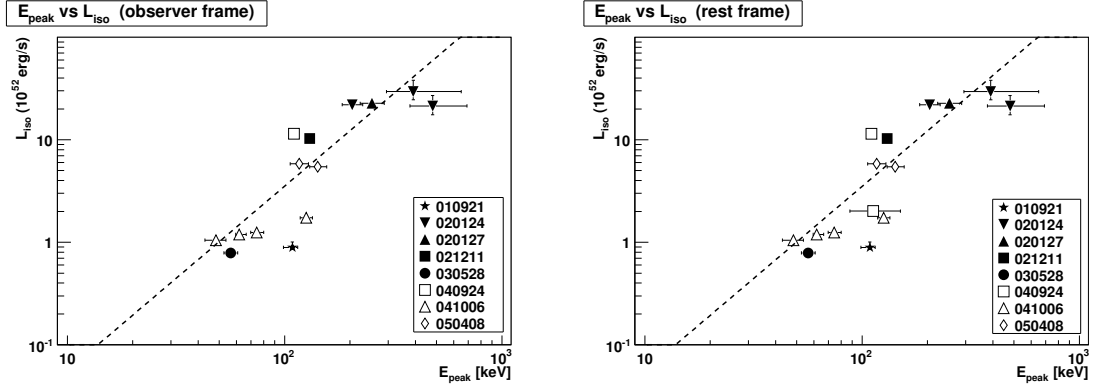


Figure 4.27: Scatter plot of E_{peak} vs. L_{iso} using the data set in the observer's (left) and rest frame (right).

4.4.2 Correlation between spectral lag and duration

The scatter plots for spectral lag τ_{lag} and duration w_0 are shown in Fig. 4.28 in the observer's frame (6–25 keV and 50–400 keV). We find a correlation between the spectral lags and durations in the both 6–25 keV and 50–400 keV. But in this case, since the confidence level of the spectral lag cannot be ignored, we test how correlated these plots are using a Monte Carlo simulation and a Spearman rank-order correlation test.

Result

We demonstrate the result as shown in Fig. 4.29. The dashed line is the best-fit function for an asymmetric Gaussian, so we derive the correlation coefficients $R = 0.66^{+0.10}_{-0.14}$ and $0.74^{+0.06}_{-0.14}$ in the 6–25 keV and 50–400 keV bands, respectively. The corresponding chance probabilities at the most probable values are 1.0×10^{-2} and 2.5×10^{-3} , so we get low chance probabilities. From Fig. 4.28, the best-fit functional form of these relations is $\log(w) = A_1 + B_1 \log(\tau_{\text{lag}})$ with $A_1 = 1.05 \pm 0.06$, $B_1 = 1.16 \pm 0.09$ and the reduced chi-square is 43.0/12 in the 6–25 keV band and $\log(w) = A_2 + B_2 \log(\tau_{\text{lag}})$ with $A_2 = 0.69 \pm 0.05$, $B_2 = 0.94 \pm 0.08$, and 45.1/12 in the 50–400 keV band.

Next, we show the scatter plots for the spectral lag τ_{lag} and the duration w_0 in Fig. 4.30 in the burst-rest frame (20–100 keV and 100–500 keV). The same trends are seen

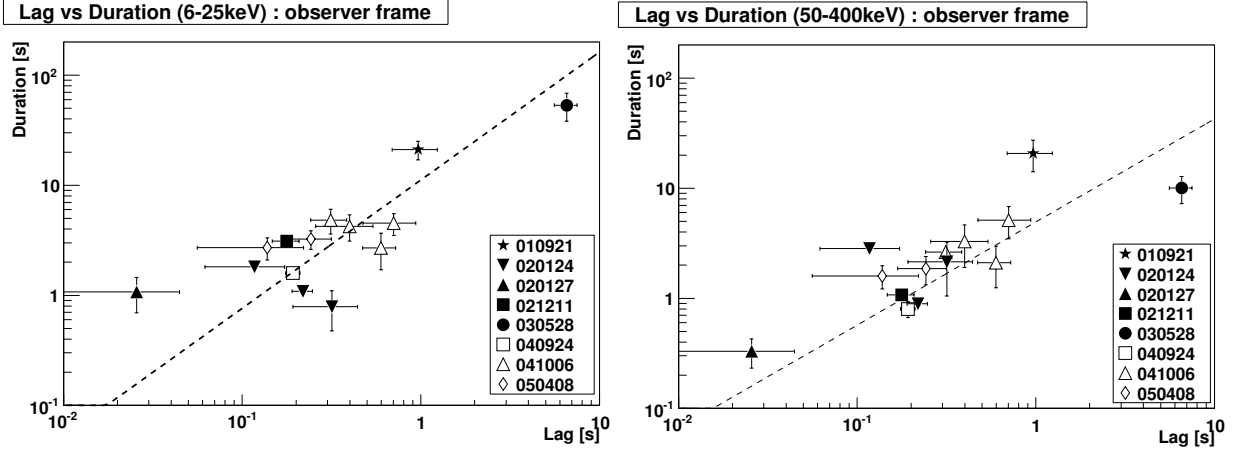


Figure 4.28: Spectral lag vs. duration in the 6 – 25 keV (Right) and 50 – 400 keV (Left) in the observer’s frame.

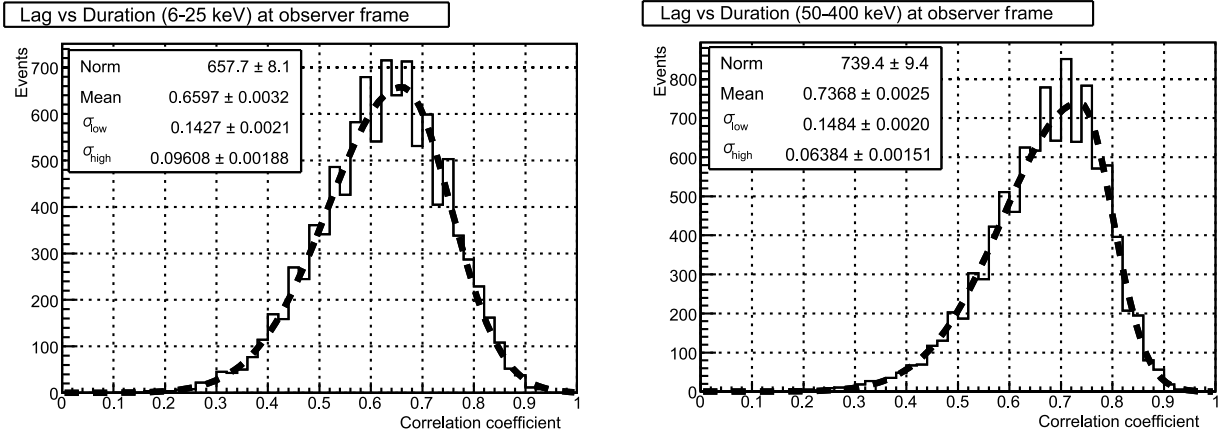


Figure 4.29: Distribution of the correlation coefficient between spectral lag and duration in the 6 – 25 keV (Left) and 50 – 400 keV (Right) in the observer’s frame.

as in Fig. 4.28. We derive the correlation coefficients $R = 0.74^{+0.06}_{-0.15}$ and $0.72^{+0.07}_{-0.22}$ with chance probabilities of 1.6×10^{-3} and 2.5×10^{-3} in the 6–25 keV and 50–400 keV bands, respectively. The best-fit functional form is $\log(w) = A_3 + B_3 \log(\tau_{\text{lag}})$ with $A_3 = 1.06 \pm 0.04$, $B_3 = 1.15 \pm 0.06$ and a reduced chi-square is 72.5/13 in the 20–100 keV and $\log(w) = A_4 + B_4 \log(\tau_{\text{lag}})$ with $A_4 = 0.67 \pm 0.06$, $B_4 = 0.73 \pm 0.09$ and a reduced chi-square 26.6/13 in the 100–500 keV band in the burst-rest frame.

These results are almost consistent with those of Hakkila et al. 2008 (index 0.85). From this, we find that the correlation between the spectral lags and durations also holds for the low energy band (< 25 keV).

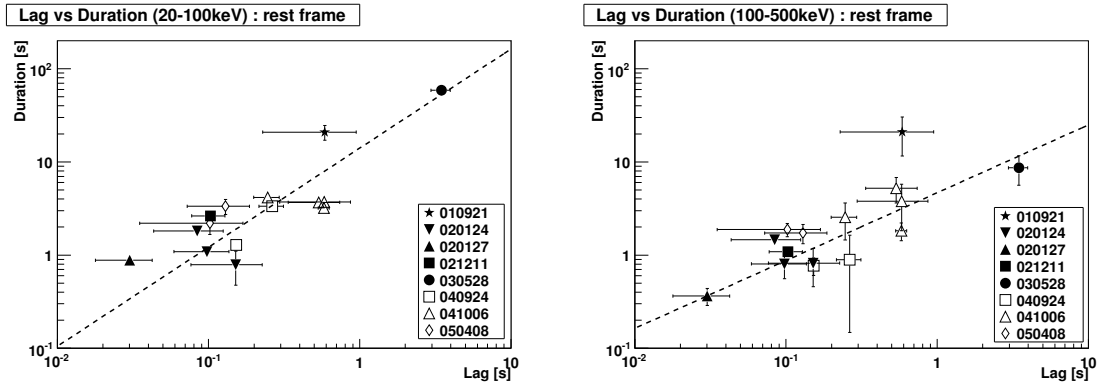


Figure 4.30: Scatter plot of spectral lag vs. duration in the 20 – 100 keV band (Left) and 100 – 500 keV band (Right) in the rest frame.

4.4.3 Correlation between spectral lag and L_{iso}

The scatter plots of the spectral lag τ_{lag} and luminosity L_{iso} are shown in Fig. 4.31 in the observer’s frame and burst-rest frame. We derive the correlation coefficients as $R = -0.79^{+0.16}_{-0.05}$ and $-0.90^{+0.12}_{-0.02}$ with chance probabilities of 7.7×10^{-4} and 4.9×10^{-6} in the observer’s and rest frame, respectively. The best-fit functional form is $\log(L_{51}) = A_5 + B_5 \log(\tau_{\text{lag}})$ with $A_5 = -0.79 \pm 0.04$, $B_5 = -1.16 \pm 0.07$; reduced chi-square is 133.2/12 in the observer’s frame and $\log(L_{51}) = A_6 + B_6 \log(\tau_{\text{lag}})$ with $A_6 = -1.09 \pm 0.04$, $B_6 = -1.23 \pm 0.07$ and the reduced chi-square is 97.1/13 in the burst-rest frame. The spectral lag’s index (~ -1) is slightly inconsistent with that of Hakkila et al. 2008 (the index ~ -0.7) The slight inconsistency seems to come from (1) the fact that the number of *HETE* GRB samples is small compared with those of Hakkila et al. 2008 and a larger number of GRB samples might make the *HETE* indices accordant with those of Hakkila et al. 2008, and (2) since Hakkila et al. 2008 uses not only GRBs with known redshifts but also without known redshifts (assuming $z \sim 1$), this could make these indices inconsistent. We will not discuss this inconsistency any further.

4.4.4 Correlation between spectral lag and E_{peak}

The scatter plots of the spectral lag τ_{lag} and E_{peak} are shown in Fig. 4.32 in the observer’s frame and burst-rest frame. We derive the correlation coefficients as $R = -0.66^{+0.15}_{-0.08}$ and $-0.81^{+0.16}_{-0.05}$ with chance probabilities of 1.0×10^{-2} and 2.5×10^{-4} in the observer’s and rest frame, respectively. The best-fit functional form is $\log(E_{\text{peak}}) = A_7 + B_7 \log(\tau_{\text{lag}})$ with $A_7 = 1.88 \pm 0.02$, $B_7 = -0.31 \pm 0.02$ and the reduced chi-square is 97.8/12 in the observer’s frame and $\log(E_{\text{peak}}) = A_8 + B_8 \log(\tau_{\text{lag}})$ with $A_8 = 1.82 \pm 0.02$, $B_8 = -0.33 \pm 0.03$; the reduced chi-square is 33.91/13 in the burst-rest frame. These results are new in this

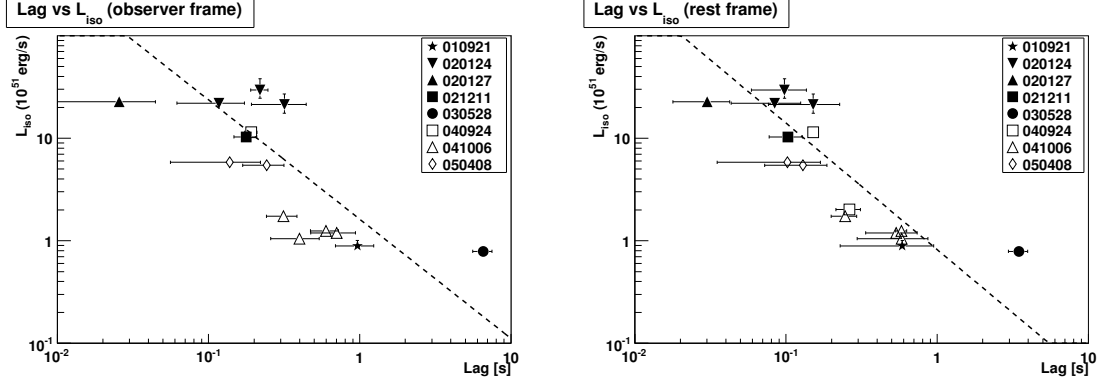


Figure 4.31: Scatter plot of spectral lag vs. luminosity in the observer’s frame (Left) and burst-rest band (Right).

analysis and the dependence of the spectral lag on E_{peak} is relatively weak (its index ~ -0.3).

From a simple estimation from the Yonetoku relation ($L_{\text{iso}} \propto E_{\text{peak}}^{1.8}$) and our analysis ($L_{\text{iso}} \propto \tau_{\text{lag}}^{-1.23}$)

$$E_{\text{peak}} \propto L_{\text{iso}}^{1/1.8} \propto \tau_{\text{lag}}^{-1.23/1.8} \propto \tau_{\text{lag}}^{-0.69} \quad (4.8)$$

The index is small compared with the value obtained ($E_{\text{peak}} \sim \tau_{\text{lag}}^{-0.3}$). The inconsistency reminds us of the redshift-dependent lag-luminosity relation (Tsutsui et al. 2008a). Tsutsui et al. 2008a pointed out that the estimated pseudo-redshift using the Yonetoku relation is weakly correlated with that using the ordinary lag-luminosity relation (Norris relation; $L_{\text{iso}} \propto \tau_{\text{lag}}^{-1.1}$). They derived the Tsutsui relation described in Sec. 1.3.2 to overcome the contradiction. We thus apply the Tsutsui relation to our *HETE* sample and discuss it in the following section.

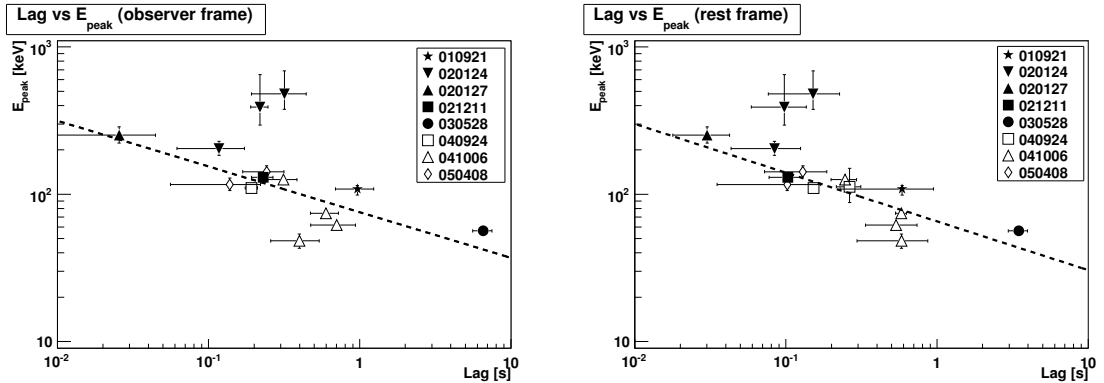


Figure 4.32: Scatter plot of spectral lag vs. E_{peak} in the observer’s frame (Left) and burst-rest frame (Right).

4.4.5 α index and spectral lag

We investigate the relation between the low-energy photon index α and spectral lag τ_{lag} in the same manner as described in Sec. 4.4. The best-fit function and correlation coefficient are $\log(\alpha) = (-1.21 \pm 0.06) - (0.96 \pm 0.12)\log(\tau_{\text{lag}})$, $R = -0.62_{-0.17}^{+0.10}$ with a chance probability of 0.02 in the energy bands of the observer's frame and $\log(\alpha) = (-1.20 \pm 0.05) - (0.72 \pm 0.11)\log(\tau_{\text{lag}})$, $R = -0.56_{-0.21}^{+0.11}$ with a chance probability of 0.03 in the energy bands of the burst-rest frame, respectively. The correlation between α and τ_{lag} is comparatively weak as the obtained coefficients are not nearer to unity or minus unity than those of other properties (durations, luminosities and E_{peak}). Furthermore, the α values are distributed within a factor of ~ 2 and significant correlations are not found.

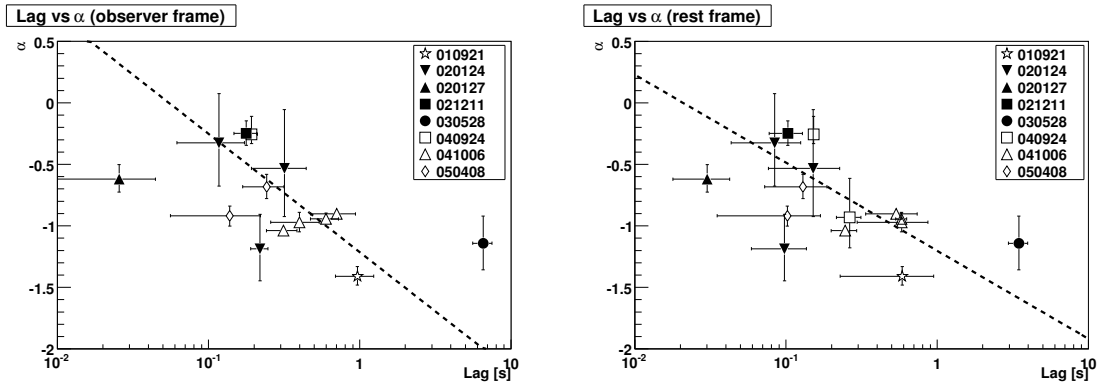


Figure 4.33: Scatter plot of spectral lag vs. α in the observer's frame (Left) and burst-rest frame (Right).

4.5 Energy dependence of spectral lag and other properties

It has been suggested that the temporal characteristics as a function of energy are determined by the curvature effect or a hydrodynamical effect. In the standard model, the rising phase of the light curve is produced by the width of the intrinsic pulse, which is associated with the shock mechanism, and the decay phase is well reproduced by the curvature effect (Qin et al., 2004, Qin & Lu, 2005, Ryde & Petrosian 2002). We test whether these models are also valid for the *HETE* GRBs.

In the previous section, we gave the result of the spectral lag analysis between the two divided energy bands. In this section, we perform the detailed energy-resolved spectral lag and temporal characteristics analysis using not only FREGATE but also WXM.

First, we introduce 4 FREGATE bands (6 – 12 keV, 12 – 40 keV, 40 – 100 keV, 100 – 200 keV and 200 – 400 keV) and 4 WXM bands (2 – 5 keV, 5 – 10 keV, 10 – 17 keV and 17 – 25 keV). Here, for some GRBs the statistics obtained by the WXM detector is poor especially when the incident angle of photons to the WXM detector is large and the photons from GRBs are screened by the coded mask. Consequently, we arbitrarily select the WXM-energy bands to collect enough events.

Furthermore, when we perform the energy-resolved analysis, it is better to select GRBs which consist of a single pulse or well separated pulses and which have a good signal to noise ratio. Thus we exclude GRB 020124 and 041006. This is because these GRB have not only overlapped-multi spikes but also poor statistics when the FREGATE bands are separated into the above 4 bands. We include GRB 030725 and GRB 060121 with unknown redshifts which consists of single pulse and have a large signal to noise ratio. If we consider the temporal properties as a function of energy, the value of the redshift does not affect the result. For example, if we calculate the power-law index between the duration and energy, the redshift affects only its normalization and the value of the power-law index is invariant with redshift. But if we consider the E_{peak} or L_{iso} , we have to adopt only GRBs with *known* redshifts because these value are redshift-dependent.

4.5.1 Definition and Fit

First, let us define new two quantities; the pulse rise timescale Δt_r and the pulse decay timescale Δt_d . Δt_r and Δt_d are defined as the time between the pulse peak and the two $1/e$ intensity points respectively. Note that Δt_r and Δt_d are close to the FWHMs in the rising phase and decaying phase, respectively, since $1/e$ is close to $1/2$. In addition, according to their definition, $\Delta t_r = \tau_{\text{rise}}$ and $\Delta t_d = \tau_{\text{dec}}$, where τ_{rise} and τ_{dec} are the pulse rise and decay timescale, respectively. Furthermore, the duration w_{FWHM} is defined as $w_{\text{FWHM}} = \tau_{\text{rise}} + \tau_{\text{dec}}$, which is the time interval where the intensities are equal to $1/e$.

We plot the energy versus the peak-maximum time τ_{peak} , then fit a power-law function ($t_{\text{peak}} \propto E^\alpha$). The same procedure is done for the rise time τ_{rise} , decay time τ_{dec} , and duration w ($= \tau_{\text{rise}} + \tau_{\text{dec}}$). using the fitted pulse model and fit a function ($w \propto E^\alpha$). Here, we define α_{lag} , α_{FWHM} , α_{rise} and α_{dec} as the power-law indices of τ_{peak} , w_{FWHM} , τ_{rise} and τ_{dec} as a function of energy, respectively.

The results are shown in Fig. 4.34, 4.35, 4.36 and 4.37. Almost all the plots are well fitted by a single power law.

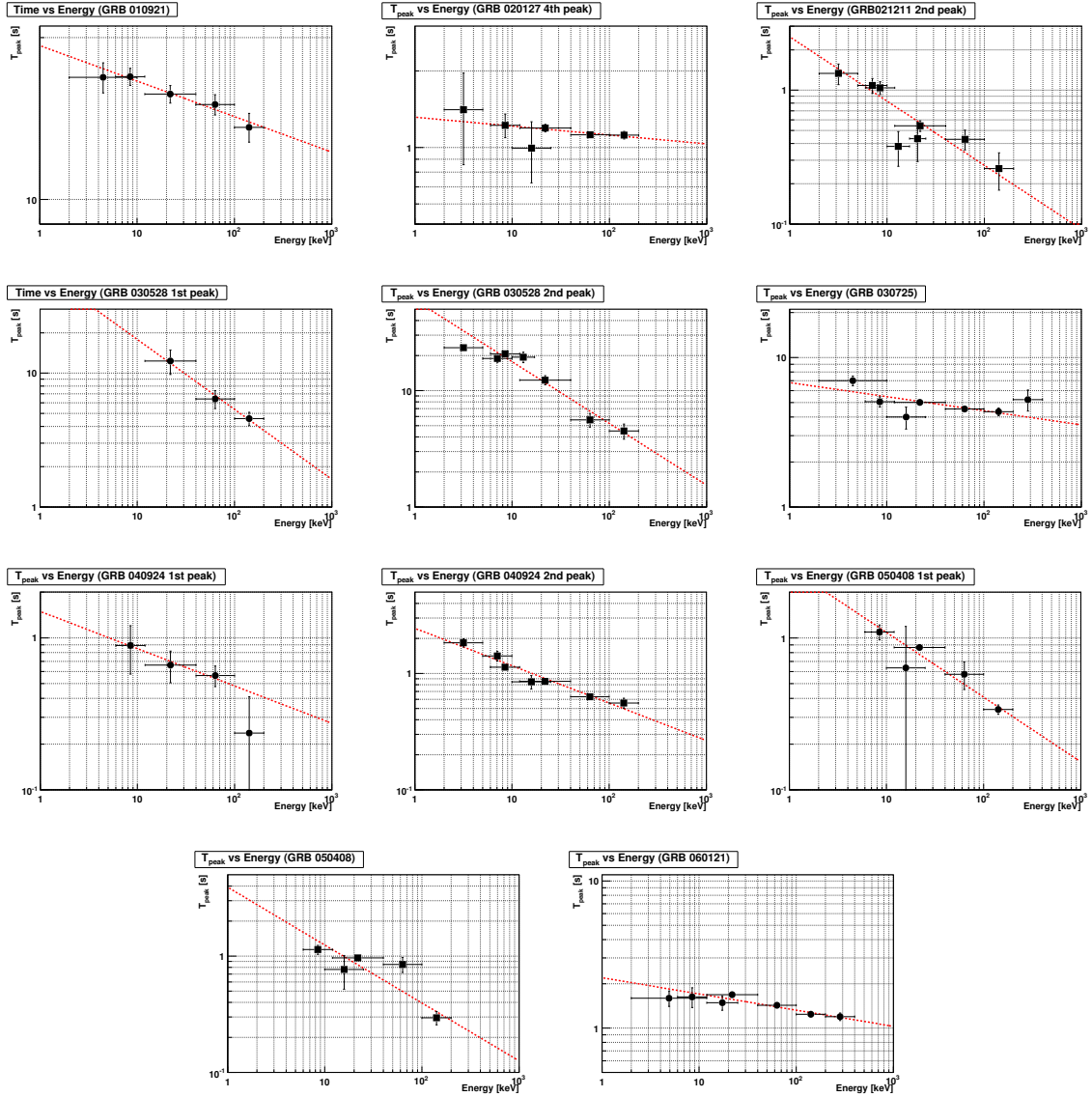


Figure 4.34: Energy vs. T_{peak} plots. The dashed line is the best-fit power-law function.

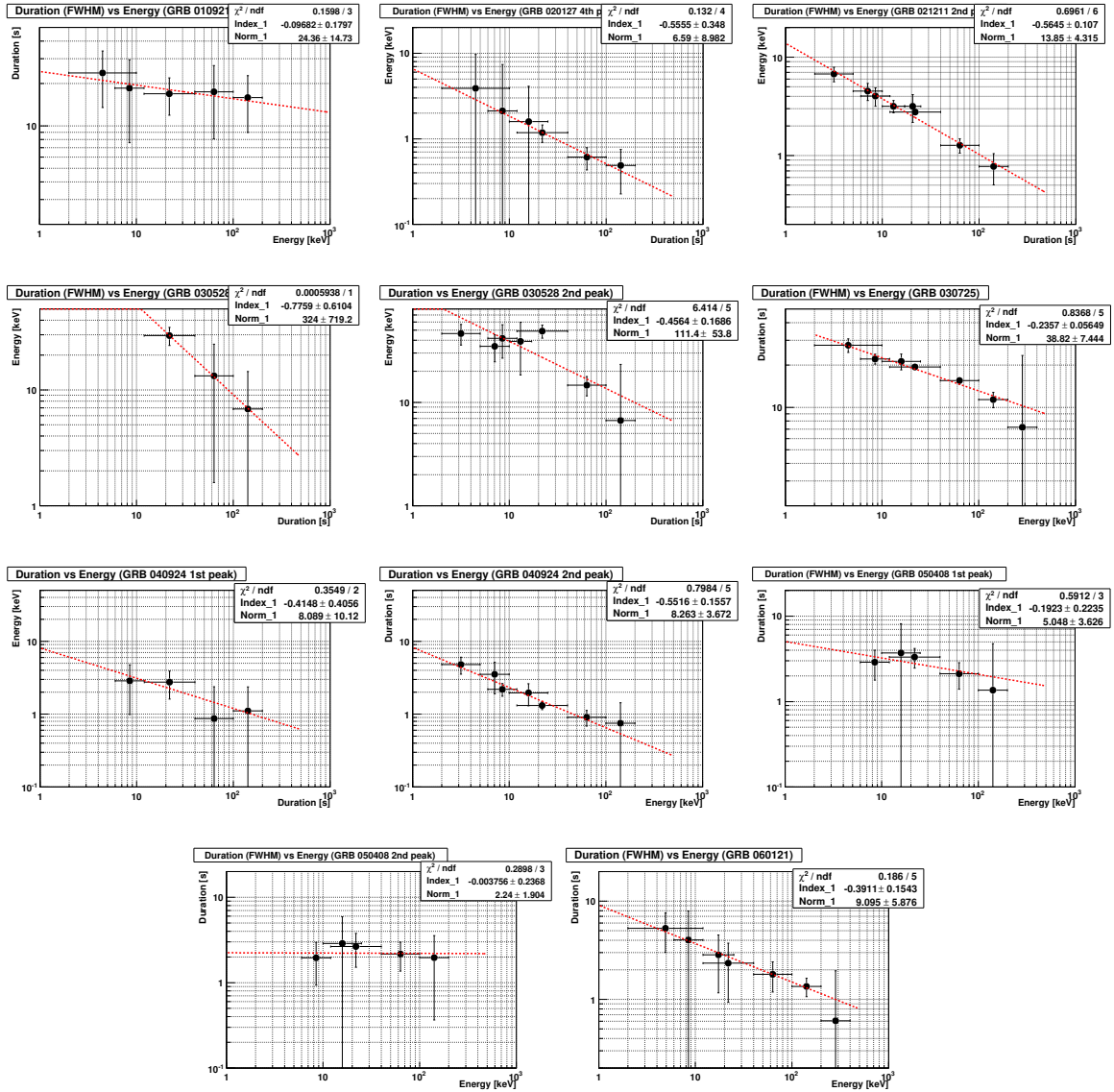


Figure 4.35: Energy vs. Duration (FWHM) plots. The dashed line is the best-fit power-law function.

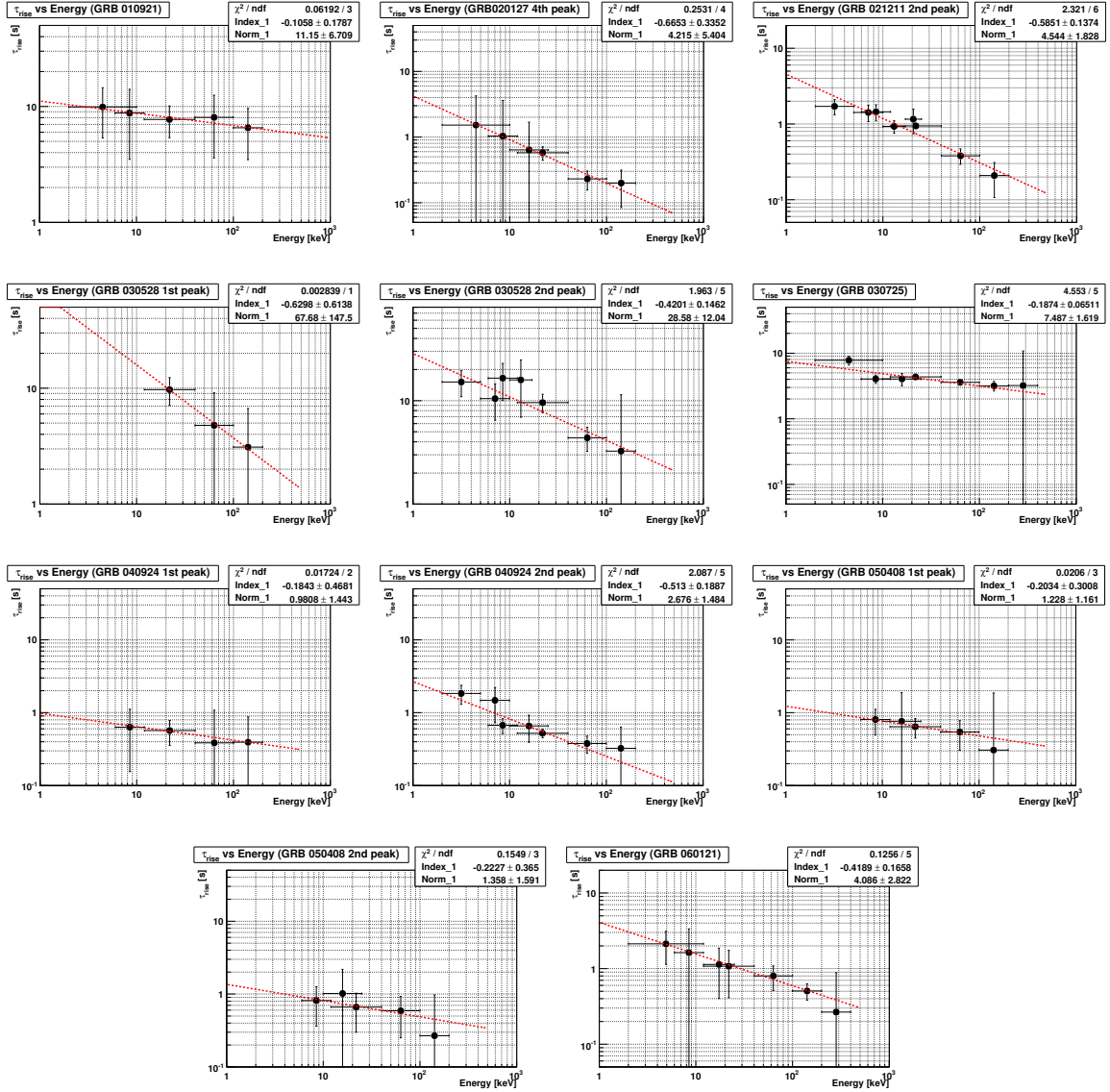


Figure 4.36: Energy vs. τ_{rise} plots. The dashed line is the best-fit power-law function.

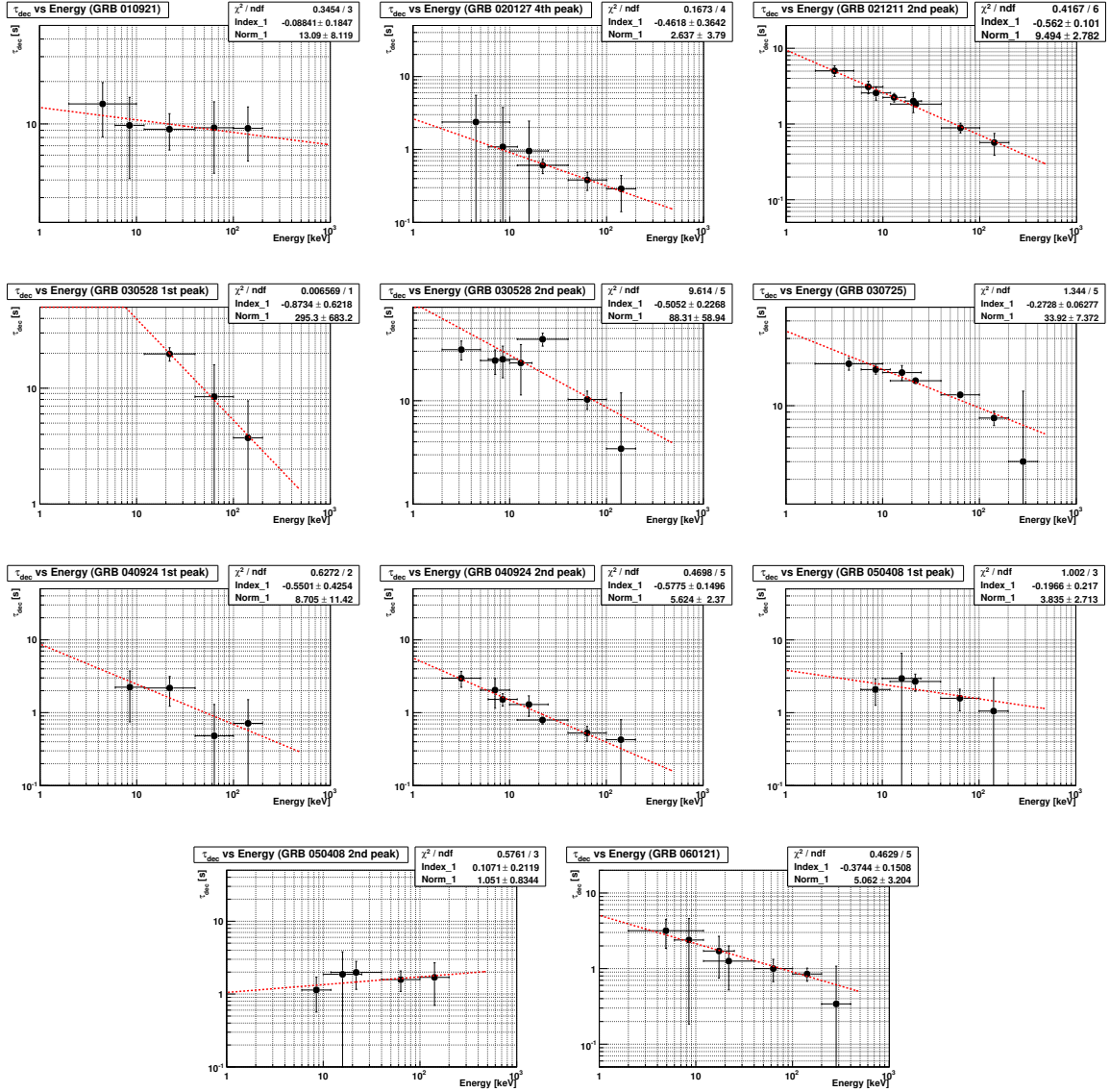


Figure 4.37: Energy vs τ_{dec} plots. The dashed line is the best-fit power-law function.

Chapter 5

Discussion of *HETE* result

We have obtained the correlation between the spectral lag and duration, L_{iso} and E_{peak} in the observer's and burst-rest frame. In particular, our result extends the energy coverage at which the lag-luminosity relation was known (> 25 keV) to a lower energy band (6–25 keV). This indicates that the GRB emission in the wide X-ray band has the same origin.

As there is no significant difference between the results in the observer's and burst-rest frame, it is natural to adopt the burst-rest frame to discuss the origin of the spectral lag. Thus, in the following discussion, we refer to the case of the burst-rest frame.

5.1 GRB with different viewing angles (off-axis model)

To account for the relation between the spectral lag and L_{iso} , let us consider the theoretical model suggested by Ioka & Nakamura 2001; off-axis model is that the detector or observer sees a constant GRB having a constant Lorentz factor $\Gamma = 1/(1 - \beta^2)^{1/2}$, a constant opening half-angle $\Delta\theta \sim 1/\Gamma$, a constant shell radius r_0 and a constant E'_{peak} in the comoving frame with different viewing angles θ_v . Fig. 5.1 shows the schematic view of the off-axis model. In this section, we adopt the same parameters as those of Ioka & Nakamura 2001; $\Gamma\Delta\theta = 1$, $r_0/c\beta\Gamma^2 = 1$. The observed spectral shape is well represented by the Band function (Band et al. 1993) and they introduced the general spectral form, $f(\nu')$, which is given as

$$f(\nu') = \left(\frac{\nu'}{\nu_0}\right)^{1+\alpha_B} \left[1 + \left(\frac{\nu'}{\nu_0}\right)^s\right]^{\frac{\beta_B - \alpha_B}{s}} \quad (5.1)$$

where α_B and β_B are the low- and high-energy indices, s describes the smoothness of the transition between the high and low energies and ν_0 is the break energy. We show this spectral shape for some s values in Fig. 5.2. A smaller s gives a smoother spectral shape and the curvature effect contributes to the smoothness. That is, the delayed emission

from high latitudes (its emission is soft compared with that from the low latitude) makes the spectrum smooth. For general s in equation 5.1, the luminosity and $\Gamma\theta_v$ are written as,

$$L_{\text{iso}} \propto \tau_{\text{lag}}^{\frac{-2+\alpha_B}{s+1}} \quad (5.2)$$

and

$$\Gamma\theta_v \propto \tau_{\text{lag}}^{\frac{1}{2(s+1)}} \quad (5.3)$$

The duration (FWHM), W_{FWHM} , is calculated using the start time T_{start} and end time T_{end} of the emission.

$$W_{\text{FWHM}} \propto (T_{\text{end}} - T_{\text{start}}) \propto \delta^{-1} \quad (5.4)$$

where δ is the Doppler factor, $\delta = \Gamma^{-1}(1 - \beta \cos \theta_v)^{-1} \simeq 2\Gamma/(1 + \Gamma^2\theta_v^2)$. Using Eq. 5.3, W_{FWHM} is written as

$$W_{\text{FWHM}} \propto 1 + \text{const} \times \tau_{\text{lag}}^{\frac{1}{s+1}} \quad (5.5)$$

The analytical results are shown in Fig. 5.3. E_{peak} is represented as

$$E_{\text{peak}} \propto \delta \propto \left(1 + \text{const} \times \tau_{\text{lag}}^{\frac{1}{s+1}}\right)^{-1} \quad (5.6)$$

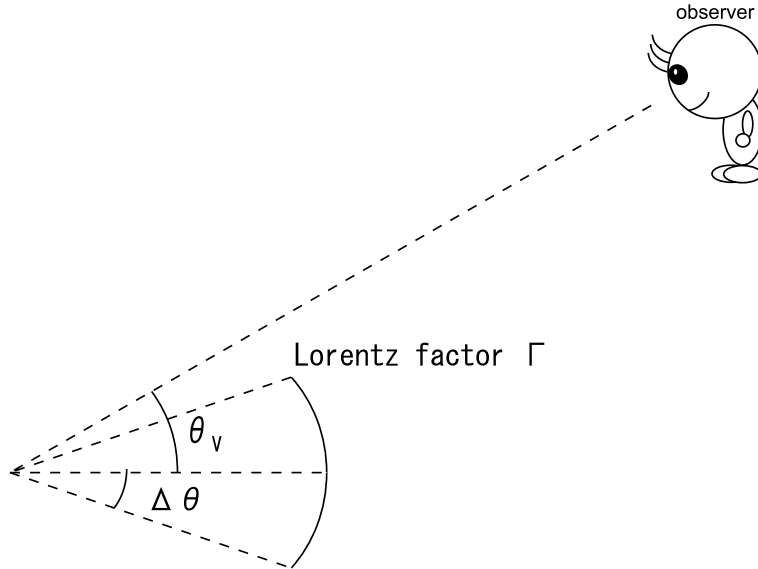


Figure 5.1: Schematic view of the off-axis model suggested by Ioka & Nakamura 2001 with the Lorentz factor Γ , opening half-angle $\Delta\theta$ and viewing angle θ_v .

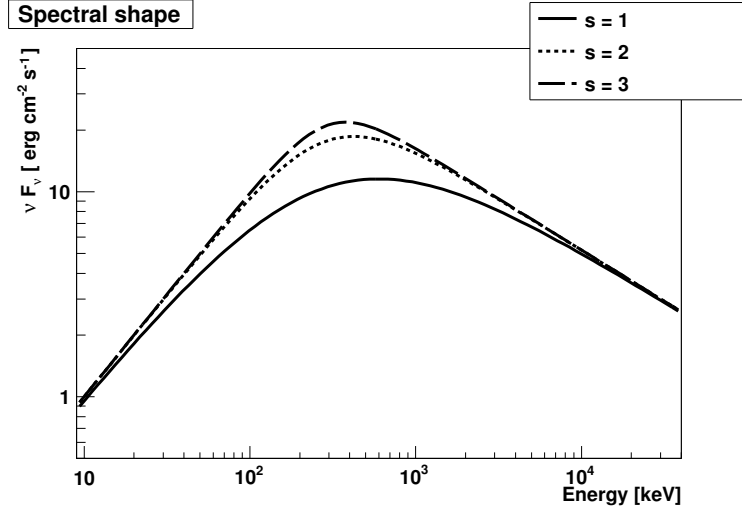


Figure 5.2: Spectral shape with different smoothness ($s = 1, 2, 3$)

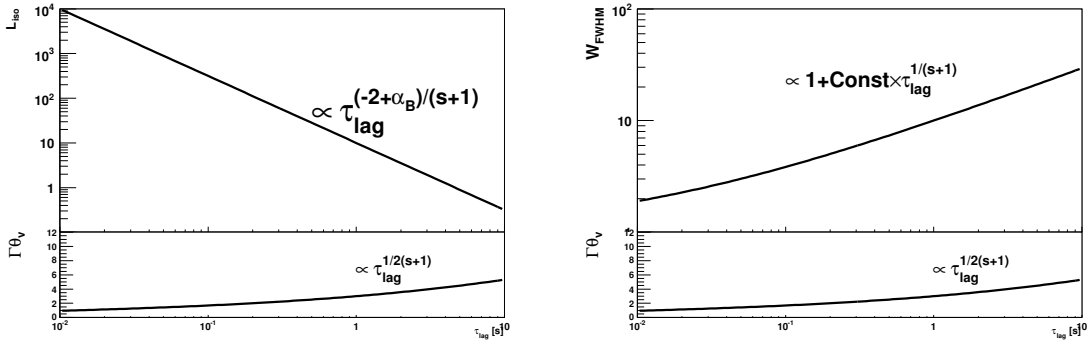


Figure 5.3: Analytical result of lag-luminosity (*left*) or -duration relation (*right*) [Ioka & Nakamura 2001].

As we have obtained $L_{\text{iso}} \propto \tau_{\text{lag}}^{-1.2}$ from the lag-luminosity relation in Fig. 4.31, we set up equation as $(-2 + \alpha_B)/(s + 1) = -1.2$ and we get the result $s = 1.5$ where we adopt $\alpha_B = -1$ because most data points are close to -1 as shown in Fig. 4.33.

The observational and theoretical results are superimposed in Fig. 5.4 in the burst-rest frame. For the lag-duration relation in the high-energy band (100–500 keV), the observational points and theoretical curve are consistent. For the lag-duration relation in the low-energy band (20–100 keV), although the observational points are consistent with the theoretical curve for small values of τ_{lag} , there are some outliers in the large τ_{lag} . This might be due to the fact that the duration evolution is due to hydrodynamical effects, and not the curvature effect. It might be dominant in the low-energy band (as we argue later, the curvature effect does not provide a large energy-dependence for the duration), or possibly we are observing overlapped pulses as a single pulse; especially in

the lower energy band the pulses are wider. For the lag- E_{peak} relation, we find consistency between the observational points and the theoretical curve. Except for some outliers, we find that the off-axis model can explain the observational results well. Furthermore, for the off-axis model the spectral lag τ_{lag} is calculated using the difference between the peak times in the different energy bands just as we calculate the spectral lag, unlike Norris et al. 2000 calculate the spectral lag using the CCF method. As the pulse corresponds to the collision of the relativistic shells, it is natural intuitively that the pulse-lag comes from the corresponding collision of the shells as Hakkila et al. 2008 suggested. From this point of view, as the Norris relation was derived from a CCF lag, the CCF just calculated total lags synthetically and the true lag relation is the Hakkila one and our lag relation. Thus, as our results are well reproduced by the off-axis model, we find that the off-axis model is valid, with the same calculation of the spectral lag.

5.2 Consistency with the *Yonetoku* relation

Let us consider the consistency with the Yonetoku relation in this section. In the preceding section, we have found that the off-axis model reproduces the observational results. We did not impose any limitations such as the Yonetoku relation ($L_{\text{iso}} \propto E_{\text{peak}}^{1.8}$).

Assuming that the Yonetoku relation is valid, from our result on the lag-luminosity relation ($L_{\text{iso}} \propto \tau_{\text{lag}}^{-1.23 \pm 0.07}$), the lag- E_{peak} relation is expected to satisfy the following,

$$E_{\text{peak,exp}} \propto L_{\text{iso}}^{1/1.8} \propto \tau_{\text{lag}}^{-1.23/1.8} \propto \tau_{\text{lag}}^{-0.69} \quad (5.7)$$

The index (-0.69) is small compared with the obtained result ($E_{\text{peak,obs}} \propto \tau_{\text{lag}}^{-0.33 \pm 0.03}$) and an inconsistency with the Yonetoku relation might exist. Denote by the subscripts “exp” and “obs” the expected and observed values, respectively. Although we take into account the uncertainty in the obtained index, the discrepancy is not in the 1- σ confidence range.

5.2.1 Systematic Uncertainty

First, we consider the fitting procedure. Because the reduced chi-squares χ_{ν}^2 of the fitted lag-results are too large ($\chi_{\nu}^2 = 97.1/13, 33.9/13$ for the lag-luminosity and $-E_{\text{peak}}$ plot, respectively), there might exist some issues with the estimate of the uncertainties. For this reason, we introduce a systematic uncertainty to the fit. We assume that the determination of the spectral lag has a systematic uncertainty of 0.05 s resulting from the overlaps of the GRB pulses or some calibration uncertainties. Furthermore GRB 030528 is suspicious because its pulse may consist not of a single pulse but of many pulses. We thus reject GRB 030528 for the conservative re-estimate. Fig. 5.5 shows

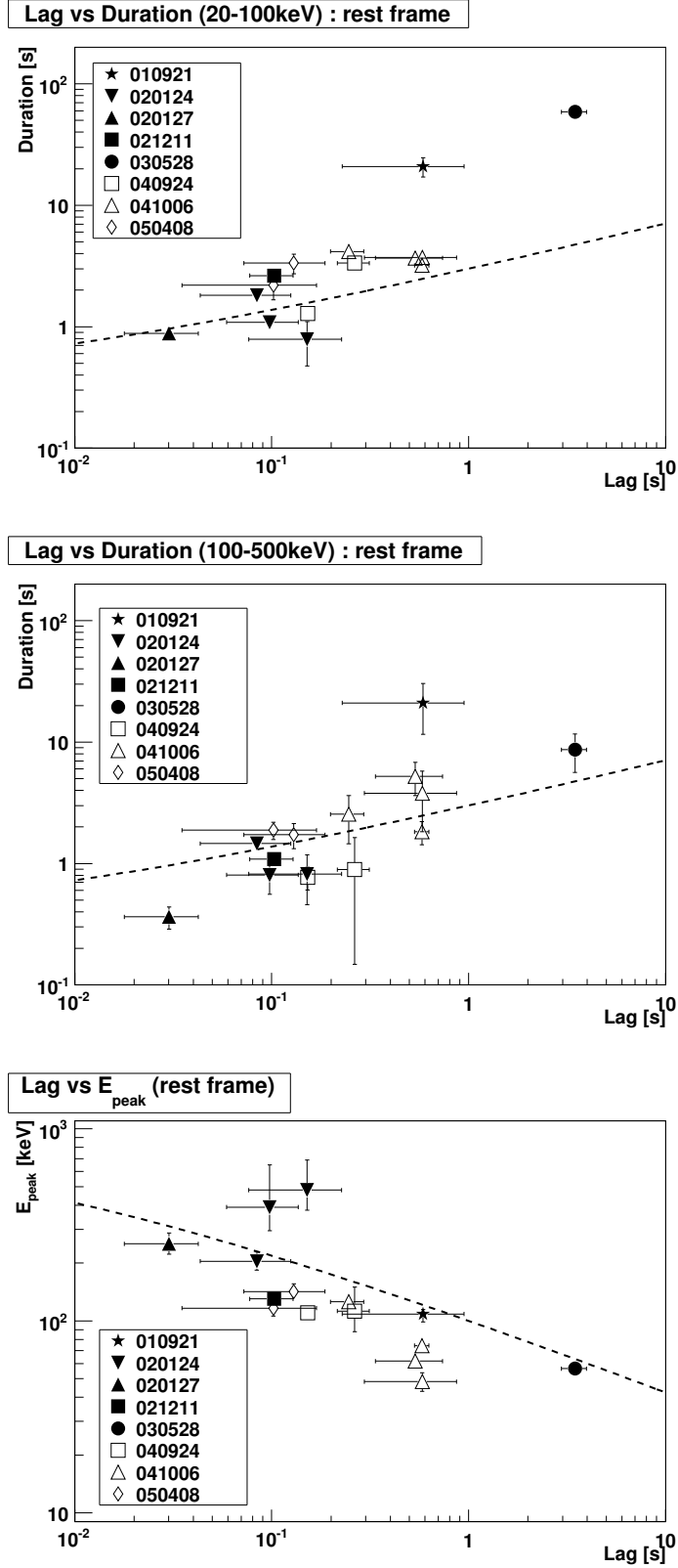


Figure 5.4: Observational result and superimposed theoretical curve (Ioka & Nakamura 2001) for lag-duration and $-E_{\text{peak}}$ relations. *Top*: lag-duration in the 20–100 keV range, *middle*: lag-duration in the 100–500 keV range, *bottom*: lag- E_{peak} . Note that all relations are in the burst-rest frame.

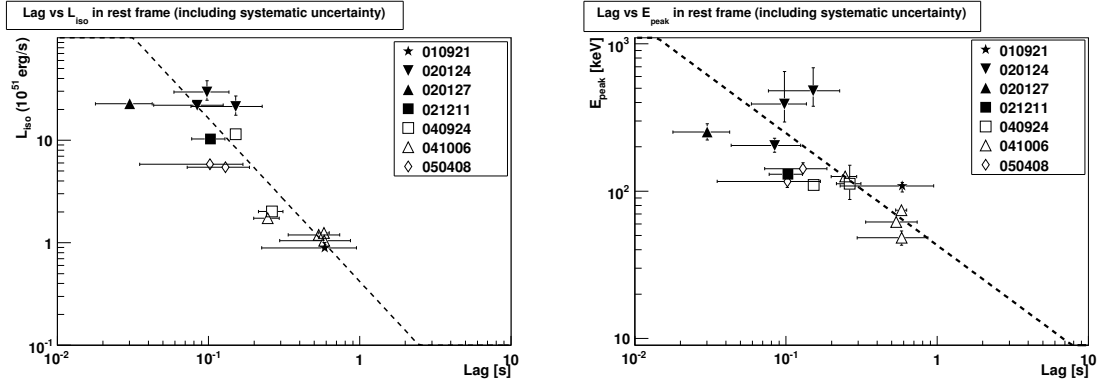


Figure 5.5: Lag-luminosity (left) and $-E_{\text{peak}}$ (right) plots including the systematic uncertainty (0.05 s). The best-fit function is presented as a dashed line.

the re-fitting results for the lag-luminosity and $-E_{\text{peak}}$ plots. The best-fit functions are $\log(L_{51}) = (-1.38 \pm 0.13) - (1.59 \pm 0.28) \log(\tau_{\text{lag}})$ with reduced chi-square $\chi^2_{\nu} = 8.2/12$ and $\log(E_{\text{peak}}) = (1.63 \pm 0.08) - (0.76 \pm 0.17) \log(\tau_{\text{lag}})$ with reduced chi-square $\chi^2_{\nu} = 12.5/12$. Using these values, the expected index is the following

$$E_{\text{peak,exp}} \propto \tau_{\text{lag}}^{-1.59/1.8} \propto \tau_{\text{lag}}^{-0.88} \quad (5.8)$$

while $E_{\text{peak,exp}} \propto \tau_{\text{lag}}^{-0.76 \pm 0.17}$. Thus the index of $E_{\text{peak,exp}}$ is consistent with that of $E_{\text{peak,obs}}$ with $1\text{-}\sigma$ uncertainty.

We also check the consistency with the off-axis model in this case. From the index of the lag-luminosity relation and Eq. 5.2, we obtain a smoothness of ~ 0.9 and the resulting lag- E_{peak} relation ($E_{\text{peak}} \propto \tau_{\text{lag}}^{-1/(s+1)} \propto \tau_{\text{lag}}^{-0.5}$) is almost consistent with the obtained value (its index is -0.76 ± 0.17) at the $1\text{-}\sigma$ confidence level.

Taken together, when we introduce the systematic uncertainty for the spectral lag ($\tau_{\text{lag}} \sim 0.05$ s), we find that the obtained results are consistent with not only the off-axis model but also the Yonetoku relation.

5.2.2 Luminosity evolution as a function of distance

Now, we consider the other interpretation of the consistency with the Yonetoku relation.

If a systematic uncertainty is not needed for some reason and there is really an inconsistency with the Yonetoku relation between the lag-luminosity and $-E_{\text{peak}}$ relations, we need another framework to explain the inconsistency.

Here the inconsistency reminds us of the redshift-dependent lag-luminosity relation (Tsutsui et al. 2008a). Tsutsui et al. 2008a pointed out that the estimated pseudo redshift using the Yonetoku relation is weakly correlated with that using the ordinary lag-

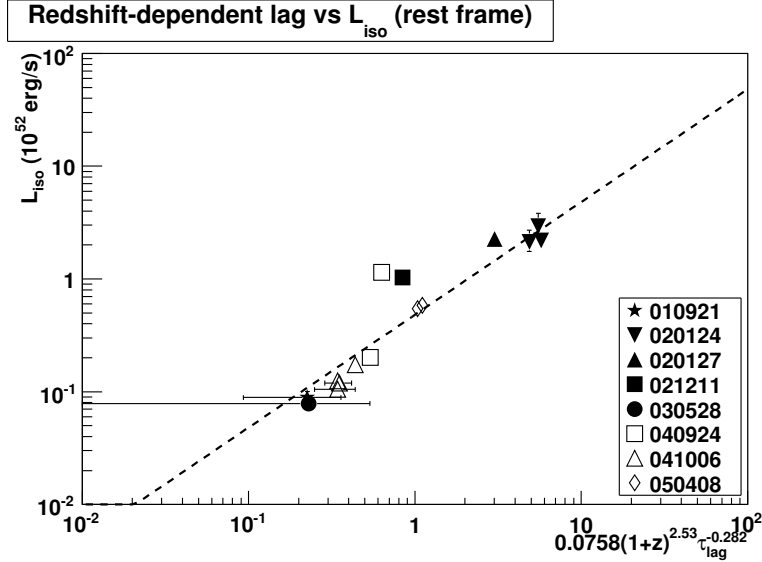


Figure 5.6: Scatter plot of redshift-dependent spectral lag vs. L_{iso} in the burst-rest band.

luminosity relation (Norris relation; $L_{\text{iso}} \propto \tau_{\text{lag}}^{-1.1}$); that is to say, if both the lag-luminosity and $-E_{\text{peak}}$ relations simply indicate the distance of GRBs, the estimated distance using the lag-luminosity relation must be consistent or highly correlated with that using the lag- E_{peak} relation. They derived redshift-dependent lag-luminosity relation described in Sec. 1.3.2 to overcome the contradiction. We thus apply the Tsutsui relation to our *HETE* sample and discuss the result in the following section.

Redshift-dependent spectral lag and L_{iso}

First, we adopt the same index of $(1+z)$ and τ_{lag} reported by Tsutsui et al. 2008a, that is, only the normalization is a free parameter. The result is shown in Fig. 5.6. The correlation coefficient is $R = 0.93^{+0.01}_{-0.05}$ with a chance probability of 1.4×10^{-7} in the burst-rest frame.

$$L_{52} = A \times 0.0758 \times (1+z)^{2.53} (\tau_{\text{lag}})^{-0.282} \quad (5.9)$$

The normalization A is 0.482 ± 0.010 with the reduced chi-square $\chi^2_{\nu} = 302.3/14$ in the burst-rest frame. Tsutsui et al. 2008a found that the standard deviation of their relation is ~ 3 and our normalization value is allowed at the confidence level of Tsutsui et al. 2008a. Furthermore, this relation gives a tighter correlation than the simple relation (e.g., ordinary lag-luminosity relation with $R = 0.86$).

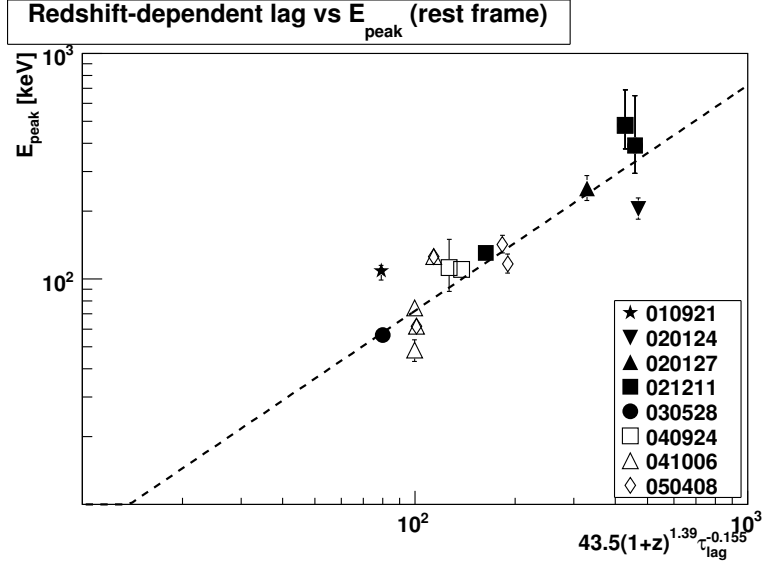


Figure 5.7: Scatter plot of redshift-dependent spectral lag vs. E_{peak} in the burst-rest band.

Redshift-dependent spectral lag and E_{peak}

In past studies (Tsutsui et al. 2008a and Kodama et al. 2008), it has been found that the Yonetoku relation seems to be robust. Here we assume that the Yonetoku relation is valid ($L_{\text{iso}} \propto \tau_{\text{lag}}^{1.8}$) and obtain the redshift-dependent lag- E_{peak} relation using the Yonetoku relation and the redshift-dependent lag-luminosity relation. Thus, we write the redshift-dependent lag- E_{peak} relation as

$$E_{\text{peak}} = B \times 43.5 \times (1+z)^{1.39} (\tau_{\text{lag}})^{-0.155} \text{ [keV]} \quad (5.10)$$

where B is the normalization factor. Using Eq. 5.10, the plot is shown in Fig. 5.7. The normalization B is 0.723 ± 0.014 with reduce chi-square $\chi^2_{\nu} = 151.6/14$ in the burst frame. The correlation coefficient is $R = 0.89$ with chance probability of 9.2×10^{-6} in the burst-rest frame. Thus, the correlation is very tight compared with that of the section 4.4.4.

Although Norris et al. 2000 and Hakkila et al. 2008 suggested that there is a good correlation between the spectral lag and the luminosity, we find that the spectral lag might have two parameters, for the luminosity (or E_{peak}) and the redshift. This result may indicate that luminosity evolution exists; the more distant GRBs are more luminous.

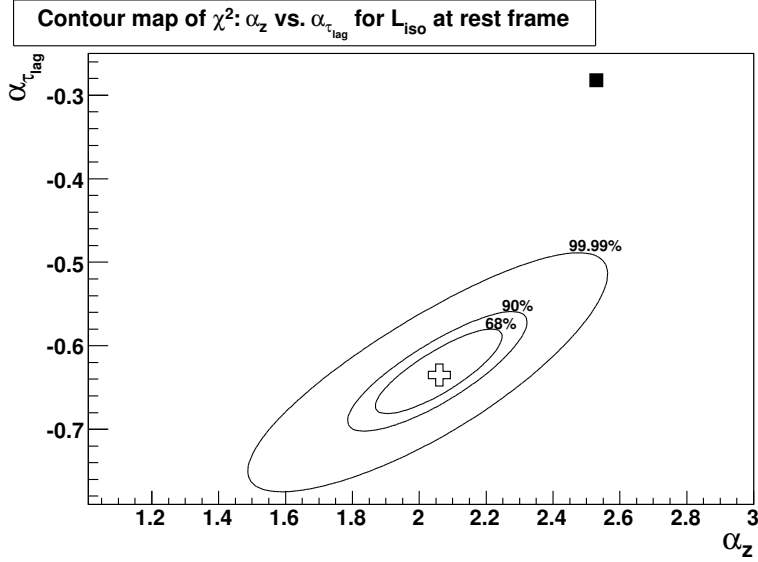


Figure 5.8: Contour map over a range of α_z and $\alpha_{\tau_{\text{lag}}}$ for L_{iso} in the burst-rest frame. The cross represents our lowest χ^2 (e.g. the best) value while the filled square represents the best-fit point of Tsutsui et al. 2008a. Each circle shows the 68%, 90%, 99.99% confidence region.

Best Indices for τ_{lag} and z

We have found that our *HETE* sample reproduces the redshift-dependent lag-luminosity relation in the previous section, and we seek the best-fit indices of the redshift and τ_{lag} using only the *HETE-2* sample.

We first seek the indices for L_{iso} ; the fitting function is,

$$L_{52} = C \times (1+z)^{\alpha_z} (\tau_{\text{lag}})^{\alpha_{\tau_{\text{lag}}}} \quad (5.11)$$

where C is the normalization factor and $\alpha_{\tau_{\text{lag}}}$ and α_z are the index of the redshift and spectral lag term, respectively. We change these values by a step of 0.005 for $\alpha_{\tau_{\text{lag}}}$ and 0.01 for α_z , respectively. Then we fit the function and calculate the corresponding χ^2 . The result is shown in Fig. 5.8 and the derived values at the lowest χ^2 are $(\alpha_{\tau_{\text{lag}}}, \alpha_z) = (-0.63 \pm 0.05, 2.06_{-0.20}^{+0.19})$. These values are slightly different from those of Tsutsui et al. 2008a (The best-fit point of Tsutsui et al. 2008a is presented as filled squares in Fig. 5.8). The derived function for L_{iso} is

$$L_{52} = (2.70 \pm 0.04) \times 10^{-2} (1+z)^{2.06_{-0.20}^{+0.19}} (\tau_{\text{lag}})^{-0.63 \pm 0.05} \quad (5.12)$$

For E_{peak} , we derive the best indices of $\alpha_{\tau_{\text{lag}}}$ and α_z , as well as the case of L_{iso} .

$$E_{\text{peak}} = D \times (1+z)^{\beta_z} (\tau_{\text{lag}})^{\beta_{\tau_{\text{lag}}}} \quad (5.13)$$

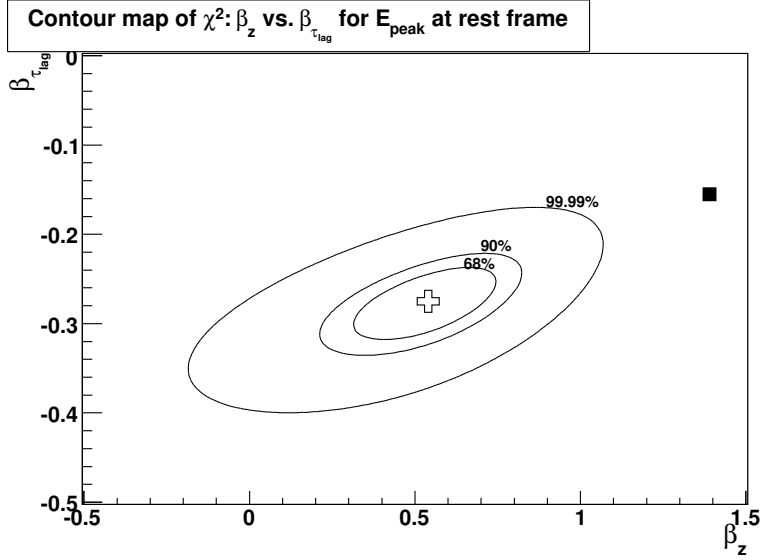


Figure 5.9: Contour map over a range of β_z and $\beta_{\tau_{\text{lag}}}$ for E_{peak} in the burst-rest frame. The cross represents our lowest χ^2 (e.g. the best) value while the filled square represents the best-fit point of Tsutsui et al. 2008a. Circles show the 68%, 90%, 99.99% confidence regions.

where D is the normalization factor and $\beta_{\tau_{\text{lag}}}$ and β_z are the index of the redshift and spectral lag term, respectively. The result is shown in Fig. 5.9 and the derived values at the lowest χ^2 are $(\beta_{\tau_{\text{lag}}}, \beta_z) = (-0.28 \pm 0.04, 0.54^{+0.21}_{-0.20})$. Thus the derived function for E_{peak} is

$$E_{\text{peak}} = (46.7 \pm 0.9) (1+z)^{0.54^{+0.21}_{-0.20}} (\tau_{\text{lag}})^{-0.28 \pm 0.04} \quad (5.14)$$

From the value of $\alpha_{\tau_{\text{lag}}}$ (-0.58), the expected value of $\beta_{\tau_{\text{lag}}}$ is $-0.58/1.8 \sim -0.3$ from the requirement of the Yonetoku relation ($L \propto E_{\text{peak}}^{1.8}$), which is in good agreement with the obtained value (-0.28 ± 0.04) within the 1σ confidence level. Similarly, from the value of α_z (2.06), the expected value of β_z is $2.06/1.8 \sim 1.1$, which is marginally consistent with the obtained value within the 99.99% confidence level. We find that the derived redshift-dependent lag-luminosity relation is consistent with the redshift-dependent lag- E_{peak} relation via the Yonetoku relation .

Tsutsui et al. 2008a calculated the spectral lags not from the pulse fit but from the CCF. Although the CCF is a good way to measure the delay of GRB emission, the CCF has the weaknesses that, (1) if GRB pulses consists of multi spikes, the greatest contribution to the CCF lag is found to come from the shortest-lag, highest-intensity pulses. In fact, the CCF lag appears to be insensitive to the presence of longer lag pulses. (2) Since decomposition of pulses is very hard, we can only calculate the lag of the entire

burst, not each pulse if we adopt CCF method. (3) Hakkila et al. 2008 reported that GRB spectral lags are “pulse” rather than “burst” properties. In this analysis, we have fitted each pulse separately using the pulse-fit model and found the differences between our best-fit value and that of Tsutsui et al. 2008a in Fig. 5.8. Thus the differences are expected to come from the such properties. Now, we verify that the redshift-dependent lag-luminosity relation is consistent with not only *bursts* but also *pulses*.

Origin of the Evolution with redshift

The redshift-dependent lag-luminosity relation indicates that luminosity evolution exists. The luminosity evolutions $(1+z)^{1.4\pm 0.5}$, $(1+z)^{2.5\pm 0.1}$ and $(1+z)^{2.60^{+0.15}_{-0.20}}$ are suggested by Lloyd-Ronning et al. 2002, Wei & Gao 2003 and Yonetoku et al. 2004 with the BATSE GRB data, respectively, and furthermore such evidence was found by Salvaterra et al. 2008 with the *Swift* GRB data. The luminosity evolution possibly comes from, (1) the jet-corrected luminosity increases with redshift, and (or) (2) the jet-opening angle is narrowly collimated with redshift.

For the first case, we consider GRB progenitors based on the collapsar model (MacFadyen & Woosley 1999). In the high-redshift (early) universe, the stellar temperature was probably higher than that at the present time, because the temperature of the cosmic background was higher in the early universe due to the cosmic expansion, the metallicity was lower (metals are created by the activity of supernovae and in the early universe most stellar gas and progenitor should be poor-metal because there has been few supernovae, which in turn means that the composition with the high (low) metallicity makes the stellar gas cool efficiently (inefficiently) and the average temperature was high). An indication of the stellar mass is given by Jeans mass

$$M_J \propto T^{3/2} \rho^{-1/2} \quad (5.15)$$

where T is the temperature and ρ is the density of the stellar gas. The Jeans mass increases as the density ρ decreases and the temperature T increases. Furthermore, for the metal-poor situation, the mass-loss rate (e.g. stellar wind) is likely to be significantly smaller before the collapse occurs (Ramirez-Ruiz et al. 2001). Thus, the higher-redshift GRB progenitors can retain higher mass. The more massive progenitors are likely to produce the more powerful GRBs, although the relation between the progenitor mass and brightness of GRBs is not trivial. From the point of view of the jet-corrected luminosity evolution, evolution is a key to the history of metallicity and GRB progenitors.

For the second case, the narrowness of the collimated jet depends on the redshift. Assuming that GRBs are the same luminosity, larger (smaller) opening angles give smaller

(larger) isotropic equivalent luminosities. Actually, the evidence for the jet evolution of $\theta_j \propto (1+z)^{-0.45}$ is suggested by Yonetoku et al. 2005. If the narrowness is associated with the progenitor mass and the metallicity (e.g. the more massive star produces a narrowly collimated jet), the jet-corrected luminosity evolution and jet-angle evolution might be highly coupled. For this sample of *HETE-2* GRBs, the opening angles were not observed as jet breaks. Thus, we can not discuss the evidence of the jet evolution in detail.

Furthermore, the derived E_{peak} evolution of $E_{\text{peak}} \propto (1+z)^{0.54^{+0.21}_{-0.20}}$ is in good agreement with that of $E_{\text{peak}} \propto (1+z)^{0.76 \pm 0.07}$ by Wei & Gao 2003. As the E_{peak} corresponds to the minimum electron energy, from Eq. 2.32 we have

$$E_{\text{peak}} \propto B\gamma_e^2\Gamma \quad (5.16)$$

Thus, the E_{peak} evolution indicates that one, two or all of B , γ_e and Γ depend(s) on the redshift. These parameters seem to be determined by the shock condition of the emitted outflows from the central engine (e.g. black hole generated after the core collapse). If the activity of the central engine reflects the properties of the progenitor and the surrounding environment, such as the metallicity, the emitted outflow and its shock condition possibly determines the parameters B , γ_e and Γ .

In this thesis, although evolution with redshift has been suggested, we cannot insist that there exists strong evidence of evolution with redshift. So we do not mention this further in our discussion.

Selection Effect

If the derived parameters (e. g., L_{iso} , τ_{lag}) are near the detection threshold, there is a possibility that the obtained correlation comes from a selection effect. To estimate the selection effect, we draw the line of the selection effect in our plot of the Tsutsui relation in Fig. 5.10. The solid line represents the boundary of $\tau_{\text{lag}} = 0.01$ s and the area below the line corresponds to the unobservable region. Similarly the dashed and long dashed lines represent the boundaries of $\tau_{\text{lag}} = 0.1$ s and 1 s assuming the minimal detectable flux is 1×10^{-7} erg cm $^{-2}$ s $^{-1}$ which is a conservative flux when for a dim GRB detected by the *HETE* FREGATE instrument. The filled triangles represent lower limits of the expected L_{iso} for the corresponding GRB. The boundary of τ_{lag} is highly dependent on the pulse shape and the statistics of the burst photons. Generally, a high luminosity burst has a short and sharp pulse shape leading to the better precision in determining τ_{lag} , while a low luminosity burst has a long and broad pulse shape leading to worse precision in determining τ_{lag} . High luminosity and small- τ_{lag} GRBs exist in the right side of Fig. 5.10, and their limits are almost comparable to the line between $\tau_{\text{lag}} = 0.01$ s and 0.1s.

Similarly low luminosity and large- τ_{lag} GRBs exist in the left side of Fig. 5.10, and their limits are almost comparable to the line between $\tau_{\text{lag}} = 0.1$ s and 1 s.

As the lower limits for some GRBs are separated from the obtained values by only an order of magnitude, the selection effect cannot be ignored in our results. However the difference between the obtained value and its lower limit is substantial for other GRBs and the effect seems not to be serious. Furthermore, as the Yonetoku relation and Amati relation also involve the same problem, ours are not the only result that suffers from selection effects.

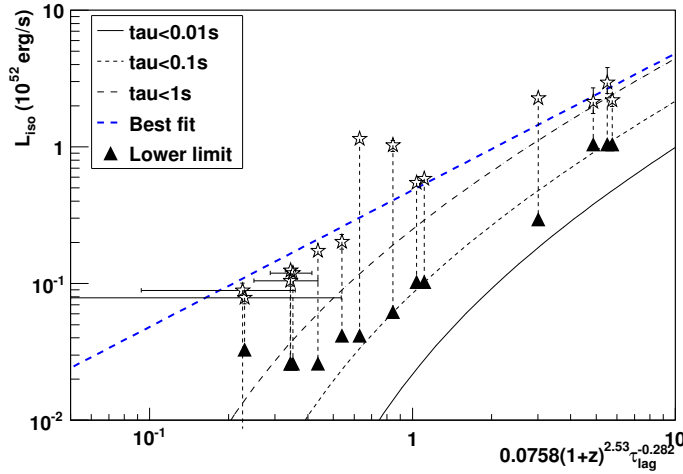


Figure 5.10: Selection effect in the derived Tsutsui relation. The solid line represents a boundary of $\tau_{\text{lag}} = 0.01$ s assuming the minimal detectable flux is 1×10^{-7} erg cm $^{-2}$ s $^{-1}$. Similarly the dashed and long dashed lines represent the boundaries of $\tau_{\text{lag}} = 0.1$ s and 1 s. The filled triangles represent the lower limits to the expected L_{iso} for the corresponding GRB. The blue line represents the best-fit function.

5.3 Detailed Energy Dependence of Spectral lag and Other properties

Next we consider the detailed energy dependence of the spectral lag and other properties (the durations including the rise and decay times, the low-energy photon index, L_{iso} and E_{peak}), besides the lag-luminosity relation described above.

We show the scatter plots of α_{lag} versus other properties in Fig. 5.11. (L_{iso} , E_{peak} , α_{FWHM} , α_{rise} , α_{dec} and α_{photon} , where α_{lag} , α_{rise} , α_{dec} and α_{photon} are the power-law indices of τ_{lag} , $\Delta\tau_{\text{r}}$ and $\Delta\tau_{\text{d}}$ as a function of energy and the low-energy photon index of the

fitted spectrum, respectively.) All the panels of Fig. 5.11 show there are no significant correlations between α_{lag} and the other parameters because the power-law indices have large uncertainties due to uncertainties in the determination.

For the plot of α_{lag} versus L_{iso} and α_{lag} versus E_{peak} shown in the top left and top right panels of Fig. 5.11, the larger α_{lag} seems to give the larger L_{iso} and larger E_{peak} , and the correlation coefficients are $R = 0.19 \pm_{-0.21}^{+0.22}$ and $0.29 \pm_{-0.19}^{+0.14}$, respectively. Thus, we cannot find strong evidence of the correlation as opposed to Sec. 4.4.3 and 4.4.4. This is because dividing into multiple energy bands makes the count statistics in the corresponding energy band poor and gives a poor determination of α_{lag} .

For the other parameters (α_{FWHM} , α_{rise} , α_{dec} and α_{photon}), there is no characteristic structure as well and α_{lag} ranges from -0.6 to -0.1. Zhang et al. 2007 also studied the dependence of the temporal properties of GRBs detected by BATSE and they showed that the value of α_{lag} is -0.27 ± 0.45 which is consistent with our result, implying that the energy dependence of these temporal properties is different for different bursts.

5.3.1 Energy Dependence of Duration, Rise and Decay phase

Zhang et al. 2007 studied the dependence of temporal properties (α_{FWHM} , α_{rise} , α_{decay}) and they found that α_{FWHM} and α_{dec} are highly correlated, while α_{FWHM} and α_{rise} , α_{FWHM} and α_{rise} are not strongly correlated. From the theoretical point of view described in Sec. 2.4, the rise phase timescale is responsible for the intrinsic pulse width (which is associated with the shock mechanism) while the decay phase timescale is responsible for the geometrical effect from the relativistic expanding shell. Furthermore, the decay time interval dominates the duration (FWHM) because the typical pulse shape is a fast rise and exponential decay (FRED). Thus, it is natural that the decay phase is highly dependent on the duration and the rise phase is not strongly related to the duration time (or decay time). So the result of Zhang et al. 2007 is valid for the theoretical model.

The top panel of Fig. 5.12 shows the scatter plot of α_{FWHM} versus α_{rise} in our *HETE* sample. Although the confidence level of each point is very large, we find a marginal linear relation with the correlation coefficient $R = 0.51 \pm_{-0.38}^{+0.18}$. The best-fit function is $\alpha_{\text{rise}} = (0.04 \pm 0.15) + (1.06 \pm 0.41)\alpha_{\text{FWHM}}$. If the rise timescale is determined only by the hydrodynamical effect, the data points should be distributed independently of the duration. However, from this result α_{FWHM} seems to be roughly proportional to α_{rise} and the rise timescale depends not only on the hydrodynamical effect but also somewhat on the curvature effect. The middle panel of Fig. 5.12 shows the scatter plot of α_{FWHM} versus α_{dec} . The best-fit function is $\alpha_{\text{dec}} = (-0.01 \pm 0.13) + (1.03 \pm 0.37)\alpha_{\text{FWHM}}$ with the correlation coefficient $R = 0.67 \pm_{-0.37}^{+0.13}$. As a relatively good proportionality between α_{FWHM}

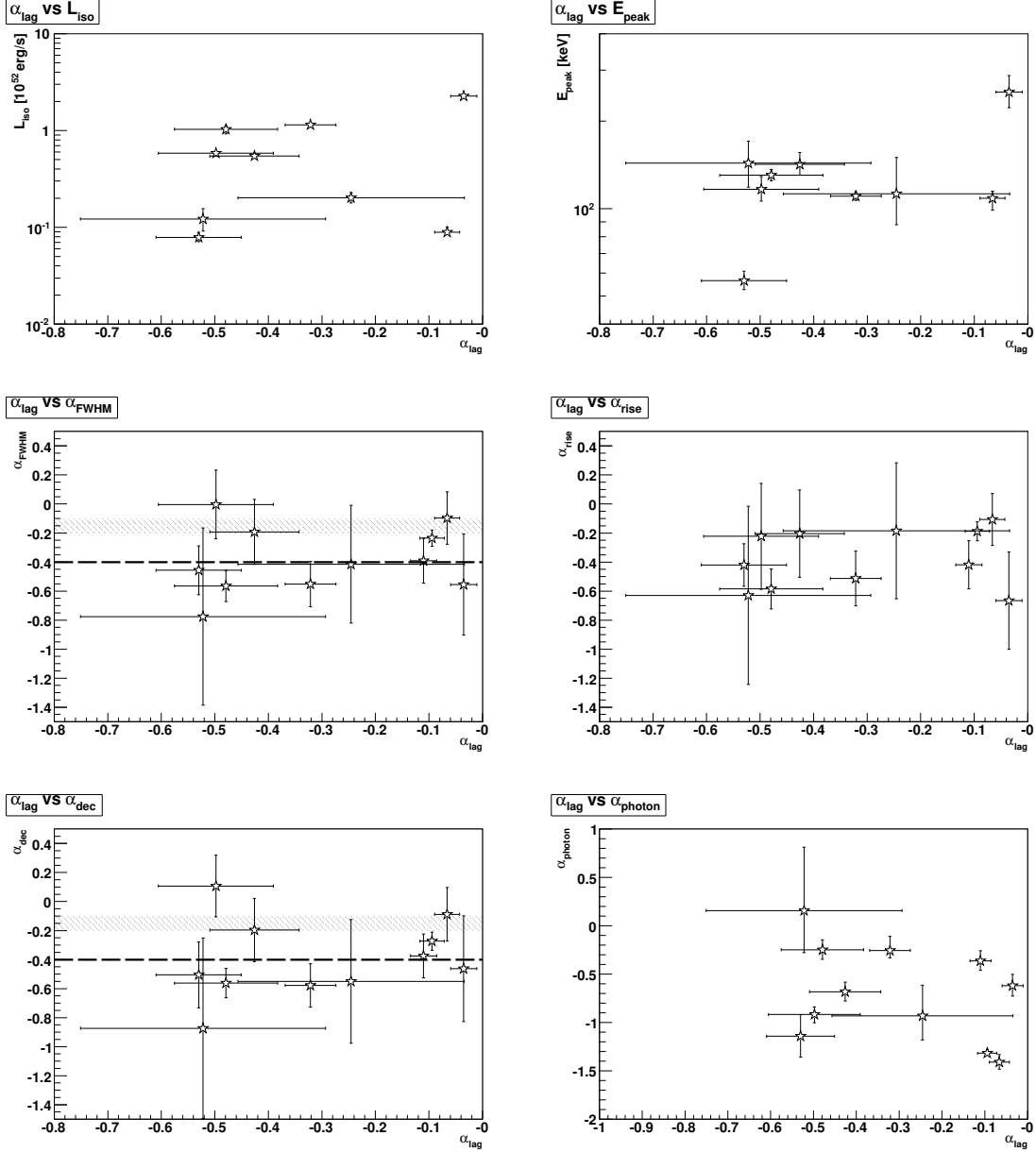


Figure 5.11: The Scatter plots of α_{lag} and α_{FWHM} , α_{rise} , α_{dec} , α_{photon} . The shaded area and dashed line represent the expected values from the simple curvature and hydrodynamical effects, respectively.

and α_{dec} exists, we find that this result supports the above interpretation (the curvature effect determines the decay timescale). The bottom panel of Fig. 5.12 shows the scatter plot of α_{rise} versus α_{dec} . The best-fit function is $\alpha_{\text{dec}} = (-0.04 \pm 0.13) + (0.99 \pm 0.40)\alpha_{\text{rise}}$ with the correlation coefficient $R = 0.46^{+0.20}_{-0.38}$. The result also seems to tell us that the rise timescale is somewhat dependent on the curvature effect because of the weak evidence of a linear relationship between α_{rise} and α_{dec} .

Although the uncertainties in the correlation coefficient and fitting parameters are

large, the relationships between α_{FWHM} , α_{rise} and α_{dec} are consistent with those of Zhang et al. 2007 (the three functional forms agree). Concerning only the result in Fig. 5.12, we do not know that what effect determines the timescale for the rise and decay phases, especially for the rise phase.

In addition, Shen et al. 2005 computed the temporal profiles of the GRB pulse in the four BATSE energy bands, with the relativistic curvature effect of an expanding fireball. They included an intrinsic ‘‘Band’’ shape spectrum and an intrinsic energy-independent emission profile, and they estimated the dependence of the duration and other properties on energy. They showed that the calculated energy dependence of the duration was $w_{\text{FWHM}} \propto E^{-0.1 \sim -0.2}$ ($\alpha_{\text{FWHM}} \simeq \alpha_{\text{dec}} = -0.1 \sim -0.2$). On the other hand, the energy dependence due to the hydrodynamical effect assuming a highly non-uniform distribution of the Lorentz factor with a simple approach (see Sec. 2.4.3) was calculated by Daigne & Mochkovitch 1998 and the its dependence is $w_{\text{FWHM}} \propto E^{-0.4}$.

In our result shown in Fig. 5.12, α_{FWHM} and α_{dec} range from -0.8 to 0 and the expected energy dependences for the hydrodynamical effect and the curvature effect are represented as a long dashed line and a shaded portion, respectively (the same as in Fig. 5.11). The curvature effect can explain the energy evolution of the temporal properties for $\alpha_{\text{FWHM}} \simeq \alpha_{\text{dec}} > -0.2$. However, the data points are scattered for α_{FWHM} and $\alpha_{\text{dec}} < -0.2$ and the curvature effect alone cannot explain these points. Here the hydrodynamical effect (in this case $\alpha_{\text{FWHM}} \simeq \alpha_{\text{dec}} = -0.4$ with the simple model) can explain the plots around $\alpha_{\text{FWHM}} \simeq \alpha_{\text{dec}} \simeq -0.4$. But these values are likely to be scattered below $\alpha_{\text{FWHM}} \simeq -0.4$, which indicates that the simple hydrodynamical model cannot reproduce all of the observational results and new hydrodynamical models which include the properties of the large energy-dependence of the duration ($\alpha_{\text{FWHM}} < -0.4$) are needed.

5.3.2 Validity of the Curvature Effect on the Spectral Lag

Liang et al. 2006 studied the spectral and temporal properties of XRF 060218, which has the longest pulse duration ($T_{90} \sim 2000\text{s}$) and spectral lag ($\sim 600\text{ s}$) observed to date, in the 0.3 – 150 keV band. Although they found that $\alpha_{\text{lag}} = -0.25 \pm 0.05$, they did not treat the origin of the spectral lag.

In this section, we try to clarify the origin of the spectral lag of our *HETE* GRBs, apart from the lag-luminosity relation described in Sec. 5.1. Here we adopt the model suggested by Lu et al. 2006. They calculated the contribution to the spectral lag of the curvature effect of fireballs for the observer viewing the shell head-on, the so-called *on-axis* model, (for more detail, see appendix D) and demonstrated that the spectral lag has a energy dependence ($\text{lag} \propto E$) below a saturated energy, E_s , shown in Fig.

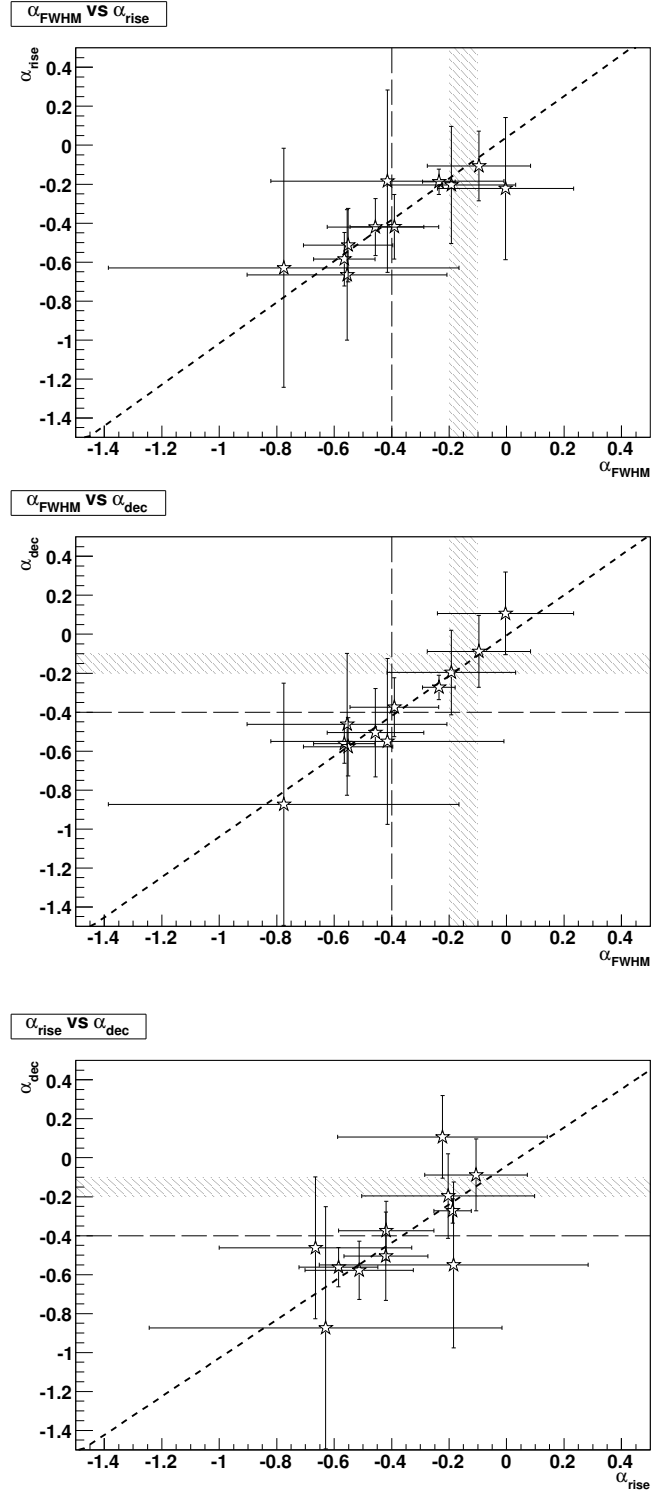


Figure 5.12: The scatter plots for indices of α_{FWHM} , α_{rise} and α_{dec} . (*Top*): α_{FWHM} vs. α_{rise} , (*Middle*): α_{FWHM} vs. α_{dec} , (*Bottom*): α_{rise} vs. α_{dec} . The dashed line shows the best-fit linear function. The shaded area and long dashed line represent the expected values from the simple curvature and hydrodynamical effects, respectively.

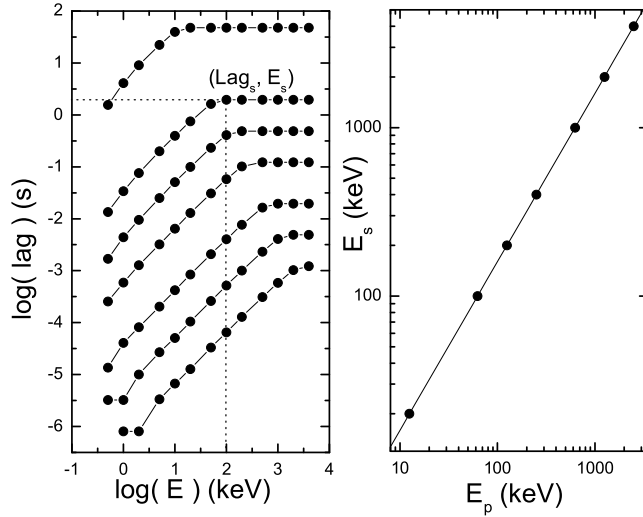


Figure 5.13: Theoretical relationship between the lag and the lower energy limit E of the corresponding high energy channel for different Γ (the left panel) and that between E_s and E_{peak} (the right panel), where the $\alpha = -1$, $\beta = -2.25$ with different E_{peak} . Solid lines from the top to the bottom in the left panel stand for $\Gamma = 10, 50, 100, 200, 500, 1000, 2000$, respectively. The solid line in the right panel is the linear fit one of the calculated data. (Lu et al. 2006)

5.13. In their calculation, the intrinsic spectral shape is a typical Band function with $\alpha = -1$, $\beta = -2.25$ and the lags are defined as the time delay between 0.2–0.4 keV and 0.5–1 keV, 1–2 keV, 2–4 keV, 5–10 keV, 10–20 keV, 20–40 keV, 50–100 keV, 100–200 keV, 200–400 keV, 500–1000 keV, 1000–2000 keV, 2000–4000 keV and 4000–8000 keV. The other parameters are the shell radius $R_c = 3 \times 10^{15}$ cm, and the intrinsic pulse width $\Delta t_{\theta,FWHM} = 10^5$ s in the source frame (Note that for the intrinsic pulse width Doppler boosting is not taken into account and the observer-timescale width is expressed as $\Delta t_{\theta,FWHM}/\Gamma^2$).

The relationship between the lag and the corresponding energy E (here E denotes the lower energy limit of the corresponding high-energy band) is presented in the left panel of Fig. 5.13. According to the Doppler effect, the amount of energy at $E > E_{\text{peak}}$ would mainly come from the area of the fireball surface around the line of sight, i.e., $\theta \sim 0$ (where θ is the angle to the line of sight). When $E > E_{\text{peak}}$, the contribution to the corresponding light curve largely comes from the high-energy portion of the rest frame spectrum, which causes the peak time of the light curve to change less, and the lag would saturate. Thus the saturated energy E_s is proportional to the corresponding peak energy

E_{peak} ($E_s \propto E_{\text{peak}}$). On the other hand, when $E \ll E_{\text{peak}}$, the contributions come only from the low-energy portion of the rest frame spectrum, emitted from the “whole” fireball surface, i.e., $0 \leq \theta \leq \pi/2$. Thus there would be almost no lag between the light curves of these two energy bands. The schematic concept of the origin of the lag caused by the curvature effect is shown in Fig. 5.14.

We choose the start time at the lowest energy (2 keV) arbitrarily to match the observational value of t_{peak} , and the spectral lag τ_{lag} is described as

$$\tau_{\text{lag}} = aE \quad (5.17)$$

where a is the normalization of the lag at the lower energy, which depends on the Lorentz factor of the relativistic shell Γ . Then t_{peak} is written as

$$t_{\text{peak}} = t_0 - \tau_{\text{lag}} = t_0 - aE \quad (5.18)$$

where t_0 is the start time. Using Eq. 5.18, we superimpose the expected lines from the curvature effect on our plots of t_{peak} versus E with different Lorentz factors. Note that the spectral lags are highly dependent on the Lorentz factor, $\text{Lag} \propto \Gamma^{-2}$ (Lu et al. 2006).

The superimposed figures are Fig. 5.15 and 5.16. Here, the energy is translated into the burst-rest-frame energy with known redshifts, and for GRB030725 and GRB060121 without known redshifts assuming that their redshifts are 1. By adopting the appropriate Γ we can reproduce the temporal-lag evolution for $\sim 60\%$ of the examined pulses with the curvature effect (see Fig. 5.15). But for the other GRBs the curvature model cannot describe the temporal-lag evolution well (e.g., GRB 021211, the 2nd pulse of GRB040924, the 2nd pulse of GRB050408 and GRB030725) for any Γ (see Fig. 5.16). In addition, to examine if the temporal evolutions of the duration and spectral lag are explained synthetically by either the curvature or hydrodynamical effect, we summarize the results of the estimated Γ , α_{FWHM} and other properties in table 5.1. From table 5.1, it is not clear if the GRBs, which can be explained by the curvature effect for the spectral lag, can be well explained by the curvature effect for the duration ($\alpha_{\text{FWHM}} = -0.2 \sim -0.1$ for the curvature effect) because of the confidence level of α_{FWHM} . Conversely, we can say that within the 1σ confidence level the model based on the curvature effect can explain the temporal evolution of both the spectral lag and duration roughly. In addition, the w_{model} in the table 5.1 roughly corresponds to the pulse duration expected by the curvature model. (it is a good indicator to estimate the order of magnitude of the expected duration). As the observed duration is consistent with that expected by Lu et al. 2006 to within a factor of 2 or 3, the value of the intrinsic pulse width ($\Delta t_{\theta, \text{FWHM}} = 10^5$ s) seems to be valid.

Since in this analysis only a finite energy range (2–400 keV) is available, there are only a small number of points for the energy range where the lag is saturated above E_s

($\sim E_{\text{peak}}$). For many GRBs, we could only plot 1 point above E_s ($\sim E_{\text{peak}}$), which leaves the possibility that a significant lag takes place above E_s (a saturated energy might not exist). Even in the study by Liang et al. 2006, although the peak energy is $E_{\text{peak}} \sim 54$ keV, they also could plot only one point for t_{peak} above E_{peak} due to the poor effective area for the higher-energy ranges. To clarify the origin of the spectral lag further, we need to detect GRB photons in the higher-energy ranges above E_{peak} to describe the light curve and determine t_{peak} with confidence.

From the spectral lag analysis in a finite-energy range, we have found that some GRBs cannot be explained by the curvature effect and the hydrodynamical effect should play a quite important role in the temporal lag and duration evolution. Moreover, theoretical studies must progress for further understanding. Some models have been proposed by Daigne & Mochkovitch 1998, Daigne & Mochkovitch 2003 and Bosnjak et al. 2008. But these are highly dependent on the shock condition or initial parameters, which is outside the scope of this thesis.

Table 5.1: Summary of the temporal evolution of the duration and spectral lag as a function of energy

GRB	Γ	α_{FWHM}	w_{obs} [s]	w_{model} [s]
010921	30	-0.11 ± 0.18	21.4 ± 2.9	13.6
020127	500	-0.67 ± 0.34	0.70 ± 0.01	0.40
030528 (1st pulse)	50	-0.63 ± 0.61	26.1 ± 14.7	40.0
030528 (2nd pulse)	30	-0.42 ± 0.15	58.8 ± 6.8	111.1
040924 (1st pulse)	160	-0.18 ± 0.47	1.8 ± 0.5	3.9
050408 (1st pulse)	110	-0.20 ± 0.30	2.8 ± 0.2	8.3
060121	150	-0.42 ± 0.17	1.8 ± 0.2	4.4
021211	-	-0.58 ± 0.14	2.4 ± 0.1	-
030725	-	-0.18 ± 0.07	19.7 ± 0.5	-
040924 (2nd pulse)	-	-0.51 ± 0.19	1.4 ± 0.1	-
050408 (2nd pulse)	-	-0.22 ± 0.36	2.0 ± 0.2	-

Note that Γ is estimated by the lag analysis in Fig. 5.15 and w_{obs} is the observed duration in the rest frame and w_{model} is $\Delta t_{\theta, \text{FWHM}} / \Gamma^2$ where $\Delta t_{\theta, \text{FWHM}} = 10^5$ s.

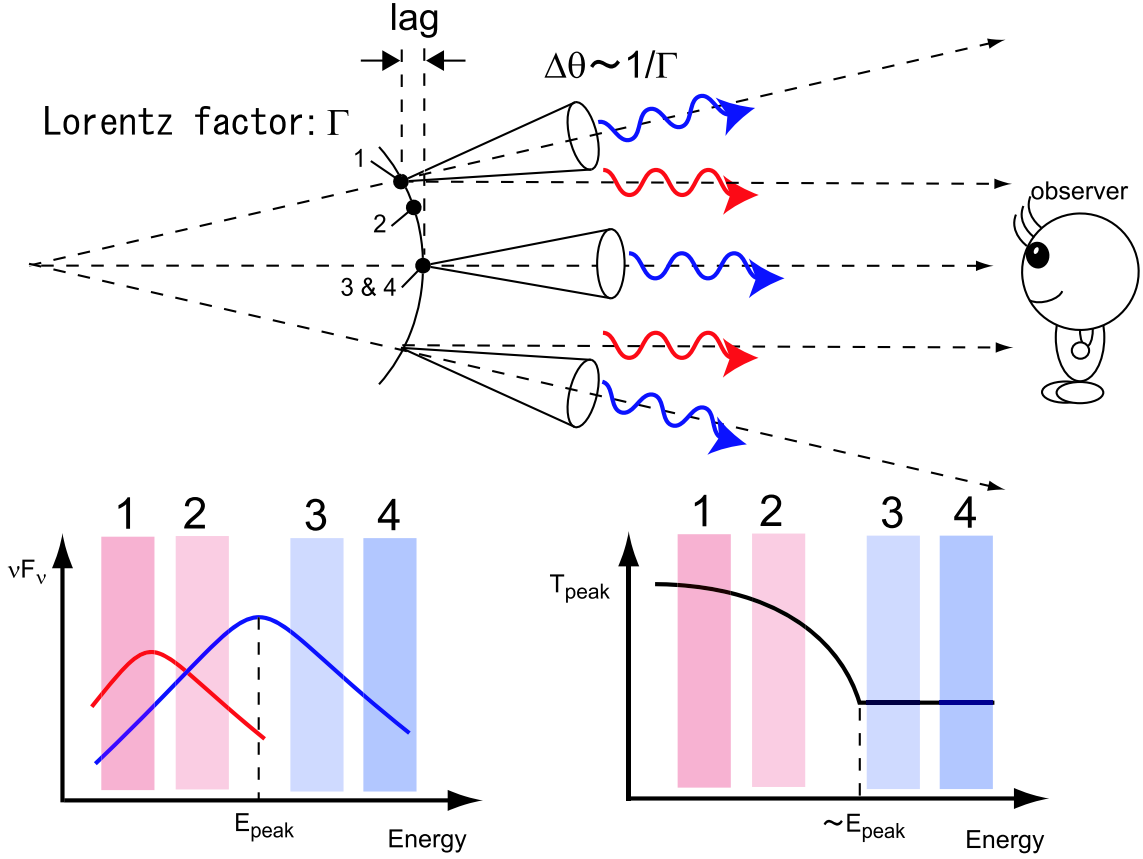


Figure 5.14: Schematic view of the spectral lag by curvature effect. The shell moves toward the observer at Lorentz factor Γ . The photons having the intrinsic Band functional shape are emitted from the shell simultaneously. Due to the beaming effect, the photons are confined within a cone ($\Delta\theta \sim 1/\Gamma$). Because the velocity of light is finite and the shell has a curvature, a spectral lag occurs. At points 3 and 4, the observer sees the photons from the line-of-sight cone (presented as blue photons) and then a significant lag is not observed above the saturated energy $E_s \sim E_{\text{peak}}$. From the high-latitude of the shell (e.g. at points 1 and 2), the comparatively weak-Doppler-shifted photons (presented as red photons) are observed. In the energy bands 1 and 2 the photons come from the whole surface of the shell, and the spectral lag is small. The largest lag is between energy bands 1 and 3 (or 4).

5.4 Towards an Unified Theory

We have found that the obtained lag-luminosity - E_{peak} -duration relations are well explained by the off-axis model suggested by Ioka & Nakamura 2001. Furthermore, by introducing the systematic uncertainty ($\sigma_{\text{lag}} = 0.05$ s), the Yonetoku relation is consistent with the obtained relations.

In addition, apart from the above relations, we have considered the origin of the spectral lag and duration for *individual* GRB pulses using the simple theoretical model based on the curvature effect suggested by Lu et al. 2006 (the so-called on-axis model). As a result, although for $\sim 60\%$ of the examined pulses the curvature effect can reproduce the lag evolution as a function of energy, the other GRB pulses cannot be explained by the curvature effect and other effects must be taken into account (e.g., the hydrodynamical effect). Furthermore, the off-axis model (Ioka & Nakamura 2001) is not compatible with the on-axis model suggested by Lu et al. 2006, because, e.g., for the on-axis model the effect caused by viewing with an off-set angle to the axis of the emission cone ($\theta = 0$ axis) is not taken into account and for the off-axis model the detailed energy-dependent characteristics are not clearly revealed.

For an unified theory to explain the spectral lag and other temporal spectral characteristics, the effect of the curvature, viewing with an offset angle to the shell and hydrodynamical effect (and redshift evolution of the physical parameters ?) synthetically must be taken into account and theoretical work must be done. To have further quantitative discussions, we need a sample which includes many GRBs having a good S/N ratio detected in a wide band (keV–GeV) with observationally known redshifts.

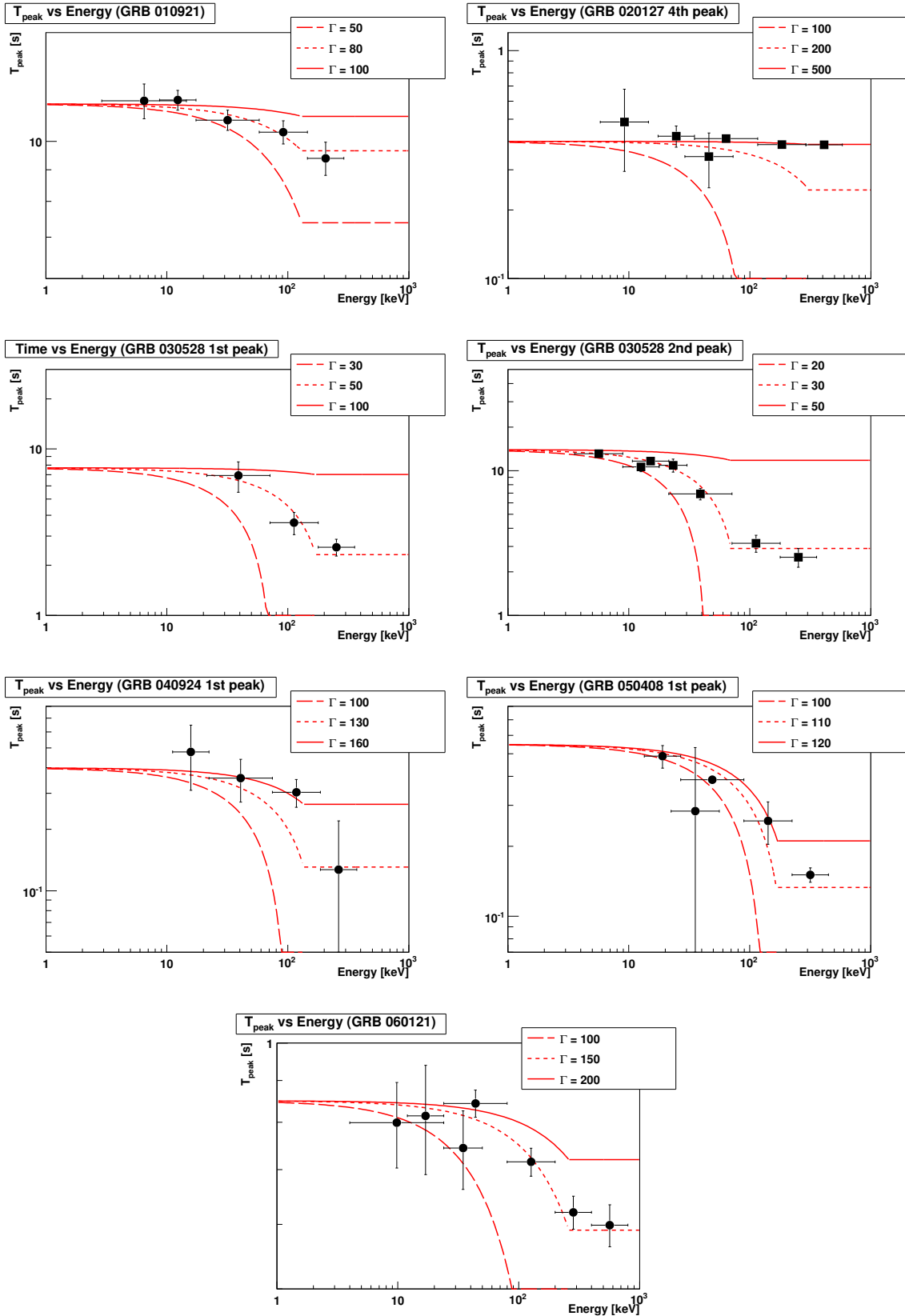


Figure 5.15: Energy vs T_{peak} plots with the theoretical model, showing good agreement with the curvature case. Each line represents the curvature-effect line at the corresponding Γ .

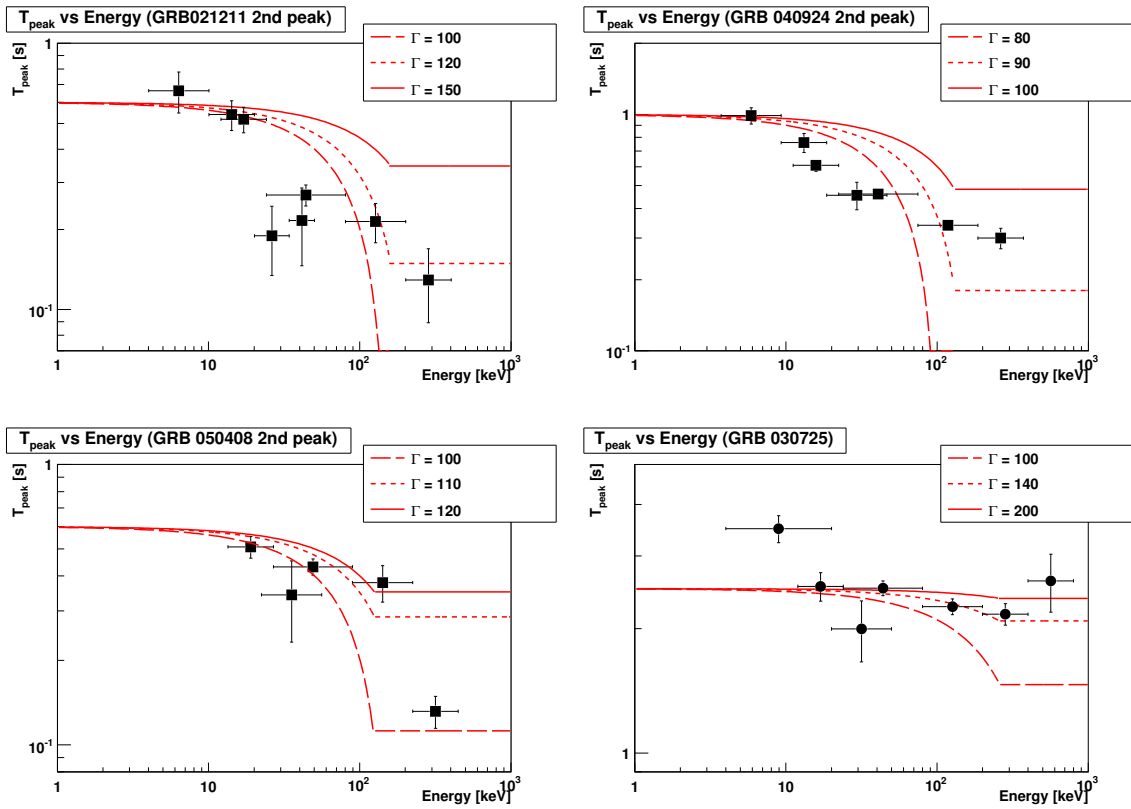


Figure 5.16: Energy vs T_{peak} plots with the theoretical model, showing poor agreement with the curvature case. Each line represents the curvature-effect line at the corresponding Γ .

Chapter 6

GRB 080916C detected by *Fermi*

6.1 Detection & Observation

GRB 080916C was detected by the GBM on the *Fermi* observatory on September 16 2008 at 00:12:45.6 UT (T_0). GRB080916C produced large signals in nine of the twelve NaI-crystal detectors and in one of the two BGO-crystal detectors. The localization was found to be RA = $08^h07^m12^s$, Dec = $-61^\circ18'00''$ (Goldstein & van der Horst 2008), with an uncertainty of 2.8° at $1-\sigma$ confidence level.

At the trigger time, the position of the GRB was $\sim 48^\circ$ away from the axis of the LAT boresight and on-ground analysis revealed a bright source consistent with the GRB position.

Follow-up X-ray and optical observations revealed a fading source (afterglow) by the Swift XRT (Perri et al., 2008) and the Gamma-Ray burst Optical/Near Infrared Detector (GROND), consistent with the LAT localization (Clemens et al., 2008). From the GROND observation, the redshift of the GRB was determined to be $z = 4.24 \pm 0.26$ (Greiner et al. 2008). The X-ray light curve of the afterglow from $T_0 + 61$ ksec to $T_0 + 1306$ ksec shows two temporal breaks at about 2 and 4 days after the trigger (Stratta et al. 2008).

This GRB is the first burst which has a lot of the high-energy photons (>100 MeV) detected since the launch of *Fermi*. The light curves of the GBM and LAT detectors are shown in Fig. 6.1, sorted from top to bottom in order of increasing energy. In the case of LAT, after applying the standard selection cuts (the events from the chosen Region of Interest, ROI, and rejection of charged particles etc.) to extract reliable directional and energy information, more than 100 events above 20 MeV were detected. In particular, the bottom panel of the Fig. 6.1. shows 14 events in total with energies greater than 1 GeV (the highest energy of the photons is $13.2_{-1.5}^{+0.7}$ GeV during the interval of d).

The light curves with different energies show that first the spiky pulse become promi-

ment and then the persistent emission lasts until $\sim T_0 + 80$ s.

6.2 Time resolved spectral analysis of the overall burst

To first determine the overall spectral characteristics of the GRB, we perform simultaneous spectral analysis of the GBM and LAT for each of the five time bins shown in Fig 6.1. The results are shown in Tab. 6.2 and Fig. 6.3. Here, for the time interval of the background, we adopt an interval $T_0 + 100$ s to $T_0 + 200$ s where there is no significant emission from the burst.

For the interval a , the low-energy photon index α is relatively small which means the amount of the low-energy photons is deficient and β is small which means the amount of high-energy photons is also deficient. After the 1st interval, no significant evolution appears in either α and β . The value E_{peak} of the second time interval b (~ 1400 keV) is larger than that of the first interval a (~ 500 keV). The values of E_{peak} decrease as time progresses, which means that there is soft to hard evolution from the first interval a to the second interval b , and then hard to soft evolution after the second interval b . It is striking that E_{peak} especially for the second time interval b is very high while the typical value is ~ 100 keV.

Table 6.1: Fit parameters for the Band function for GRB 080916C

Time range [s]	E_{peak} [keV]	α	β	Flux $^\diamond$ [10^{-6} ergs cm^{-2} s^{-1}]	L_{iso} † [10^{51} erg s^{-1}]
a (0.0 to 3.6)	506_{-25}^{+43}	$-0.60_{-0.05}^{+0.03}$	$-2.76_{-0.13}^{+0.09}$	$5.15_{-0.24}^{+0.27}$	1027_{-48}^{+54}
b (3.6 to 7.7)	1382_{-131}^{+255}	$-1.01_{-0.03}^{+0.02}$	$-2.34_{-0.05}^{+0.03}$	$8.81_{-0.57}^{+0.49}$	1758_{-113}^{+98}
c (7.5 to 15.9)	744_{-117}^{+164}	$-1.02_{-0.04}^{+0.04}$	$-2.24_{-0.04}^{+0.04}$	$2.99_{-0.20}^{+0.26}$	597_{-40}^{+52}
d (15.9 to 54.8)	505_{-38}^{+41}	$-0.92_{-0.02}^{+0.03}$	$-2.32_{-0.02}^{+0.02}$	$2.11_{-0.07}^{+0.07}$	420_{-14}^{+14}
e (54.8 to 100.9)	219_{-46}^{+79}	$-0.78_{-0.15}^{+0.17}$	$-2.17_{-0.04}^{+0.03}$	$3.17_{-0.22}^{+0.24} \times 10^{-1}$	$63.2_{-4.4}^{+4.8}$
a-e (0.0 to 100.9)	521_{-35}^{+39}	$-0.90_{-0.02}^{+0.02}$	$-2.29_{-0.02}^{+0.02}$	$1.63_{-0.05}^{+0.05}$	325_{-10}^{+10}

$^\diamond$: the flux is calculated between 1 keV to 10 MeV in the observer's frame

† : the luminosity is calculated in the same energy range as the flux assuming that the corresponding luminosity distance $d_L = 1.26 \times 10^{29}$ cm for $z = 4.2$.

An additional high-energy component for each time interval cannot be found and no significant excess appears because the Band function is consistent with the high-energy range (\sim GeV) as shown in Fig. 6.3.

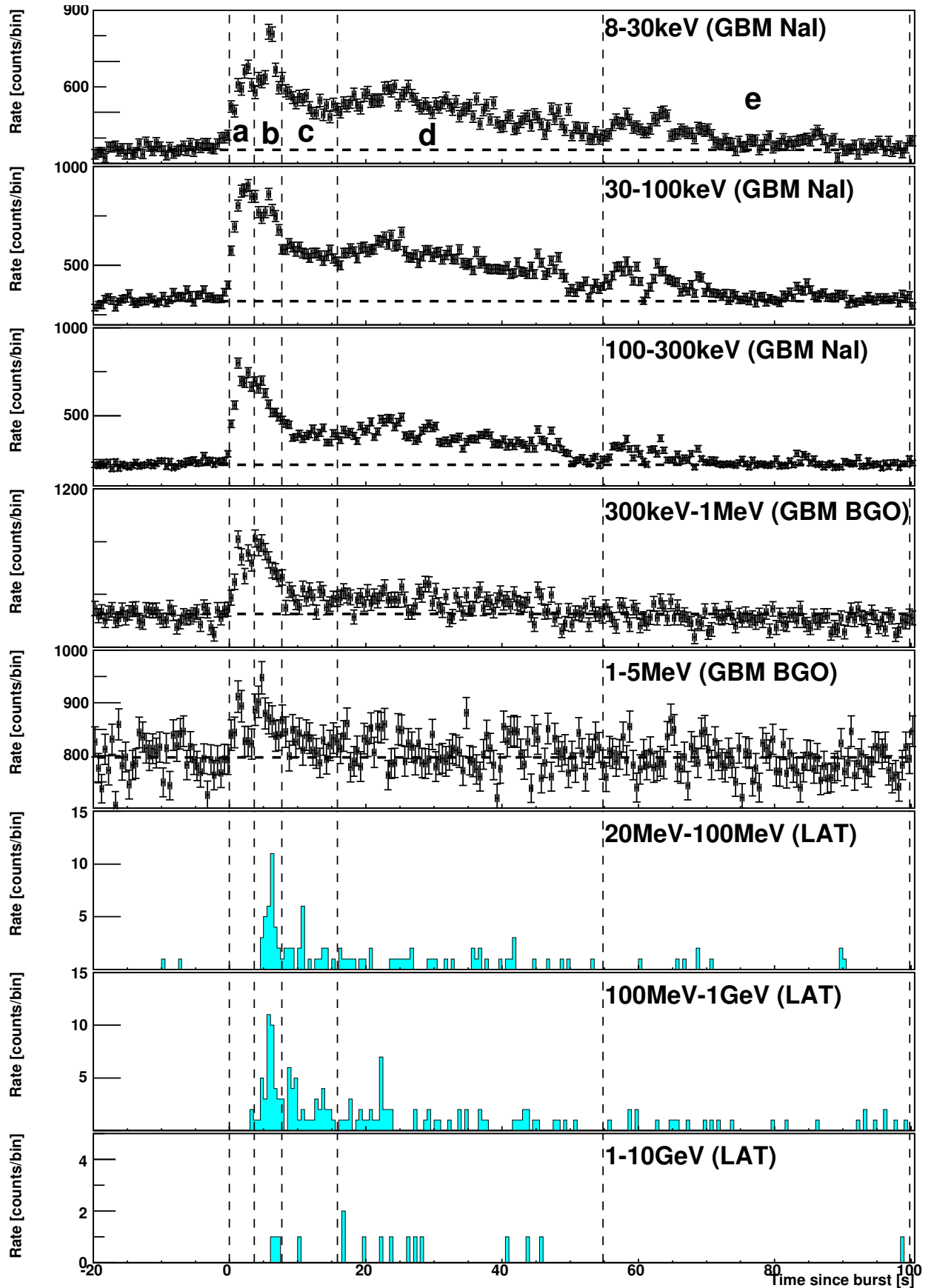


Figure 6.1: Light curve of 080916C observed by the GBM and LAT detectors, from lower to higher energies.

The value of E_{peak} represents the typical energy of synchrotron radiation initiated by electrons. Since E_{peak} is much higher than that of typical GRBs and the flux is extremely high, high-energy gamma-rays from such intense regions can be strongly attenuated by lower-energy photons via pair production. However, in this case, a cutoff indicative of attenuation cannot be found. Pair production opacity can be reduced if the emission region is moving toward us at highly relativistic speeds with Lorentz factor Γ . The radius of the shell, R , can be estimated from the variability timescale Δt from geometry.

$$R = \frac{2\Gamma^2 c \Delta t}{1+z} \quad (6.1)$$

Since larger W (larger Γ) can make a smaller optical thickness even at the same variability timescale, from the typical value of E_{peak} the minimum Lorentz factor Γ_{min} can be derived. The estimated value of Γ_{min} is 600 and 870 ± 40 in time bins (d) and (b), respectively (Abdo et al. 2008). These limits are much higher than the previous estimate of $\Gamma \sim 100$ from GRB 990123 (Lithwick & Sari 2001).

6.2.1 EBL Effect

Since GRB 080916C occurred at $z = 4.2$, the Extragalactic Background Light (EBL) effect must be taken into account. The EBL effect is the attenuation effect in the very high-energy spectra (GeV – TeV) of extragalactic sources caused by pair production $\gamma + \gamma \rightarrow e^+ + e^-$. The EBL consists of background photons over ~ 20 decades of energy, from radio waves (10^{-7} eV) to high energy gamma-ray photons up to a few hundred GeV (Hauser & Dwek, 2001). When we observe GeV – TeV emission from the extragalactic source, the infrared to ultra-violet (UV) photons contribute to the attenuation. The ultra-violet photons come from the starlight emitted and redshifted through the history of the Universe while the infrared photons are generated by re-processing of the starlight by dust, its extinction and re-emission. If γ_1 with energy E_1 interacts with γ_2 having energy E_2 , the threshold energy where pair creation occurs is given by,

$$E_1 E_2 \gtrsim (m_e c^2)^2 \quad (6.2)$$

where m_e is the electron mass. Adopting $E_1 = 10$ GeV, $E_2 \sim 10$ eV (UV band) contributes to the attenuation by the EBL effect. But the EBL is difficult to measure directly due to contamination by zodiacal and Galactic light (Hauser & Dwek, 2001). Furthermore from the studies by Gilmore et al. 2008, Kneiske et al., 2002, Razzaque et al. 2008 and Stecker et al. 2007, the critical energy corresponding to the optical depth $\tau_{\gamma\gamma} = 1$ is above 10 GeV at $z = 4.2$ for various models of the EBL. Thus, we ignore the EBL effect for energies below 10 GeV in this analysis.

6.2.2 Amati and Yonetoku relations

Here we verify the compatibility with the Amati and Yonetoku relations. For the Yonetoku relation the isotropic-equivalent peak-luminosity (L_{iso}) is defined as the luminosity at each interval of the individual pulse (not the whole duration), while for the Amati relation the isotropic-equivalent energy (E_{iso}) is defined as the energy over the whole duration. From Eq. 4.6 and the table 6.2, the value of E_{iso} is calculated ($E_{\text{iso}} = 6.31 \pm 0.19 \times 10^{54}$ ergs) and the result is shown in the left panel of Fig. 6.2 (Amati relation). In addition, each value of L_{iso} is plotted in the right panel of the Fig. 6.2 (Yonetoku relation). The obtained value of E_{iso} is consistent with the Amati relation. For the obtained L_{iso} values, the point in interval of *a* is consistent with the Yonetoku relation and the other points are marginally consistent with the relation within a factor of ~ 10 . The difference is thought to be due to the fact that individual pulses are unclear in intervals *c*, *d* and *e* and we calculate more of an *average* luminosity than a *peak* luminosity.

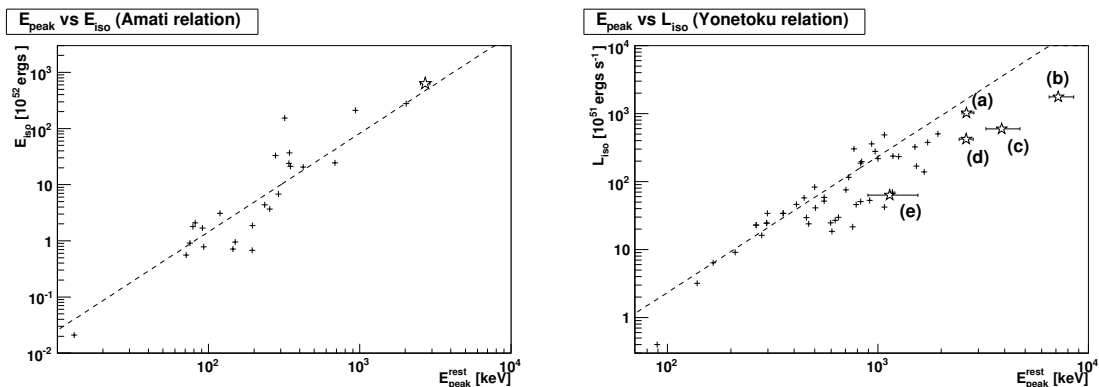


Figure 6.2: Plots of GRB080916C for the Amati (*left*) and Yonetoku (*right*) relations. The dashed lines are the best-fit correlation reported by Amati 2006 (*left*) and Yonetoku et al. 2004 (*right*). The crosses represent the GRBs previously detected by *HETE* and *BATSE*.

6.3 Delayed Emission Analysis

It is striking that the GeV emission is delayed from the first pulse at interval *a*. For a more detail analysis, we focus on the first and second intervals (*a* and *b*) and perform the same pulse-fit analysis described in the previous chapter.

As shown in Fig. 6.4, in the 8 – 100 keV band, after the occurrence of the first pulse, a second significant pulse is found from $T_0 + 5$ s to $T_0 + 7$ s. In the higher energy range 100 – 300 keV, there is no prominent pulse at that time while the first peak is found

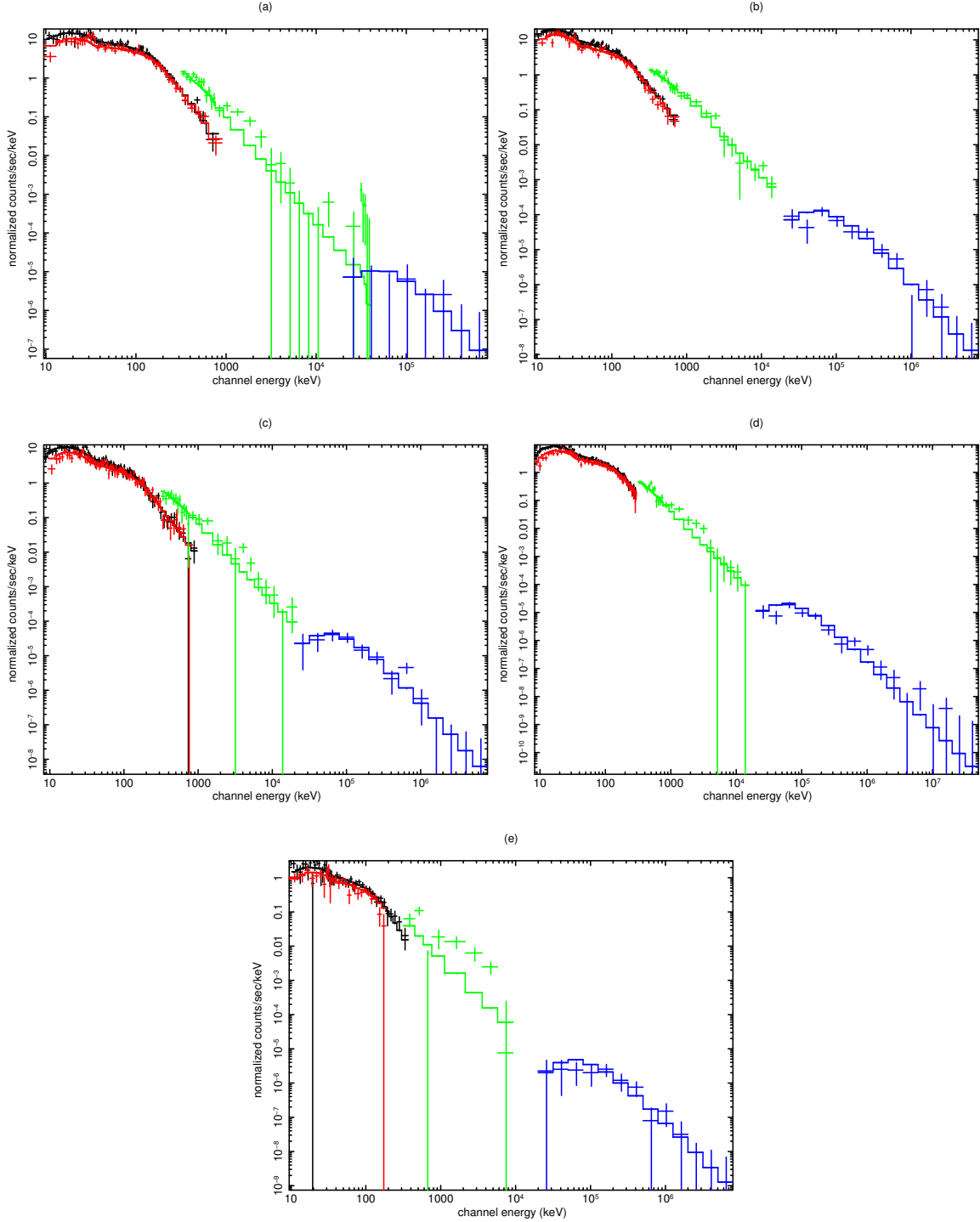


Figure 6.3: Count spectra for corresponding time intervals of (a), (b), (c), (d) and (e). All the spectra are fitted by the Band function. The red and black points, green points and blue points represents the two NaI detector, the BGO detector and the LAT, respectively.

clearly. In the higher energy range 300 keV – 5 MeV, the first pulse decays rapidly and the second pulse rises more rapidly as energy increases. The second peak in the 300 keV – 5 MeV range leads to that in the 8 – 300 keV range. In the 20 MeV – 1 GeV LAT

energy range, the pulse almost coincides with the second pulse in the 8 – 100 keV band.

The result of the fitted peak lag and duration w is shown in Tab. 6.5. Here, the lag is defined as the time difference between t_{peak} in the lowest energy band (8–30 keV) and t_{peak} in the corresponding higher energy band. The positive lag agrees with the classical case (in the higher energy ranges, the peak comes earlier). The duration w is the time interval where intensities are reduced by a factor of e^{-3} . From table 6.5, there is no significant lag between 8–30 keV and 30–100 keV, 20–100 MeV and 0.1–1 GeV, while a positive lag exists at 0.3–1 MeV and 1–5 MeV. Thus it seems that there is significant lag between the 8–100 keV and 0.3–5 MeV ranges, but the evolution of the duration is extremely strange. The durations in the 0.3–1 MeV and 1–5 MeV bands (~ 10 s) are much larger than those in the 8–30 keV and 30–100 keV, 20–100 MeV and 0.1–1 GeV bands (~ 2 s), which indicates that the origin of the second peak at 0.3–1 MeV and 1–5 MeV is different from those in the other bands.

Here, we rebin the light curve of GRB 080916C. As before, the bin size of the light curve of the GBM detector in Fig. 6.4 is 0.5 s. For the NaI detector, we divide the total light curve into 2 bands (8–80 keV and 80 – 300 keV) and show the two light curves of the NaI detector and 1 light curve of the BGO detector whose bin widths are 0.1 s and 0.2 s, respectively in Fig. 6.6.

The middle and right panels of Fig. 6.6 show that the variability timescale is below 0.5 s, and we find that the former analysis ignores the short variability timescale, which means that the pulse fit represents the time evolution of the entire burst, not the pulse, roughly. However the left panel of Fig. 6.6 suggests that the pulse peak at $T_0 + 6$ s seems not to have a short variability timescale, and correlates with the GeV emission because the variability timescale of the GeV emission is the almost same as that of the 8–80 keV emission (~ 2 s).

For just reference, the other all GRBs (GRB 080825 and GRB 081024B) detected by the *Fermi* LAT also have the GeV emission delayed from the first X-ray pulse (see appendix E). Although the detected GeV events are very few (< 10), the result also favors the possibility that the GeV emission site is distinct from the X-ray emission as well as in the case of GRB 080916C.

From the spectral lag, duration and variability timescale analysis, we can say that the GeV emission is associated with 8–80 keV emission and furthermore the difference of the variability timescale between the second pulse and the neighboring pulses implies that the emission site of the second pulse including the GeV emission is distinct from that of the other pulses. In the following section, we investigate the detailed spectral analysis for the second pulse.

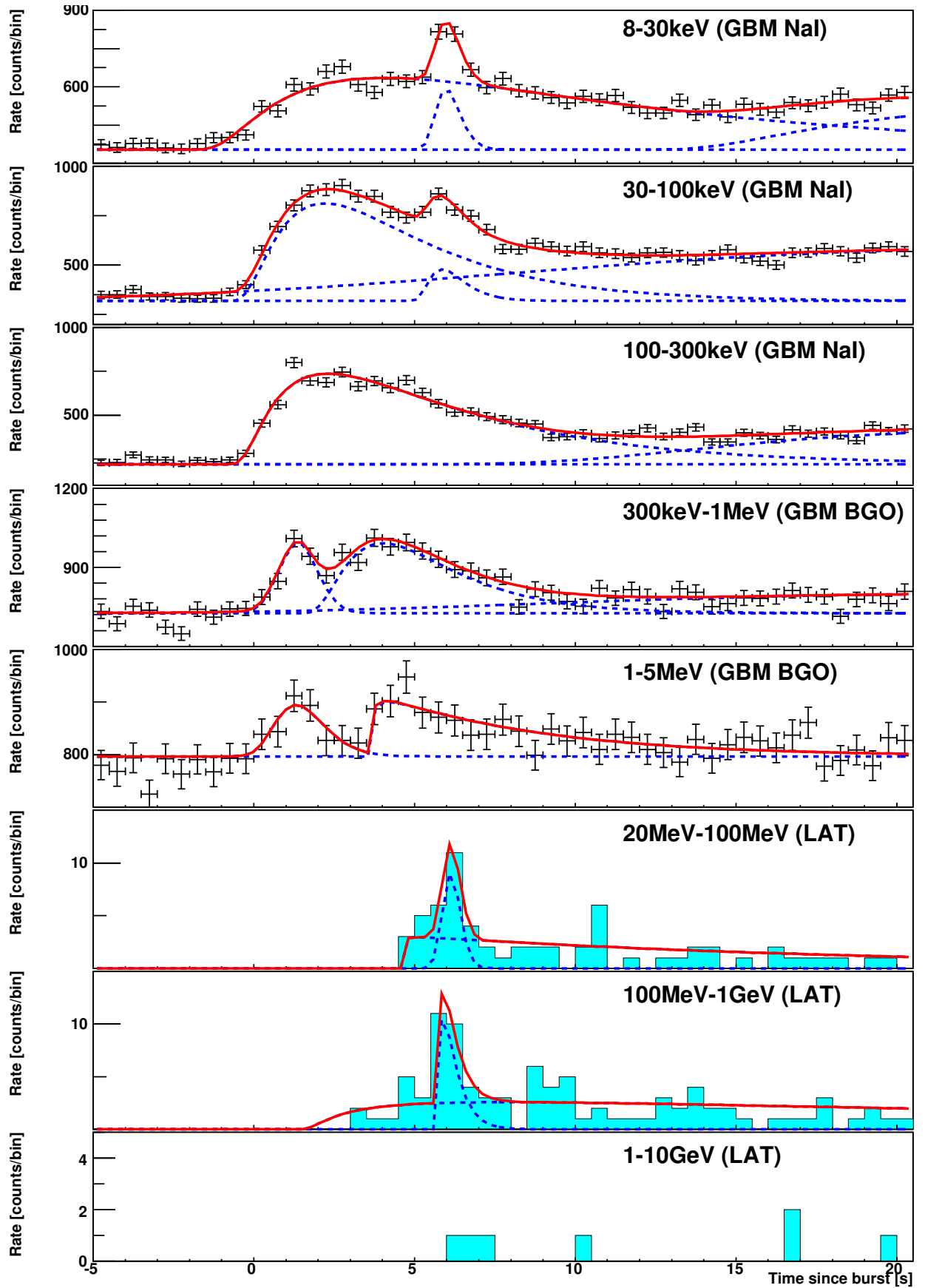


Figure 6.4: Light curve of 080916C at $T_0 - 5$ s to $T_0 + 20$ s and pulse-fit result.

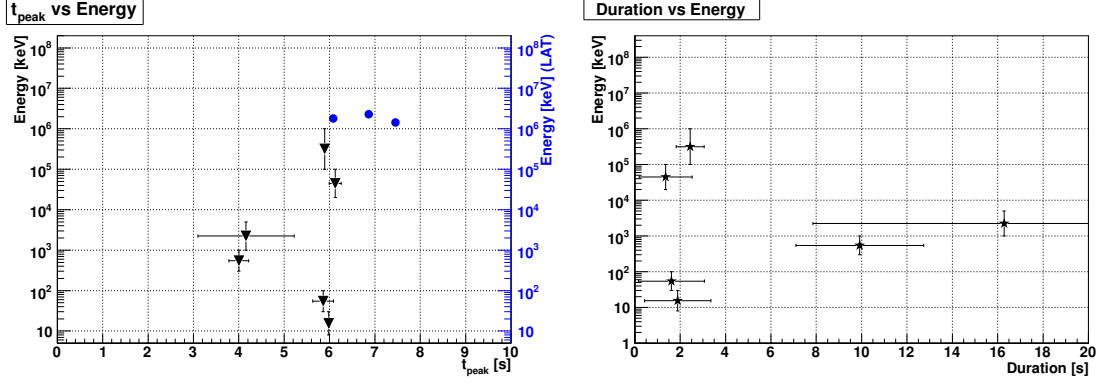


Figure 6.5: Energy vs. t_{peak} plots (Left). The circles show the highest energy photons corresponding to the bottom of Fig. 6.4. Energy vs. duration plots (Right) for GRB 080916C

Table 6.2: Lag at different energies for GRB 080916C. The lag is defined as the time delay between t_{peak} at the lowest energy (8–30 keV) and the corresponding higher energy.

	8-30 keV	30-100 keV	0.3-1 MeV	1-5 MeV	20-100 MeV	0.1-1 GeV
Lag [s]	-	0.12 ± 0.24	1.98 ± 0.23	1.82 ± 1.06	-0.15 ± 0.15	0.09 ± 0.10
w [s]	1.89 ± 1.46	1.61 ± 1.46	9.92 ± 2.82	16.28 ± 8.43	1.36 ± 1.17	2.44 ± 0.61

6.4 Detailed Spectral Analysis for the first phase

We perform the detailed spectral analysis using GBM (NaI and BGO) and LAT for the first phase (T_0 to $T_0 + 10$ s) of GRB 080916C with finer time resolution (~ 1 s) as shown in Fig. 6.7. The top to bottom panels of Fig. 6.7 show the evolution of α & β , E_{peak} , and the energy flux at 8–100 keV and 100 keV – 5 MeV, respectively .

This result also shows the trend of the soft to hard and then the hard to soft evolution

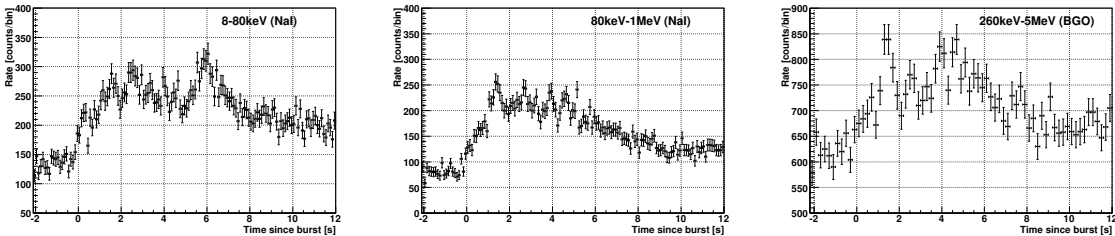


Figure 6.6: Zoom on the light curve from -2 s to 12 s in the low energy band of NaI (left), the high energy band of NaI (middle) and the total band of BGO (right) with fine time resolution.

(see Tab. 6.2). Furthermore, the highest value of E_{peak} is ~ 2000 keV and this value is 1.5 times larger than that of interval b in table 6.2.

The GeV emission correlated with the 8–80 keV pulse ranges from $T_0 + 5$ s to $T_0 + 7$ s approximately. E_{peak} is almost constant from $T_0 + 5$ s to $T_0 + 7$ s and there does not seem to be a large spectral difference between α and β from $T_0 + 4$ s to 5s and $T_0 + 7$ s to 8 s which are adjacent to the GeV emission.

We now try to decompose the pulses and perform a decomposed spectral fit in order to extract only the pulse correlated with the GeV emission. First of all, to estimate the underlying emission beneath the second pulse, we adopt the time intervals $T_0 + 4$ s to 5 s and $T_0 + 7$ s to 8 s where there is no large spectral evolution described above. Although the underlying emission consists of a lot of spikes, we assume that there is no significant spectral evolution from $T_0 + 4$ s to $T_0 + 8$ s for the underlying emission. Furthermore, the decay function for the underlying emission is almost linear. In this case, we could regard the underlying emission as the average spectrum during $T_0 + 4$ s to 5 s and $T_0 + 7$ s to 8 s.

The estimated spectrum of the underlying emission during $T_0 + 4$ s to 5 s and $T_0 + 7$ s to 8 s is shown in Fig. 6.8. Here, we try two methods to estimate the decomposed spectrum for the second pulse; (1) the time interval for the foreground (FG) is $T_0 + 5$ s to 7 s and the time interval for the background (BG) is $T_0 + 4$ s to 5 s and $T_0 + 7$ s to 8 s, namely, the background spectrum corresponds to the underlying emission spectrum. For the LAT spectrum, we do not try to subtract the BG spectrum from the FG spectrum because the number of the LAT events is very small; (2) the time interval for the FG is $T_0 + 5$ s to 7 s as well as (1), and the time interval for the BG is $T_0 + 100$ s to 200 s and we *superimpose* the underlying spectrum on the FG spectrum.

Table 6.3: Fit parameters for the underlying emission

(average spectrum during $T_0 + 4$ s to 5 s and $T_0 + 7$ s to 8 s)

	α	β	E_{peak}	Normalization [ph cm ⁻² s ⁻¹ keV ⁻¹]	C _{stat} (bin)
Band	$-0.97^{+0.05}_{-0.03}$	$-2.56^{+0.09}_{-0.07}$	1810^{+255}_{-470}	$6.14^{+0.90}_{-0.32} \times 10^{-3}$ †	121.8 (94)

†: Normalization at 500 keV

6.4.1 Spectrum subtracted from the underlying emission

The left panel of Fig. 6.9 shows the background subtracted spectrum fitted by a single powerlaw function, where the background spectrum corresponds to the underlying emis-

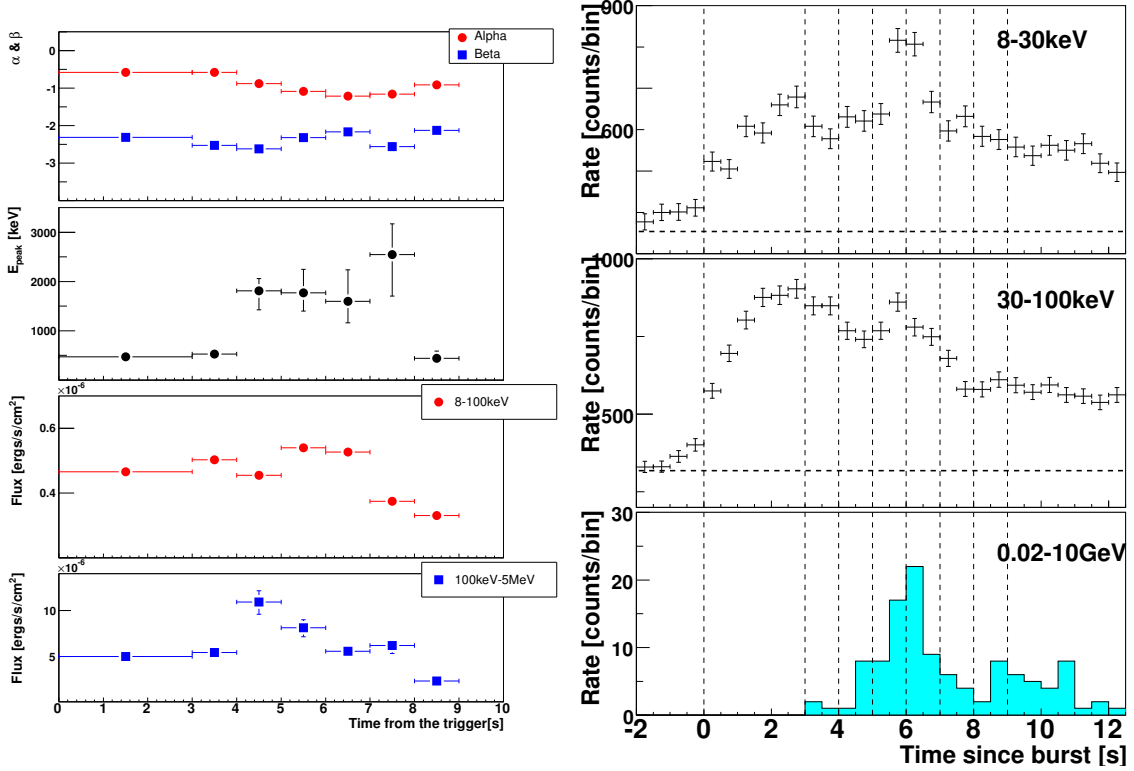


Figure 6.7: Detailed spectral analysis for the first phase of GRB 080916C (left) at the corresponding time interval (right).

sion spectrum, with the best-fit function represented by the dashed line. The background subtracted spectrum demonstrates that evidence for the extra high-energy component exists. Furthermore, the right panel of Fig. 6.9 shows the existence of a two component model (e.g., synchrotron emission and inverse Compton emission). These spectral parameters are shown in table 6.4. The value of C_{stat} provides a goodness-of-fit if there are enough counts and this could be equal to χ^2 . In our analysis, due to the poor statistics of the LAT we have performed spectral analysis using not the χ^2 fit method but the maximum likelihood method. The value of C_{stat} does not provide the goodness-of-fit but provides only the residual between the data point and fit. From the comparison between the C_{stat} values in table 6.4, the cutoff power-law or two component model (cutoff powerlaw plus Band function) are preferred.

But one can question whether the subtraction to estimate the pure second pulse is carried out correctly in Fig. 6.9. We show the count spectrum to draw attention to the subtraction in Fig. 6.10. The figure shows that the counts are negative around the MeV band and the background has been overestimated. Thus we need to re-estimate the background flux correctly, but it is impossible to reproduce the background flux completely because the *true* evolution of the underlying emission is not known. To avoid

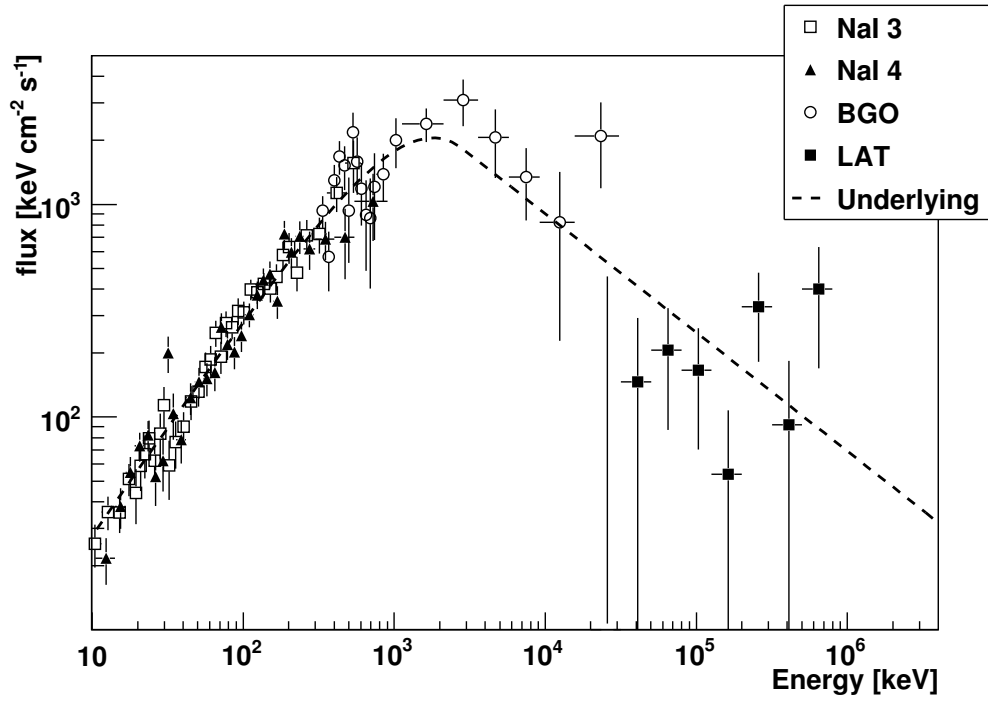


Figure 6.8: Average spectrum during $T_0 + 4$ s to 5 s and $T_0 + 7$ s to 8 s (underlying emission)

this problem, we utilize another method in the next section.

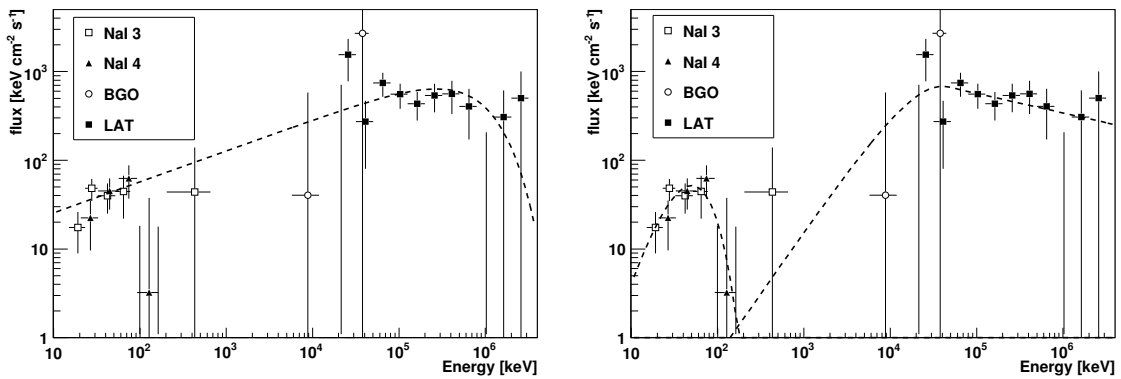


Figure 6.9: Underlying emission subtracted spectrum, where the background corresponds to the underlying emission. left: dashed line indicates the cutoff power-law model. right: dashed line indicates the cutoff power-law plus the Band function.

Table 6.4: Fit parameters for the underlying emission subtracted spectrum

	α	β	E_{peak}	Normalization [ph cm ⁻² s ⁻¹ keV ⁻¹]	C_{stat} (bin)
powerlaw	$-1.68^{+0.02}_{-0.03}$	-	-	$1.3 \pm 0.1 \times 10^{-4} \dagger$	50.11 (28)
cutoff p.l.	$-1.65^{+0.03}_{-0.01}$	-	271^{+143}_{-74} MeV	$1.3 \pm 0.1 \times 10^{-4} \dagger$	29.57 (28)
cutoff p.l. (soft)	$1.14^{+1.86}_{-1.16}$	-	$50.0^{+8.6}_{-7.5}$ keV	$5.6 \pm 1.8 \times 10^{-3} *$	22.08 (28)
& Band (hard)	-0.60 (fixed)	$-2.22^{+0.14}_{-0.17}$	40^{+20}_{-42} MeV	$1.0^{+1.7}_{-0.2} \times 10^{-6} \diamond$	

\dagger : Normalization at 1 MeV, $*$: Normalization at 1 keV, \diamond : Normalization at 100 MeV

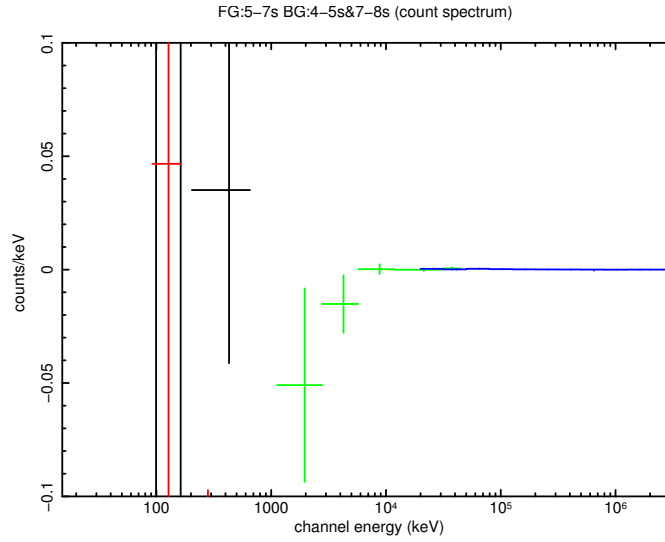


Figure 6.10: Subtracted count spectrum around 0 counts/keV. The red and black points, green points and blue points represents the two NaI detector, the BGO detector and the LAT, respectively.

6.4.2 The spectrum superimposing the underlying emission

The preceding way has a problem with the estimation of the background flux level. In this section, we try a second way where we make the underlying emission superimposing, not subtracting, the spectrum as described before. First of all, to avoid over- or under-estimation of the underlying emission, we set the normalization of the underlying emission spectrum to a variable parameter with α , β , and E_{peak} fixed. Due to the uncertainty in the amount of the underlying emission, we cannot derive a completely correct value for the flux. But by setting its normalization to a variable parameter, we can obtain a reasonable normalization value.

The fitted spectra and best-fit parameters are shown in Fig. 6.11 and table 6.5,

respectively. For only the underlying emission, the residual is relatively larger than that of other models and, by adding a certain component (e.g., the powerlaw function etc.), the residual becomes significantly smaller. For the addition of the powerlaw or cutoff powerlaw function, there is no significant difference between the residuals while the two component model (cutoff powerlaw plus Band function) gives a better value of the residual.

The addition of the powerlaw or cutoff powerlaw function indicates that there is extra synchrotron emission, in the form of a component having the higher E_{peak} for the underlying emission, or possibly extra hadron induced emission; protons accelerated to high energies cause a cascade process with $p + \gamma \rightarrow n + \pi^0$ or $p + \pi^0$, the neutral pions decay as $\pi^0 \rightarrow \gamma + \gamma$, the photons make electron positron pairs $\gamma + \gamma \rightarrow e^- + e^+$, and the synchrotron and inverse Compton emission are radiation from the secondary e^\pm .

In the next section, we discuss the origin of the extra component.

6.5 Origin of the extra high energy component

6.5.1 Inverse Compton emission (SSC model) ?

First, to explain the spectrum in the bottom panel of Fig. 6.11, we investigate the possibility of the one-zone synchrotron self Compton (SSC) model. Here, relativistic electrons upscatter a seed photon and then the scattered photon, whose energy is transferred from the electron, can be observed by the observer as a high-energy photon. In such a case the scattering process is called *inverse Compton* (IC). The ‘‘one-zone SSC’’ means that the synchrotron and IC scattering occur at the same place (shell).

We assume the Lorentz factor Γ of the shell moving toward us is 1000 since the minimum Lorentz factor is ~ 870 as described in Sec. 6.2. Moreover, in the rest frame of the electrons, we can neglect the relativistic correction and treat the process as a classical case, like Thomson scattering in the Klein-Nishina formula, as long as $h\nu \ll m_e c^2$. This process therefore converts a low-energy photon to a high-energy one by a factor of order $\gamma_{e,\text{min}}^2$, where $\gamma_{e,\text{min}}^2$ is the minimum electron Lorentz factor. Assuming that the low-energy X-ray bump (~ 110 keV) provides the seed photons and scattered photons are the high energy component (~ 19 MeV), we find that $\gamma_{e,\text{min}}^2 = 19 \text{ MeV} / 110 \text{ keV} \sim 200$ ($\gamma_{e,\text{min}} \sim 14$). The energy of the seed photon $h\nu_{\text{seed}}$ in the rest frame of the electron is

$$h\nu_{\text{seed}} = 110\text{keV} \times \frac{\gamma_{e,\text{min}}}{\Gamma} \sim 1.5 \left(\frac{\Gamma}{1000} \right)^{-1} \left(\frac{\gamma_{e,\text{min}}}{14} \right) \text{ keV}$$

So this satisfies $h\nu_{\text{seed}} \ll m_e c^2$ and we can treat the process as a classical case.

Table 6.5: Spectral-fit results of underlying emission and extra components

Models	Underlying emission		1st extra component			2nd extra component				C_{stat} (bin)
	Normalization [ph/cm ² /s/keV]		α	E_{peak}	Normalization [ph/cm ² /s/keV]	α	β	E_{peak} [MeV]	Norm [ph/cm ² /s/keV]	
No	$6.99^{+0.12}_{-0.13} \times 10^{-3}$ †	-	-	-	-	-	-	-	-	211.8 (107)
powerlaw	$5.59^{+0.16}_{-0.21} \times 10^{-3}$ †	1.76 ± 0.02	-	-	$8.66^{+1.24}_{-0.88} \times 10^{-5}$ *	-	-	-	-	116.6 (107)
$\frac{1}{51}$ cutoff	$5.48^{+0.18}_{-0.21} \times 10^{-3}$ †	$1.71^{+0.03}_{-0.02}$	293^{+402}_{-127} †	$1.07^{+0.09}_{-0.05} \times 10^{-4}$ *		-	-	-	-	114.0 (107)
$\frac{53}{55}$ cutoff + Band	$5.14^{+0.18}_{-0.16} \times 10^{-3}$ †	$0.87^{+0.11}_{-0.12}$	115^{+21}_{-15} ♣	$1.30^{+0.09}_{-0.12} \times 10^{-1}$ ◇		$0.6(\text{fixed})$	$2.11^{+0.13}_{-0.16}$	$19.2^{+15.6}_{-8.0}$	$1.80^{+2.03}_{-1.15} \times 10^{-6}$ ‡	97.3 (107)

Note— Corresponding confidence level is 1σ .

†: Normalization at 500 keV

*: Normalization at 1 MeV

◇: Normalization at 15 keV

‡: Normalization at 100 MeV

∇: MeV unit

♣: keV unit

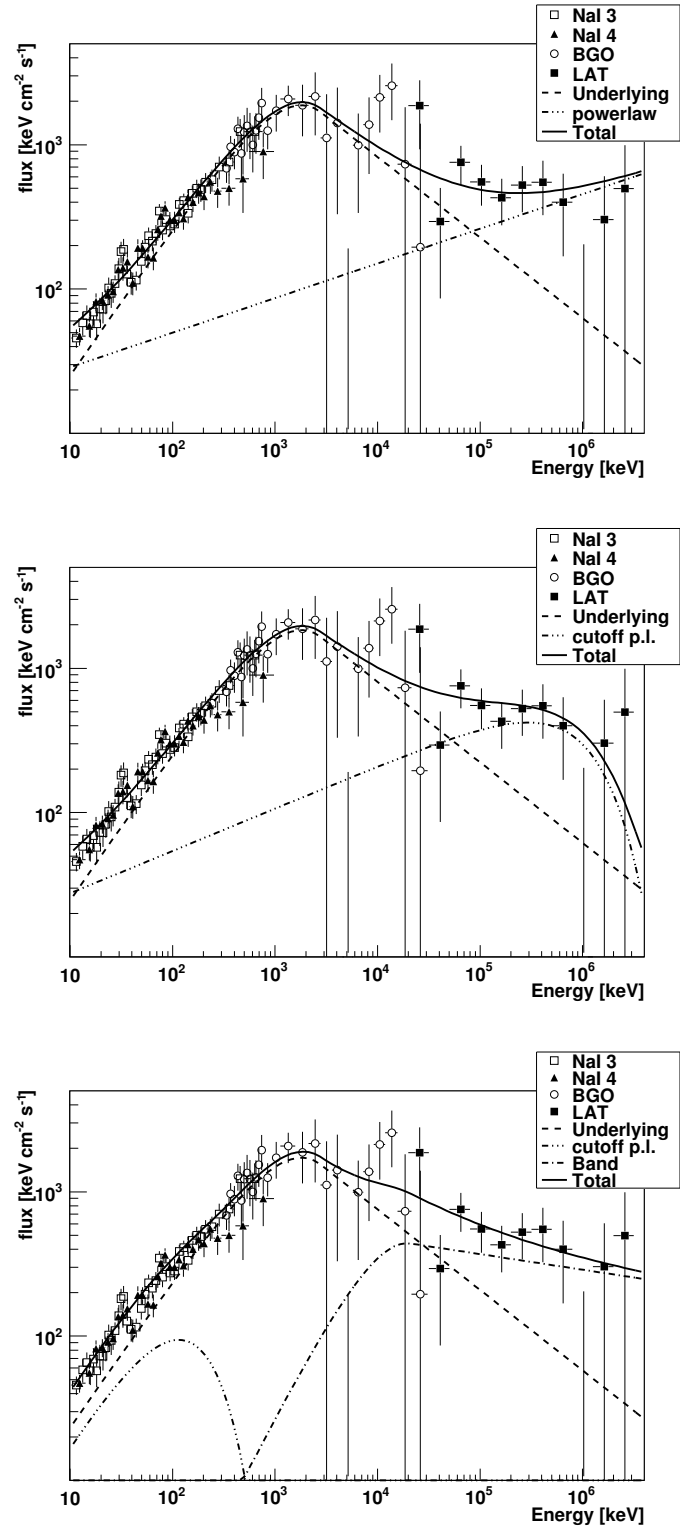


Figure 6.11: Underlying emission superimposed on the extra spectrum, (*top*) with the best-fit powerlaw function, (*middle*) with the best-fit cutoff powerlaw function, (*bottom*) with the best-fit cutoff powerlaw and Band functions.

The width W of the shell can be written as,

$$W = \frac{R}{\Gamma^2} = \frac{W'}{\Gamma} \quad (6.3)$$

where the prime denotes the comoving frame, and R is the radius of the shell. The emission volume V' in the comoving frame is written as,

$$V' = 4\pi R^2 W' \quad (6.4)$$

The energy E of the shell emitting photons towards the observer is Lorentz boosted by a factor of Γ compared to that in the comoving frame,

$$E = \Gamma E' \quad (6.5)$$

Then the energy density of the shell at the comoving U'_γ is

$$U'_\gamma = \frac{E'}{V'} = \frac{E/\Gamma}{4\pi R^3/\Gamma} = \frac{E}{4\pi R^3} \quad (6.6)$$

Here from Tab. 6.5, the fluence of the lower-energy bump (e.g., cutoff powerlaw component) is 2.4×10^{-7} ergs cm^{-2} using the duration ~ 2 s. Thus E_{seed} of the seed photons can be calculated as,

$$E_{\text{seed}} = \frac{\text{fluence} \times 4\pi d_L^2}{(1+z)} = 8.2 \times 10^{51} \text{erg} \quad (6.7)$$

where $z = 4.2$. Thus using the duration $\Delta t = 2 \text{ s}/(1+z) = 0.4$ s in the burst-rest frame, the electron energy density is,

$$U'_\gamma = 7000 \left(\frac{\Gamma}{1000} \right)^{-6} \left(\frac{\Delta t}{0.4 \text{ s}} \right)^{-3} \text{erg cm}^{-3} \quad (6.8)$$

The ratio of synchrotron emissivity to inverse Compton emissivity is determined by $(\frac{dE}{dt})_{IC}/(\frac{dE}{dt})_{sync} = U_\gamma/U_B$ (Rybicki & Lightman 1986) (U_B is the magnetic energy density $B^2/8\pi$) and in this case, $(\frac{dE}{dt})_{IC}/(\frac{dE}{dt})_{sync} \sim 4$ from the bottom panel of Fig. 6.11. So $U_\gamma/U_B = U'_\gamma/U'_B \sim 4$ and the estimated B is

$$B = 200 \left(\frac{\Gamma}{1000} \right)^{-3} \left(\frac{\Delta t}{0.4 \text{ s}} \right)^{-1.5} \text{Gauss} \quad (6.9)$$

The typical (or minimum) synchrotron frequency ν_m emitted from electrons with $\gamma_{e,\text{min}}$ is given by Longair 1997 and Rybicki & Lightman 1986,

$$\begin{aligned} \nu_m &= 0.29 \frac{3}{2} \gamma_{e,\text{min}}^2 \frac{eB}{2\pi m_e} \Gamma \\ &= 1.22 \times 10^6 \gamma_{e,\text{min}}^2 B \Gamma \text{ [Hz]} \end{aligned}$$

Converting Hz into eV and reducing the energy by a factor of $1/(1+z)$ due to cosmological expansion,

$$h\nu_m = 5.05 \times 10^{-9} \gamma_{e,\min}^2 B \Gamma (1+z)^{-1} \text{ [eV]} \quad (6.10)$$

$$= 40 \times 10^{-3} \left(\frac{\Gamma}{1000} \right)^{-2} \left(\frac{\Delta t}{0.4 \text{ s}} \right)^{-1.5} \text{ [eV]} \quad (\ll 110 \text{ keV}) \quad (6.11)$$

If this is compatible with our result, we should observe synchrotron emission with $E_{\text{peak}} = 40 \times 10^{-3} \text{ [eV]}$, but the value of the energy does not agree with our value ($\sim 110 \text{ keV}$) by seven orders of magnitude, which means that the one-zone SSC model cannot explain the spectrum and another model is required.

Other possible inverse Compton models are the following; (1) the emission site is not a single place and the place (shell) where the seed photon radiates is very different from that where the IC scattered photons radiates. In this case since we can adopt any values of $\gamma_{e,\min}$, B without constraints (e.g., $(\frac{dE}{dt})_{IC}/(\frac{dE}{dt})_{sync} = U_\gamma/U_B$ etc.), we can reproduce the spectrum easily. (2) if lower-energy seed photons exist, the one-zone SSC model is still valid. In this case, the energy of the seed photon is $110 / \gamma_{e,\min}^2 \text{ keV} \sim 0.6 \text{ keV}$. The observed X-ray bump ($\sim 110 \text{ keV}$) corresponds to the spectrum of single-IC scattering while the observed gamma-ray bump ($\sim 19 \text{ MeV}$) corresponds to the spectrum of double-IC scattering. In this scenario, however, since there is no evidence for the ultra-violet seed photons from the observations, we cannot endorse the double-IC model strongly.

The fact that there is no significant spectral lag between the X-ray and GeV emission is likely to be consistent with the IC model because the primary synchrotron and IC components occur almost simultaneously according to a recent hydrodynamical study (Bosnjak et al. 2008).

6.5.2 Synchrotron emission with very high E_{peak} ?

Next, we consider the case where the extra component is a powerlaw or cutoff powerlaw function as shown in the top and middle panel of Fig. 6.11. We discuss the possibility of synchrotron emission with the very high E_{peak} .

Here, the result of no significant spectral lags between X-ray and GeV emission might be valid for this model. This is because the different synchrotron emissions come from different shells. In this model, it does not matter if a significant delay between the low-energy emission and the high-energy emission exists.

The number of protons N'_p in the shell moving toward us at Lorentz factor Γ in the

comoving frame is ,

$$\begin{aligned} N'_p &= \frac{E_{\text{tot}}}{\gamma_{\text{sh}} m_p c^2 \Gamma} \\ &= \frac{E_{\text{ph}}}{\gamma_{\text{sh}} m_p c^2 \Gamma \epsilon_e} \end{aligned} \quad (6.12)$$

where E_{tot} is the total thermal energy of the GRB, ϵ_e measures the fraction of E_{tot} that goes into random motions of the electrons, E_{ph} is the observed gamma-ray energy , $\sim 10^{54}$ erg, given by $E_{\text{ph}} = \epsilon_e E_{\text{tot}}$, γ_{sh} is the relative Lorentz factor across the corresponding shock (of the order of a few in the case of internal shocks) and m_p is the proton mass. The emission volume V' in the comoving frame is

$$V' = 4\pi R^2 \frac{R}{\Gamma} \quad (6.13)$$

The the proton number density n'_p is described as

$$\begin{aligned} n'_p &= \frac{N'}{V'} = \frac{E_{\text{ph}}}{4\pi R^3 m_p c^2 \gamma_{\text{sh}} \epsilon_e} \\ &= 3.6 \times 10^6 \epsilon_e^{-1} \gamma_{\text{sh}}^{-1} \left(\frac{E_{\text{ph}}}{10^{54} \text{ erg}} \right) \left(\frac{\Gamma}{1000} \right)^{-6} \left(\frac{\Delta t}{0.4 \text{ s}} \right)^{-3} \text{ cm}^{-3} \end{aligned} \quad (6.14)$$

Most of the kinetic energy is carried by protons, so the internal energy is generated via shock dissipation and the energy is transferred from protons to electrons. Assuming that $n_e = f n_p$, where n_e is the electron number density, f is the fraction of electrons assumed to be accelerated by protons. Note that most GRB studies (prompt and afterglow emission modeling; e.g. Piran 1999) are restricted to the case $f = 1$ (all electrons are accelerated). Here, we adopt $f = 1$ in the meantime. The minimum Lorentz factor of the electron, $\gamma_{e,\text{min}}$, is

$$\gamma_{e,\text{min}} = \frac{1}{f} \frac{m_p p - 2}{m_e p - 1} \epsilon_e \gamma_{\text{sh}} \quad (6.15)$$

where p is the electron powerlaw index assuming that $p > 2$, $\epsilon_e \equiv U_e/e$, e is the total thermal energy density ($e \equiv E_{\text{tot}}/V$, $U_e \equiv E_{\text{ph}}/V$). Here using $m_p/m_e \sim 2000$, $\gamma_{e,\text{min}}$ is nearly equal to $2000 \epsilon_e$. Since the magnetic field energy density U_B is equal to $\epsilon_B e$, where ϵ_B is the ratio of the magnetic field energy density to the total thermal energy density ($e = \gamma_{\text{sh}} n'_p m_p c^2$),

$$U_B = \frac{B^2}{8\pi} = \epsilon_B \gamma_{\text{sh}} n'_p m_p c^2 \quad (6.16)$$

Thus,

$$B = 3.8 \times 10^2 \epsilon_B^{\frac{1}{2}} \epsilon_e^{-\frac{1}{2}} \left(\frac{E_{\text{ph}}}{10^{54} \text{ erg}} \right)^{\frac{1}{2}} \left(\frac{\Gamma}{1000} \right)^{-3} \left(\frac{\Delta t}{0.4 \text{ s}} \right)^{-\frac{3}{2}} \text{ Gauss} \quad (6.17)$$

and we have the expected E_{peak} in the observer frame using Eq. 6.10 ;

$$E_{\text{peak}} = 1.5 f^{-2} \epsilon_e^{\frac{3}{2}} \epsilon_B^{\frac{1}{2}} \gamma_{\text{sh}}^2 \left(\frac{E_{\text{ph}}}{10^{54} \text{ erg}} \right)^{\frac{1}{2}} \left(\frac{\Gamma}{1000} \right)^{-2} \left(\frac{\Delta t}{0.4 \text{ s}} \right)^{-\frac{3}{2}} \text{ keV} \quad (6.18)$$

where ϵ_e and ϵ_B are approximately unity. This value is considerably smaller than the obtained result (~ 200 MeV), and much less than the underlying emission ($E_{\text{peak}} \sim 1800$ keV). To explain the very high E_{peak} , we re-examine the three possibilities (1) very large $\gamma_{\text{sh}} \gg 1$, (2) extremely large $\epsilon_B \gg 1$ and (3) small $f \ll 1$.

High γ_{sh} ?

A large γ_{sh} would agree with the observed high E_{peak} . Here the relative Lorentz factor γ_{sh} across the corresponding shock is written as,

$$\gamma_{\text{sh}} = \gamma_r \gamma_s - \sqrt{\gamma_r^2 - 1} \sqrt{\gamma_s^2 - 1} \sim \frac{\gamma_r}{2\gamma_s} \quad (6.19)$$

where $\gamma_r > \gamma_s$. The typical γ_{sh} in the case of internal shocks is a factor of 10 lower; e.g. $\gamma_r = 1000$ and $\gamma_s = 100$ gives $\gamma_{\text{sh}} \sim 5$. In the regime of internal shocks, we cannot make γ_{sh} larger than ~ 10 . Thus if we make γ_s smaller, which means that γ_s is unity, we can enlarge γ_{sh} , e.g. $\gamma_r = 600$ and $\gamma_s = 1$ gives $\gamma_{\text{sh}} \sim 300$.

$$E_{\text{peak}} = 200 f^{-2} \epsilon_e^{\frac{3}{2}} \epsilon_B^{\frac{1}{2}} \left(\frac{\gamma_{\text{sh}}}{300} \right)^2 \left(\frac{E_{\text{ph}}}{10^{54} \text{ erg}} \right)^{\frac{1}{2}} \left(\frac{\Gamma}{1000} \right)^{-2} \left(\frac{\Delta t}{0.4 \text{ s}} \right)^{-\frac{3}{2}} \text{ MeV} \quad (6.20)$$

However this situation is the external shock model. If the forward shock is ultra-relativistic as described in Sec. 2.2 (which corresponds to the ultra-relativistic external forward shock case), we can increase the E_{peak} . For the variability timescale (~ 0.4 s), if the shocked region is a dense ISM or wind, this timescale could be attained. Thus the high γ_{sh} scenario can be valid for the high E_{peak} .

Situation where $\epsilon_B \gg 1$?

Another possibility to increase E_{peak} is to increase ϵ_B above 100. This scenario corresponds to a Poynting-dominated jet model. When the jet is launched from the central engine, the energy content is mainly in the magnetic part. Namely we have a Poynting-dominated flow. As the flow accelerates, it gains kinetic energy converting Poynting flux into kinetic energy flux (Fendt & Ouyed 2004, Lyutikov & Blackman 2001). But assuming that $e \sim U_e$ if $\epsilon_B > 100$, E_B (which is the magnetic field energy) must be above 10^{56} erg because the observed $E_{\text{ph}} \sim 10^{54}$ erg. So this case is hardly feasible due to the extremely large E_B .

Not all electrons are accelerated

Although we have assumed that $f = 1$ which is adopted in many GRB models, GRB models are poorly understood and there is no physical guarantee that such a condition exists. For $f < 1$, all the electrons are not accelerated (only the fraction f of all the electrons are accelerated) and this situation corresponds to one where the number $1/f$ of protons having energy of ϵ transfer their energies to an electron by ϵ/f intuitively. Actually, Eichler & Waxman 2005 and Spitkovsky 2008 pointed out the possibility that f is not equal to unity.

Thus if we have $f \sim 3.2 \times 10^{-3}$, we can obtain the E_{peak} value of 200 MeV as well as 1800 keV for the underlying emission in the case of $f \sim 0.03$, and we can reproduce the high E_{peak} .

$$E_{\text{peak}} = 200 \left(\frac{f}{3.2 \times 10^{-3}} \right) \epsilon_e^{\frac{3}{2}} \epsilon_B^{\frac{1}{2}} \gamma_{\text{sh}}^2 \left(\frac{E_{\text{ph}}}{10^{54} \text{ erg}} \right)^{\frac{1}{2}} \left(\frac{\Gamma}{1000} \right)^{-2} \left(\frac{\Delta t}{0.4 \text{ s}} \right)^{-\frac{3}{2}} \text{ MeV}$$

6.5.3 Proton induced emission ?

We finally discuss the possibility of the proton-induced emission.

Waxman 1995, Vietri 1995 and Milgrom & Usov 1996 pointed out that GRBs are the dominant candidate of the observed ultra-high-energy cosmic rays (UHECRs) whose internal shocks allow maximum energies $\geq 10^{20}$ eV. It is likely that the Fermi-accelerated protons in the internal shock are involved in the processes photomeson ($p\gamma$) interactions and secondary pion, muon and pair injection, ($p + \gamma \rightarrow n + \pi^0$, $\pi^0 \rightarrow \gamma + \gamma$, $\gamma + \gamma \rightarrow e^- + e^+$, or $p + \gamma \rightarrow n + \pi^+$, $\pi^+ \rightarrow \mu^+ + \nu_\mu$, $\mu^+ \rightarrow e^+ + \nu_e + \bar{\nu}_\mu$) and we could observe the very high-energy spectrum which is created by the secondary electrons or muon synchrotron and IC (Asano et al. 2008).

Assuming that the energy of accelerated protons is much larger than that of accelerated electrons ($\epsilon_e \ll \epsilon_p$) and the injected proton distribution $n_p(\gamma_p) \propto \gamma_p^{-p_p}$ with $\gamma_{p,\text{min}} \leq \gamma_p \leq \gamma_{p,\text{max}}$, then the primary electrons are injected with a power-law distribution $n_e(\gamma_e) \propto \gamma_e^{-p_e}$ with a range of Lorentz factors $\gamma_{e,\text{min}} \leq \gamma_e \leq \gamma_{e,\text{max}}$.

The maximum electron energy $\gamma_{e,\text{max}}$ is given by the balance between Fermi acceleration and radiative cooling timescales. The maximum proton energy $\gamma_{p,\text{max}}$ is similarly obtained from this analogy. So $\gamma_{p,\text{max}}$ is determined by the balance between the acceleration time $t_{\text{acc}} = \gamma_p m_p c^2 / e B c$ in the relativistic shock and the cooling time, $\min(t_{\text{exp}}, t_{\text{loss}})$, where $t_{\text{exp}} = l/c$ (l is the shell width at the comoving frame) is the expansion time and $t_{\text{loss}} = l/c$ is the energy loss time due to synchrotron, IC and $p\gamma$ cooling (Asano 2005). In this analysis, we can not derive the analytical proton-induced spectrum because the cascade

evolution cannot be expressed as an analytical solution. In such a case, the Monte Carlo technique can be used to reproduce the cascade evolution.

We newly introduce $\epsilon_p \equiv U_p/$ (the total thermal energy), where U_p is the energy density of the protons. Adopting the total isotropic energy of the accelerating protons $E_p = 3 \times 10^{55}$ erg, $\Delta t = R/(c\Gamma^2) = 0.2$ s, $\Gamma = 800$, $\epsilon_e/\epsilon_p = 10^{-3}$ and $\epsilon_B/\epsilon_p = 10^{-5}$, we obtain the spectrum shown in Fig. 6.13. Here p_{ini} and p_{fin} are the initial (before the

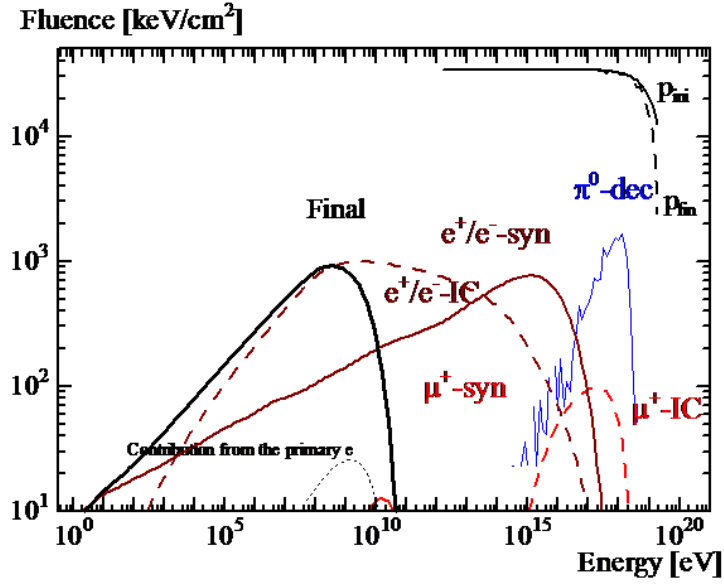


Figure 6.12: Theoretical proton-induced spectrum of GRB 080916C

cascade) and final proton spectrum (after the cascade) respectively, the blue line represents photons created by π -decay process, the brown solid line represents synchrotron photons from electrons and positrons, the brown dashed line represents photons through inverse Compton scattering by electrons and positrons, the red solid line represents synchrotron photons from muons, and the red dashed line represents photons through inverse Compton scattering by muons. These secondary electrons, positrons and muons are created by the cascade, and the secondary emission totally overwhelms any primary electron component. Finally the expected proton-induced spectrum are represented as the thick black line and the sharp spectral cutoffs at high energy are due to $\gamma\gamma$ absorption. The spectrum fits the data well and the scenario seems to be valid for explaining the high-energy component. However, E_p (3×10^{55} erg) is too large and it seems to be unattainable.

In this case, X-ray and GeV emissions come from the secondary electrons and positrons emitting the synchrotron photons and IC scattering photons. The synchrotron component

originating from the primary electrons is overwhelmed by the emission from the secondary cascade electrons and positrons. From the point of view of the model, no significant spectral lags are consistent with the proton-induced emission model.

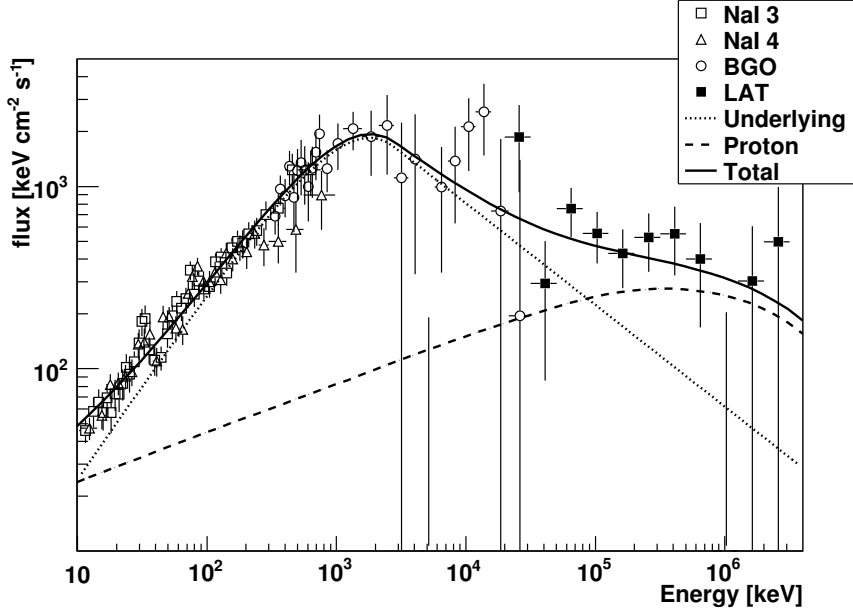


Figure 6.13: Proton-induced spectrum of GRB 080916C superimposed on the observational data

6.5.4 Summary of the origin

We summarize the origin of the extra high-energy component.

1. For the IC model, we can exclude the possibility of the one-zone SSC model while the double IC model in the same shell or the single IC model where the seed photons are scattered in different shells from the shell where the seed photons are generated, are still valid.
2. For synchrotron emission with a high E_{peak} , if either the external forward shock is ultra-relativistic or the electrons and protons have $f < 1$ which means not all the electrons are accelerated, we can explain the high-energy emission (~ 200 MeV). However since the existence of the high-energy cutoff in the spectrum is not well established, it is possible that a higher value of E_{peak} exists. In this case we require a large Lorentz factor for the external forward shock or lower f to obtain the higher E_{peak} .

3. Proton-induced emission might be a valid model to explain the extra high-energy component if the protons can have an extremely large energy ($\sim 10^{55}$ erg).

Chapter 7

Conclusions & Future Prospects

7.1 Conclusions

We have studied the spectral lag (τ_{lag}) of the prompt emission of GRBs detected by the WXM and FREGATE instruments aboard *HETE-2* and the LAT and GBM instruments aboard *Fermi*.

1. Using the 8 *HETE* GRBs with known redshifts, we derived the lag-luminosity relation ($L_{\text{iso}} \propto \tau_{\text{lag}}^{-1.2}$), and the lag-duration relation ($w \propto \tau_{\text{lag}}^{1.2}$) between the 6–25 keV and 50–400 keV bands in the observer’s frame. These relations are well known in the higher energy ranges (25–50 keV and 100–400 keV band) and we have verified that these relations are valid for the lower energy ranges and there also exists a lag- E_{peak} relation ($E_{\text{peak}} \propto \tau_{\text{lag}}^{-0.3}$). Furthermore, we have found that these relations are valid for the same energy bands not only in the observer’s frame (6–25 keV and 50–400 keV) but also in the burst-rest frame (20–100 keV and 100–500 keV), which indicates that the GRB emission in the X-ray band has the same origin.
2. We have applied the derived relations (lag-luminosity, $-E_{\text{peak}}$ and lag-duration) to the off-axis model. The relations are well explained by the off-axis model with only a few outliers. The off-axis model results from the curvature effect and the outliers could be caused by the hydrodynamical effect which is unclear and model-dependent.
3. If we assume that the Yonetoku relation ($L_{\text{iso}} \propto E_{\text{peak}}^{1.8}$) is valid, there is a contradiction between obtained lag-luminosity relation and the lag- E_{peak} relation. To explain this, we consider the possible two cases; (1) By taking into account the systematic uncertainty ($\sigma_{\text{sys}} \sim 0.05$ s), the lag-luminosity relation is consistent with the lag- E_{peak} relation within the 1- σ confidence level via the Yonetoku relation. (2) Introducing the redshift-dependent lag-luminosity relation, we can overcome this

contradiction. From the *HETE* GRBs data set, we have newly derived the dependences for the redshift and τ_{lag} on L_{iso} ($L_{\text{iso}} \propto (1+z)^{2.06} \tau_{\text{lag}}^{-0.63}$) and the dependence is almost consistent with that of Tsutsui et al. 2008a. Furthermore, the estimate of our spectral lag comes from the pulse-fit (pulse lags) technique, not the cross correlation function method (CCF; whole burst lags) while the past redshift-dependent lag-luminosity relation comes from the CCF lags. Taken together, we have found that the redshift-dependent lag-luminosity relation is still valid for the individual pulses, and this result is consistent with the view that the spectral lags are characterized by the pulses of GRBs, not by the whole burst. However, we cannot determine if the redshift-dependent lag-luminosity relation is required or not, and a bigger sample of bursts with good S/N is needed to obtain a secure result (see the next section).

4. From the multi-divided spectral-lag analysis thanks to the wide energy band of *HETE*, we have found that some GRBs' spectral lags are well explained by the curvature effect which is a geometric effect in the expanding relativistic shell. However other GRBs' spectral lags cannot be explained by the curvature effect. In these cases, the hydrodynamical effect is quite important and further theoretical studies are required. Similarly, for the energy dependence of the pulse duration, the curvature effect cannot explain the obtained results and hydrodynamical effects must be taken into account.
5. From the spectral lag analysis of the GeV emission for GRB 080916C detected by *Fermi*, we have found that the GeV emission has a different origin from the X-ray one. In addition, we have performed detailed temporal and spectral analyses and evidence for an extra high-energy component was found. The one-zone synchrotron self Compton (SSC) model cannot explain the high energy emission due to the low magnetic field and low minimal Lorentz factor of the electrons. Proton-induced emission is not appropriate for the high-energy emission either due to the requirement of the extremely large energy (3×10^{55} erg). The most probable origin is synchrotron emission where not all the electrons were accelerated. In particular in GRB 080916C it is expected that less than 0.3% electrons were accelerated. A relativistic external forward shock in the early afterglow phase also can reproduce the high-energy emission.

7.2 Future Prospects

The *HETE-2* results showed that the derived lag-luminosity relation holds not only for a lower-energy band (6–25 keV) than the BATSE-energy band in the observer’s frame but also for the energy bands in the rest frame. However the results cannot determine whether the redshift-dependent lag-luminosity relation is required or not.

Future simultaneous observations by *Swift* and *Fermi* will provide a clear conclusion. The X-Ray Telescope (XRT: 0.5–10 keV) and Burst Alert Telescope (BAT: 15–150 keV) instruments aboard *Swift* localize GRBs with arc-minute positional accuracy and rapidly relays their positions to the ground via GCN circular. This quick coordinate information leads to prompt follow-up optical and infrared afterglow observations to a measurement of the redshift, while the instruments aboard *Swift* cannot determine the spectral shape well (E_{peak} , α and β) due to the narrow X-ray coverage (15–150 keV in the case of the prompt emission). In contrast, the GBM and LAT instruments aboard *Fermi* can detect the photons from GRBs in an extremely wide band (GBM: 6 keV – 20 MeV, LAT: 20 MeV – 200 GeV) and determine the spectral shape well, although its precision for localization is not good (a few degrees) for the GBM detector (however, if the LAT instrument detects tens of GeV photons, the precision is a few arc-minutes). Simultaneous observations of GRBs by *Swift* and *Fermi* cover each other’s weaknesses in a *mutually complementary* form and provide further scientific data (good S/N and a large number of GRBs).

Furthermore, the origin of the GeV emission seems to be different from that of the classical X-ray one from our *Fermi* analysis (see also appendix E). But the number of the detected bursts is also very small (only 3 !) and perhaps the GRBs to be detected in the future will have both X-ray and GeV photons at the same time, indicating that the origin of the GeV emission may be the same as that of the X-rays. To clarify the correlation between the X-ray and GeV bands, more observational samples are needed. In particular the observations of the photons in the GeV band are direct tools to unveil the origin of the particle acceleration (e.g., how magnetized is the shell ?, what kinds of emission process are dominant ? and so on).

Appendix A

The Doppler effect

The prompt emission originates from a relativistic jet. In such a relativistic system, the relativistic Doppler effect must be taken into account.

For example, we have seen that an interval for any phenomenon in the jet-comoving frame K' will appear to have a longer interval by a factor γ when viewed by observers in frame K . If, on the other hand, we measure the arrival times of pulses or another phenomenon that propagates with the velocity of light, then there will be an additional effect on the observed interval due to delay times for light propagation. The joint effect is called the *Doppler effect*.

In the rest frame of the observer K imagine that the moving source emits one period of radiation as it moves from point 1 to point 2 at velocity V . If the frequency of the radiation in the rest frame of the source is ω' , then the time Δt taken to move from point 1 to point 2 in the observer's frame is given by the time-dilation effect

$$\begin{aligned}\Delta t &= \frac{2\pi\gamma}{\omega'} \\ &= \gamma\Delta t'\end{aligned}$$

If the observer sees the the moving source with an offset angle θ , the difference in arrival times Δt_A of the radiation emitted at 1 and 2 is equal to Δt minus the time taken for radiation to propagate a distance d . Thus we have

$$\Delta t_a = \Delta t - \frac{d}{c} = \Delta t \left(1 - \frac{v}{c} \cos \theta\right)$$

Therefore, the observed frequency ω will be

$$\omega = \frac{2\pi}{\Delta t_A} = \frac{\omega'}{\gamma \left(1 - \frac{v}{c} \cos \theta\right)} = \delta\omega' \tag{A.1}$$

where δ is the term of the relativistic Doppler effect. The factor γ^{-1} is purely a relativistic effect, whereas the $1-(v/c) \cos \theta$ factor appears in the classical formula.

Appendix B

The pulse fitting function

From general experience with GRBs, we understand that a pulse model is desired that (1) minimizes unnecessary flexibility, namely, a model with $\tau_{\text{rise}} < \tau_{\text{dec}}$, but otherwise allows for a continuum in asymmetry, (2) is continuously differentiable from pulse onset through rise, peak and decay, and (3) reflects some general physical intuition with regard to the source, even though we are not treating the problem as one of radiation transfer. For fitting purposes, it is also preferable that the partial derivatives with respect to the pulse shape parameters have relatively simple expressions. From proportional to the inverse of the product of two exponentials, one increasing and one decreasing with time, satisfies the requirements

$$\begin{aligned} I(t) &= A\lambda \exp(-\tau_1/(t - t_{\text{start}}) - (t - t_{\text{start}})/\tau_2) \\ &= A\lambda \exp(-\tau_1/(t + \tau_{\text{peak}} - t_{\text{peak}}) - (t + \tau_{\text{peak}} - t_{\text{peak}})/\tau_2) \quad t > t_{\text{start}} \end{aligned}$$

where $\mu = (\tau_1/\tau_2)^{1/2}$ and $\lambda = \exp(2\mu)$, and the time of pulse onset with respect to $t = 0$ is t_{start} . At $t = \tau_{\text{peak}} = (\tau_1/\tau_2)^{1/2}$, the intensity is at its maximum, normalized by λ to the peak intensity, A . The effects of τ_1 and τ_2 correctly correspond to the rise and decay times, since their influence arises as the combined exponential in the denominator, with both terms operating across the pulse's duration. First note that at pulse onset the first exponential alone affects the rise rate; but, since at peak maximum τ_1 and τ_2 contribute equivalently, the term of τ_2 takes over during the rise phase. After the peak the relative strength of the $\exp(-\tau_1/t)$ factor drops quickly, and the dominant terms are the $\exp(-t/\tau_2)$.

The pulse width defined as the time intervals where intensities are equal to $1/e$ is

$$w = \Delta\tau_{1/e} = \tau_2(1 + 4\mu)^{1/2}$$

Since $\mu \propto \tau_1^{1/2}$, the τ_2 timescale is dominant in w . In the case of calculations of lower intensities (e.g., at $1/e^\nu$ intensity if $\nu > 1$), the duration is $\Delta_{\tau_{(1/e)^\nu}} = \tau_2 \nu (1 + 4\mu/\nu)^{1/2}$. The the pulse asymmetry κ is given by,

$$\kappa = \frac{\tau_{\text{dec}} - \tau_{\text{rise}}}{\tau_{\text{dec}} + \tau_{\text{rise}}} = \frac{t_{1/e(\text{dec})} - \tau_{\text{peak}} - (\tau_{\text{peak}} - t_{1/e(\text{rise})})}{w}$$

or

$$\kappa = (1 + 4\mu)^{-1/2} = \tau_2/w$$

It has a weak dependence on both τ_1 and τ_2 but allows a symmetric pulse in the limit as $\mu = (\tau_1/\tau_2)^{1/2} \rightarrow \infty$. From the term w and κ , we see that narrow, nearly symmetric pulses are produced for large τ_1 and small τ_2 . For reference, τ_{dec} and τ_{rise} are expressed as

$$\tau_{\text{dec,rise}} = \frac{1}{2}w(1 \pm \kappa) = \frac{1}{2}\tau_2[(1 + 4\mu)^{1/2} \pm 1]$$

where the plus and minus signs represent τ_{dec} and τ_{rise} respectively.

Appendix C

Figure of various
correlation-coefficient distributions

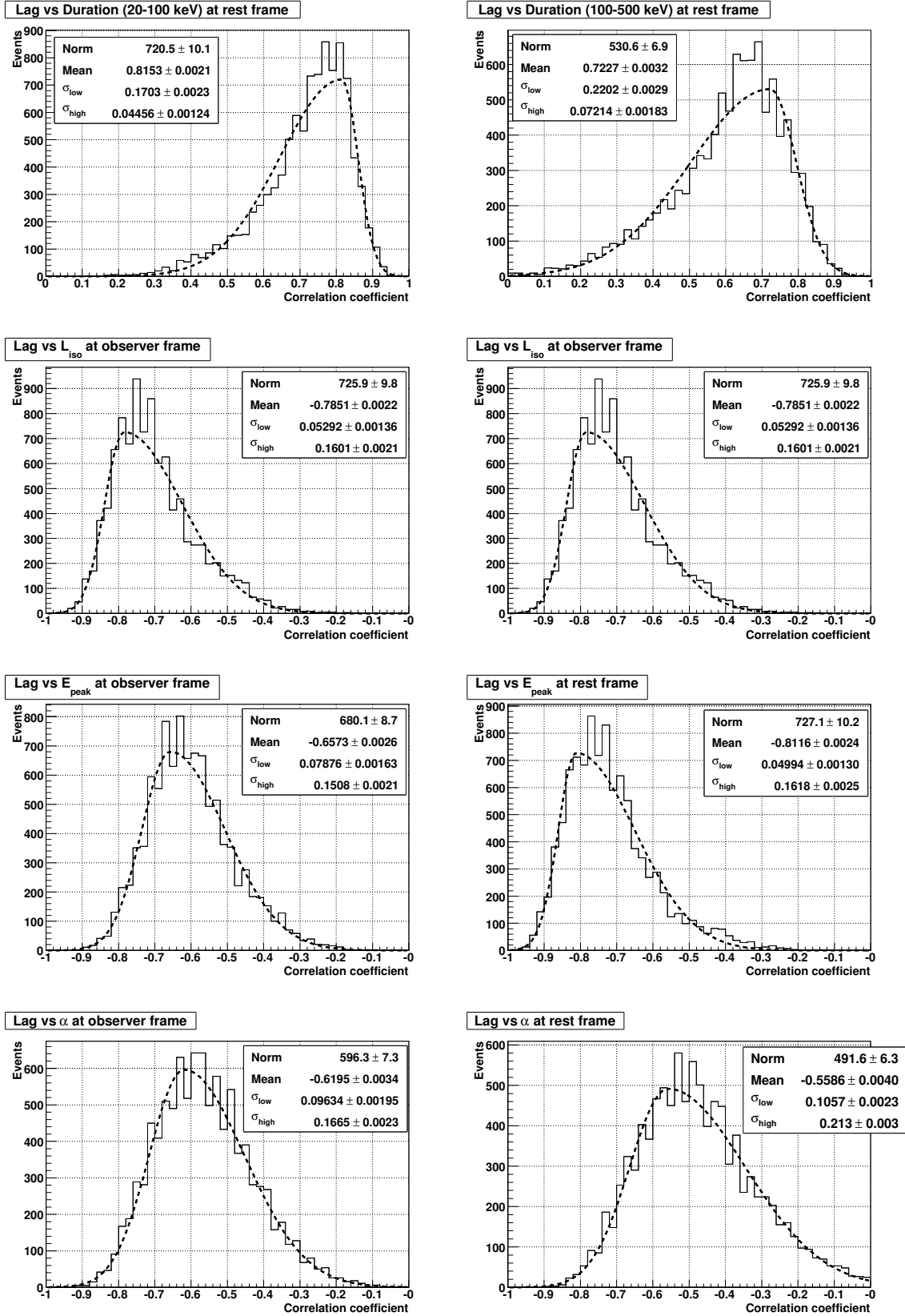


Figure C.1: Distributions of the correlation-coefficient.

Appendix D

Theoretical model of the curvature effect

We review the latest theoretical and numerical studies of the curvature effect for expanding fireballs. The model we are reviewing is by Lu et al. 2006 based on Qin & Lu, 2005, Qin & Lu, 2005 and Qin 2002.

We consider a fireball expanding at a constant velocity $v = \beta c$ (where c is the speed of light) and adopt a spherical system with its origin at the center of the fireball and its axis being the line of sight. Consider radiation from the rest frame differential surface, $ds_{0,\theta,\phi}$, of the fireball at proper time $t_{0,\theta}$, where θ denotes the angle to the line of sight and ϕ denotes the other angular coordinate (azimuthal angle) of the fireball surface. Let $ds_{\theta,\phi}$ be the corresponding differential surface in the observer's frame, where $ds_{0,\theta,\phi}$ moves at velocity v relative to $ds_{\theta,\phi}$.

Let t_θ be the corresponding coordinate time when $ds_{\theta,\phi}$ coincides with $ds_{0,\theta,\phi}$ at $t_{0,\theta}$. According to special relativity theory, t_θ and $t_{0,\theta}$ are given by

$$t_\theta - t_c = \Gamma (t_{0,\theta} - t_{0,c}) \quad (\text{D.1})$$

where t_c and $t_{0,c}$ are constants (here we assign $t_\theta = t_c$ when $t_{0,\theta} = t_{0,c}$) and Γ is the Lorentz factor of the fireball, $\Gamma = 1/\sqrt{1-\beta^2}$. The area of $ds_{\theta,\phi}$ is

$$ds_{\theta,\phi} = R^2(t_\theta) \sin \theta d\theta d\phi \quad (\text{D.2})$$

where $R(t_\theta)$ is the radius of the fireball at t_θ . The radius follows

$$R(t_\theta) = \beta c(t_\theta - t_c) + R_c \quad (\text{D.3})$$

where R_c is the radius at time $t_\theta = t_c$. As assigned above, t_θ and $t_{0,\theta}$ correspond to the same moment, so applying Eq. D.1 the radius can also be expressed as

$$R_0(t_{0,\theta}) = R(t_\theta(t_{0,\theta})) = \Gamma \beta c(t_{0,\theta} - t_{0,c}) + R_c \quad (\text{D.4})$$

Let us consider an observation within the small intervals $t-t+dt$ and $\nu-\nu+d\nu$ carried out by an observer with a detector having effective area Δs_{ob} at a distance D (D is the distance between the observer and the center of the fireball), where $D \gg R(t_\theta)$. Suppose radiation from $ds_{0,\theta,\phi}$ arriving at the observer within the above observation intervals is emitted within the proper time interval $t_{0,\theta} - t_{0,\theta} + dt_{0,\theta}$ and the rest frame frequency interval $\nu_{0,\theta} - \nu_{0,\theta} + d\nu_{0,\theta}$. According to the Doppler effect (see the appendix A), ν and $\nu_{0,\theta}$ are related by

$$\nu = \frac{\nu_{0,\theta}}{\Gamma(1 - \beta \cos \theta)} \quad (\text{D.5})$$

Consider the light traveling time from the fireball to the observer, we get

$$c(t - t_\theta) = D - R(t_\theta) \cos \theta \quad (\text{D.6})$$

Note that cosmological effects are ignored. Combining Eq. D.1, D.3 and D.6 yields,

$$t_\theta = \frac{t - t_c - D/c + (R_c/c) \cos \theta}{1 - \beta \cos \theta} + t_c \quad (\text{D.7})$$

and

$$t_{0,\theta} = \frac{t - t_c - D/c + (R_c/c) \cos \theta}{\Gamma(1 - \beta \cos \theta)} + t_{0,c}. \quad (\text{D.8})$$

The radius of the fireball then can be written as

$$R[t_\theta(t)] = R_0[t_{0,\theta}(t)] = \frac{\beta[c(t - t_c) - D] + R_c}{1 - \beta \cos \theta} \quad (\text{D.9})$$

where we use $D \gg R_c$. Suppose photons, which are emitted from $ds_{0,\theta,\phi}$ within a proper time interval $t_{0,\theta} - t_{0,\theta} + dt_{0,\theta}$ and then reach the observer at $t - t + dt$, pass through $ds_{\theta,\phi}$ in coordinate time interval $t_\theta - t_\theta + dt_\theta$. Since both $ds_{\theta,\phi}$ and the observer are in the same frame, $dt_\theta = dt$ (when cosmological effects are ignored). Of course, the frequency interval $\nu - \nu + d\nu$ for the photons measured by both $ds_{\theta,\phi}$ and the observer must be the same. Suppose the radiation is independent of direction. Then from the view of $ds_{\theta,\phi}$ (which is also the view of the observer), the amount of energy emitted from $ds_{0,\theta,\phi}$ from $t_{0,\theta} - t_{0,\theta} + dt_{0,\theta}$ and $\nu_{0,\theta} - \nu_{0,\theta} + d\nu_{0,\theta}$ (which would pass through $ds_{\theta,\phi}$ in $t_\theta - t_\theta + dt_\theta$ and be measured within $\nu - \nu + d\nu$) towards the observer would be

$$dE_{\theta,\phi} = I_\nu(t_\theta, \nu) \cos \theta ds_{\theta,\phi} d\omega d\nu dt, \quad (\text{D.10})$$

where $I_\nu(t_\theta, \nu)$ is the intensity of radiation measured by $ds_{\theta,\phi}$ or by the observer and $d\omega$ is the solid angle of Δs_{ob} with respect to the fireball, which is,

$$d\omega = \frac{\Delta s_{\text{ob}}}{D^2} \quad (\text{D.11})$$

It is clear that any elements of emission from the fireball are independent of ϕ due to the symmetric nature of the object. Thus,

$$dE_{\theta,\phi} = \frac{\Delta s_{\text{ob}} R^2(t_\theta) I_\nu(t_\theta, \nu) \cos \theta \sin \theta d\nu dt d\theta d\phi}{D^2}, \quad (\text{D.12})$$

where Eq. D.2 and D.11 have applied.

The total amount of energy emitted from the whole fireball surface detected by the observer within the above observation intervals is an integration of $dE_{\theta,\phi}$ over that area, which is

$$dE = \frac{2\pi \Delta s_{\text{ob}} d\nu dt}{D^2} \int_{\bar{\theta}_{\text{min}}}^{\bar{\theta}_{\text{max}}} R^2(t_\theta) I_\nu(t_\theta, \nu) \cos \theta \sin \theta d\theta \quad (\text{D.13})$$

where we use $\int d\phi = 2\pi$, and $\bar{\theta}_{\text{max}}$ and $\bar{\theta}_{\text{min}}$ are determined by the fireball surface itself together with the emitted ranges of $t_{0,\theta}$ and $\nu_{0,\theta}$. Thus, the expected flux in unit of area, frequency and time would be

$$f_\nu(t) = \frac{2\pi}{D^2} \int_{\bar{\theta}_{\text{min}}}^{\bar{\theta}_{\text{max}}} R^2(t_\theta) I_\nu(t_\theta, \nu) \cos \theta \sin \theta d\theta \quad (\text{D.14})$$

where we divide Eq. D.13 by $\Delta s_{\text{ob}} d\nu$ and dt . If during some period the radiation of the fireball is dominated by a certain mechanism, then within this interval of time the intensity can be expressed as

$$I_\nu(t_\theta, \nu) = I(t_\theta) g_\nu(\nu) \quad (\text{D.15})$$

where $I(t_\theta)$ represents the time evolution of the intensity magnitude in the observer's frame and $g_\nu(\nu)$ is the spectrum in the observer's frame. The observer's frame spectrum $g_\nu(\nu)$ is related to the rest frame intensity $g_{0,\nu}(\nu_{0,\theta})$ by

$$g_\nu(\nu) = \left(\frac{\nu}{\nu_{0,\theta}} \right)^3 g_{0,\nu}(\nu_{0,\theta}) \quad (\text{D.16})$$

from Rybicki & Lightman 1986. As $\nu/\nu_{0,\theta} = 1/\Gamma(1 - \beta \cos \theta)$ from Eq. D.5, the flux can be rewritten as

$$f_\nu(t) = \frac{2\pi}{D^2 \Gamma^3} \int_{\bar{\theta}_{\text{min}}}^{\bar{\theta}_{\text{max}}} \frac{R_0^2(t_\theta) I(t_\theta) g_{0,\nu}(\nu_{0,\theta}) \cos \theta \sin \theta}{(1 - \beta \cos \theta)^3} d\theta \quad (\text{D.17})$$

Using Eq. D.4 and D.7, Eq. D.17 is rewritten as

$$f_\nu(t) = \frac{2\pi c^2 [(t - t_c - D/c)\beta + R_c/c]^2}{D^2 \Gamma^3} \int_{\bar{\theta}_{\text{min}}}^{\bar{\theta}_{\text{max}}} \frac{I(t_\theta) g_{0,\nu}(\nu_{0,\theta}) \cos \theta \sin \theta}{(1 - \beta \cos \theta)^5} d\theta \quad (\text{D.18})$$

Assume that the area of the fireball surface is confined within

$$\theta_{\text{min}} \leq \theta \leq \theta_{\text{max}} \quad (\text{D.19})$$

and the emission time t_θ is confined within

$$t_c \leq t_{\theta,\min} \leq t_\theta \leq t_{\theta,\max} \quad (\text{D.20})$$

and that there are no other constraints to the integral limit $\bar{\theta}_{\min}$ and $\bar{\theta}_{\max}$. According to Eq. D.19 and D.20, one can verify that the lower and upper integral limits of $\bar{\theta}_{\min}$ and $\bar{\theta}_{\max}$ can be determined by

$$\bar{\theta}_{\min} = \cos^{-1} \min \left[\cos \theta_{\min}, \frac{t_{\theta,\max} - t + D/c}{(t_{\theta,\max} - t_c)\beta + R_c/c} \right] \quad (\text{D.21})$$

and

$$\bar{\theta}_{\max} = \cos^{-1} \min \left[\cos \theta_{\max}, \frac{t_{\theta,\min} - t + D/c}{(t_{\theta,\min} - t_c)\beta + R_c/c} \right] \quad (\text{D.22})$$

respectively, where Eq. D.3 and D.20 are applied.

Light curves of GRBs are always presented in terms of count rates within a certain energy range. The count rate within energy channel $\nu_1 \leq \nu \leq \nu_2$ is determined by

$$\frac{dn(t)}{dt} = \int_{\nu_1}^{\nu_2} \frac{f_\nu(t)}{h\nu} d\nu \quad (\text{D.23})$$

Using Eq. D.18,

$$\frac{dn(t)}{dt} = \frac{2\pi c^2 [(t - t_c - D/c)\beta + R_c/c]^2}{hD^2\Gamma^3} \int_{\bar{\theta}_{\min}}^{\bar{\theta}_{\max}} \frac{I(t_\theta) \cos \theta \sin \theta}{(1 - \beta \cos \theta)^5} d\theta \int_{\nu_1}^{\nu_2} \frac{g_{0,\nu}(\nu_{0,\theta})}{\nu} d\nu \quad (\text{D.24})$$

Assign

$$\tau_\theta \equiv \frac{t_\theta - t_c}{R_c/c}, \quad \tau_{\theta,\min} \equiv \frac{t_{\theta,\min} - t_c}{R_c/c}, \quad \tau_{\theta,\max} \equiv \frac{t_{\theta,\max} - t_c}{R_c/c}, \quad \tau \equiv \frac{t - t_c - D/c + R_c/c}{R_c/c} \quad (\text{D.25})$$

One would find that

$$\tau_\theta = \frac{\tau - (1 - \cos \theta)}{1 - \beta \cos \theta}, \quad \tau_{\theta,\min} \leq \tau_\theta \leq \tau_{\theta,\max}, \quad (\text{D.26})$$

and

$$1 - \cos \theta_{\min} + (1 - \beta \cos \theta_{\min})\tau_{\theta,\min} \leq \tau \leq 1 - \cos \theta_{\max} + (1 - \beta \cos \theta_{\max})\tau_{\theta,\max} \quad (\text{D.27})$$

(which is the range of τ within the radiation defined in Eq. D.19 and D.20 is observable).

One can verify that, in terms of the integral of τ_θ , the count rate Eq. D.28

$$\begin{aligned} C(\tau) \equiv \frac{dn[t(\tau)]}{d\tau} &= \frac{2\pi R_c^3}{hcD^2\Gamma^3(1 - \beta)^2(1 + k\tau)^2} \int_{\bar{\tau}_{\theta,\min}}^{\bar{\tau}_{\theta,\max}} \bar{I}(\tau_\theta)(1 + \beta\tau_\theta)^2(1 - \tau + \tau_\theta) d\tau_\theta \\ &\times \int_{\nu_1}^{\nu_2} \frac{g_{0,\nu}(\nu_{0,\theta})}{\nu} d\nu \end{aligned} \quad (\text{D.28})$$

where τ is constrained by Eq. D.27 and $\bar{I}(\tau_\theta) \equiv I[t_\theta(\tau_\theta)]$, $k \equiv \beta/(1 - \beta)$. $\bar{\tau}_{\theta,\min}$ and $\bar{\tau}_{\theta,\max}$ are determined by

$$\bar{\tau}_{\theta,\min} = \max \left(\tau_{\theta,\min}, \frac{\tau - 1 + \cos \theta_{\max}}{1 - \beta \cos \theta_{\max}} \right) \quad (\text{D.29})$$

and

$$\bar{\tau}_{\theta,\max} = \min \left(\tau_{\theta,\max}, \frac{\tau - 1 + \cos \theta_{\min}}{1 - \beta \cos \theta_{\min}} \right) \quad (\text{D.30})$$

In this calculation, we employ a local Gaussian pulse for $\bar{I}(\tau_\theta)$ and the Band function for $g_{0,\nu}(\nu_{0,\theta})$ in the following.

$$\bar{I}(\tau_\theta) = I_0 \exp \left[- \left(\frac{\tau_\theta - \tau_{\theta,0}}{\sigma} \right)^2 \right] \quad (\text{D.31})$$

where I_0 and σ are constants and we assign $\tau_{\theta,0} = 10 \sigma + \tau_{\theta,\min}$ so that the interval between $\tau_{\theta,\min}$ and $\tau_{\theta,0}$ would be large enough to make the rising phase of the local pulse close to that of the Gaussian pulse. We also assign $R_c = 3 \times 10^{15}$ cm, $\tau_{\theta,\min} = 0$, $\theta_{\min} = 0$, and $\theta_{\max} = \pi/2$.

Appendix E

Other GRBs detected by the *Fermi* LAT

E.1 GRB 080825C

GRB 080825C triggered the GBM at 14:13:48 UTC on August 25th 2008 (van der Horst & Connaughton 2008) with the NaI detectors. The ground localization of GRB 080825C was $(\text{RA}, \text{Dec}) = (222.6^\circ, -4.9^\circ)$ with a statistical uncertainty of 1.5 deg at the 1σ confidence level. The position of the GRB determined by the GBM was 60° from the LAT boresight at the trigger time which put it at the edge of the LAT field-of-view. The light curves are shown in the left panel of Fig. E.1 superimposing the pulse-fit function, and an enlarged illustration is shown in the right panel of Fig. E.1. Interestingly no LAT events coincide with the first GBM X-ray peak and the sub-GeV emission seems to coincide with the second X-ray pulse like in GRB 080916C. The X-ray emission has a dramatic variation and the hard-to-soft feature typical of GRBs (Longer durations at lower energies) is seen. Figs. E.2 and E.3 show the pulse-fit results of the spectral analysis. The spectral result also shows the hard-to-soft evolution as a function of time and the pulse-fit result shows the typical feature of the spectral lag; the higher-energies photons lead the lower-energy photons for most pulses.

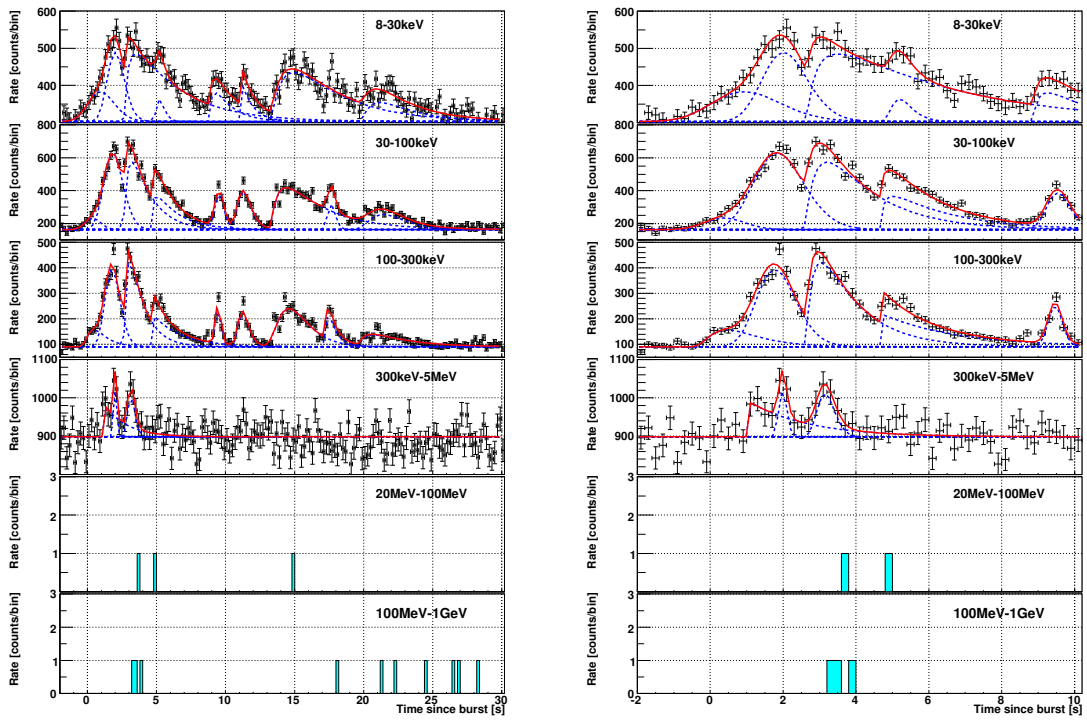


Figure E.1: Light curve of 0800825C observed by the GBM and LAT detectors (Left) -2 s to 30 s from the trigger. (Right) -2 to 10 s from the trigger.

Although in the classical X-ray and gamma-ray bands this burst has typical features, above 20 MeV the behavior is quite different from that in the classical band. The sub-GeV emission is delayed from the X-ray emission, and in addition the long sub-GeV emission lasts ~ 200 s after the end of the X-ray emission as shown in Fig. E.4 , which indicates that the classical X-ray emission mechanism is quite different from the GeV (sub-GeV) one or the emission sites are different.

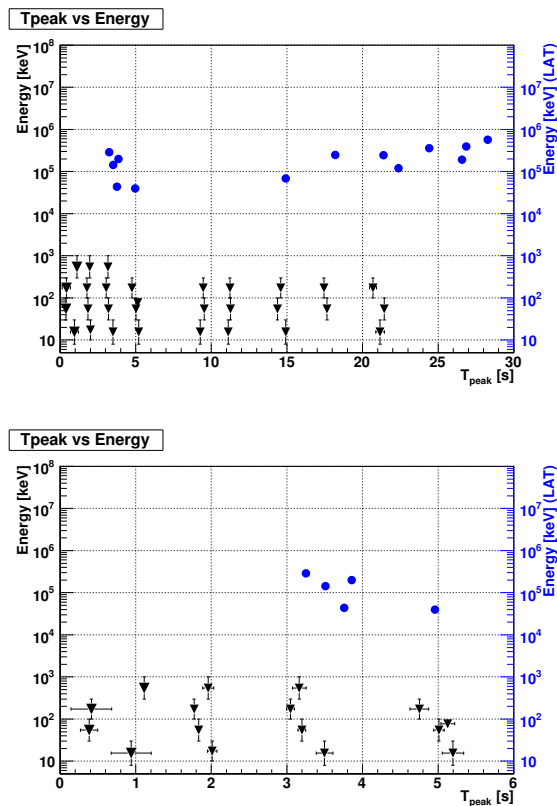


Figure E.2: Pulse-fit result for GRB 080825C. (Top) -2 s to 30 s from the trigger. (Bottom) -2 to 10 s from the trigger. Blue dots represent the energies of the LAT events.

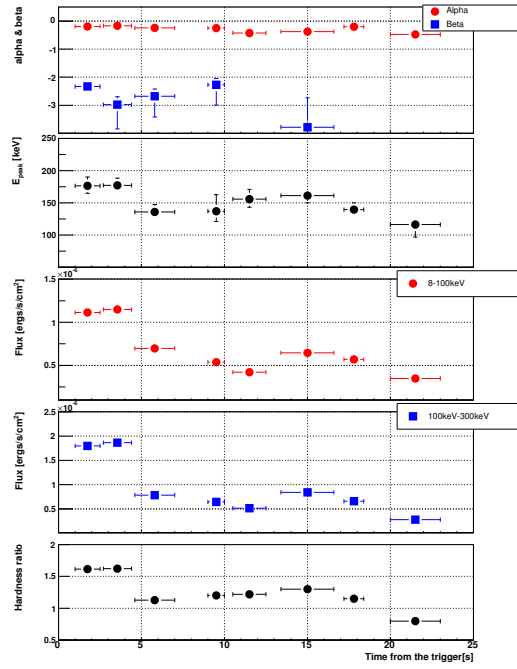


Figure E.3: Spectral-fit result for GRB 080825C

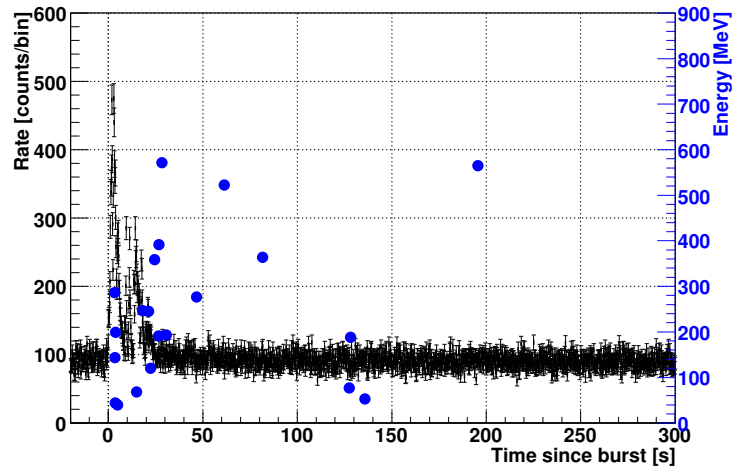


Figure E.4: Long sub-GeV emission. Blue dots represent the energies of the LAT events.

E.2 GRB 081024B

GRB 081024B triggered the *Fermi* LAT telescope (Omodei 2008) and the GBM detector (Connaughton & Briggs 2008) at 21:22:41 UTC on August 25th 2008. The burst was at 21.3 degrees from the LAT boresight. The LAT telescope localized the burst to (RA, Dec) = (21:31:36.00, 21:12:14.4) within a statistical uncertainty of 0.16 degrees at the 1σ confidence level which is consistent with the calculated position from the GBM detectors independently. Follow-up observations were performed and the *Swift* XRT (e.g. Guidorzi et al. 2008) and a ground-based optical telescope (Cenko & Kasliwal 2008) detected several candidates for the afterglow.

The light curves are shown in Fig. E.5. In the X-ray band, the total duration of GRB 081024B is ~ 700 ms and the burst seems to consist of 2 pulses; a very short pulse with duration ~ 200 ms represented by (a) and a broad pulse with duration ~ 500 ms represented by (b). Interestingly enough, the GeV emission detected by the LAT telescope does not coincide with the first pulse but rather the second pulse, and the same trend of the delayed GeV emission has been seen in GRB 080916C and GRB 080825C described above. In addition the long (~ 3 s) GeV emission continues after the end of the X-ray emission. The highest energies for the detected photons by LAT are 3068 ± 307 MeV and 1682 ± 168 MeV at ~ 0.5 s and 2.1 s from the trigger.

The spectral-fit analysis is given in Table E.1. For the first pulse E_{peak} is ~ 1 MeV because the cutoff powerlaw function gives a better χ^2 compared with the powerlaw function while for the second pulse a significant E_{peak} does not appear.

This burst has a duration < 2 s and may be a short GRB. As Nakar 2007 suggested that short GRBs show a symmetric distribution of spectral lags that ranges between ± 30 ms in the classical X-ray band. In our spectral analysis, we calculate the spectral lags in two ways; pulse-fit and CCF. For the pulse-fit analysis, the result is shown in Fig. E.6 and there are no significant spectral lags for both pulses. For the CCF analysis, we make the light curve in 30 ms time bins and calculate the CCF in the manner of Band 1997. The result is shown in Fig. E.7. Although the statistical fluctuations are large, a significant lag does not appear (The highest CCF is at lag = 0. The peak at -0.3 s corresponds to the second peak). From this analysis, it is highly possible that GRB 081024B is a short GRBs. This suggests that the GeV emission is delayed from the first emission in the X-ray band no matter what the type of GRB is. Since generally the origin of short GRBs is different from that of long GRBs (e.g. Gehrels et al. 2005), this fact impacts the standard theory of GRBs greatly.

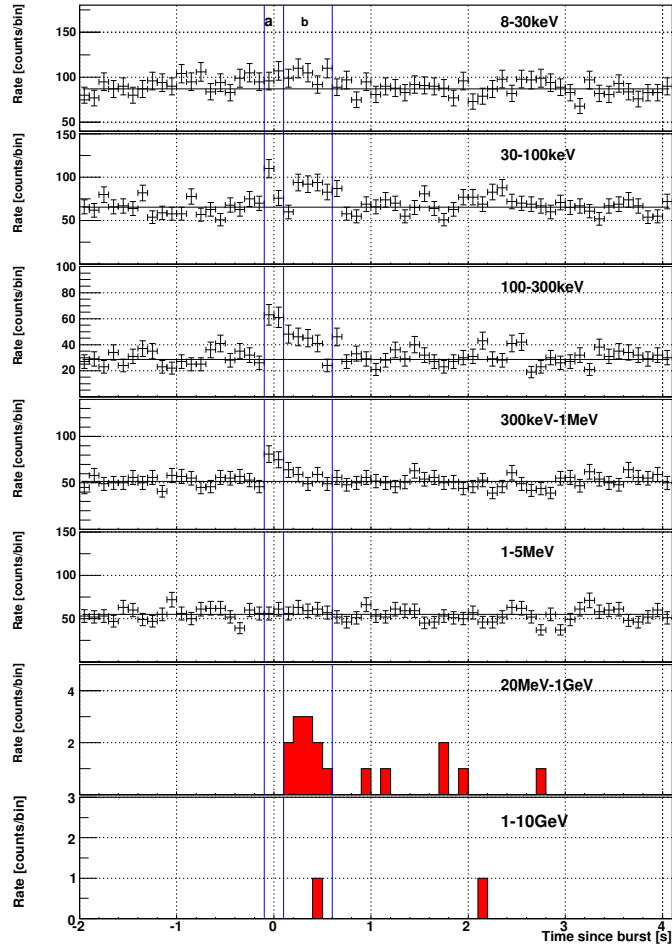


Figure E.5: Light curves for GRB 081024B

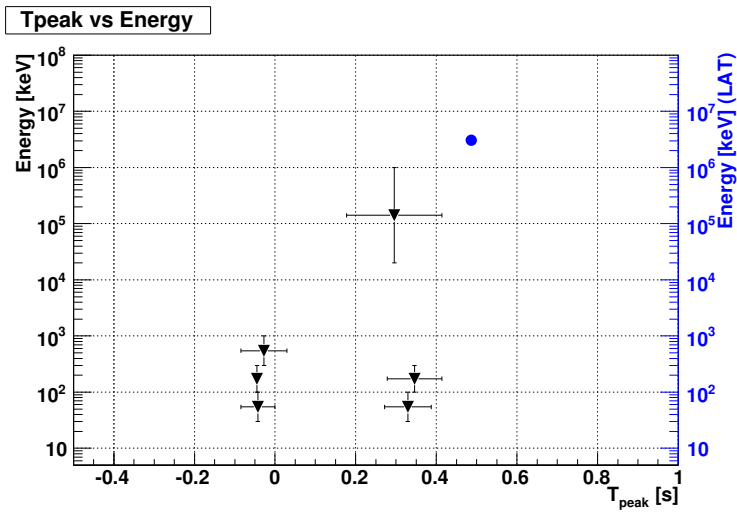


Figure E.6: Energy vs. t_{peak} plot for GRB081024B. Blue dots show the energy of LAT events above 1 GeV.

Table E.1: Spectral properties for GRB 081024B

Region	Model	$E_{\text{peak}}^{\text{obs}}$ [keV]	α	β	Normalization [†] [ph cm ⁻² s ⁻¹ keV ⁻¹]	χ_{ν}^2 (d.o.f.)
(a)	powerlaw	-	$-1.10^{+0.07}_{-0.07}$	-	$8.99^{+1.47}_{-1.48} \times 10^{-3}$	1.28(20)
(a)	cutoff p.l.	1028^{+472}_{-342}	$-0.38^{+0.45}_{-0.32}$	-	$1.19^{+0.29}_{-0.24} \times 10^{-2}$	0.96(20)
	Model	$E_{\text{peak}}^{\text{obs}}$ [MeV]	α	β	Normalization* [ph cm ⁻² s ⁻¹ keV ⁻¹]	C_{stat} (PHA bins)
(b)	powerlaw	-	$-1.77^{+0.04}_{-0.04}$	-	$8.46^{+1.37}_{-1.18} \times 10^{-5}$	23.84(19)
(b)	cutoff p.l.	231^{+2747}_{-39}	$-1.72^{+0.06}_{-0.05}$	-	$9.63^{+1.88}_{-1.65} \times 10^{-5}$	22.67(19)

†: Normalization at 100 keV

*: Normalization at 1 MeV

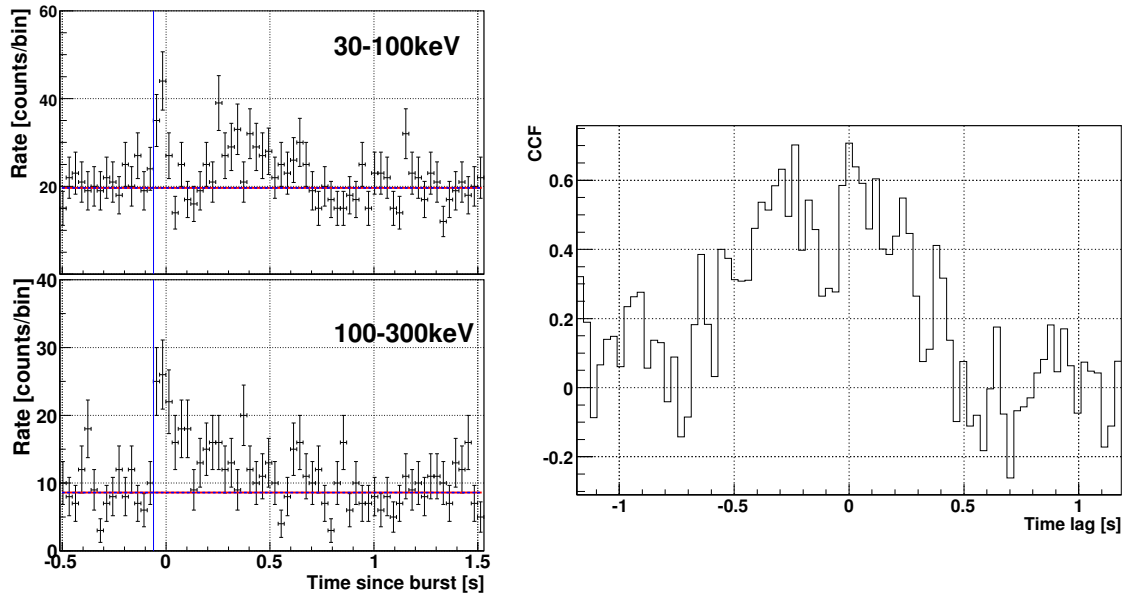


Figure E.7: Spectral lag of CCF for GRB 081024B. The peak at around -0.3 s corresponds to the second peak.

Appendix F

Works

F.1 Paper

1. J. Kataoka, T. Saito, Y. Kuramoto, T. Ikagawa, Y. Yatsu, J. Kotoku, M. Arimoto, N. Kawai, Y. Ishikawa, N. Kawabata “Recent progress of avalanche photodiodes in high-resolution X-rays and γ -rays detection” Nuclear Instruments and Methods in Physics Research A 541 398-404 (2005)
2. R. Sato, T. Sakamoto, J. Kataoka, A. Yoshida, M. Suzuki, J. Kotoko, Y. Urata, Y. Yamamoto, M. Arimoto, T. Tamagawa, Y. Shirasaki, K. Torii, M. Matsuoka, Y. Nakagawa, T. Yamazaki, K. Tanaka, M. Maetou, M. Yamauchi, K. Takakishi, D. Lamb, J.-L. Atteia, R. Vanderspek, C. Graziani, G. Prigozhin, Villasenor, J.G. Jernigan, G.B. Crew, K. Hurley, G.R. Ricker, E. Woosley, N. Butler, A. Levine, J.P. Doty, T.Q. Donaghy, E. Fenimore, M. Galassi, M. Boer, J.-P. Dezalay, J.-F. Olive, J. Braga, R. Manchanda, G. Pizzichini, N. Kawai ”HETE-2 Localization and Observations of the Gamma-Ray Burst GRB 020813” Publications of the Astronomical Society of Japan, Vol. 57, No. 6, 1031-1039 (2005)
3. Nakagawa Yujin E., Yoshida Atsumasa, Sugita Satoshi, Tanaka Kaoru, Ishikawa Nobuyuki, Tamagawa Toru, Suzuki Motoko, Shirasaki Yuji, Kawai Nobuyuki, Matsuoka Masaru, Atteia Jean-Luc, Pelangeon Alexandre, Vanderspek Roland, Crew Geoffrey B., Villasenor Joel S., Butler Nat, Doty John P., Ricker George R., Pizzichini Graziella, Donaghy Timothy Q., Lamb Donald Q., Graziani Carlo, Sato Rie, Maetou Miki, Arimoto Makoto, Kotoku Jun’ichi, Jernigan J. Garrett, Sakamoto Takanori, Olive Jean-Francois, Boer Michel, Fenimore Edward E., Galassi Mark, Woosley Stanford E., Yamauchi Makoto, Takagishi Kunio, Hatsukade Isamu “An Optically Dark GRB Observed by HETE-2: GRB 051022” Publications of the As-

tronomical Society of Japan, Vol.58, No.4, pp. L35-L39 (2006)

4. Y. Kanai, M. Ueno, J. Kataoka, M. Arimoto, N. Kawai, K. Yamamoto, T. Mizuno, Y. Fukazawa, M. Kiss, T. Ylinen, C. M. Bettolo, P. Carlson, W. Klamra, P. Chen, B. Craig, T. Kamae, G. Madejski, J.S.T. Ng, R. Rogers, H. Tajima, T. S. Thurston, Y. Saito, T. Takahashi, S. Gunji, C.-I. Bjornsson, S. Larsson, F. Ryde, G. Bogaert, S. Kishimoto “Beam test of a prototype phoswich detector assembly for the PoGOLite astronomical soft gamma-ray polarimeter” Nuclear Instruments and Methods in Physics Research A Vol. 570 pp. 61-71 (2007)
5. M. Suzuki, N. Kawai, T. Tamagawa, A. Yoshida, Y. Nakagawa, K. Tanaka, Y. Shirasaki, M. Matsuoka, G.R. Ricker, R. Vanderspek, N. Butler, D.Q. Lamb, C. Graziani, G. Pizzichini, R. Sato, M. Arimoto, J. Kotoku, M. Maetou, M. Yamauchi “Discovery of a New X-Ray Burst/Millisecond Accreting Pulsar HETE J1900.1-2455” Publications of the Astronomical Society of Japan, Vol. 59, No. 1, 263-268 (2007)
6. J. Kataoka, J.N. Reeves, K. Iwasawa, A.G. Markowitz, R.F. Mushotzky, M. Arimoto, T. Takahashi, Y. Tsubuku, M. Ushio, S. Watanabe, L.C. Gallo, G.M. Madejski, Y. Terashima, N. Isobe, M.S. Tashiro, T. Kohmura “Probing the Disk-jet Connection of the Radio Galaxy 3C120 Observed with Suzaku” Publications of the Astronomical Society of Japan, Vol. 59, No. 2, 279-297 (2007)
7. Nakagawa Yujin E., Yoshida Atsumasa, Hurley Kevin, Atteia Jean-Luc, Maetou Miki, Tamagawa Toru, Suzuki Motoko, Yamazaki Tohru, Tanaka Kaoru, Kawai Nobuyuki, Shirasaki Yuji, Pelangeon Alexandre, Matsuoka Masaru, Vanderspek Roland, Crew Geoffrey B., Villasenor Joel S., Sato Rie, Sugita Satoshi, Kotoku Jun'ichi, Arimoto Makoto, Pizzichini Graziella, Doty John P., Ricker George R. “A Comprehensive Study of Short Bursts from SGR1806-20 and SGR1900+14 Detected by HETE-2” Publications of the Astronomical Society of Japan, Vol. 59, p. 653 (2007)
8. M. Arimoto, N. Kawai, M. Suzuki, R. Sato, N. V. Pazmino, T. Shimokawabe, T. Ishimura, J. Kotoku, A. Yoshida, T. Tamagawa, Y. Shirasaki, M. Matsuoka, Y. E. Nakagawa, N. Ishikawa, A. Kobayashi, S. Sugita, I. Takahashi, M. Kuwahara, M. Yamauchi, K. Takagishi, I. Hatsukade, J.-L. Atteia, A. Pelangeon, R. Vanderspek, C. Graziani, G. Prigozhin, Villasenor, J. G. Jernigan, G. B. Crew, K. Hurley, T. Sakamoto, G. R. Ricker, E. Woosley, N. Butler, A. Levine, J. P. Doty, T. Q. Donaghy,

- E. Fenimore, M. Galassi, M. Boer, J.-P. Dezalay, J. -F. Olive, J. Braga, R. Manchanda, and G. Pizzichini “HETE-2 Observation of the X-Ray Flash XRF 040916” Publications of the Astronomical Society of Japan, Vol 59, No. 3, 695 (2007)
9. M. Axelsson, O. Engdegrd, F. Ryde, S. Larsson, M. Pearce, L. Hjalmarsson, M. Kiss, C. Marini Bettolo, M. Arimoto, C.-I. Bjrnsen, P. Carlson, Y. Fukazawa, T. Kamae, Y. Kanai, J. Kataoka, N. Kawai, W. Klamra, G. Madejski, T. Mizuno, J. Ng, H. Tajima, T. Takahashi, T. Tanaka, M. Ueno, G. Varner and K. Yamamoto “Measuring energy dependent polarization in soft γ -rays using Compton scattering in PoGOLite” Astroparticle Physics, Vol. 28, Issue 3, 327-337 (2007)
 10. S. Tanaka, J. Kataoka, Y. Kanai, Y. Yatsu, M. Arimoto, M. Koizumi, N. Kawai, Y. Ishikawa, S. Kawai, N. Kawabata “Development of wideband X-ray and gamma-ray spectrometer using transmission-type, large-area APD” Nuclear Instruments and Methods in Physics Research A, Vol. 582, pp. 562-568. (2007)
 11. Y. Shirasaki, A. Yoshida, N. Kawai, T. Tamagawa, T. Sakamoto, M. Suzuki, Y. Nakagawa, A. Kobayashi, S. Sugita, I. Takahashi, M. Arimoto, T. Shimokawabe, N. V. Pazmino, T. Ishimura, R. Sato, M. Matsuoka, E. E. Fenimore, M. Galassi, D. Q. Lamb, C. Graziani “Multiple-Component Analysis of the Time-Resolved Spectra of GRB041006: A Clue to the Nature of the Underlying Soft Component of GRBs” Publications of the Astronomical Society of Japan, Vol. 60, No. 1, p. 919 (2008)
 12. Kamae Tuneyoshi, Andersson Viktor, Arimoto Makoto, Axelsson Magnus, Marini Bettolo Cecilia, Bjrnsen Claes-Ingvar, Bogaert Gilles, Carlson Per, Craig William, Ekeberg Tomas, Engdegrd Olle, Fukazawa Yasushi, Gunji Shuichi, Hjalmarsson Linnea, Iwan Bianca, Kanai Yoshikazu, Kataoka Jun, Kawai Nobuyuki, Kazejev Jaroslav, Kiss Mozsi, Klamra Wlodzimierz, Larsson Stefan, Madejski Grzegorz, Mizuno Tsunefumi, Ng Johnny, Pearce Mark, Ryde Felix, Suhonen Markus, Tajima Hiroyasu, Takahashi Hiromitsu, Takahashi Tadayuki, Tanaka Takuya, Thurston Timothy, Ueno Masaru, Varner Gary, Yamamoto Kazuhide, Yamashita Yuichiro, Ylinen Tomi “PoGOLite A high sensitivity balloon-borne soft gamma-ray polarimeter” Astroparticle Physics, Volume 30, Issue 2, p. 72-84. (2008)
 13. A. Abdo, M. Ackermann, M. Arimoto, K. Asano, W. B. Atwood, M. Axelsson, L. Baldini, J. Ballet, D. L. Band, G. Barbiellini, M. G. Baring, D. Bastieri, M. Battelino, B. M. Baughman, K. Bechtol, F. Bellardi, R. Bellazzini, B. Berenji, P. N. Bhat, E. Bissaldi, R. D. Blandford, E. D. Bloom, G. Bogaert, J. R. Bogart, E. Bonamente, J. Bonnell, A. W. Borgland, A. Bouvier, J. Bregeon, A. Brez, M.

S. Briggs, M. Brigida, P. Bruel, T. H. Burnett, D. Burrows, G. Busetto, G. A. Caliandro, R. A. Cameron, P. A. Caraveo, J. M. Casandjian, M. Ceccanti, C. Cecchi, A. Celotti, E. Charles, A. Chekhtman, C. C. Cheung, J. Chiang, S. Ciprini, R. Claus, J. Cohen-Tanugi, L. R. Cominsky, V. Connaughton, J. Conrad, L. Costamante, S. Cutini, M. DeKlotz, C. D. Dermer, A. de Angelis, F. de Palma, S. W. Digel, B. L. Dingus, E. do Couto e Silva, P. S. Drell, R. Dubois, D. Dumora, Y. Edmonds, P. A. Evans, D. Fabiani, C. Farnier, C. Favuzzi, J. Finke, G. Fishman, W. B. Focke, M. Frailis, Y. Fukazawa, S. Funk, P. Fusco, F. Gargano, D. Gasparrini, N. Gehrels, S. Germani, B. Giebels, N. Giglietto, P. Giommi, F. Giordano, T. Glanzman, G. Godfrey, A. Goldstein, J. Granot, J. Greiner, I. A. Grenier, M.-H. Grondin, J. E. Grove, L. Guillemot, S. Guiriec, G. Haller, Y. Hanabata, A. K. Harding, M. Hayashida, E. Hays, J. A. Hernando Morata, A. Hoover, R. E. Hughes, G. Jhannesson, A. S. Johnson, R. P. Johnson, T. J. Johnson, W. N. Johnson, T. Kamae, H. Katagiri, J. Kataoka, A. Kavelaars, N. Kawai, H. Kelly, J. Kennea, M. Kerr, R. M. Kippen, J. Knudsen, D. Kocevski, M. L. Kocian, N. Komin, C. Kouveliotou, F. Kuehn, M. Kuss, J. Lande, D. Landriu, S. Larsson, L. Latronico, C. Lavalley, B. Lee, S.-H. Lee, M. Lemoine-Goumard, G. G. Lichti, F. Longo, F. Loparco, B. Lott, M. N. Lovellette, P. Lubrano, G. M. Madejski, A. Makeev, B. Marangelli, M. N. Mazziotta, S. McBreen, J. E. McEnery, S. McGlynn, C. Meegan, P. Mszros, C. Meurer, P. F. Michelson, M. Minuti, N. Mirizzi, W. Mitthumsiri, T. Mizuno, A. A. Moiseev, C. Monte, M. E. Monzani, E. Moretti, A. Morselli, I. V. Moskalenko, S. Murgia, T. Nakamori, D. Nelson, P. L. Nolan, J. P. Norris, E. Nuss, M. Ohno, T. Ohsugi, A. Okumura, N. Omodei, E. Orlando, J. F. Ormes, M. Ozaki, W. S. Paciesas, D. Paneque, J. H. Panetta, D. Parent, V. Pelassa, M. Pepe, M. Perri, M. Pesce-Rollins, V. Petrosian, M. Pinchera, F. Piron, T. A. Porter, R. Preece, S. Rain, E. Ramirez-Ruiz, R. Rando, E. Rapposelli, M. Razzano, S. Razzaque, N. Rea, A. Reimer, O. Reimer, T. Reposeur, L. C. Reyes, S. Ritz, L. S. Rochester, A. Y. Rodriguez, M. Roth, F. Ryde, H. F.-W. Sadrozinski, D. Sanchez, A. Sander, P. M. Saz Parkinson, J. D. Scargle, T. L. Schalk, K. N. Segal, C. Sgr, T. Shimokawabe, E. J. Siskind, D. A. Smith, P. D. Smith, G. Spandre, P. Spinelli, M. Stamatikos, J.-L. Starck, F. W. Stecker, H. Steinle, T. E. Stephens, M. S. Strickman, D. J. Suson, G. Tagliaferri, H. Tajima, H. Takahashi, T. Takahashi, T. Tanaka, A. Tenze, J. B. Thayer, J. G. Thayer, D. J. Thompson, L. Tibaldo, D. F. Torres, G. Tosti, A. Tramacere, M. Turri, S. Tuvi, T. L. Usher, A. J. van der Horst, L. Vigiani, N. Vilchez, V. Vitale, A. von Kienlin, A. P. Waite, D. A. Williams, C. Wilson-Hodge, B. L. Winer, K. S. Wood, X. F. Wu, R. Yamazaki, T. Ylinen, and M. Ziegler “Fermi

Observations of High-Energy Gamma-Ray Emission from GRB 080916C” *Science*, Volume 323, Issue 5922, pp. 1688- (2009)

14. T. Mizuno , Y. Kanai, J. Kataoka, M. Kiss, K. Kurita, M. Pearce, H. Tajima, H. Takahashi, T. Tanaka, M. Ueno, Y. Umeki, H. Yoshida, M. Arimoto, M. Axelsson, C. Marini Bettolo, G. Bogaert, P. Chen, W. Craig, Y. Fukazawa, S. Gunji , T. Kamae, J. Katsuta, N. Kawai, S. Kishimoto, W. Klamra, S. Larsson, G. Madejski, J. S. T. Ng, F. Ryde, S. Rydström, T. Takahashi, T. S. Thurston, and G. Varner “A Monte Carlo Method for Calculating the Energy Response of Plastic Scintillators to Polarized Photons below 100 keV” *Nuclear Instruments and Methods in Physics Research A* in press

F.2 International conference and symposium

1. J. Kataoka, Y. Kanai, M. Arimoto, T. Ikagawa, N. Kawai, T. Kamae, G. M. Madejski, P. Chen, T. Mizuno, H. Tajima, J. Hg, J. W. Mitchell, L. M. Barbier, A. Harding, J. F. Krizmanic, R. E. Streitmatter, E. Groth, D. R. Marlow, S. Gunji, T. Takahashi, Y. Saito, Y. Fukazawa, P. Carlson, W. Klamra, M. Pearce, S. Larsson, G. Bogaert, “Low-energy response of a prototype detector array for the PoGO astronomical hard X-ray polarimeter” *Proc. SPIE*, 5898, 133-143, (2005)
2. T. Kotani, N. Kawai, K. Yanagisawa, J. Watanabe, M. Arimoto, H. Fukushima, T. Hattori, M. Inata, H. Izumiura, J. Kataoka, H. Koyano, K. Kubota, D. Kuroda, M. Mori, S. Nagayama, K. Ohta, T. Okada, K. Okita, R. Sato, Y. Serino, Y. Shimizu, T. Shimokawabe, M. Suzuki, H. Toda, T. Ushiyama, Y. Yatsu, A. Yoshida, M. Yoshida “MITSuME—Multicolor Imaging Telescopes for Survey and Monstrous Explosions” *Nuovo Cimento C Geophysics Space Physics C*, Vol. 28, pp. 755. (2005)
3. M. Arimoto, Y. Kanai, M. Ueno, J. Kataoka, N. Kawai, T. Tanaka, K. Yamamoto, H. Takahashi, T. Mizuno, Y. Fukazawa, M. Axelsson, M. Kiss, C. Marini Bettolo, P. Carlson, W. Klamra, M. Pearce, P. Chen, B. Craig, T. Kamae, G. Madejski, J. S. T. Ng, R. Rogers, H. Tajima, T. S. Thurston, Y. Saito, T. Takahashi, S. Gunji, C.-I. Bjornsson, S. Larsson, F. Ryde, G. Bogaert, G. Varner, “Performance assessment study of the balloon-borne astronomical soft gamma-ray polarimeter PoGOLite” *Physica E Low-Dimensional Systems and Nanostructures*, Vol. 40, pp. 438-441. (2007)
4. Arimoto Makoto, Tsubuku Yoshihiro, Toizumi Takahiro, Kobayashi Mitsuyoshi,

Yatsu Yoichi, Shimokawabe Takashi, Kataoka Jun, Kawai Nobuyuki, Omagari Kuniyuki, Fujiwara Ken, Konda Yasumi, Tanaka Yohei, Maeno Masaki, Yamanaka Tomio, Ashida Hiroki, Nishida Junichi, Fujihashi Kouta, Ikeda Takuro, Inagawa Shinichi, Miura Yoshiyuki, Matunaga Saburo “X-ray polarimetry small satellite TSUBAME” American Institute of Physics Conference Series, 1000, 607 (2008)

5. Arimoto Makoto, Kawai Nobuyuki, Suzuki Motoko, Sato Rie, Pazmino Nicolas Vasquez, Shimokawabe Takashi, Ishimura Takuto, Nakagawa Yujin E., Pelangeon Alexandre, Atteia Jean-Luc, Hurley Kevin, Pizzichini Graziella, Lamb Donald Q. “HETE-2 observation of the evidence of a long acting engine in the extremely soft XRF 040916” American Institute of Physics Conference Series, 1000, 331 (2008)
6. M. Arimoto, N. Kawai, N. Vasquez and HETE-2 member “Spectral lag analysis of GRBs detected by HETE-2” Astrophysics with All-Sky X-Ray Observations, Proceedings of the RIKEN Symposium, held 10-12 June, 2008. RIKEN, and JAXA Suzuki Umetaro Hall, RIKEN Wako, Saitama, Japan., p.248, 248 (2009)
7. M. Arimoto, N. Kawai, K. Asano ”Spectral lags of GRBs as Distance indicator” International Symposium on Nanoscience and Quantum Physics nanoPHYS’09, P1-21, International House of Japan, Roppongi Tokyo, March 2009

F.3 National conference and symposium

1. 有元 誠, 片岡淳, 河合誠之, 水野恒史, 釜江常好, 山下祐一郎, 郡司修一, 斉藤芳隆, 高橋忠幸, 深沢泰司, John W. Mitchell, Robert Streitmatter, Daniel Marlow “天体硬 X 線偏光検出器 PoGO の開発試験 (I)” 日本天文学会、2004 年秋季年会、W40a、岩手大学、2004 年 9 月
2. 有元誠, 河合誠之, 玉川徹, 吉田篤正, 白崎裕治, 松岡勝, 坂本貴紀, 鈴木素子, 古徳純一, 佐藤理江, 下川辺隆史, 中川友進, 田中薫, 前當未来, 杉田聡司, 石川信行, 小林明菜, G.Ricker, 他 HETE-2 チーム “HETE-II 衛星による XRF040916 の観測” 日本天文学会、2005 年秋季年会、H19a, 札幌, 2005 年 10 月
3. 有元誠, 金井義和, 植野優, 片岡淳, 河合誠之, 山本和英, 水野恒史, 深沢泰司, Tomi P. Ylinen, Mozsi Kiss, 田島宏康, 釜江常好, 郡司修一, 高橋忠幸, 斉藤芳隆, John W. Mitchell, Daniel Marlow, Mark Pearce “気球硬 X 線偏光検出器 PoGO の開発 (I)” 日本天文学会、2006 年春季年会、W15a, 和歌山大学, 2006 年 3 月

4. 有元誠, 金井義和, 植野優, 片岡淳, 河合誠之, 田中琢也, 山本和英, 水野恒史, 深沢泰司, 田島宏康, 釜江常好, 郡司修一, 高橋忠幸, 斉藤芳隆, Mark Pearce “気球硬 X 線偏光計 PoGOLite の開発 (I) 検出器開発” 日本天文学会, 2006 年秋季年会, W83a, 北九州, 2006 年 9 月
5. 有元誠, 河合誠之, Nicolas Vasquez, 下川辺隆史, 吉田篤正, 中川友進, 杉田聡司, 高橋一郎, 玉川徹, 桑原允, 松岡勝, 鈴木素子, 佐藤理江, 白崎裕治, 坂本貴紀, G. Ricker, 他 HETE-2 チーム “HETE-2 衛星を用いたガンマ線バーストのスペクトルラグの解析” 日本天文学会, 2008 年秋季年会, J17a, 岡山理科大学, 2008 年 9 月
6. 有元誠, 河合誠之, 浅野勝晃, Nicolas Vasquez, 下川辺隆史, 吉田篤正, 中川友進, 杉田聡司, 高橋一郎, 玉川徹, 桑原允, 松岡勝, 鈴木素子, 佐藤理江, 白崎裕治, 坂本貴紀, G. Ricker, 他 HETE-2 チーム “HETE-2 によるガンマ線バーストのラグ光度関係の検証” 日本天文学会, 2009 年春季年会, J47a, 大阪府立大学, 2009 年 3 月
7. 有元誠 “高エネルギー天体からの偏光 X 線検出器 PoGO の開発” 高エネルギー宇宙物理連絡会第 5 回研究会, 東京都立大学, 2004 年 10 月
8. 有元誠 “硬 X 線偏光検出器 PoGOLite の開発現状” 高エネルギー宇宙物理連絡会第 8 回研究会, 青山学院大学, 2007 年 10 月
9. 有元誠 “HETE-2 衛星と Fermi 衛星を用いたガンマ線バーストのスペクトラルラグの研究” 第 9 回高エネルギー宇宙物理連絡会・第 7 回博士論文発表会, 愛媛大学, 2009 年 3 月

Bibliography

Abdo, et al. *submitted* 2008

Amati, L., et al. 2002, *A&A*, 390, 81

Amati, L. 2006, *MNRAS*, 372, 233

Arimoto, M., et al. 2006, *GRB Coordinates Network*, 4550, 1

Arimoto, M., et al. 2007, *PASJ*, 59, 695

Arnaud, K. A. 1996, *Astronomical Data Analysis Software and Systems V*, 101, 17

Asano, K. 2005, *ApJ*, 623, 967

Asano, K., Inoue, S., & Mészáros, P. 2008, *arXiv:0807.0951*

Atteia, J.-L., et al. 2003, *Gamma-Ray Burst and Afterglow Astronomy 2001: A Workshop Celebrating the First Year of the HETE Mission*, 662, 17

Atwood, W. B., et al. 2007, *Astroparticle Physics*, 28, 422

Atwood et al. 2008, *ApJ*, submitted

Band, D., et al. 1993, *ApJ*, 413, 281

Band, D. L. 1997, *ApJ*, 486, 928

Berger, E., et al. 2002, *ApJ*, 581, 981

Berger, E., Gladders, M., & Oemler, G. 2005, *GRB Coordinates Network*, 3201, 1

Berger, E., Fox, D. B., Kulkarni, S. R., Frail, D. A., & Djorgovski, S. G. 2007, *ApJ*, 660, 504

Blandford, R. D., & McKee, C. F. 1976, *Physics of Fluids*, 19, 1130

Bloom, J. S., et al. 1999, *Nature*, 401, 453

- Bloom, J. S., van Dokkum, P. G., Bailyn, C. D., Buxton, M. M., Kulkarni, S. R., & Schmidt, B. P. 2004, *AJ*, 127, 252
- Boella, G., Butler, R. C., Perola, G. C., Piro, L., Scarsi, L., & Bleeker, J. A. M. 1997, *A&AS*, 122, 299
- Bosnjak, Z., Daigne, F., & Dubus, G. 2008, arXiv:0811.2956
- Briggs, M. S., et al. 1999, *ApJ*, 524, 82
- Butler, N., Dullighan, A., Ford, P., Ricker, G., Vanderspek, R., Hurley, K., Jernigan, J., & Lamb, D. 2004, *Gamma-Ray Bursts: 30 Years of Discovery*, 727, 435
- Cenko, S. B., & Kasliwal, M. M. 2008, *GRB Coordinates Network*, 8417, 1
- Clemens, C., Rossi, A., Greiner, J., McBreen, S., Kruehler, T., Yoldas, A., Yoldas, A. K., & Szokoly, G. 2008, *GRB Coordinates Network*, 8272, 1
- Chornock, R., Li, W., Filippenko, A. V., & Jha, S. 2002, *GRB Coordinates Network*, 1754, 1
- Connaughton, V., & Briggs, M. 2008, *GRB Coordinates Network*, 8408, 1
- Costa, E., et al. 1997, *Nature*, 387, 783
- Crew, G., et al. 2002, *GRB Coordinates Network*, 1734, 1
- Crew, G. B., Villasenor, J., Monnelly, G., Doty, J., Vanderspek, R., & Ricker, G. 2003, *Gamma-Ray Burst and Afterglow Astronomy 2001: A Workshop Celebrating the First Year of the HETE Mission*, 662, 66
- Crew, G. B., Vanderspek, R., Doty, J., Villasenor, J., Monnelly, G., Butler, N., Prigozin, G., & Ricker, G. 2003, *Gamma-Ray Burst and Afterglow Astronomy 2001: A Workshop Celebrating the First Year of the HETE Mission*, 662, 70
- Crew, G. B., et al. 2003, *ApJ*, 599, 387
- da Costa, G. S., Noel, N., & Price, P. A. 2004, *GRB Coordinates Network*, 2765, 1
- Daigne, F., & Mochkovitch, R. 1998, *MNRAS*, 296, 275
- Daigne, F., & Mochkovitch, R. 2003, *MNRAS*, 342, 587
- de Ugarte Postigo, A., et al. 2006, *ApJ*, 648, L83

de Ugarte Postigo, A., et al. 2007, A&A, 462, L57

Djorgovski S. G. et al., 2001, GRB Coordinates Network, 1108, 1

Eichler, D., & Waxman, E. 2005, ApJ, 627, 861

Fendt, C., & Ouyed, R. 2004, ApJ, 608, 78

Fenimore, E. E., in 't Zand, J. J. M., Norris, J. P., Bonnell, J. T., & Nemiroff, R. J. 1995, ApJ, 448, L101

Fenimore, E. E., et al. 2004, GRB Coordinates Network, 2735, 1

Fishman, G. J., et al. 1994, ApJS, 92, 229

Fishman, G. J., & Meegan, C. A. 1995, ARA&A, 33, 415

Fox, D. W., & Price, P. A. 2002, GRB Coordinates Network, 1731, 1

Fox, D. B., & Moon, D.-S. 2004, GRB Coordinates Network, 2734, 1

Fruchter, A., Levan, A., Vreeswijk, P., Holland, S. T., & Kouveliotou, C. 2002, GRB Coordinates Network, 1781, 1

Galama, T. J., et al. 1998, Nature, 395, 670

Galassi, M., et al. 2004, GRB Coordinates Network, 2770, 1

Gehrels, N., & Swift Team 2005, Bulletin of the American Astronomical Society, 37, 1324

Gehrels, N., et al. 2005, Nature, 437, 851

Gilmore, R. C., Madau, P., Primack, J. R., & Somerville, R. S. 2008, arXiv:0811.1984

Goldstein, A., & van der Horst, A. 2008, GRB Coordinates Network, 8245, 1

González, M. M., Dingus, B. L., Kaneko, Y., Preece, R. D., Dermer, C. D., & Briggs, M. S. 2003, Nature, 424, 749

Greiner, J., Peimbert, M., Estaban, C., Kaufer, A., Jaunsen, A., Smoke, J., Klose, S., & Reimer, O. 2003, GRB Coordinates Network, 2020, 1

Greiner, J., Rau, A., & Klose, S. 2003, GRB Coordinates Network, 2271, 1

Greiner, et al. *in preparation* 2008

Guidorzi, C., Margutti, R., & Mao, J. 2008, GRB Coordinates Network, 8410, 1

- Hakkila, J., Giblin, T. W., Norris, J. P., Fragile, P. C., & Bonnell, J. T. 2008, *ApJ*, 677, L81
- Hauser, M. G., & Dwek, E. 2001, *ARA&A*, 39, 249
- Hearty, F., et al. 2006, *GRB Coordinates Network*, 4611, 1
- Heise, J., et al. 1997, *IAU Circ.*, 6654, 2
- Hjorth, J., et al. 2003, *ApJ*, 597, 699
- Hjorth, J., et al. 2003, *Nature*, 423, 847
- Hoover, A. S., et al. 2008, *American Institute of Physics Conference Series*, 1000, 565
- Huang, K. Y., et al. 2005, *ApJ*, 628, L93
- Hurley, K., et al. 1994, *Nature*, 372, 652
- Hurley, K., et al. 2003, *Gamma-Ray Burst and Afterglow Astronomy 2001: A Workshop Celebrating the First Year of the HETE Mission*, 662, 42
- Ioka, K., & Nakamura, T. 2001, *ApJ*, 554, L163
- Ioka, K., Kobayashi, S., & Zhang, B. 2005, *ApJ*, 631, 429
- Jakobsson, P., et al. 2005, *ApJ*, 629, 45
- Katz, J. I. 1994, *ApJ*, 422, 248
- Katz, J. I. 1994, *ApJ*, 432, L27
- Kawai, N., et al. 2003, *Gamma-Ray Burst and Afterglow Astronomy 2001: A Workshop Celebrating the First Year of the HETE Mission*, 662, 25
- Khamitov, I., et al. 2004, *GRB Coordinates Network*, 2740, 1
- Klebesadel, R. W., Strong, I. B., & Olson, R. A. 1973, *ApJ*, 182, L85
- Kneiske, T. M., Mannheim, K., & Hartmann, D. H. 2002, *A&A*, 386, 1
- Kocevski, D., Ryde, F., & Liang, E. 2003, *ApJ*, 596, 389
- Kodama, Y., Yonetoku, D., Murakami, T., Tanabe, S., Tsutsui, R., & Nakamura, T. 2008, *MNRAS*, 391, L1
- Kosugi, G., et al. 2004, *PASJ*, 56, 61

- Lamb, D. Q., York, D. G., McMillan, R. J., & Johnston, D. 2002, GRB Coordinates Network, 1230, 1
- Levan, A. J., et al. 2006, ApJ, 648, L9
- Liang, E., Kusunose, M., Smith, I. A., & Crider, A. 1997, ApJ, 479, L35
- Liang, E. W., et al. 2006, ApJ, 646, 351
- Liang, E.-W., Zhang, B.-B., Stamatikos, M., Zhang, B., Norris, J., Gehrels, N., Zhang, J., & Dai, Z. G. 2006, ApJ, 653, L81
- Lithwick, Y., & Sari, R. 2001, ApJ, 555, 540
- Lloyd-Ronning, N. M., Fryer, C. L., & Ramirez-Ruiz, E. 2002, ApJ, 574, 554
- 1997, Irish Astronomical Journal, 24, 83
- Lu, R.-J., Qin, Y.-P., Zhang, Z.-B., & Yi, T.-F. 2006, MNRAS, 367, 275
- Lyutikov, M., & Blackman, E. G. 2001, MNRAS, 321, 177
- MacFadyen, A. I., & Woosley, S. E. 1999, ApJ, 524, 262
- Malesani, D., Antonelli, L. A., Covino, S., Palazzi, E., Andreuzzi, G., & Tassicini, G. 2006, GRB Coordinates Network, 4561, 1
- Mangano, V., La Parola, V., Mineo, T., Tagliaferri, G., Romano, P., O'Brien, P., & Burrows, D. N. 2006, GRB Coordinates Network, 4560, 1
- Matheson, T., et al. 2003, ApJ, 599, 394
- Medvedev, M. V. 2000, ApJ, 540, 704
- Meegan, C. A., Fishman, G. J., Wilson, R. B., Horack, J. M., Brock, M. N., Paciasas, W. S., Pendleton, G. N., & Kouveliotou, C. 1992, Nature, 355, 143
- Meegan, C., et al. 2008, American Institute of Physics Conference Series, 1000, 573
- Meszáros, P., & Rees, M. J. 1994, MNRAS, 269, L41
- Meszáros, P. 2006, Reports on Progress in Physics, 69, 2259
- Metzger, M. R., Djorgovski, S. G., Kulkarni, S. R., Steidel, C. C., Adelberger, K. L., Frail, D. A., Costa, E., & Frontera, F. 1997, Nature, 387, 878

- Milgrom, M., & Usov, V. 1996, *Astroparticle Physics*, 4, 365
- Mirabal, N., & Halpern, J. P. 2003, *GRB Coordinates Network*, 2273, 1
- Moiseev, A. A., Hartman, R. C., Ormes, J. F., Thompson, D. J., Amato, M. J., Johnson, T. E., Segal, K. N., & Sheppard, D. A. 2007, *Astroparticle Physics*, 27, 339
- Monnelly, G., et al. 2003, *Gamma-Ray Burst and Afterglow Astronomy 2001: A Workshop Celebrating the First Year of the HETE Mission*, 662, 49
- Nakar, E. 2007, *Phys. Rep.*, 442, 166
- Nolan, P. L., et al. 1992, *IEEE Transactions on Nuclear Science*, 39, 993
- Norris, J. P., Marani, G. F., & Bonnell, J. T. 2000, *ApJ*, 534, 248
- Norris, J. P., Bonnell, J. T., Kazanas, D., Scargle, J. D., Hakkila, J., & Giblin, T. W. 2005, *ApJ*, 627, 324
- Nousek, J. A., et al. 2006, *ApJ*, 642, 389
- Omodei, N. 2008, *GRB Coordinates Network*, 8407, 1
- Pélangéon, A., et al. 2008, *A&A*, 491, 157
- Perri, M., Preger, B., & Stratta, G. 2008, *GRB Coordinates Network*, 8261, 1
- Piran, T. 1999, *Phys. Rep.*, 314, 575
- Piran, T. 2005, *Reviews of Modern Physics*, 76, 1143
- Preece, R. D., Briggs, M. S., Mallozzi, R. S., Pendleton, G. N., Paciasas, W. S., & Band, D. L. 1998, *ApJ*, 506, L23
- Preece, R. D., Briggs, M. S., Mallozzi, R. S., Pendleton, G. N., Paciasas, W. S., & Band, D. L. 2000, *ApJS*, 126, 19
- Price, P. A., et al. 2002, *ApJ*, 571, L121
- Pugliese, G., et al. 2005, *A&A*, 439, 527
- Qin, Y.-P. 2002, *A&A*, 396, 705
- Qin, Y.-P., Zhang, Z.-B., Zhang, F.-W., & Cui, X.-H. 2004, *ApJ*, 617, 439
- Qin, Y.-P., & Lu, R.-J. 2005, *MNRAS*, 362, 1085

- Ramirez-Ruiz, E., Dray, L. M., Madau, P., & Tout, C. A. 2001, *MNRAS*, 327, 829
- Rau, A., et al. 2004, *A&A*, 427, 815
- Rau, A., Salvato, M., & Greiner, J. 2005, *A&A*, 444, 425
- Razzaque, S., Dermer, C. D., & Finke, J. D. 2008, arXiv:0807.4294
- Ricker, G., et al. 2001, GRB Coordinates Network, 1096, 1
- Ricker, G., et al. 2002, *ApJ*, 571, L127
- Ricker, G., et al. 2002, GRB Coordinates Network, 1220, 1
- Ricker, G., et al. 2002, GRB Coordinates Network, 1229, 1
- Ricker, G. R., et al. 2003, *Gamma-Ray Burst and Afterglow Astronomy 2001: A Workshop Celebrating the First Year of the HETE Mission*, 662, 3
- Riess, A. G., et al. 2007, *ApJ*, 659, 98
- Rybicki, G. B., & Lightman, A. P. 1986, *Radiative Processes in Astrophysics*, by George B. Rybicki, Alan P. Lightman, pp. 400. ISBN 0-471-82759-2. Wiley-VCH, June 1986.,
- Ryde, F., & Petrosian, V. 2002, *ApJ*, 578, 290
- Ryde, F. 2004, *ApJ*, 614, 827
- Sakamoto, T., et al. 2005, *ApJ*, 629, 311
- Sakamoto, T., et al. 2005, GRB Coordinates Network, 3189, 1
- Sakamoto, T., et al. 2008, *ApJ*, 679, 570
- Sari, R., & Piran, T. 1995, *ApJ*, 455, L143
- Salvaterra, R., Guidorzi, C., Campana, S., Chincarini, G., & Tagliaferri, G. 2008, arXiv:0805.4104
- Sari, R., Narayan, R., & Piran, T. 1996, *ApJ*, 473, 204
- Sari, R., Piran, T., & Narayan, R. 1998, *ApJ*, 497, L17
- Sato, R., Kawai, N., Suzuki, M., Yatsu, Y., Kataoka, J., Takagi, R., Yanagisawa, K., & Yamaoka, H. 2003, *ApJ*, 599, L9
- Sato, R., et al. 2005, *PASJ*, 57, 1031

- Shen, R.-F., Song, L.-M., & Li, Z. 2005, MNRAS, 362, 59
- Shirasaki, Y., et al. 2003, PASJ, 55, 1033
- Shirasaki, Y., et al. 2003, GRB Coordinates Network, 2322, 1
- Shirasaki, Y., et al. 2008, PASJ, 60, 919
- Spitkovsky, A. 2008, ApJ, 682, L5
- Stanek, K. Z., Garnavich, P. M., Kaluzny, J., Pych, W., & Thompson, I. 1999, ApJ, 522, L39
- Stanek, K. Z., et al. 2005, ApJ, 626, L5
- Stecker, F. W., Malkan, M. A., & Scully, S. T. 2006, ApJ, 648, 774
- Stecker, F. W., Malkan, M. A., & Scully, S. T. 2007, ApJ, 658, 1392
- Stratta, G., Perri, M., Preger, B., Barthelmy, S. D., Burrows, D. N., Hoversten, E. A., Roming, P., & Gehrels, N. 2008, GCNR, 166, 1-2 (2008), 166, 1
- Tajima, H. 2006, Nuclear Instruments and Methods in Physics Research A, 569, 140
- Terada, H., Akiyama, M., & Kawai, N. 2004, GRB Coordinates Network, 2750, 1
- Tsutsui, R., Nakamura, T., Yonetoku, D., Murakami, T., Tanabe, S., & Kodama, Y. 2008, MNRAS, 386, L33
- Tsutsui, R., Nakamura, T., Yonetoku, D., Murakami, T., Kodama, Y., & Takahashi, K. 2008, arXiv:0810.1870
- Urata, Y., et al. 2004, ApJ, 601, L17
- van der Horst, A. J., & Connaughton, V. 2008, GRB Coordinates Network, 8141, 1
- Vanderspek, R., et al. 2004, ApJ, 617, 1251
- Vietri, M. 1995, ApJ, 453, 883
- Villasenor, J. N., et al. 2003, Gamma-Ray Burst and Afterglow Astronomy 2001: A Workshop Celebrating the First Year of the HETE Mission, 662, 33
- Villasenor, J., et al. 2003, Gamma-Ray Burst and Afterglow Astronomy 2001: A Workshop Celebrating the First Year of the HETE Mission, 662, 107

- Villasenor, J., et al. 2003, GRB Coordinates Network, 2261, 1
- Vreeswijk, P., Fruchter, A., Hjorth, J., & Kouveliotou, C. 2003, GRB Coordinates Network, 1785, 1
- Waxman, E. 1995, Physical Review Letters, 75, 386
- Wei, D. M., & Gao, W. H. 2003, MNRAS, 345, 743
- Wiersema, K., Starling, R. L. C., Rol, E., Vreeswijk, P., & Wijers, R. A. M. J. 2004, GRB Coordinates Network, 2800, 1
- Yonetoku, D., Murakami, T., Nakamura, T., Yamazaki, R., Inoue, A. K., & Ioka, K. 2004, ApJ, 609, 935
- Yonetoku, D., Yamazaki, R., Nakamura, T., & Murakami, T. 2005, MNRAS, 362, 1114
- Zhang, F.-W., Qin, Y.-P., & Zhang, B.-B. 2007, PASJ, 59, 857

Acknowledgment

I would like to thank to Professor Nobuyuki Kawai who gave me great opportunities to study such wonderful sciences. Thanks to his great work and contribution to some communities, I could spend invaluable life as a astrophysicist in Kawai laboratory. I am also grateful to Dr. Katsuaki Asano who gave me the fruitful advice and suggestion for this thesis and without his support I could not accomplish the thesis. I would like to express my gratitude for Dr. Jun Kataoka who taught me the basis of astrophysics, experimental technique and mental attitude to the research.

I greatly thanks to all *HETE* and *Fermi* members who gave me the opportunity for affiliation to the teams and analyzing the scientific observational data.

I also would like to express my deep gratitude for the Kawai and Terasawa laboratory members, especially Takashi Shimokawabe, Yoshikazu Kanai, Yoichi Yatsu, Rie Sato and Takeshi Nakamori who encouraged me to spend my research life and accomplish the doctoral thesis. I appreciate Yasuyuki Tanaka who is a buddy for my doctorate life. Thanks to his discussion and support, I can not only amplify my knowledge for high-energy astrophysics but also achieve our doctoral life mentally. Toizumi Takahiro provided me the nice pictures in this thesis in response to my hard requirements. I am deeply grateful to Nicolas Vasquez and Kevin Hurley who has improved English in this manuscript.

Finally, I would like to acknowledge my mother, father, grand mother and father, senior and junior brothers and lovely dogs sincerely who has supported my life economically and mentally.